Measuring and Modelling Towline Response Using GPS Aided Inertial Navigation

John A. MacSween

23rd May 2017

Thesis submitted to the University of Strathclyde in fulfillment of the requirements for the award of the degree of Doctor of Philosophy.

Department of Naval Architecture and Marine Engineering.

Signed:

Date: 23rd May 2017

Dedication

Personal

Completing post graduate studies such as these never happen in a vacuum and this one is no different. I would like to thank my family for all their support. Bethan, Eilis and Roddy for welcome distractions, Claire for her unwavering encouragement in getting it over the line and Maureen, for the use of the house in Girvan for a final week of writing up and editing.

Educational

I would like to thank Prof. Incecik for his support over the years and willingness to meet for progress reviews and offering valued advice whenever needed.

Professional

I would like to thank the various tug Masters, Chief Mates and Engineers who assisted me on the placement of loggers over the years. Their curiosity and willingness to help was always appreciated.

During the course of this research, due to issues with the hardware, there have been many trial voyages and would like to thank Hamish from Clyde Marine Motoring Ltd for allowing me access to his vessels for early tests, the ACA Transportation Team for allowing the sanitised data to be logged and the team from Anchor Marine Transportation for their staff's assistance in completing the numerous tug voyage logs.

On occasion, I have been unable to meet tug and barge at the arrival ports and I would like to thank the teams at Malin Group for their patience in carrying the loggers back to home base in Glasgow when asked.

Lastly I would like to thank Steve and Jarek at JRD for assistance in the logger development itself.

Abstract

The offshore towage of large floating structures has been the broad subject of research since the 1960's. The selection of a tug to engage in a tow is based on rules laid down by class and marine warranty surveyors derived from years of experience but a rigorous assessment of these rules based on a comprehensive real world datasets has not been possible.

This is principally due to the nature of these tows, usually employing tugs chartered at short notice from the spot market, the long towline lengths when under tow and the high value of the tow itself.

Given the commercial implications in being able to better match a suitable tug to any given tow, this research lays down the requirements of an ideal dataset, i.e. one that has a record of towline tensions, complete 6DOF of both the tug and tow all recorded to a universal timeline, along with the seastate experienced by the tow at any given point. It then reviews the historical restrictions in gathering this data and that the key issue has been gathering the motions of the unpowered tow and recording the towline tensions.

A methodology is then developed which requires no interference with the towline and draws upon Kalman filters for optimal state estimation of the tug and tow's position and attitude in 3D space driving a lumped mass simulation of the towline coded in MatLab. The stiffness properties of key elements of the towline are assessed by FEA and observations made on areas where normal industry practice's may be lacking.

Observations on advances in sensor technology as well as other areas for development are then made that provide fertile areas for further research. Finally the full code base for a MatLab, lumped mass simulator is presented in an appendix for future use.

Contents

List of Figures

List of Tables

Nomenclature

AP	Aft perpendicular
BL	Baseline of vessel
CL	Centreline of vessel
CoG	Centre of gravity
$A_{towline}$	Cross sectional area of towline
$A_{C(i\pm\frac{1}{2})}$	Cross sectional areas of the line segments on either side of lumped mass at node “i”
$L_{towline}$	Deployed length of towline
$D_{towline}$	Diameter of towline
$D_{(i\pm\frac{1}{2})}$	Diameter of the line segments on either side of lumped mass at node “i”
D^m	Down position measurements from GPS chipset
$F_{DN(i)}$	Drag force (normal) at node “i”
E^m	East position measurements from GPS chipset
D^K	Estimated Down offsets at a connection point
$\dot{D}^K$	Estimated Down velocities at a connection point
E^K	Estimated East offsets at a connection point
$\dot{E}^K$	Estimated East velocities at a connection point
N^K	Estimated North offsets at a connection point (subscripts “T” and “B” map to “tug” and “barge” respectively where indicated in the text)
$\dot{N}^K$	Estimated North velocities at a connection point
$C_\alpha, C_\beta, C_\gamma$	Euler rotation matrices about longitudinal, transverse and vertical axis respectively
$z_N\,(t)$	Forced towline oscillations at node N (tug) mapped to the Down global direction

$x_N\,(t)$	Forced towline oscillations at node N (tug) mapped to the East global direction
$y_N\,(t)$	Forced towline oscillations at node N (tug) mapped to the North global direction
$z_0\,(t)$	Forced towline oscillations at node 0 (barge) mapped to the Down global direction
$x_0\,(t)$	Forced towline oscillations at node 0 (barge) mapped to the East global direction
$y_0\,(t)$	Forced towline oscillations at node 0 (barge) mapped to the North global direction
α^K,β^K,γ^K	Kalman filtered vessel roll, pitch and yaw estimates
$\dot{\alpha}^K$,$\dot{\beta}^K$,$\dot{\gamma}^K$	Kalman filtered vessel roll, pitch and yaw velocity estimates
$[\bar{x}]_k$	Kalman filter "a priori state" vector at time index k
$[P]$	Kalman filter estimation covariance matrix
$[K]$	Kalman filter gain matrix
$[E]$	Kalman filter innovation or error vector
$[C]$	Kalman filter measurement matrix
$[y]_k$	Kalman filter "measurement" vector at time index k
$[S_w]$,$[S_z]$	Kalman filter process noise covariance and measurement noise covariance matrices
$[A]$	Kalman filter state transition matrix
$[x]_k$	Kalman filter "state" vector at time index k
$l_{i\pm\frac{1}{2}}$	Length of the line segments on either side of lumped mass at node “i”
$k_{towline}$	Linear stiffness of towline
$\triangle x^c$	Longitudinal offset between CoG and towline connection point on vessel (+ve forward)
$\triangle x^d$	Longitudinal offset between sensor and CoG on vessel (+ve forward)
$\dot{D}^m$	Measured Down velocities at a connection point
$\dot{E}^m$	Measured East velocities at a connection point
$\dot{N}^m$	Measured North velocities at a connection point
$C_{N(i\pm\frac{1}{2})}$	Normal drag coefficient of the line segments on either side of lumped mass at node “i”
N^m	North position measurements from GPS chipset
N	Number of lumped masses in towline
n	Number of springs in bridle section

α^m,β^m	Roll and pitch measurement as recorded at a data logger position
$\dot{\alpha_t}$,$\dot{\beta}_t$,$\dot{\gamma_t}$	Roll, pitch and yaw velocity as recorded at a data logger position
k_c	Stiffness of bridle chain
k_b	Stiffness of bridle segment
k_{bridle}	Stiffness of bridle system
k_t	Stiffness of bridle tri-plate
k_s	Stiffness of shackle component
$\ddot{x^K}$,$\ddot{y^K}$,$\ddot{z^K}$	Surge, sway and heave acceleration as estimated at a towline connection point
$\ddot{x^m}$,$\ddot{y^m}$,$\ddot{z^m}$	Surge, sway and heave acceleration as recorded at a data logger position
$\ddot{x^d}$,$\ddot{y^d}$,$\ddot{z^d}$	Surge, sway and heave acceleration as recorded at a data logger position but corrected for gravity vector
$\ddot{x^g}$,$\ddot{y^g}$,$\ddot{z^g}$	Surge, sway and heave acceleration as translated to vessel CoG position from a logger position
$C_{T(i\pm\frac{1}{2})}$	Tangential drag coefficient of the line segments on either side of lumped mass at node "i"
$T_{i\pm\frac{1}{2}}$	Tensions in the line segments on either side of lumped mass at node "i"
Δt	Time step for numerical simulation
j	Time step index in Lumped mass pseudo code
C_{6x36}	Towline metallic area factor
$\triangle y^c$	Transverse offset between CoG and towline connection point on vessel (+ve starboard)
$\triangle y^d$	Transverse offset between sensor and CoG on vessel (+ve starboard)
$\triangle z^d$	Vertical offset between sensor and CoG on vessel (+ve downward)
$\triangle z^c$	Vertical offset offset between CoG and towline connection point on vessel (+ve downward)
$V_{N(i\pm\frac{1}{2})}$	Water velocity normal to the line segments on either side of lumped mass at node "i"
x_i,y_i,z_i	x, y and z positions of the lumped mass at node "i"
γ^m	Yaw angle derived from GPS reported heading
E_s	Young's Modulas of steel
$E_{i\pm\frac{1}{2}}$	Young's Modulas of the line segments on either side of lumped mass at node "i"

Chapter 1

Introduction

1.1 Background

The heavy-lift market has seen significant expansion and change in the last couple of decades [Van Hoorn (2008), Banks (2008)] with both existing shipowners expanding and upgrading their fleet, and new owners entering the market with new-builds and conversions of their own. The tug market too has seen growth and change [Beegle (2007)] with larger capacity tugs becoming the norm. In addition, associated dry transportation barges are also increasing in size and number with the standard "North Sea Barge", 90m x 27.5m x 6.1m @ circa. 10,000 Te DWT, which previously represented the bulk of the higher capacity barge supply being replaced by a newer generation of barges of the order of 130m x 34m x 7.5m @ circa 19,000 Te DWT and above.

There are numerous studies which examine the various aspects of transportation of cargoes on powered vessels, for example [Bos (2008), Aalbers et al (1996)] and this area of research has been well served. This is due to the exposure of this aspect of the industry as well as the relative ease by which data can be gathered, i.e. powered vessels provide infrastructure for on-board, real-time measuring equipment and the complexity of the problem is bounded by the conventional 6 Degrees of Freedom (DOF) system of a single floating body albeit, often with complicating factors, such as exceptionally high or overhanging cargo (see figure 1.1.1 for typical examples of a towed and untowed transport).

The tug and barge system has also been studied widely with research utilising models of differing degrees of complexity. However a common factor amongst the research reviewed to date is a lack of comprehensive field data of the combined response of the tug and tow under varying conditions both for reference and verification of models proposed.

In terms of research in this field, an ideal, continuous data-set would include the 6 DOF response of both tug and tow, towline loads and relative position of tug and tow at all phases of the voyage, all against a universal and common time-line .

The ability to asses the utilisation of a tug's bollard pull and effectiveness in various sea states based on comprehensive field data is of great interest, not only in academia, but also has significant commercial implications to various operators. The ability, margins of safety and detailed capability of their tonnage to execute a particular tow is currently based on a wide range of different methodologies all of which make their own assumptions on the effectiveness of various parameters.

Therefore any research that can comment on this assessment of tonnage for a particular tow has significant safety implications, while also being of great commercial interest as well.

Without comprehensive data from the field, however, a meaningful assessment of the principle methodologies currently employed is not possible, therefore it is the opinion of the author that any research that can add meaningfully to this discussion is not only worthwhile, but essential.

1.2 Objectives

It is, therefore, the objective of this research to explore novel options for obtaining field data of the interaction between the tug and tow. It will also explore any limitations and restrictions intrinsic to the operations themselves and propose solutions or areas worthy of further investigation. It must be borne in mind at all times, that these are commercial operations, i.e. no tugs and barges were actually chartered specifically for the benefit of this research and therefore any system that will be of practical, long term use must be easily deployed to "voyages of opportunity", non invasive and self sufficient for long periods of unmanned operations. In this way, the restrictions placed on this research are wholly representative of the challenges facing others in the field in the past. These will be covered in more detail in the literature review to follow.

The relative lack of a means of recording the full response of the system during such towages proves a barrier to better understanding the actual real world response of a number of towages and leaves the industry with little means of easily and economically assessing the utilisation of their, often expensive, assets on such operations.

A hardware based device was developed which records both global positions derived from the GPS network and local motions based on solid state, Micro electromechanical Systems (MEMS). As these devices were not developed specifically for this purpose, the accuracy of the MEMs and GPS systems will be reviewed and their adequacy, or otherwise, commented upon. Two such devices will be deployed

(a) Powered voyage example (www.dockwise.com)

(b) Towed voyage example (http://www.flickr.com/photos/qeclasscarriers)

Figure 1.1.1: Typical powered and towed heavy cargo sea transportation projects

for any given tow, one on the tug and one on the barge. The data will be explored and the viability examined of extracting accurate towline tensions which can then be used in future research for recording and deriving towage effort and tug utilisation. A versatile numerical simulator of the towline response, capable of being driven by measured responses, will be developed.

Chapter 2

Literature Review of Related Work

Due to the relatively broad scope of this thesis, the review of existing and applicable literature will be split into three sections.

First, in section 2.1, existing industry guidelines will be reviewed, as they stand at the time of writing, and discussed in terms of their recommendations for pairing any given tow with a suitable towing vessel including the equipment required for connecting tow to the towing vessel. This will allow a review of the range of tug bollard pull (BP) and equipment minimum breaking loads (MBL) later in the thesis.

Thereafter, in section 2.2.1, literature relating to the numerical approach adopted in the simulations for this research will be reviewed. A brief history of the methods used, and where they have developed from will be explored. Here, it will also be shown that the specific theory selected is both applicable to the cases in question and has precedence in such simulations.

Finally, in section 2.2.2, as these simulations are driven by real data gathered on live towage operations, a summary of the current state of the technology behind the data capture and processing options will be given. Its development and use in general navigation problems as well as specific marine applications will be discussed with data processing techniques also touched upon before being expanded in greater detail later in the thesis.

2.1 Applicable Industry Guidelines

Reference material and guidance for commercial towages in Europe historically focused on 2 principle publications namely [DNV (1996)] and [GL Noble Denton (2013)] with the relatively new [ISO 19901-6 (2009)] added in 2009. Extracts of the relevant rules and how they specifically affect sizing and selection of towing gear is covered in more detail in section 5.1.2 on page 94 later.

The newer DNV offshore standards, [DNV (2015)] and [DNV (2012)], superseded [DNV (1996)] and themselves, represented the definitive standard under DNV until mid 2016.

During 2016, the development of standards employed in the offshore heavy transport industry has seen a period of consolidation resulting in a single unified approach.

Noble Denton merged with Germanischer Lloyd in 2009 and the merged entity “GL Noble Denton” was officially launched during 2010 marketing itself as the oil and gas business of Germanischer Lloyd. GL Noble Denton guidelines in use within the industry during the time of execution of this research were the 2010 revision, [GL Noble Denton (2010)], latterly updated to [GL Noble Denton (2013)]. This change reflected acknowledged issues with the older regulations especially when applied to the sizing of equipment for very large tugs (280 Te bollard pull and above) as well as issues faced where towing bridles, normally supplied with the barge and pre-fitted for charterers use, was incompatible with a project that ended up using a tug drawn from the spot market that was “over specified” for the tow in question. This can arise as barge towing equipment is normally specified in relation to the minimum breaking strength (MBL) of the main towline which itself, in turn, is related to the certificated bollard pull of the tug.

It was then announced in 2012 that GL and DNV were to merge. This then preceded a final merger of rules replacing [DNV (2015)], [DNV (2012)], and [GL Noble Denton (2013)] with a new standard [DNVGL (2016)] during the summer of 2016 and further updated in November of that same year.

Parallel to this, perhaps to offer industry an alternative standard while this consolidation took place, the ISO/TC 67 Technical Committee charged with the “Standardization of the materials, equipment and offshore structures used in the drilling, production, transport by pipelines and processing of liquid and gaseous hydrocarbons within the petroleum, petrochemical and natural gas industries” worked on the development of a series of documents under the ISO 19901 standard. These cover a broad range of subjects related to the offshore exploitation of hydrocarbons including met ocean considerations, seismic design, topside structural design, geotechnical considerations, weight control, stationkeeping and, of specific interest here, marine operations [ISO 19901-6 (2009)]. These later guidelines pull together, into one location, a large number of details on a range of key subjects for offshore marine operations but largely duplicates work already found both in the original DNV and GL Noble Denton standards as well as the newer, harmonised version.

There are also a set of guidelines written by London Offshore Consultants in the late nineties, [LOC (1999)], and published by Oilfield Publications Ltd. These largely repeat/restate guidance already available in other publications and is rarely referred to in the authors experience in the industry today. The publishers also advise that these are now no longer maintained and so mentioned here only for completeness.

In addition to commercial guidelines the UK and US navies also have their own, internal publications giving guidance for mooring and towage operations.

In the UK, the MOD's Defence Standard (DefStan) most applicable to this research is "Requirements for Anchoring, Berthing, Towing and Securing to a Buoy", [MOD (2002)] however it largely deals with the equipment found on board, or for the use of, MOD assets and how to connect/access them for towage and mooring operations. There is no significant mention of requirements for the sizing of suitable tugs and towing equipment for non naval ship tows other than offering guidance on calculating the expected drag on the tow. This DefStan has since been declared obsolete and experience with the MOD's salvage and marine operations team has shown that they tend to refer to the industry guidelines above where matters are not covered by their own internal seamanship guidelines.

The U.S. Navy's towing manual, [US Navy (2002)] goes into great detail on matters relating to tug selection and towage for the full range of vessels within the American fleet as well as an overview the following:

- Operations overview
- Overview of towing vessels
- Towing system design
- Towline system components
- Tow planning and preparation
- Special tows
- Heavy lift transport
- Appendices A through R covering broad range of practical checklists and equipment guidance for the towing of vessels and floating bodies.

For a newcomer to the industry, it serves as an excellent introduction to the field.

2.2 Theoretical Literature Review

2.2.1 Numerical Towline Simulation

The simulation of marine cables has had broad academic attention over the last 50 - 60 years due to its prevalence in a wide variety of offshore and marine problems with particular significance in both Naval and Offshore Oil and Gas sectors.

The modeling of subsea cables, moorings and towlines can be achieved by one of either two, broad, methodologies namely the Continuum Method (CM) or the Lumped Mass(LM)/Finite Element Methods (FEM).

The continuum method relies on, as its name suggests, continuous mathematical descriptions of the towline to model its behaviour in that the cable is modelled as a continuous system. Mathematically, it is simulated via partial differential equations which are solved to determine the cables motions and dynamic tensions.

Lumped mass and finite element methodologies, on the other hand, discretise the towline into segments for simulation in the time domain. The cable is modelled as a series of discrete lumped masses connected by massless spring. The governing equations, based on Newton's law of motion, are then solved via a, suitable, numerical algorithm.

The focus here is on the development of the lumped mass/finite element method as it is the chosen numerical method employed in this research. The benefit this technique brought to the research was the ease by which complex cables and situations could be simulated in the time domain. Composite arrangements of wire cables, chain bridles and significant dead weights along the length of the line as well as varying drag and stiffness characteristics could all be easily incorporated.

Finite element methods discretise the line as entities that can have both constant or varying properties along the length of each segment. The elastic response, hydrodynamic drag and bending resistance is resolved over the length of each element and modeled to varying degrees of mathematical and physical accuracy, depending on the particular implementation in question. These simplifications are then applied solely at the ends of elements, i.e. at the interface with its neighbour.

With lumped mass methodologies the towline is modeled as a series of massless springs connecting a string of concentrated masses [Huang (1994)]. The springs have an associated stiffness value that represent the axial stiffness of the segment in question and this need not be constant from element to element nor even be constant with respect to time. The remaining physical properties and environmental effects acting on each element in the discretised model are treated as acting on a point mass concentrated at the virtual, or assumed, junction between adjacent elements, i.e. the mass, buoyancy and drag are "lumped" at the nodes of the model. It can also take account of, or ignore, bending stiffness between the elements. Detail on how this was achieved here is discussed in greater detail in section 5.3.1.1 and illustrated in figure 5.3.1 later, which is as outlined in the original paper [Huang (1994)].

A comparison of LM and FEM was performed by [Leonard and Nath (1980)] who found that both methods were equally accurate if proper attention was paid to the boundary conditions and the degree of discretisation and [Huang (1994)] showed that, in the limit, the ordinary differential equations used to

model the LM method pass over into the continuous partial differential governing equations for the Continuum Method.

Reviews of the progression of the numerical technique are well documented in many of the papers published on the subject since the early 1960's. One of the earliest works which used a LM technique in a marine cable application, albeit in two dimensions, was a simulation of a subsea mooring for the US Navy [Walton and Polachek (1959)], although even this work is significantly pre-dated by work of Johann Bernoulli in the 1720s, [Stewart (2012)] who modeled instrument strings as masses joined together by springs. In [Walton and Polachek (1959)] the authors looked at the specific problem of modeling, efficiently, the transient motions of a mooring to a subsea anchor location but already they had recognised the wider application of the method to numerical simulation of a wider range of problems such as cable laying and the towing of ships or other, floating, marine structures.

Since then the method has been widely developed and the three dimensional numerical method employed in this thesis can be traced through the works of [Strandhagen and Thomas (1963)] followed by [Boeing (1966)] and [Schram and Reyle (1968)] with [Cannon and Genin (1972)] and [Choo and Casarella (1972)] culminating in the work of [Sanders (1982)] which in turn preceded the rigorous development of the 3 dimensional technique modified and employed here, [Huang (1994)].

As mentioned above, it was recognised at the earliest stages of the development of the procedure [Walton and Polachek (1959)], that the numerical methodology has a wide range of applications and many papers have been published covering moorings, riser simulation, subsea deployment of equipment, towed arrays and single body objects as well as towage of floating structures such as vessels and barges. It is work on the latter that is of particular interest to this author and a review of key literature on this subject is summarised in the remainder of this section.

A significant body of work in the field of towline modeling arose around the mid 1980's due to an extensive research programme being instigated by the Dutch Foundation for the Coordination of Maritime Research, the aim of which was to gain a better understanding in the dynamic response of towlines during wet towage of floating bodies. In an example in [van den Boom (1986)] reference is made to a series of recordings made during a number of full scale towages. The recordings were of short duration, approximately 35 minutes each, and captured the full 6 degrees of freedom on the tug only. These readings were used in the paper to derive a spectra of tow force for each tow and some discussion on this was made. Numerical runs, using two dimensional lumped mass code presented in [van den Boom (1986)], were made with the tug end of the towline subject to irregular motions derived from the full scale readings as well as baseline harmonic motions on a variety of towline configurations. The tow end of the towline was assumed to remain fixed. Comment was made on the effect of the towline makeup and stiffness on the dynamic amplification of maximum tensions and some conclusions drawn on broad recommendations for towline selection and arrangements. Interestingly no direct comparisons were made between

the numerical and recorded runs in the main body of the paper although some plots were published in the discussions and the author noted that subsequent work had been done on this and those plots presented seemed to show reasonable correlation between the two. Also as the code employed was 2 dimensional, only surge and heave motions were taken into account. Sway motions were ignored yet the time line traces shown in the report indicated that these were of a greater magnitude than the surge and heave motions albeit acting parallel to the principle elongation axis of the towline and so assumed to have little effect.

As no readings were made of the motions of the tow, the effect of these on the towline tension could not be made however the author made the assumption that the motions of the tug and tow were uncoupled and comparing the typical difference between the mass, inertia and hydrodynamic response of the tug and the tow the first order motions of the tug in heavy seas represented the most significant contribution. A particularly interesting observation that was made by the author, and repeated in subsequent work by him, [van den Boom and Walenkamp (1986)], and others was that, although counter intuitive, reducing the stiffness of the towline, and often its strength, may serve to increase the margins of safety by reducing the dynamic amplification of towline tensions given that they are a function of towline stiffness. It was also commented that there are means of reducing the towline stiffness by using alternative materials such as polypropylene stretchers, that has no effect on the safe working load of towline as a whole. It is noted in [GL Noble Denton (2013)] however that there are maintenance and operational issues to contend with associated with using less physically robust elements within a wire/chain towline arrangement.

A number of thesis and experiments can be found produced by staff and postgraduates at the Massachusetts Institute of Technology under the supervision of Professor Jerome Milgram. Of particular relevance to this research is the work presented in [Christensen (1989)] where a proposal was developed for a full scale towing model verification experiment. In his research Christensen realised that portability, self sufficiency and low power footprint were all of paramount importance in the success of the data capture. Here he proposed a real time telemetry link between the tug and the tow to maintain the accurate and common baseline time line required for the integration of data together to form a fully cohesive data set. The final implementation of data recording required a technician to be ferried to the tow, start up a generator and commence logging data in 30 - 45 min burst sessions. The recording of data was the best that could be realistically achieved with the technology readily available at the time but does not meet the criteria laid down here for this research.

In [Thomas (1994)] a test program was put together in conjunction with the US Navy to validate the empirical model being used at the time, which itself was developed by [Milgram et al (1988)], and thereafter investigate issues noted following an instrumented tow reported in [Frimm and Milgram (1991)] where a semi-empirical correction was proposed to account for low frequency fluctuations identified during instrumented towage runs. [Thomas (1994)] developed a numerical model which was partly validated against

measured data and was then used to directly review the effect of composite towlines incorporating a “stretcher” and the ability of the same to reduce peak tensions. The thesis also verified the significance of low frequency tension variations. The measurement programme in this particular study identified four important and key areas of data acquisition, namely tug motions, tow motions, towline tension/elongation, and environmental conditions. Again, due to issues with the power consumption of the equipment employed, data runs were limited to batches of 30 minutes duration each.

Towline tension was recorded by means of load-cells installed at the tow end (a defuelled nuclear submarine), and via a “carpenter stopper” (see figure 3.3.1 for an example set of a “carpenter stopper”) at the tug end, thereby allowing the wire to remain spooled on the tug’s winch drum at all times. The GPS system employed on both the tug and the tow were noted to have an error margin of +/-30m each and therefore decided not to be of sufficient accuracy to calculate towline extension and shearing of the tow, therefore a hand held laser range finder was employed and manually trained on a target on the submarine’s bridge. Issues with “drop outs” and spurious readings were noted due to measurements often being taken in heavy seas. Despite the limitations of the data captured for reasons beyond the author’s control (an electrical failure on the submarine prevented the capture of any motion data for the tow end), the potential of the method was demonstrated and, interestingly, it was also noted in the conclusions that “the difficulties associated with acquiring data on a ’Tow of Opportunity’ were reaffirmed during the test program” and that, “Though useful data and insight were gained during the test program, the incurred costs were quite high.”

Around the mid nineties work was also done in Japan looking at Lumped Mass modeling of towlines and examining the effect various parameters had on peak tensions. In [Inoue et al (1994)], for example, a dynamic model of a tug/tanker ocean going tow system was made and it assumed the tug motions dominated the response of the system. Correspondence with studies in irregular seas and equivalent harmonic analysis was found and the effect of higher frequency motions on the cross flow drag on the wire, effectively immobilising the wire even where a significant catenary is present, and pulling into play the elastic stretch spring mechanism of the towline was noted. Thereafter, the corresponding, dramatic, increase in maximum tensions this brings was recorded. ([DNV (2011)] refers to this "tunneling effect" as “drag locking” where the towline responds as if it is constrained with a “virtual” tunnel thereby allowing only the elastic, inline response of the towline to be exercised). The validation of the lumped mass method in this case, [Inoue et al (1994)], was via an empirical method of analysing the peak tensions in a towline configuration.

Since the late nineties there seems to have been little major developments in the lumped mass model with most technical research interested in implementing the system, such as [Fitriadhy et al. (2013)] for towed floating structures, albeit in 2D or documenting efficiency improvements or applications with the addition of bending stiffness, [Buckham and Nahon (2001)], or analysing complex interactions with the

seabed, [Long and Jia-han (2006)].

2.2.2 Aided Inertial Navigation Systems

Inertial navigation systems estimate the position of a host vehicle using single and double integration of linear acceleration and angular velocity, respectively, to produce a dead reckoned offset from a known starting point. It is obvious, therefore, due to the integration steps involved, the error in the final position can be highly susceptible to errors and inaccuracies propagated, via this integration, from the initial measurement. There are a variety of means of reducing this error principally by taking an alternative source of position estimate by different means, but with "complimentary" error characteristics

For this reason, and the risks associated with errors in vessel position propagated over long periods of time, traditional inertial navigation systems on waterborne craft have employed bulky, precisely manufactured, earth-centric gimbaled equipment which provides for low drift on estimates. Such systems typically have significantly lower error budgets [Titterton et al (2004)] however both the power consumption requirements and physical size and geometry of such equipment renders it impractical for the application in question here even before considering the extremely high purchase cost.

In recent years there has been an increase in the usage of Micro electromechanical Systems (MEMS sensors) which employ very small (of the order of 1 to 100 micrometres) mechanical systems to detect accelerations and rotational velocity, typically via "mass cantilever" and "vibration/Foucault pendulum" principles respectively. This is principally due to the increasing accuracy and corresponding reduction in fabrication costs of key components of such sensor arrays.

The principle difference in application between the traditional solution of employing gimballed, gyrostabilised inertial logging platform and those utilising MEMS based logging platforms is the fact that the MEMS based devices are physically bound, or "strapped down", to the host body and therefore log accelerations that are in the bodies local frame. This then requires additional transformations involving knowledge of the body's attitude to bring them from the "Body frame" to the "Navigation frame" and therefore allow tracking of the body's position in a useful context.

A review of the published literature concerning "strapdown inertial devices" results in an vast wealth of papers and publications representing the ever increasing interest in these components for use as small, discrete low power inertial sensing packages. These have, in modern times, found themselves integrated into the printed circuit boards of many modern systems from mobile phones and game controllers to laptops and automobiles all fueling growing roles in automotive, civil, defence, biotech and aerospace industries, [Mostov et al (1997)], [Li et al (2003)] and [Pfau et al (2005)].

Limiting the search to general navigation, strapdown MEMS based devices have had limited takeup in serious applications simply due to the fact that, despite improvements in accuracy, they are still susceptible to accumulation of large errors. However a literature review does demonstrate an active interest in their use in this field [Bijker et al (2008)], [Hide et al (2006)], [Maklouf et al (2012)], [Maung et al (2011)], [Motwani et al (2012)] due to the promise of exploiting the benefits of an uninterruptable means of estimating position that does not rely on any external signal or visual aid, enjoyed by their more expensive "military grade" cousins within a much more economical package. Such military grade, non MEMS based INS systems are, now, very much standard equipment in key defence and aerospace applications [Schmidt (2003)] and the benefits of these technological breakthroughs are finding their way down the technological food chain to commercial and even hobbyist applications ([Amahah (2009)] and [DIYDrones.com]). They are also finding their way into more esoteric applications in which their accuracy is not limited to the assumption that the parent body is in fact rigid and local body deformations in large aircraft, as in the case of [Wagner and Kasties (2004)] and bridge structures, as in the case of [Li et al (2003)], are also tracked as part of the filtered solution.

The recent trend of integrating such MEMS devices within mobile handsets and smart phones already equipped with Global Positioning Sensors has accelerated the development of these and reduced their costs, making them more accessible to the research community at large. There has, therefore, been an explosion of interest in their use for dead reckoning problems which is of particular interest to the research presented here.

Full 6 degrees of freedom (6 DOF) Inertial Navigation Systems (INS) typically employ pairs of orthogonally mounted angular rate gyros and linear accelerometers although there has been efforts to look at the effectiveness of carefully positioning a larger array of accelerometers to remove any requirement for gyro sensors, [Chen et al (1994)], [Mostov et al (1997)] and [Nevalainen (2008)].

The aided aspect of this technique implies that the integration errors are corrected by complimentary sensors such as GPS, [Hide et al (2007)], but equally can use other means of fixing ones position such as visual/radar based tracking systems in many aeronautical [Amahah (2009)] and motion capture applications or even pressure transducers such as in [Fernandez et al (2009)] for Autonomous Underwater Vehicles (AUVs) applications.

An excellent background to the use of GPS aided Kalman filters for augmented dead reckoning systems is given in [Omerbashich (2002)] where the background to the kinematics of the system are covered, in this case for aircraft, but equally applicable in slightly modified forms to land or waterborne vehicles. Thereafter he goes on to cover the unbounded error characteristics of uncorrected INS systems before looking at integrating GPS readings into the filter producing blended position estimates that have a bounded error less than, or at least equal to, the GPS position estimate alone.

In GPS Aided Kalman filters, GPS signals are employed to complement and remove the unbounded error resulting from the double integration of accelerometer readings. The crux of the system is that the signals from the relatively low frequency GPS readings are used to continuously correct and update the errors in the much higher frequency accelerometer readings thereby providing the best possible estimate of the sensors position in navigation space taking fully into account the error characteristics of both readings.

It has been appreciated that the relative strengths and weaknesses of GPS and MEMS based INS systems compliment each other. Particularly in defence applications, where jamming of GPS systems exposes troops and mobile assets to disorientation, the supplementation of technologies with autonomous dead reckoning INS systems is an area of active research. In work carried out under contract for the Canadian defence agency by [Arden (2007)], the specific task tackled is to "research, design and build a working prototype of an integrated MEMS/GPS system".

Within marine applications too, the use of augmented INS systems are of interest and their specific use in marine based navigation and survey applications was thoroughly explored in [Moore et al (2008)] which reported on a study commissioned by the General Lighthouse Authorities of the UK and Ireland on "an assessment of the impact that the integration of Global Navigation Satellite Systems (GNSS) with Inertial Navigation Systems (INS) would have on the aids to navigation (AtoN) services currently provided and those to be provided in the future". Most critically, he noted that unbounded horizontal position errors in low cost MEMS based systems were of the order of 26m after 30 seconds, 102m after 1 minute and 429m after 2 minutes. Therefore update times for GPS fixes to correct drifting integration errors were to be kept as low as possible.

Furthermore the use of optimal state Kalman filters for state estimation has an established position in marine research through its use in dynamic positioning systems for offshore vessels and drill units as discussed originally in [Balchen et al (1976)]. More recent trends and applications are summarised in [Cadet (2003)] and in [Fossen and Perez (2009)], where they "introduce the elements of a ship motion-control system, describe the models used for position-regulation and course-keeping control, and discuss how the Kalman filter is used for wave filtering".

2.3 Chapter Summary

In the literature review the state of research and industry guidelines applicable to the body of work that follows have been introduced. A gap in existing capabilities has been demonstrated, the reasons for this summarised, i.e. difficulties in obtaining detailed and comprehensive datasets for "towages of opportunity", as well as moving on to demonstrate that improvements in understanding and technological

capabilities of equipment that, when coupled with established numerical simulation techniques, could provide an novel opportunity to plug this capability gap and, through its application, knowledge gap.

Chapter 3

Data Collection

In order to gather sufficient data to drive our numerical model of the towline with motions exciting both ends of its deployed length, one must, by definition, capture a complete record of the tug and tow's motions throughout a towage operation. This chapter deals with the issues associated with capturing such a dataset and what form the final system employed takes.

3.1 Ideal Dataset

With reference to the summary of existing literature made in chapter 2, the existence of full and complete datasets of tug and barge motions is lacking. The ideal dataset should contain complete information about the 6 DOF of motion on both the tug and the barge against a consistent time line for the entire duration of the tow. Most existing datasets do not contain this level of information with either certain degrees of freedom missing or in some cases, no information on the tow at all, where it is assumed to track the tug with constant speed, and often these missing degrees of freedom are considered to be of lesser importance. In [Thomas (1994)] the 6 full DOF of the tug was recorded but only the offset between the tug and the tow (which was a defueled nuclear submarine in transit for decommissioning) recorded to give an estimate of the surge response of the tow. In this case heading could only be estimated and not accurately tracked.

Therefore in order to capture this degree of fidelity in the dataset required for post-processing into towline tensions, the following key requirements must be met:

- Record of motions in all 6DOF on both tug and tow required
- Consistent timeline for tug and tow data to allow correlation of recordings after the event

- Full dataset for the entire tow duration
- Seastate information
- Deployed towline length
- Bollard Pull/Tug power employed during tow

In order to capture this complete dataset the motions will be captured by a series of triaxial accelerometers and gyroscopes. The long term drift of these will be corrected by periodic GPS readings which in turn will be timestamped on each recording device from a common source (i.e. the GPS satellite clock itself) and therefore allow regular updates to the internal clock of each device against an external source. This timestamp will then be reflected in each of the high frequency readings recorded across the sensor suite.

See figure 3.1.1 for graphical overview of key features of the process with the Kalman filter block diagram expanding on the processing of data covered in chapter 4.1, reference figure 4.1.2.

Data was sampled at a rate sufficient to capture the required detail and previous reports have found that relatively low frequency capture rates have been sufficient to describe the surge response of the towline, in [van den Boom (1986)] a sampling rate of 4Hz was employed successfully for each of the 35 minute duration recording runs. For this work a sampling rate of 10 Hz is proposed. This will be sufficient to capture the shorter term response of the rolling and pitching of the vessels as well as providing a sound base for the integration scheme required to convert these motions recordings into positional data. GPS updates are governed by the quality of the signal but data capture target of updates around every 1-2 secs was achieved. More detail on the quality of data gathered will be outlined in chapter 6

For use later on in this research, the time series, after post processing through the various estimate improvement filters, will be upsampled for numerical stability for inputting into the lump mass routines.

This system essentially represents a simple, standalone inertial navigation system which was then deployed to known locations on each of the tug and tow. By combining the knowledge of attachment locations to the geometry of the vessels and assumed centres of rotation, the motions could then be translated into end point motions on the towline. The characteristics of the sensor suite within this simple INS system and more specific details of each of the components is outlined in the remainder of this chapter.

For capturing voyage specific data a log form was drawn up which was then presented to the master with the request that he complete every change of the watch or during any relevant change in circumstances of interest to the study (such as taking in or paying out of the towline or change in weather or seastate). The cover sheet and recording tables of these forms are shown in figure 3.1.3.

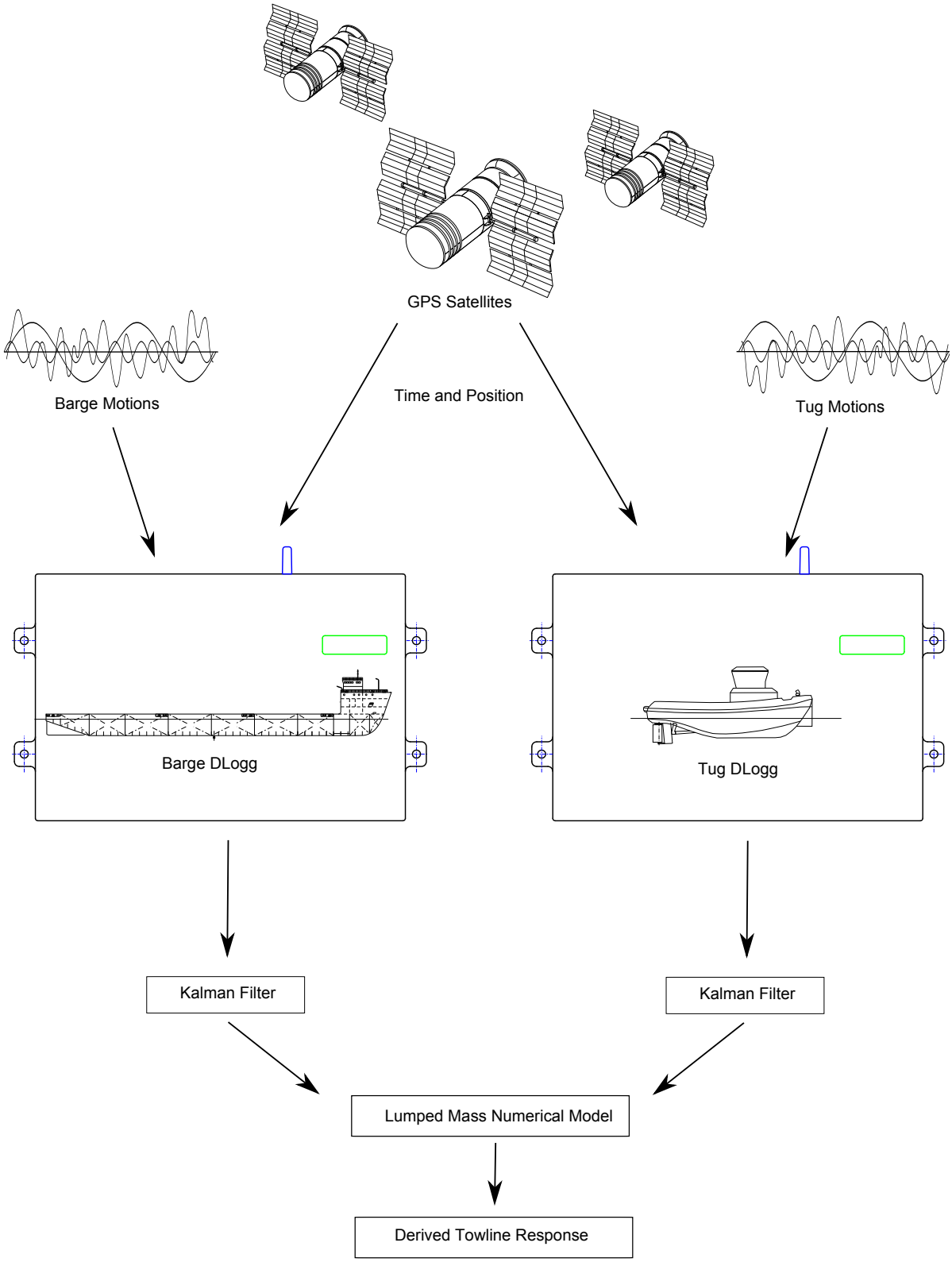

Figure 3.1.1: Graphical overview of data capture

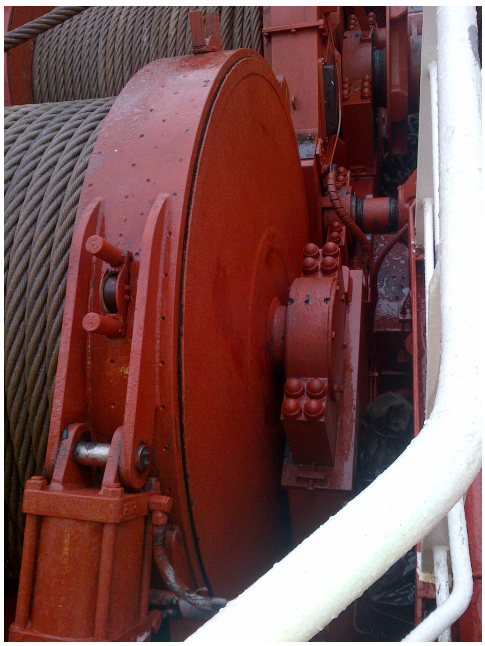

Figure 3.1.2: Image showing typical congestion around towing winch foundation

With respect to deployed towline length, this is the actual wire that has been spooled off the winch drum and adjusted for the distance between the drum and the aft end of the vessel where the towline passes over the stern between the bulwarks. For the numerical simulations this is taken as the end point of the towline at the tug and assumed to rest continually on the vessel's centreline. Any movement of this line sliding, as it will naturally do, from port to starboard is effectively ignored and this simplification is discussed later on. This value of towline length deployed is shown in an electronic readout on the bridge of the tug and is based on a tachometer reading of the number of winch drum revolutions. The accuracy of this is of paramount importance as it has been shown previously that the towline length is critical to the response of the towline in the numerical model [MacSween (2011)]. An additional magnetic sensor has been developed for use on tugs that allow the attachment of same to verify the data gathered by the bridge readout. This is designed for attaching to the side of the winch drum and allows a "counting" of the total cumulative clockwise and anti-clockwise rotations. However due to the congested nature of the winch drum walls and supporting equipment on the tug, see figure 3.1.2 for typical arrangements on one of the tugs in this study, the ultimate use of this is was not possible. Alternative means for verifying the data from the crew as discussed in chapter 8 later.

The assessment of towline tensions during the data runs, as recorded on the data sheets, were based primarily on nominal readings from the winch's foundation or brake sensor and represented a mean of averaged readout of the bollard pull encountered. None of the tugs employed during the course of this study had anything more than a rolling readout of the towline tension with no means of capturing this to disk or any other solid state media for future post-processing. This is also discussed later in chapter 8.

Finally the master or officer of the watch was asked to make an assessment of the sea state encountered by the tow during the voyage. To allow for as consistent a reporting base across tows as possible, given

HENRY ABRAM & SONS
ESTABLISHED 1899

Towing Vessel Details							
Towing Vessel Name	Displacement	Draught Aft	Draught Fwd	KMT	KML	VCG	LCG
Towed Vessel/Barge Details							
Tow/Barge Name	Displacement	Draught Aft	Draught Fwd	KMT	KML	VCG	LCG

Tow Record			
Departure Port	Destination Port	Tow wire Diameter/Details	Notes

Voyage Details						
Time	Date	Deployed length of tow line (m)	Estimated Sea State			Tug Utilisation
			Seastate (ref images over)	Significant Wave Height (m)	Wave Direction	Average Bollard Pull or Engine Power at time of record

1

Figure 3.1.3: Cover sheet of research's "voyage log"

that they could be at different times of the year and by different masters, the forms were standardised and included reference images of each of the sea states, see figure 3.1.4 for details of the images used. Regardless of these visual queues it should be appreciated that this assessment of seastate is nothing more than an objective one and although the master or officer of the watch may be considered as a "trained observer" it cannot replace the use of instrumented wave height measurements representing as true an assessment of the actual seastate as is reasonably possible. However as these are commercial tows, the deployment of "waverider" measurement systems, or similar, was not feasible.

Chapter 8 of [World Meteorological Organisation (1998)] gives a good, albeit brief, overview of the issues and pitfalls associated with observing and reporting on waves from a floating vessel. It does note that "visual observations of wave height tend to approximate the significant wave height" and while it is accepted that there are methods and formula available to convert visual data to significant wave height, for most practical purposes it is unlikely to be worth the transformation therefore data recorded left "as is". While not utilised, in this research it is available for future work.

Figure 3.1.4: Reference sea state images used in voyage log

3.2 Inertial Navigation System Sensors

3.2.1 Background

The background to INS systems has been covered in the literature review in section 2.2.2. The recorder used for this research is a bespoke device designed and manufactured in conjunction with Transmission Dynamics, who specialise as a provider of robust, self contained vibration and strain monitoring equipment. The device, known as DLogg, was developed for the author's company, primarily as a means of monitoring and reporting on cargo handling for long duration deep sea shipping, but the capabilities lend themselves to their use in this research. See figure 3.2.1 for detailed layout of the device and figure 3.2.2 for image of same. It is worth noting that there are other similar devices in existence that could also be used as input to the numerical routines and processes developed in this work.

The device employed for this study is equipped with a sensor suite that permits the recording of accelerations and angular rotations along and around three orthogonal axis, reference figure 3.2.6 which, when installed to the vessel being monitored, align with the longitudinal, transverse and vertical axis of the parent vessel.

More specifically the sensor suite consists of a dual axis gyroscope chip [ST (2009-2)] detecting roll and pitch angular velocity paired with a second single axis chip [ST (2009-1)] detecting yaw angular velocity both from ST Microelectronics in conjunction with a triaxial accelerometer chip [Freescale (2008)] from Freescale Semiconductor. In addition to these MEMs based sensors the logger is also equipped with a electrolyte based tilt sensor [Fredericks (2011)] aligned to the pitch and roll axis from The Fredericks Company as well as a GPS sensor embedded in a mobile GPRS chipset [Siemens (2007)] from Siemens.

As outlined in section 2.2.2, MEMs based INS aided navigation systems are enjoying increased popularity and, due to their size, robustness and power requirements, they are finding their way into more diverse applications. For strapdown INS based systems where the sensor suite is fixed to the local body axis planes and rotates with the body being monitored there is a computational overhead which is larger than that of "gimbal" or "stable platform" based systems, see figure 3.2.3, where the sensor suite remains in the global frame as the body being monitored rotates around it.

Therefore, while it can be seen that stable platform based systems can directly read off the current orientation in roll, pitch and yaw, strapdown systems need to derive their orientation computationally as they are rigidly attached to the body in question and so must sense their orientation in the local frame and translate this to the global frame by integrating the angular velocity with respect to time and adding this to a known starting orientation. This overhead also tends to propagate errors in the readings due to the

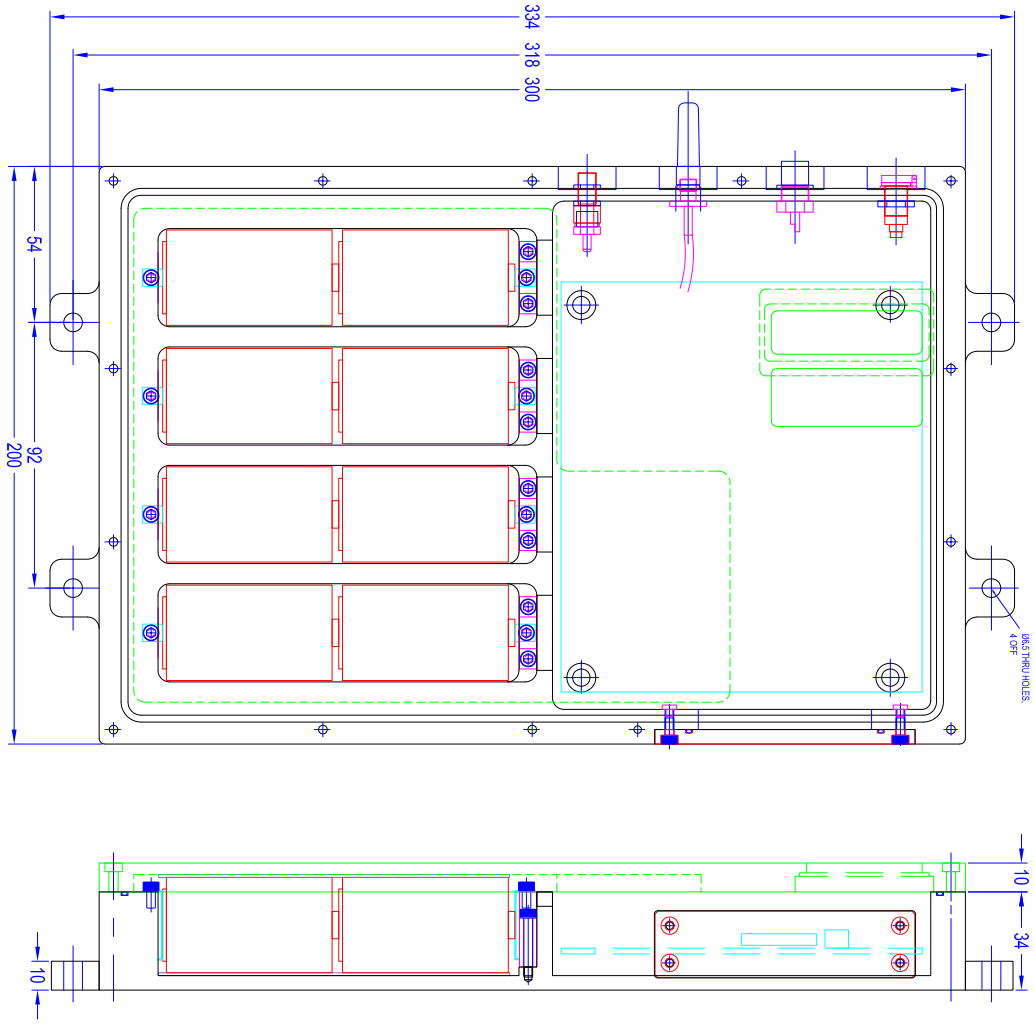

Figure 3.2.1: DLogg technical layout

Figure 3.2.2: Image of DLogg sensor device

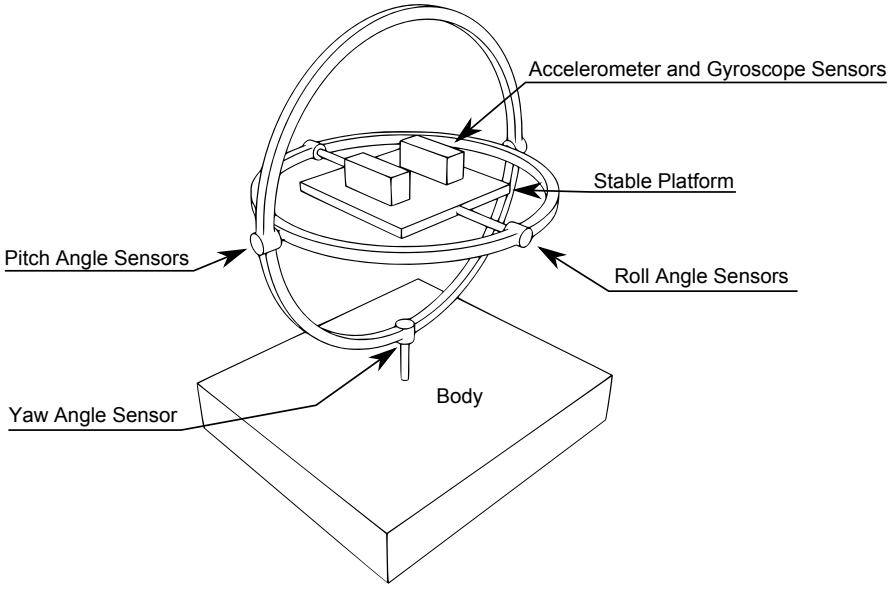

Figure 3.2.3: Stable Platform INS Setup

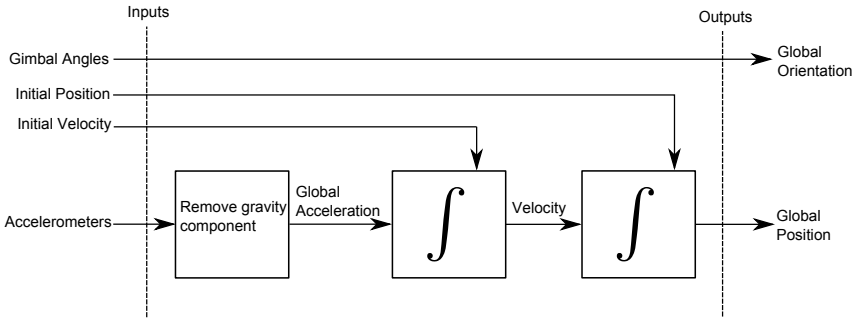

Figure 3.2.4: Stable platform integration algorithm

integration steps required to obtain attitude and position from angular velocity and linear acceleration, see figures 3.2.4 and 3.2.5 for a high level graphical representation of the algorithms of stable platform and strapdown systems.

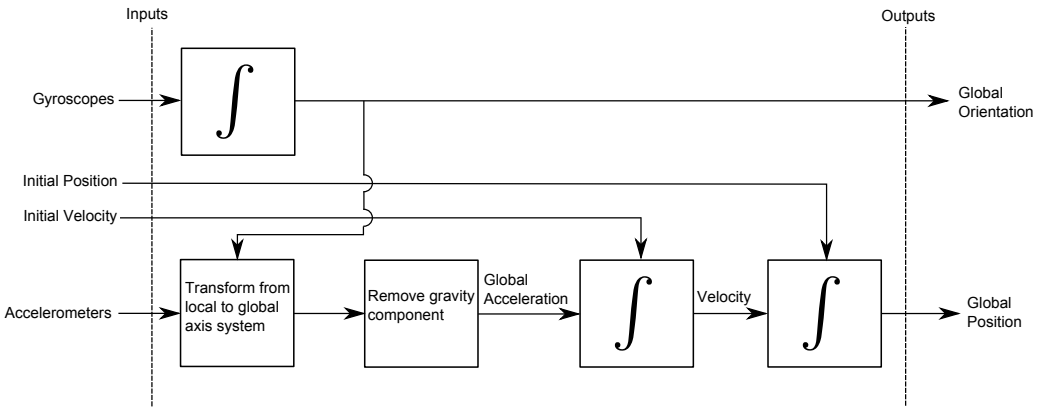

Figure 3.2.5: Strapdown platform integration algorithm

3.2.2 MEMs Based Sensors

[Woodman (2007)] and [Hou (2004)] provide a very good primer into the various error characteristics of MEMS based sensors within inertial navigation systems. Fundamentally these types of sensors are prone to:

- Bias
- Internal thermo-mechanical white noise
- Flicker noise
- Temperature Effects
- Calibration effects

Taking each in turn, their potential impact on the final solution will be outlined with details of the specific characteristics of the system employed here.

Bias The bias of sensors can be split into a deterministic component known as the "Bias Offset" and a random component known as the "Bias Drift". In addition there is also "Bias Asymmetry" and "Bias Instability".

As a simplification, random fluctuations in the bias over time are not accounted for and only the deterministic bias offset of each of the sensors on each logger are incorporated into the adjustment of sensor readings to a real world state estimate. As the full data series is segmented into 1 hour runs any significant shift in the bias between one run and the next in conjunction with the fact that there are other sensors whose input to the state estimate is not reliant on integration, that the influence of random bias fluctuations in the final calculated line tensions would not be significant.

The bias offset of the solid state accelerometers and gyroscopes is the average reading when the device is not undergoing any motion. For balanced sensors it should sit as close to the mid range of the sensor's capabilities as possible to ensure as much benefit of the component's sensitivity can be utilised before hitting "floor" or "ceiling" outputs.

The accelerometers used here have 2 settings of sensitivity (namely +/- 1.50g and 6.00g) and for all voyages here the setting of +/- 6.00g was utilised. It was felt that this was generally a little course for the purposes of this research but the risk of exceeding the maximum and minimum values on a range of +/- 1.5g was too great. These range values are specified by the user in a settings file stored on the memory card of the device. This is then fed through an analogue to digital converter, ADC, which converts this range to a integer with a value between 0 and 2048. This figure is then stored on the internal memory card in a series of binary files. This range results in a sensitivity granularity of 6/2048 g.

The conversion of the ADC integer value to a real world one is as follows:

ADC to Voltage for a given sensor where $Bias$ is the calculated soak test bias for the sensor in question:

$$V = \frac{3.3\,(ADC - Bias)}{1023}\ (volts) \tag{3.2.1}$$

Accelerometer conversion to real world value, where $Scale$ refers to the sensitivity setting and is equal to 0.8 volts/g when set to +/- 1.5 g and 0.206 volts/g when set to +/- 6.0 g:

$$Accel = \frac{V}{Scale}\ (g) \tag{3.2.2}$$

For the gyroscope this has a single sensitivity setting which has $Scale$ equal to 0.0083 volts/(degrees/second). The operating range for the gyroscope is +/-120 degrees/second and angular velocity can be calculated as per:

$$Ang_{Vel} = \frac{V}{Scale}\ (deg/sec) \tag{3.2.3}$$

These produce the real world estimates before corrections for alignment and scale, i.e. calibration, factors. See sections 3.2.3 and 3.2.4 later for details of the conversion and extraction of tilt and GPS information.

Figure 3.2.6 shows the internal axis orientations of the individual sensors as soldered to the pcb of the logger and so indicates the convention used for the saving of binary data to the removable memory card. Below the device the lid may be seen where the vessel local axis conventions have been milled and dyed to aid alignment during installation for data capture runs. With reference figures 4.1.5 and

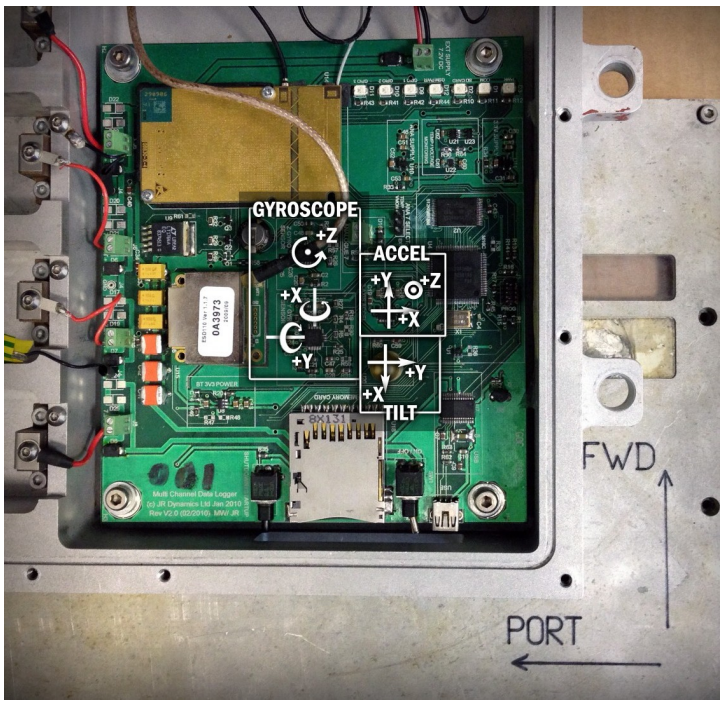

Figure 3.2.6: Mapping of internal axis to external local body axis on vessel (ref JRD)

4.1.6, one can define the sign conversions required to ensure correct alignment of data exported from the c++ conversion routine used to extract data from the binary files. Conversion from this raw data to real world values was done in MatLab as follows (where subscript LB refers to "Local Body" i.e. vessel axis and $Logger$ refers to logger naming and axis conventions on the PCB, reference figure 3.2.6):

$$\begin{bmatrix} \ddot{x} \\ \ddot{y} \\ \ddot{z} \\ \alpha \\ \beta \\ \dot{\alpha} \\ \dot{\beta} \\ \dot{\gamma} \end{bmatrix}_{LB} = \begin{bmatrix} 0 & 1 & 0 & 0 & 0 & 0 & 0 & 0 \\ -1 & 0 & 0 & 0 & 0 & 0 & 0 & 0 \\ 0 & 0 & 1 & 0 & 0 & 0 & 0 & 0 \\ 0 & 0 & 0 & 0 & 1 & 0 & 0 & 0 \\ 0 & 0 & 0 & -1 & 0 & 0 & 0 & 0 \\ 0 & 0 & 0 & 0 & 0 & 1 & 0 & 0 \\ 0 & 0 & 0 & 0 & 0 & 0 & 1 & 0 \\ 0 & 0 & 0 & 0 & 0 & 0 & 0 & 1 \end{bmatrix} \begin{bmatrix} \ddot{x} \\ \ddot{y} \\ \ddot{z} \\ x_{Tilt} \\ y_{Tilt} \\ \dot{x_{Gyro}} \\ \dot{y_{Gyro}} \\ \dot{z_{Gyro}} \end{bmatrix}_{Logger} \tag{3.2.4}$$

Two DLoggs were used for this project and they were consistently placed on Tug and Tow from voyage to voyage. With reference to the sensor data sheets, [ST (2009-1), ST (2009-2)], it is noted that the zero level voltage can change after mounting due to stress effects intrinsic to the fabrication and assembly process of constructing the pcb therefore these should be ascertained prior to use in the field. Taking the range above and analysing the sensors on each logger one can calculate the sensor bias based on 30 minute soak tests at 10Hz, see table 3.2.1 on the next page for specific values. Both loggers and all sensors showed good stability over this period. It is also worth noting that following mounting to the milled aluminium case, the loggers were attached to the vessels during sea voyages using ratchet

Table 3.2.1: MEMs Sensor bias's (in dimensionless, raw form) for Tug and Barge loggers

	Accel			Gyro		
	x	y	z	x	y	z
Tug Logger	535.12	521.96	562.64	442.31	421.64	443.22
Barge Logger	522.85	518.06	561.57	453.80	446.16	446.36

lashings or simple clamps, rather than bolted directly to the vessel so additional induced stress due to an overly rigid connection was avoided.

Sensor bias is trivial to allow for and once known can simply be subtracted from the actual readings to obtain a corrected value. For gyroscopes, bias related errors increase linearly with time however for accelerometers the error increases quadratically with respect to time elapsed due to the double integration required to convert acceleration to distance.

The assessment of bias for accelerometers is complicated slightly by the fact that, even when at rest, it will record a positive acceleration along the z axis due to gravity. This is normally corrected for by placing the device on a calibrated surface and recording the values at known orientations allowing the effect of the gravity field to be allowed for. The values shown in table 3.2.1 are taken as Z axis aligned to the local gravity vector. The device here surmounts this issue by utilising a combination of sensors with different characteristics, i.e. acceleration and gyroscopes are not the only on board sensors available for sensing orientation and position. This "complimentary sensor fusion" approach is covered in sections 3.2.3, 3.2.4 and 4.1 later.

Internal Thermo-mechanical White Noise MEMs based sensors are subject to internal thermo-mechanical white noise. These are zero mean (after removing any bias and gravity effects in the signal), uncorrelated random variables that perturb the reading. The effect of integrating this noise to derive the estimated orientation (via gyroscopes) and position (via accelerometers) is a "random walk" in the reported orientation and position that grows with time. This random walk may be thought of as the path a person may take if given random instructions on the direction of each step they take. Data sheets for such sensors report these as functions of frequency, representing effective bandwidth, resulting in a FFT noise density figure.

This random walk can be demonstrated by taking the results of a "rested" soak test and integrating them. In figure 3.2.7 the output of the roll gyroscopes for each logger has been integrated over a series of 250 batches of 175 second runs each. Here you can see that the distribution of end angles result in a maximum unbounded error of approximately 50 degrees in roll, and 20 degrees in both pitch and yaw. For illustrative purposes a detailed plot of the first 0.5 seconds of data is shown in figure 3.2.7 illustrating the random nature of the integrated noise signal. It is also obvious from the plots by considering the maximum and minimum slopes on the graph, that the error is linear with respect to time.

Table 3.2.2: MEMs Sensor Measurement Noise Variances (in dimensionless, raw form) for Tug and Barge loggers

	Accel			Gyro		
	x	y	z	x	y	z
Tug Logger	11.894E-5	5.1830E-5	8.2184E-5	0.0326	0.1343	0.0262
Barge Logger	8.2618E-5	5.7716E-5	9.1415E-5	0.0403	0.0360	0.0193

Doing the same for the logger's derived position, see figure 3.2.8, by double integrating the signals on the surge, heave and sway axis one finds that the maximum unbounded error found is approximately 100m for surge, 500m for sway and 200m for heave after only 175 seconds of run time. Again a detailed plot on the heave axis show the chaotic nature of the noise and, as opposed to the derived angular position, the effect of the double integration of accelerometer data causing the error to diverge quadratically with respect to time.

The key here is the "unbounded" nature of these errors and so it may be seen the intrinsic limitations of the technology for the application of long data runs over many days where accuracy of logger orientation and position relative to each other is of paramount importance to confidently simulate the towline response. Therefore an estimate of position and orientation is required by combining readings from sensors with complimentary features, i.e. sensors whose estimate does not grow unbounded

This sensor fusion is looked at in much greater detail later, reference chapter 4.1.1, but it is worth noting here that it does require the magnitude of noise polluting the measurements to be understood. One aspect of this is the measurement noise and this is recorded as the variance of the reported values of the sensors while at rest and obtained from the same soak test data that was used for the derivation of the constant bias offsets. These values are reported in table 3.2.2. It was noted throughout this study that the readings on the pitch gyroscope within the Tug logger consistently reported more noise than the other sensors. The magnitude was not such that it caused any major issues and the Kalman filter was able to account for it. The reason for this additional noise was not known and put down to a minor fault with the chip or connection of same to the board data bus in question.

Flicker Noise Sensors can also be susceptible to variances in bias which can wander over time and results in noise effects which are of a relatively low frequency. Flicker noise is defined in terms of bias stability and assuming a random walk model results in second order random walk in angle for gyroscopes and a third order random walk in position which grows proportionally to $t^{\frac{5}{2}}$ [Woodman (2007)]. As noted earlier, the bias flicker here when looked at in the context of 1 hour runs, the use for the data in question and post processing via the Kalman filter, was not deemed to have a significant effect.

With both accelerometers and gyroscopes, temperature effects tend to produce a variance in the bias of the device which is often highly non linear. To understand and quantify these effects on the bespoke loggers used in this study, a ~48hr soak test against a modest temperature range was carried out and

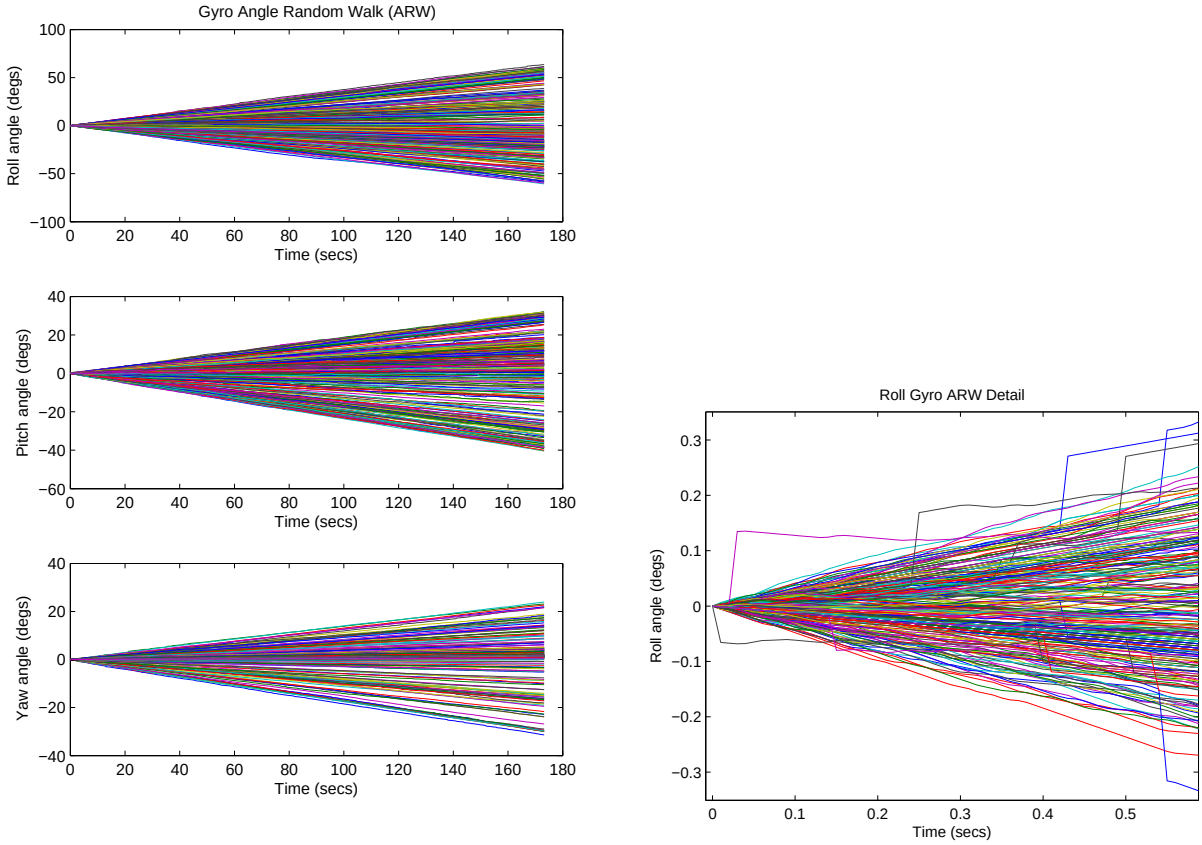

Figure 3.2.7: Multiple runs of roll, pitch and yaw Angle Random Walk (ARD) for logger gyro

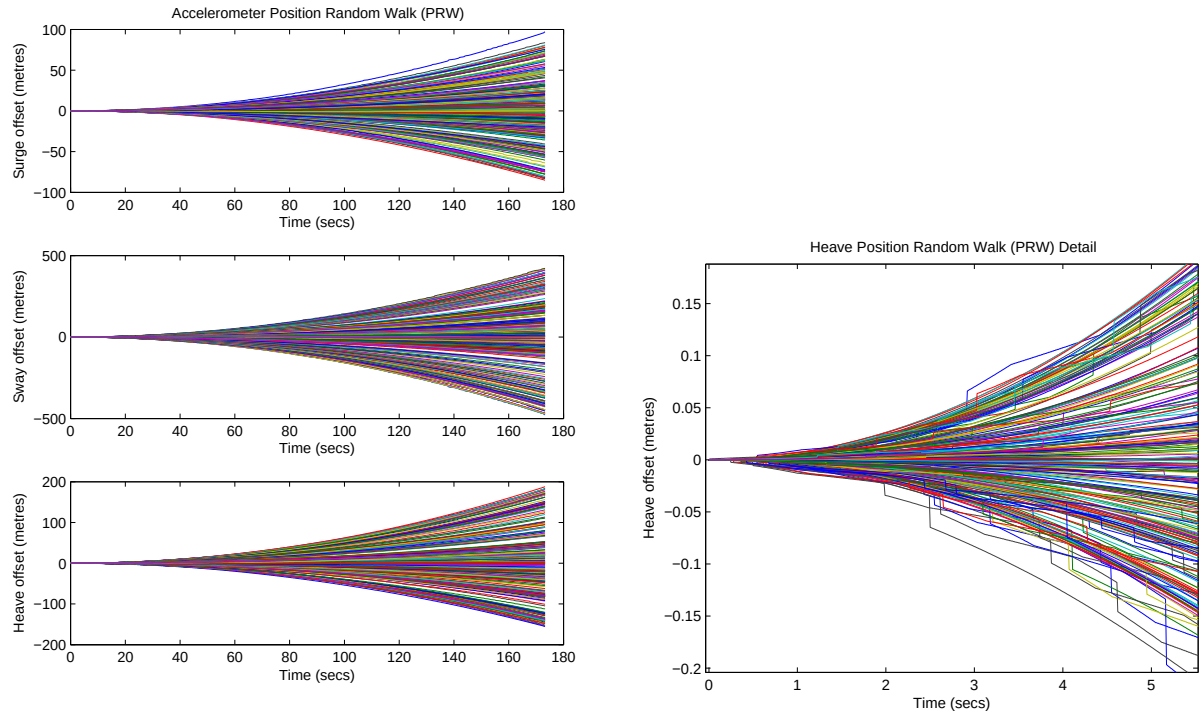

Figure 3.2.8: Multiple runs of surge, sway and heave Position Random Walk (PRW) for logger triaxial accelerometer

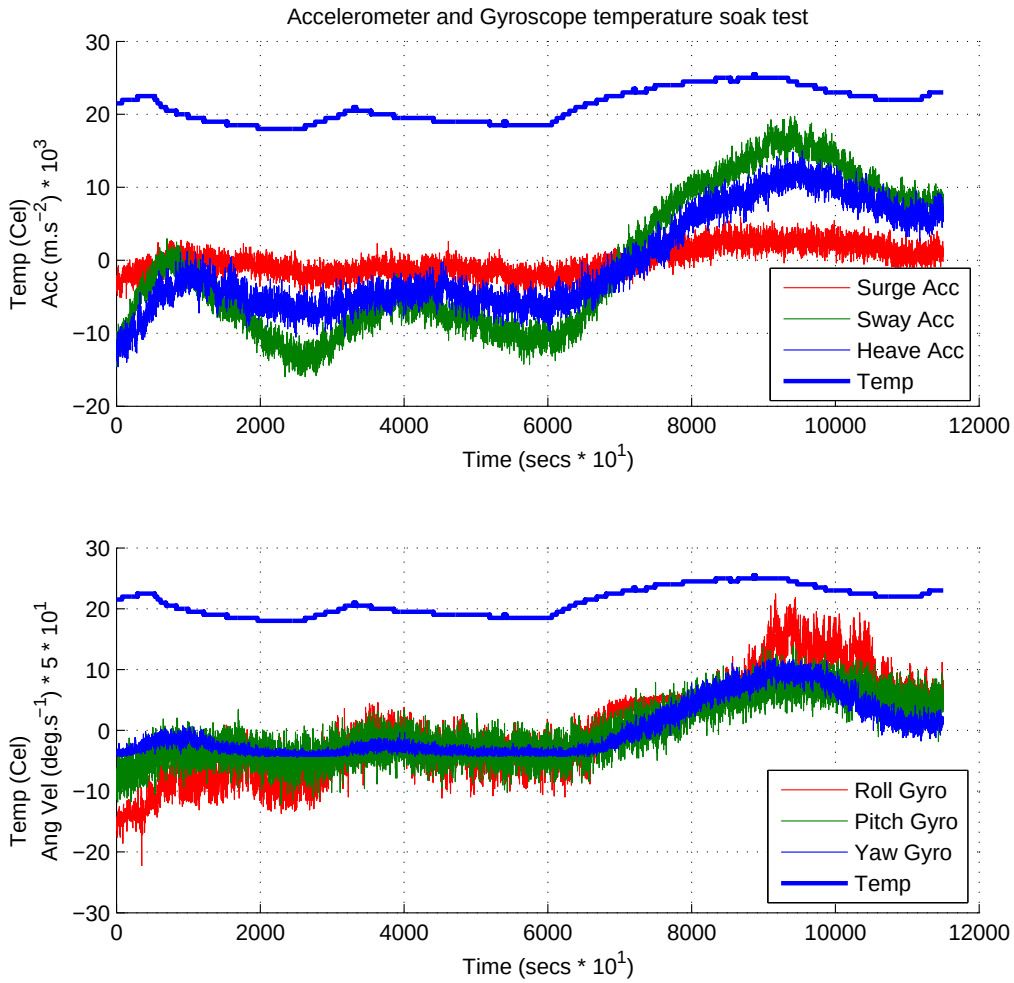

Figure 3.2.9: Temperature/bias sensitivity soak tests

the plots of the results are shown in figure 3.2.9. Note that to make the variations in sensor bias visible the values have been scaled by three orders of magnitude and so over represent, graphically, the extent of the fluctuations. It can be seen that the bias of the gyroscopes and accelerometers track temperature variations relatively consistently but the levels of change are relatively small.

As temperature data for the trips was not recorded, the attached demonstrates a small uncontrolled potential for error in the data and results.

Calibration Effects Calibration errors refer to a variety of factors such as non-linearity of sensors and misalignment in axis relative to the body being monitored or misalignment in the mounting of individual components to the printed circuit boards themselves.

As there are a number of complimentary sensors on board the logger, some of which have the capability

of recording angles relative to the gravity vector, they must be calibrated against each other and an external source for optimum Kalman filter performance. As the calibrations must be run against an external source the non-linearity of the sensors can also be tracked. In addition, by rotating the device and running multiple calibrations it is also possible to get an understanding of the degree of any internal misalignment of the sensor mountings to the pcbs relative to the external orientation markings.

The calibration process utilised a series of "tilt tests" which were carried out on a simple test jig constructed from wood, reference figure 3.2.10. It had a solid oak test bed which pivots about a base point with an arm allowing the test bed to be locked at pre-determined angles while the sensors readings settle.

All orientation, acceleration and angular velocity sensors were calibrated during the same series of tilt tests and the results for the accelerometers are discussed here with the non linearities and corrections for tilt sensors referenced in section 3.2.4.

As the accelerometers register the gravity vector when at rest and the output, in conjunction with a known angle of tilt and known local gravity vectors, can be combined to calibrate the accelerometers over this range. This is not as comprehensive as a full dynamic range calibration but access to such equipment was not available for this study. However as the full dynamic range is not likely to be significantly greater than 2g, the tests conducted here were felt to be acceptable.

Each logger was run through the same tilt process with angles recorded by a digital inclinometer. The full test process was as outlined in table 3.2.3 where angles shown were those recorded for the tug logger tests. Barge logger tests registered very similar angles, within 0.4 of a degree, but important to note all calculations resolving angles from gravity vector were based on those actually measured for each tilt test, so differences between the two are of anecdotal interest only in that they show reasonable consistency of approach between the two tests. The angle across the tilt table consistently recorded 0.9 degrees across all angles of tilt in the tug logger tests and 1.2 degrees in the barge logger tests. With the exception of the first tilt from level to approximately 14 degrees, each subsequent steps were between 8 and 9 degrees.

Raw plots for the tug and barge logger tilt tests can be seen in figure3.2.11. These figures show the signal output from the accelerometers as the loggers are inclined at various angles. The misalignment effects of the sensors mounted on the pcbs can be clearly seen in the tug loggers plot for examples with undulations in the output for roll sensor at points [A] and [B], pitch sensor at points [C] and [D] and then for surge at points [E] and [F] and finally sway at points [G] and [H]. The magnitude of the misaligments and the extreme angles at which their effect becomes apparent has been ignored as the effect would simply be swamped by the effect of any local misalignments with the vessel centreline when setting up the loggers in the field prior to a towage.

(a) Tilt test at low angle

(b) Tilt test at high angle

Figure 3.2.10: Tilt test setup

Table 3.2.3: Tilt test sequence (tug angles in degrees noted with barge angles similar)

Sequence	Angle (deg)	Orientation
1	0.4	level
2 to 5	-14.4 to -39.6	bow up
6	-48.2	max. bow up
7 to 10	-39.6 to -14.4	bow up
11	0.4	level
- Rotate logger 180 degrees -		
12	-0.4	level
13 to 16	14.3 to 39.5	stern up
17	48.2	max. stern up
18 to 21	39.6 to 14.2	stern up
22	-0.4	level
- Rotate logger 90 deg -		

Sequence	Angle (deg)	Orientation
23	0.4	level
24 to 27	-14.2 to -39.6	starboard up
28	-48.3	max. starboard up
29 to 32	-39.6 to -14.3	starboard up
33	0.4	level
- Rotate logger 180 degrees -		
34	-0.4	level
35 to 38	14.1 to 39.7	port up
39	48.6	max. port up
40 to 43	40.0 to 14.1	port up
44	-0.4	level
- Test end -		

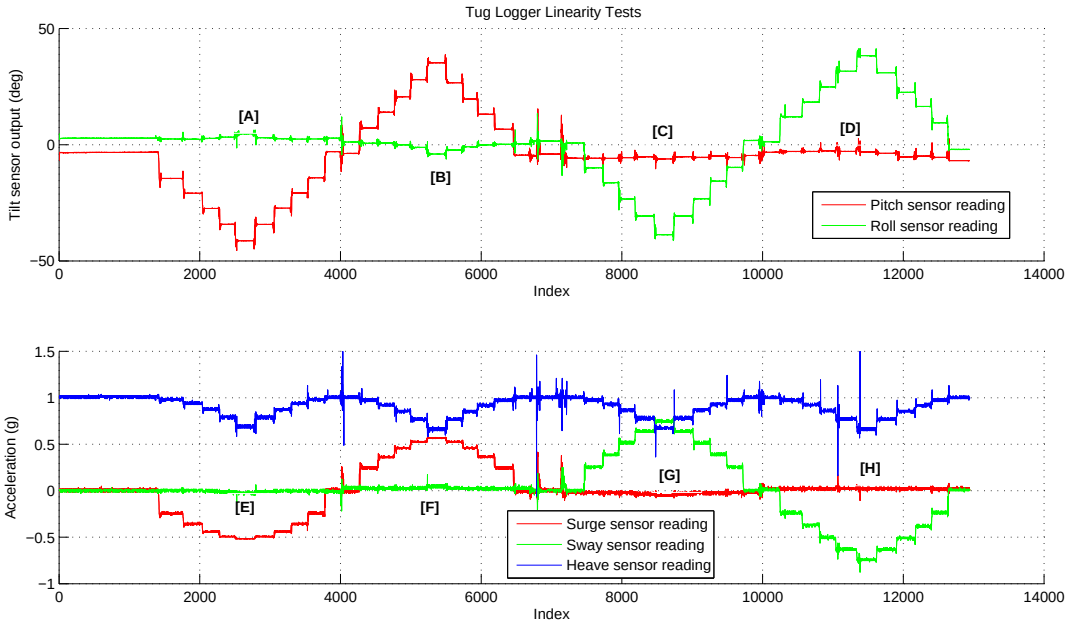

(a) Tug logger tilt tests

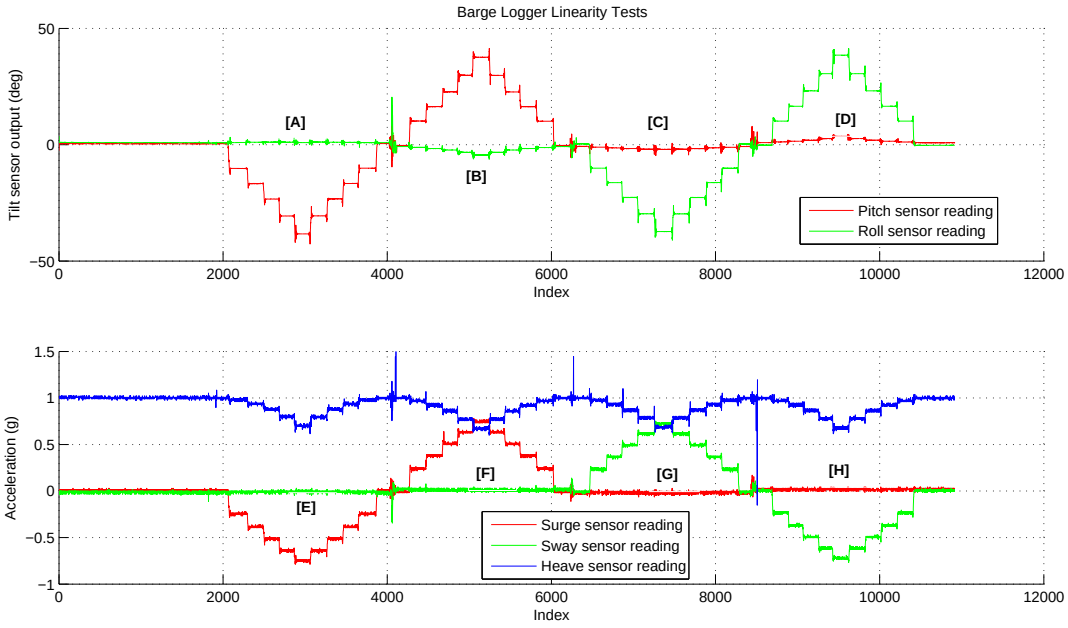

(b) Barge logger tilt tests

Figure 3.2.11: Logger tilt tests

Table 3.2.4: Accelerometer scaling factors

Logger	Surge axis	Sway axis	Heave axis
Tug	0.9701	1.0065	0.9920
Barge	0.9915	1.0260	0.9932

The output from these tests is a series of calibration curves or values for each accelerometer and tilt sensor. The calibrations for the tilt sensor are detailed later (see section 3.2.4 and figure 3.2.18).

For the accelerometers the scaling factors, reference figures 3.2.12 and 3.2.13, were derived from the difference between gravity vector recorded and the theoretical value based on measured angles of tilt. For the surge and sway axis, the tests realised two cycles each over a range between, approximately, -49 degrees to +49 degrees, over which scaling factors could be assessed whereas the heave axis recorded, as would be expected, 4 cycles due to its orientation normal to the plane on which both the surge and sway axis lay.

The scaling factors seem to have little non linearities that could not be reasonably attributed to system noise and were also all very close to the ideal value of 1.0. Therefore the scaling factors for each axis were taken to be the average of the scaling factor across all tests against each respective axis and no significant non linearities were noted in the output over the range tested. The values used in the filter code are as reported in table 3.2.4.

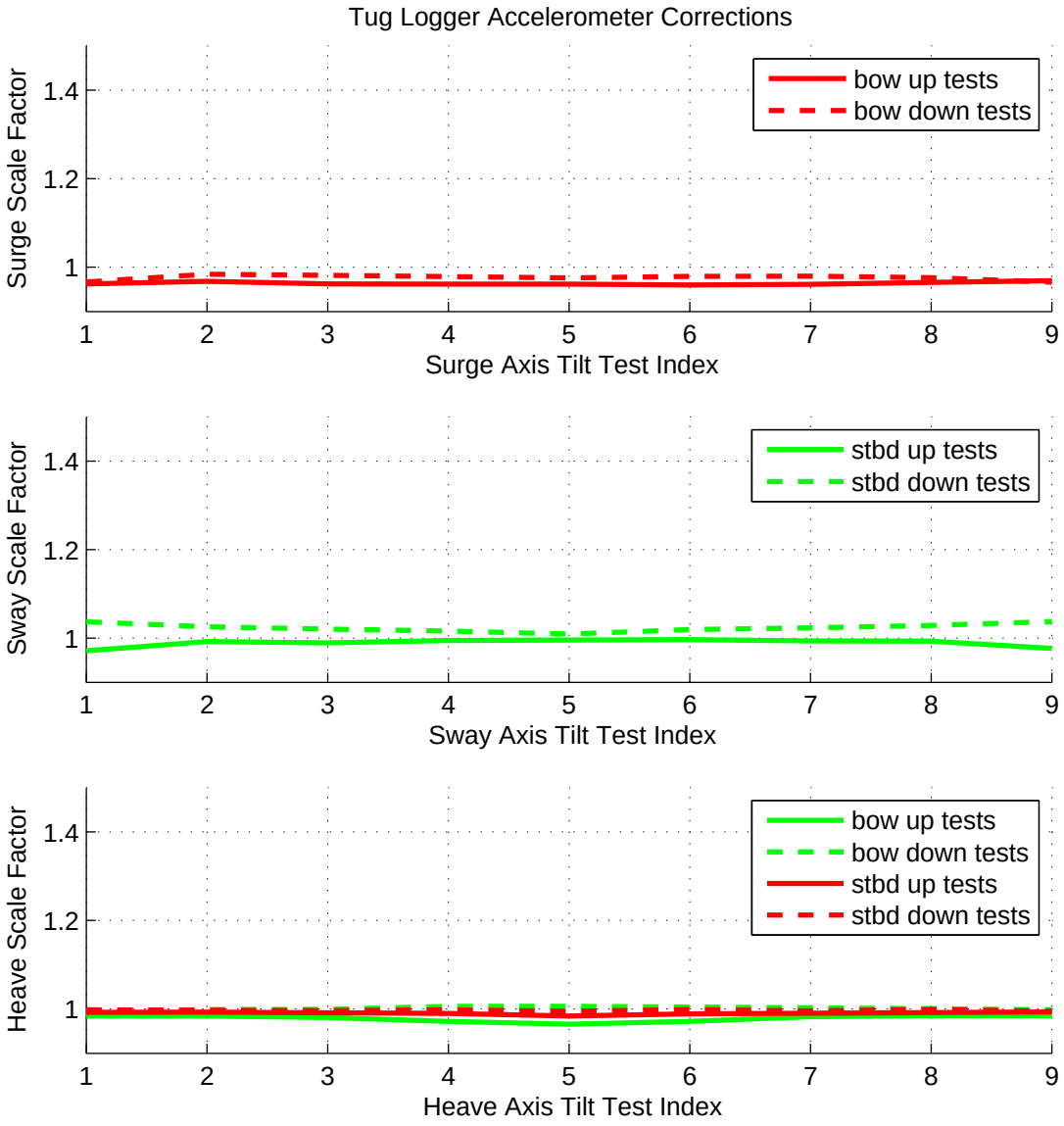

Figure 3.2.12: Tug accelerometer scaling factors

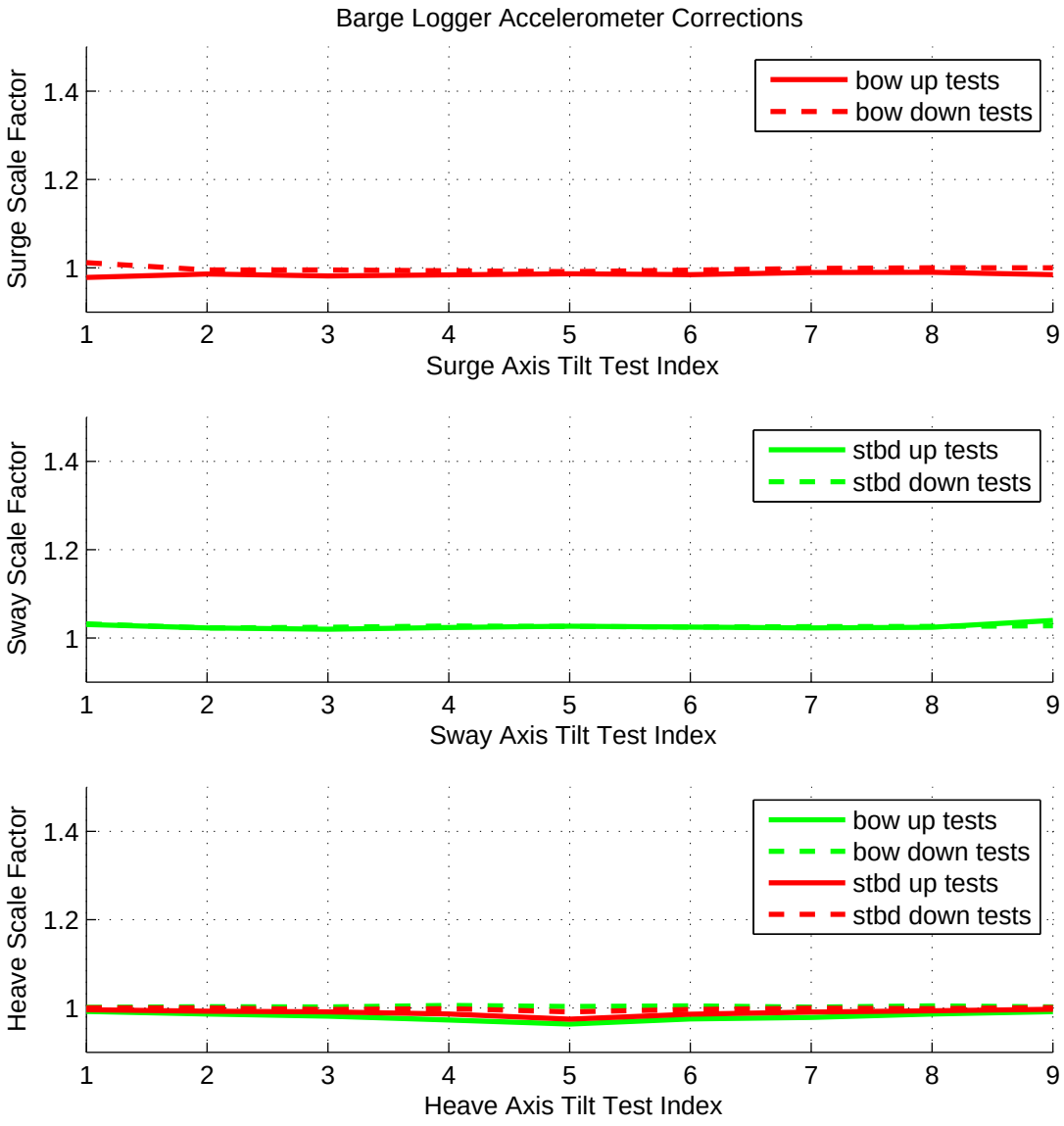

Figure 3.2.13: Barge accelerometer scaling factors

3.2.3 GPS Sensors

The logger features on board communication tools which includes a bluetooth module for short range data transmission (circa. 70m) and a GSM chipset for longer range data transmission and communication. The GSM module also has an integrated GPS chipset which is used here to obtain satellite fixes. Details of the modules may be found in the product's data sheet [Siemens (2007)].

GPS relies on a series of 24 satellites that surround the earth in geostationary orbit. These each have on board, highly accurate atomic clocks that, simply put, transmit their current recorded time. The difference in the time as received by a receiver on earth is then used triangulate ones position, after taking into account adjustments for relative velocities and proximity to earth. For determining position in 2D on the surface of the earth and only an estimate of altitude, 3 satellites are required whereas 4 satellite readings allow a full fix on the sensors 3D position. For most readings at sea, consistent 3 fix readings were noted.

For every fix, the GPS module reports:

- fix time based on the satellite clock and recorded as seconds after 00:00 hrs 01/01/1970 (UNIX time).
- Latitude and longitude in micro degrees
- Speed in knots based on GPS recordings only.
- Heading, again based on 2D interpretation of GPS longitude and latitude fixes only.
- Data quality, reported simply as the number of satellite readings available for obtaining a fix.

GPS accuracy is measured, primarily, as a function of Circular Error Probable, (CEP), giving a measure of error on a 2D plane with circular boundary, and Spherical Error Probable, (SEP), which gives a measure of error applied to 3D space with a spherical enclosing volume. [Koks (2007)] describes the CEP as follows:

> The radius of a circle drawn around the emitter that encompasses 50% of all estimates made of its position. Thus 50% of the time, the emitter will lie somewhere within a circle drawn around the estimate. In other words, one can be 50% confident that the emitter lies within the CEP distance of any particular estimate made. Increasing this parameter to a higher certainty, say 95%, can increase the corresponding CEP figure greatly.

The quoted position accuracy for the on board GPS is 2.5m CEP and 5.0m SEP [Siemens (2007)]. A 21 hr soak test with GPS readings averaging one every 1.1 seconds was conducted. The scatter plot

Table 3.2.5: GPS chipset soak test long/lat standard deviations

Longitude (x)	Latitude (y)
1.9483	3.1981

in figure 3.2.14 shows these plotted against a 5m grid. Due to the sheer number of fixes concentrated into a small area around the sensor's location, a histogram heat map in figure 3.2.15 emphasises the concentration around the expected true position. Although the "true position" is not known, it is taken as the mean latitude and longitude recorded and the grid then centred on this location for reporting purposes. While most figures are concentrated into a 20m x 20m square area, sporadic "wandering" away from the mean position may be seen, for example the track that drifts north before returning back again over approx 2 minutes of readings. This emphasises the consistent nature of the GPS errors and while random in nature they are nevertheless "bounded" as opposed to the accelerometer's double integration errors which will not tend to return to the mean but continue to drift indefinitely. The effect of this random walk of GPS signal is explored further in section 5.4.

This soak test indicates an measured CEP radius of 3.0364m based on the standard deviation of the x and y locations (reference table 3.2.5), converted as per equation 3.2.5 which matches reasonably well with the reported accuracy as per the data sheet.

$$CEP = 0.59\,(\sigma_x + \sigma_y) \tag{3.2.5}$$

For this soak test and other measurements in this research, latitude and longitude readings are converted locally to offset distance from a local origin using almanac data based on 1972 World Geodetic System ellipsoid. Details of the algorithm used and methodologies are given in section 5.3.1.

While this soak test was run for a full 21 hours to assess the long term accuracy characteristics of the GPS sensor, the final data sets are to be post processed in one hour segments. Taking the 21 hours of data presented here and assessing the CEP figures for each segment the results are as shown in table 3.2.6.

Note that this table shows the variation of the accuracy of the GPS over time in the static test case. It was observed that while the GPS receiver was moving in a straight line, this variance from the mean direction was significantly less, as would be expected, due to the fact that the GPS is operating its own, on board, Kalman Filter [Siemens (2007)]. This essentially improves the error characteristics of the GPS fixes while underway at sea, but the precise measure of this improvement is not defined. As details of the implementation of the on board filter within the GPS chipset are not available, while this improves the accuracy of the fixes while the tug and tow are underway, the readings are taken "as is" for inputting into the cascade of filters employed for the research here. However, as a worse case, sensitivity of the

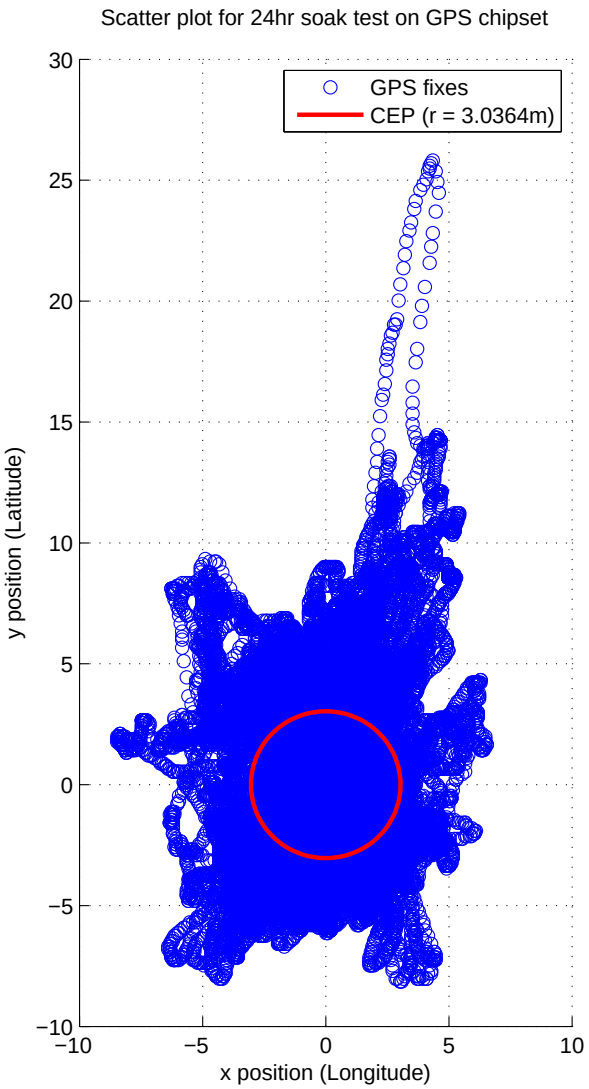

Figure 3.2.14: GPS 21hr soak test - Scatter plot

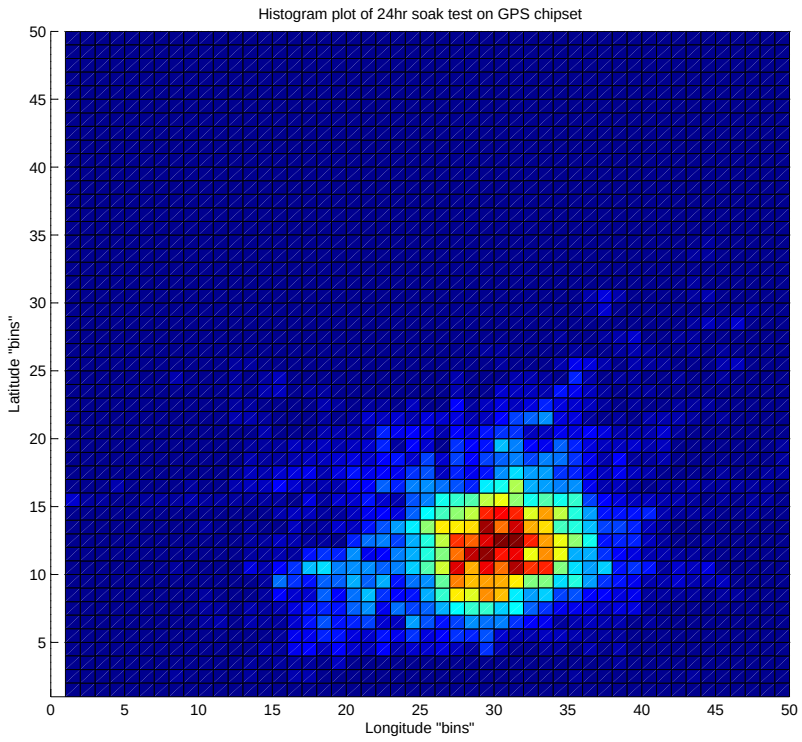

Figure 3.2.15: GPS 21hr soak test - Histogram plot

model to initial errors at the initiation of the post processing of each segment as well as towline tension variations from this "jitter" in the towline end points from GPS noise is reviewed later in section 5.4.

For yaw, the error characteristics for the direction of travel was derived in a different manner. Yaw angle, or "heading", is derived, in the final process, from the relative north and east velocities in the GPS output and so this cannot be taken from soak test data as the scatter of GPS readings when at rest would not provide a true understanding of the direction of travel on which the estimate of yaw is derived as the random scatter of the position reported would result in a random value for heading. Error characteristics for heading are therefore random when stationary and significantly improved when the logger is moving, again as would be expected from its own on board Kalman Filter. It was found that the heading information for the logger when traveling at a nominal towing speed was very stable and so an estimate of the measurement error was derived from a series of readings taken from data capture with the logger traveling in a straight line on land. The speed was maintained, approximately, at a representative 10 knots and the worst case variance recorded of 1.1597 degrees based on a series of 2 minute runs with around 120 data points to each run.

Table 3.2.6: Hourly CEP and std deviation results for GPS soak test

Segment (hr)	std(x) (m)	std(y) (m)	CEP (m)
1	0.7733	1.0333	1.0659
2	0.9810	1.2783	1.3330
3	1.0271	2.3428	1.9882
4	0.6213	1.2299	1.0922
5	1.0366	3.0768	2.4269
6	1.7437	4.4264	3.6404
7	2.1050	1.4147	2.0766
8	2.7829	1.9354	2.7838
9	1.3163	2.8021	2.4299
10	0.9872	1.3248	1.3641
11	1.3082	1.6549	1.7482
12	1.2131	3.5827	2.8295
13	1.4149	1.1308	1.5020
14	1.3362	5.5784	4.0796
15	1.0858	1.8449	1.7291
16	0.7173	1.2818	1.1795
17	0.8781	3.0775	2.3338
18	1.1027	1.5215	1.5483
19	1.4055	1.3312	1.6146
20	2.0243	1.2665	1.9416
21	0.9085	1.9704	1.6986

3.2.4 Tilt Sensor

The tilt sensor employed in the data loggers is an electrolyte based device which records angles of inclination against the horizontal plane by measuring the movement of liquid contained within [Fredericks (2011)]. Again, looking to increase the robustness of the data recorded by combining sensors with complimentary error characteristics, the tilt sensor has an advantage of reporting constant angles of inclination with an error that does not grow or change with time. The device is, however, susceptible to “sloshing” of the electrolyte which reads as changes in angle when subjected to lateral movement only. This occurs at frequencies typically higher than those of interest to this research and is only an issue if the logger is subjected to vibrations or shock loads which careful placement on the tug and barge looked to minimise. The filter employed will look to account for this and allow the data from the tilt sensor to correct any drift in the integration scheme which derives the roll and pitch angle from gyroscope readings. See figure 3.2.16 for typical readings where the sensor is at rest initially then subjected to circa 200mm lateral movements in the surge direction only at a frequency of approximately 2 Hz. Overlaying the estimated pitch, as output from the Kalman Filter, with the recorded pitch from the tilt sensor, the effect of the filtering process can be clearly seen.

For the conversion of ADC values to tilt angle, the sensors exhibits slight, non-linearity, as depicted in figure 3.2.17. This graph is based on digitised information as provided by the system manufacturer and the look-up table shown was produced to allow interpolation for intermediate figures. To highlight the non linearity in the output of this sensor, a "best fit" straight line is shown through the data point.

Table 3.2.7: Tug and barge logger tilt sensor conversion table

(a) Tug logger conversion table

Roll angle	Roll ADC	Pitch angle	Pitch ADC
-48.2	543.76	-48.60	582.10
-39.6	671.12	-39.85	697.09
-30.9	772.12	-31.00	800.72
-22.65	856.65	-22.70	879.26
-14.4	934.33	-14.10	957.20
-0.4	1051.86	-0.40	1064.78
0.4	1063.40	0.40	1083.84
14.25	1178.43	14.25	1193.44
22.6	1256.68	22.65	1268.37
30.9	1340.74	30.85	1363.72
39.55	1439.76	39.60	1470.52
48.2	1565.41	48.30	1609.34

(b) Barge logger conversion table

Roll angle	Roll ADC	Pitch angle	Pitch ADC
-47.7	552.95	-47.80	536.08
-39.1	678.52	-39.10	665.00
-30.45	777.29	-30.40	764.94
-22.25	859.02	-22.20	845.98
-13.85	935.32	-13.80	920.92
-0.4	1046.90	-0.40	1032.30
0.4	1055.96	0.40	1038.70
13.85	1168.42	13.80	1153.25
22.2	1244.57	22.20	1228.85
30.5	1327.35	30.40	1312.32
39.1	1429.07	39.10	1412.43
47.7	1559.62	47.70	1540.13

To verify this theoretical curve, the output from the tilt sensors were calibrated during a series of tilt tests and the ADC output logged against actual, measured, angles of inclination. The results of these calibration tests may be seen in figure 3.2.17 and table 3.2.7. It is interesting to note the relative differences in quality between the components used. It can be seen that the tilt sensors in the barge logger shows smooth curves that track, but are offset from, the manufacturer's theoretical curve closely whereas the tugs tilt sensor appears to have a defect that manifests itself in an increase in the non linearities for negative tilt angles but positive tilt angles appear unaffected. It may also be seen that the manufacturer's conversion values significantly underestimates angles reported, effectively reducing the sensitivity of the sensors.

Due to the nature of the tilt tests carried out, each value of the conversion graph, with the exception of the maximums, are based on the average of two representative inclinations. A series of soak tests were also run for each logger and the static bias' were noted, reference table 3.2.8.

These correction values were fitted to a series of 2d splines in the MatLab filter code. Thereafter correction values interpolated against actual recorded readings could be found, effectively giving each logger its own set of calibration curves for each axis of each tilt sensor.

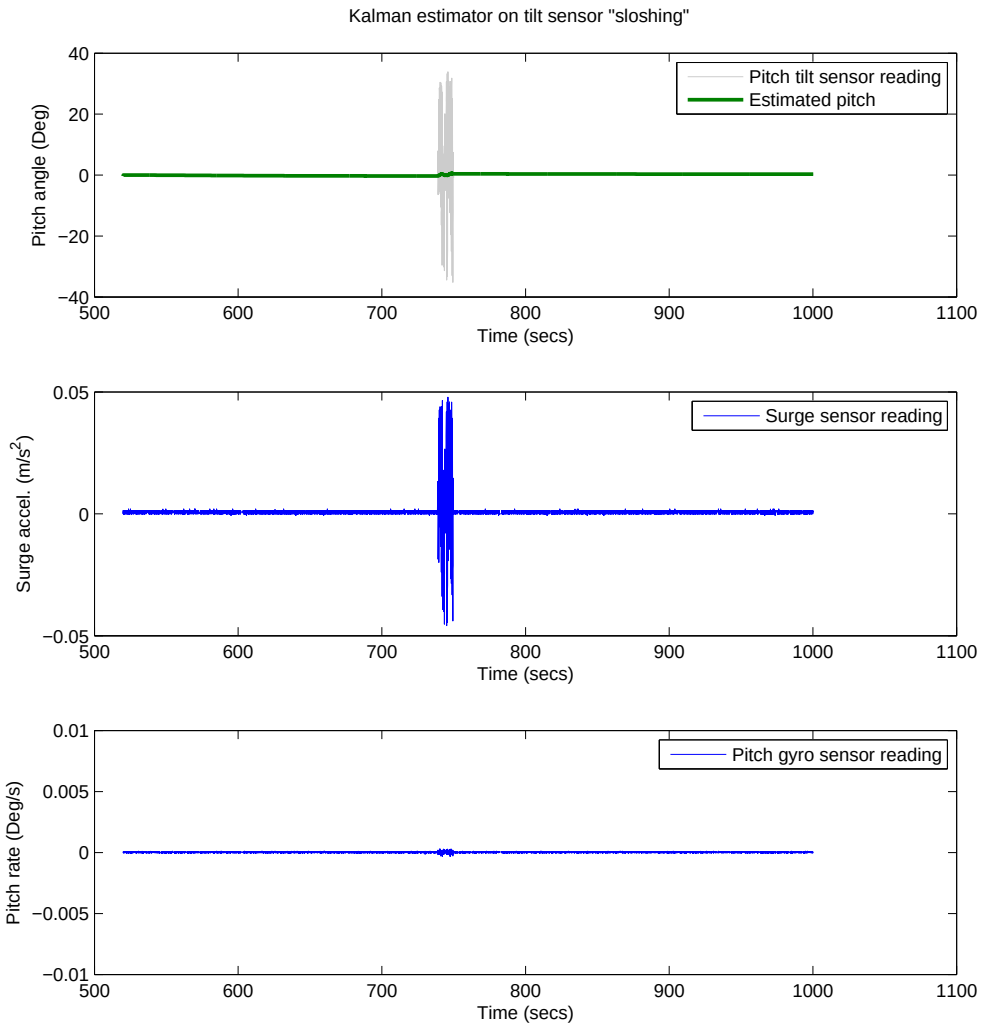

Figure 3.2.16: Examples of tilt sensor “sloshing” errors

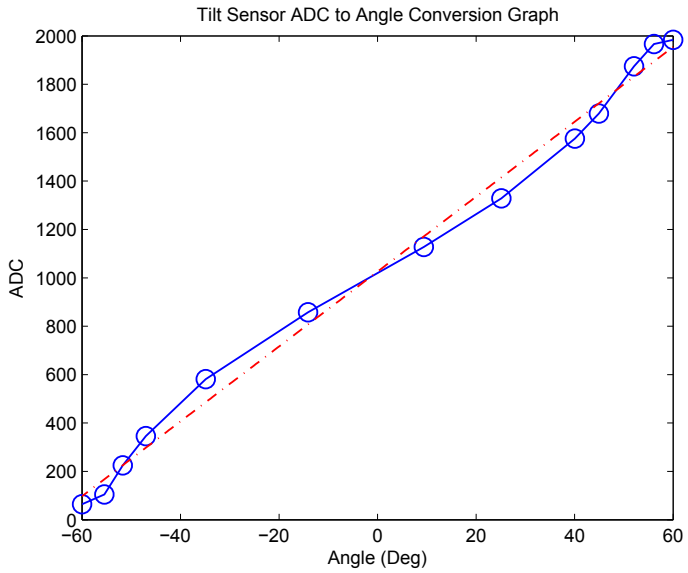

Angle	ADC
-60.00	64.22
-55.46	104.45
-51.73	225.14
-47.03	345.83
-34.86	581.47
-14.11	857.33
9.41	1127.45
25.14	1328.60
40.05	1575.73
44.92	1679.18
52.05	1874.58
56.11	1966.54
60.00	1983.78

Figure 3.2.17: Manufacturer generic tilt sensor conversion graph

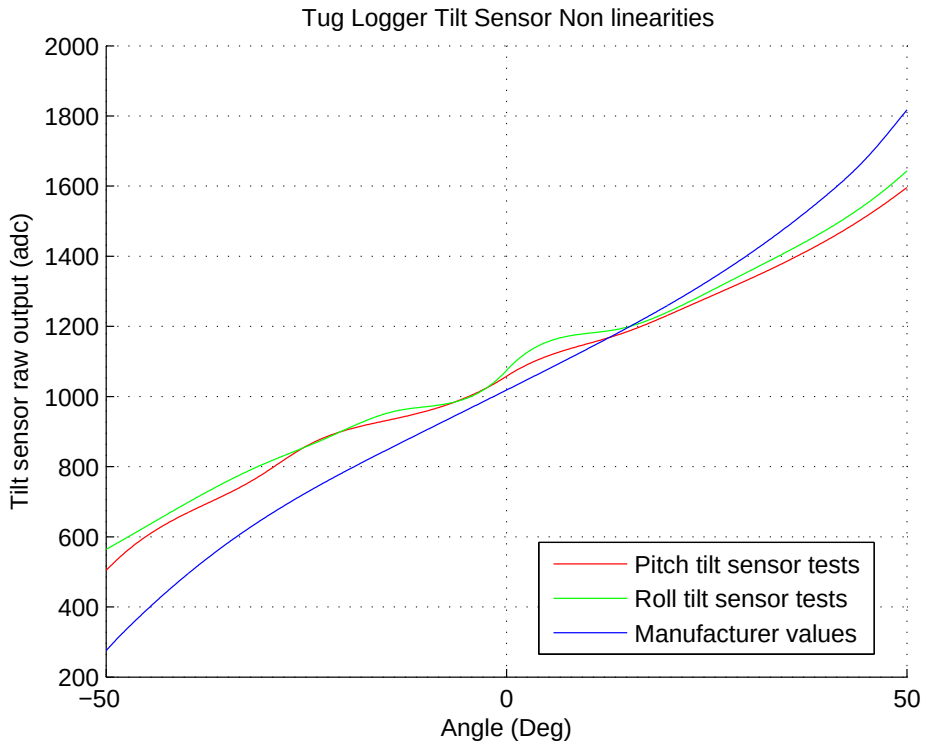

(a) Tug logger tilt sensor non linearities

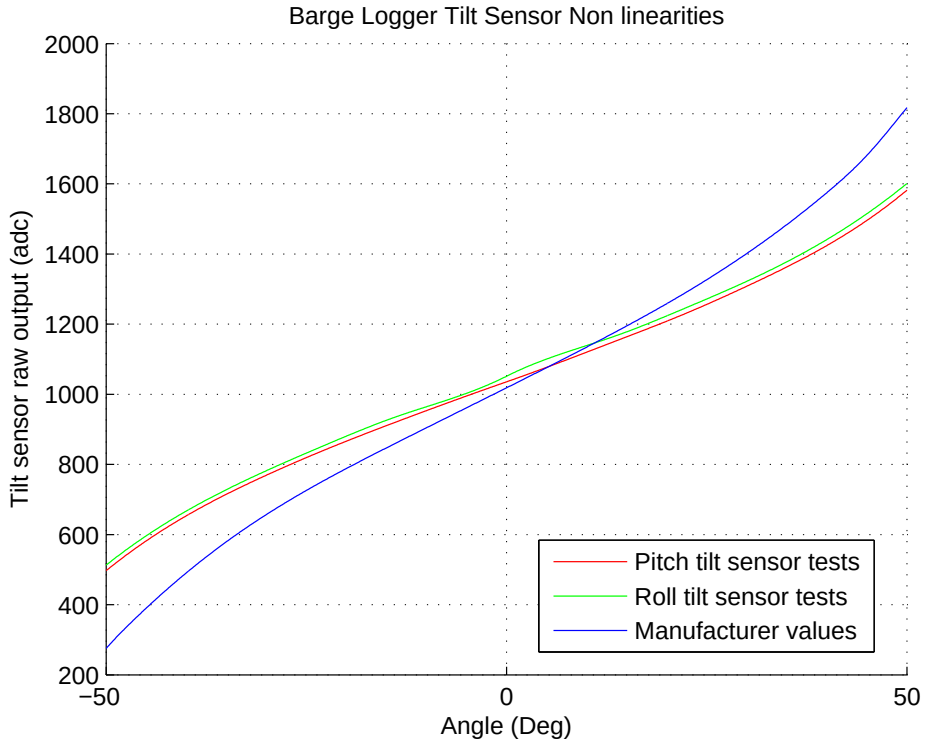

(b) Barge logger tilt sensor non linearities

Figure 3.2.18: Tilt test conversion graphs

Table 3.2.8: Tilt Sensor bias' for Tug and Barge loggers

	Tilt	
	x (roll)	y (pitch)
Tug Logger	1078.75	1098.35
Barge Logger	1035.69	1050.46

Table 3.2.9: Tilt sensor measurement noise variances for Tug and Barge loggers

	Tilt	
	x (roll)	y (pitch)
Tug Logger	0.0206	0.0232
Barge Logger	0.0240	0.0267

3.3 Towline Tensions

The difficulty of recording actual towline tensions during commercial towages or "towages of opportunity" has been well established in the introductory sections of this thesis. While there were no opportunities to actually undertake such verification for this work, the reasons for which were noted so that any restrictions may be better understood. The validity of applying lump mass or continuum models to obtain towline tensions has also been well established, [van den Boom (1986)] and [Thomas (1994)] and so, with suitably accurate means of recording end point motions coupled with a validated lump mass numerical model, this was deemed to be still the case.

Accurately recording the inline towline tensions, as opposed to deriving them from other measurements, can be achieved by either inserting a recording device into the towline makeup directly at a convenient junction or recording the force at either end of the line (i.e. at either the tug or tow's connection point).

3.3.1 Inline tension recording

The simplest means of measuring load in a towline is via inline load cells. These are machined blocks of steel fitted with strain gauges and calibrated against known loads to provide tension readouts. These are then connected inline between towline and bridle such that loads experienced by the tow are transmitted through the load cell and registered by strains in the body of the cell. The load readout can be to a hard-wired hand held device or to a wireless receiver. The output can be logged to a PC or other smaller microcomputer or logging device. The main issue with this approach is deciding where and how to locate the device. The most obvious location is at the point where the towline connects to the permanently fitted bridle located on the barge's bow. Unfortunately this point in the line spends the vast majority of the voyage underwater, typically only coming up above the water's surface when the towline is "shortened up" (i.e. when the tug is in close proximity to the tow for inshore maneuvering purposes) or the tow experiences extreme weather, see figure 5.1.3 for an example of the former. The logging of data in this situation for further post processing and analysis is further exacerbated by the fact that this point in the towline is typically 500m to 1km aft of the tug and data transmission over these distances is not economically practical nor particularly feasible within the power and footprint constraints on data capture and storage present in voyages of opportunity such as these.

Figure 3.3.1: Example use of a “Carpenter Stopper” in a salvage operation (image credit www.maritime.org)

There exists on the market towline sensors that are both submersible and can log data internally however these are expensive and irrespective of the device chosen, means of accurately synchronising data between the inline sensor and the external loggers is problematic. A potential solution was designed to incorporate the same logging technology as in the motion logging devices. These have a spare channel to the logging device and their geometry is such that it could be housed in a suitably sized milled and profiled solid steel block. High level detail of this arrangement may be seen in Appendix C later. For this research it was not taken any further however presents a potential area for future development in that a sensor of this nature would measure both the tensions and motions at a “node” on the lumped mass scheme as well as GPS time when surfaced at the start and end of tows giving the same reference timeline as that used on the on board motion loggers themselves.

In [Thomas (1994)] a "carpenter stopper" was used at the tug end of the line to choke the towline and provide a connection point allowing load cell to be anchored to a strong point on the tug and the towline connected to this with the main towing winch backed off and slack (figure 3.3.1 shows an example of a “carpenter stopper” in use on a salvage project). This requires working the deck while the towline is under load and also does not permit further paying out or hauling in of the towline without dismantling the equipment again. This suited the research in question as data gathering was for shorter term periods only and was able to take advantage that the research itself was funded by the US Navy and executed on US Navy tugs undertaking official defence related activities. Deploying this method for the entire duration of a commercial tow would be impractical, both in terms of commercial acceptability and degradation of crew safety.

Other means of monitoring inline tensions include deflection measurement whereby a known deflection is induced in the towline via a series of three offset pulleys and figure 3.3.2 shows an example of a commercially available device. The lateral force is recorded in the central pulley by monitoring shear in

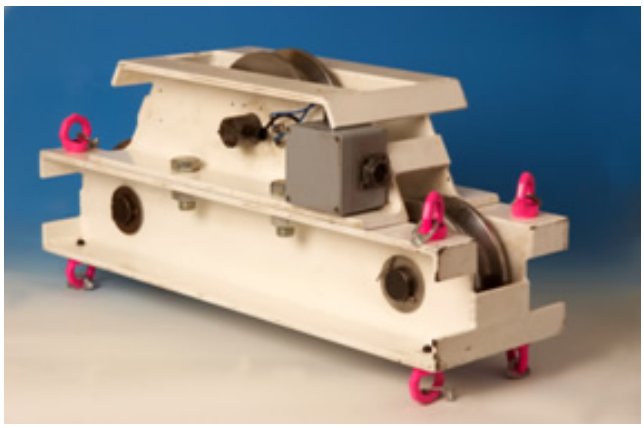

Figure 3.3.2: Line deflection meter (www.davysystems.com)

its central pin. This again requires bulky equipment to be installed and maintained on the aft deck of the tug and anecdotal evidence from users of such equipment indicates that it can be temperamental and difficult to calibrate for different types of wire. However this system could, in theory, be deployed and then not require any further maintenance during the voyage and allow the tug to adjust the deployed length of its tow line as required.

3.3.2 End force recording

The option to record the towline tensions can also be achieved by registering the force at either end of the towline. The towline between a typical tug and tow arrangement is between the drum on the tug and the towline connection points on the tow (SMIT bracket, figure 5.1.2, or similar). Options for measuring the force at the connection points are, therefore, limited to monitoring the tension of the rope on the winch drum, via strain gauges mounted to the winch's brakes or foundations, or monitoring loads through the connection point at the tow.

Most towline tensions are monitored via the readout of the winches load sensors which tends to be displayed in the bridge of the tug. The tow used for the post processing and presentation later in this thesis was one where the tug did not have the means of electronically storing continuous towline tensions and was limited to display only. Therefore only the estimated mean load at defined points in time were noted by the master and recorded on the voyage record sheet. It is also worth noting that very often these winch load monitors are not subject to any ongoing calibration throughout the tugs life and so the figures they report should be taken as a guide only.

3.4 Chapter Summary

In the preceding chapter the ideal dataset has been noted as well as an outline of the complications with meeting this goal, what attempts have been made in the past to overcome these and how the logging process proposed here improves matters further. Thereafter the particular characteristics of these sensors and their complimentary limitations were outlined and documented.

Means of obtaining such information in the field has been examined and it is worth noting that any such recording of motions or a system's actual "state" can only ever be an estimate of such. The following section looks at how this "state estimate" can be improved.

Chapter 4

Post processing of Measured Data

Given the quality of sensors available for this research, this chapter looks at the implementation of a state estimation scheme that aims to improve and translate the data recorded during a voyage of opportunity on which this research is based.

This chapter addresses, the full end to end sequence of post processing the data taking, as its input, the noisy and biased output from the sensors themselves, and through a series of combinations and transformations, outputting these as a time series of offsets in 3D space aligned to a suitable and useful navigation frame in readiness for feeding into the lumped mass numerical model developed in the next chapter.

4.1 Combining Data From Multiple Data Sources - designing a suitable Kalman filter

4.1.1 Fundamentals of the multi-tier Kalman filter employed

It is important to understand that it is not possible to measure, and therefore "know", perfectly the state of a system and any readings related to that system are merely estimates of either the system's state or of factors governing that system's state. The issue is how to get the best possible estimation of a system's state using all information available whether derived from sensor readings, known inputs to the system or from mathematical models of the system itself. With reference to the previous descriptions of the sensors available to us, it may be seen that the data gathered has differing error characteristics, i.e. GPS and tilt sensors will give a low and high frequency position and orientation estimate, respectively,

whose error is random and not directly linked to time elapsed, whereas the inertial sensors give a high frequency position estimate with an error that grows with respect to time elapsed.

The combination of these two readings to provide an “optimum state estimate” is a subject that has been widely explored since a seminal paper by Richard Kalman published in 1960 [Kalman (1960)]. The high level principle is that by combining a model of your system, which in itself may have known or unknown inaccuracies and imperfections, with a number of sensor readings of your system state, again with known or unknown noise and error characteristics, you can produce a mathematical "best fit" of the state of your system. The introductory chapter of [Maybeck (1979)] gives one of the clearest demonstrations of the principles behind the Kalman filter found during the execution of this research and asks the reader to consider the optimum means of combining two estimates of a system state. It is worth repeating and condensing the principles here as a primer to the detailed descriptions to follow of the filter designed and implemented in this research.

In his treatment Maybeck asks the reader to consider, appropriately enough, the problem with fixing one’s position at sea at night. The case is given for a single dimension only with a sighting on a star yielding an estimate of one’s position denoted z_1 which has an uncertainty, standard deviation, of σ_{z_1}, see figure 4.1.1. Then it is suggested that a second reading is taken at the same time, or so close to it so as to make no difference, by a navigator with greater skill which yields a second estimate of position denoted z_2 which has an uncertainty, standard deviation, of σ_{z_2}. These can be combined to produce a mathematically optimum estimate z_c with a decreased uncertainty of variance σ^2as follows (as shown in figure 4.1.1 by the solid plotted distribution):

$$z_c = \left[\frac{\sigma_{z_2}^2}{\sigma_{z_1}^2 + \sigma_{z_2}^2}\right] z_1 + \left[\frac{\sigma_{z_1}^2}{\sigma_{z_1}^2 + \sigma_{z_2}^2}\right] z_2 \tag{4.1.1}$$

$$\frac{1}{\sigma^2} = \frac{1}{\sigma_1^2} + \frac{1}{\sigma_2^2} \tag{4.1.2}$$

Equation 4.1.1 can be re-written as follows:

$$z_c = z_1 + \left[\frac{\sigma_{z_1}^2}{\sigma_{z_1}^2 + \sigma_{z_2}^2}\right] (z_2 - z_1) \tag{4.1.3}$$

And re-arranged into a final form:

$$z_c = z_1 + K\,(z_2 - z_1) \tag{4.1.4}$$

Where:

$$K = \left[\frac{\sigma_{z_1}^2}{\sigma_{z_1}^2 + \sigma_{z_2}^2}\right] \tag{4.1.5}$$

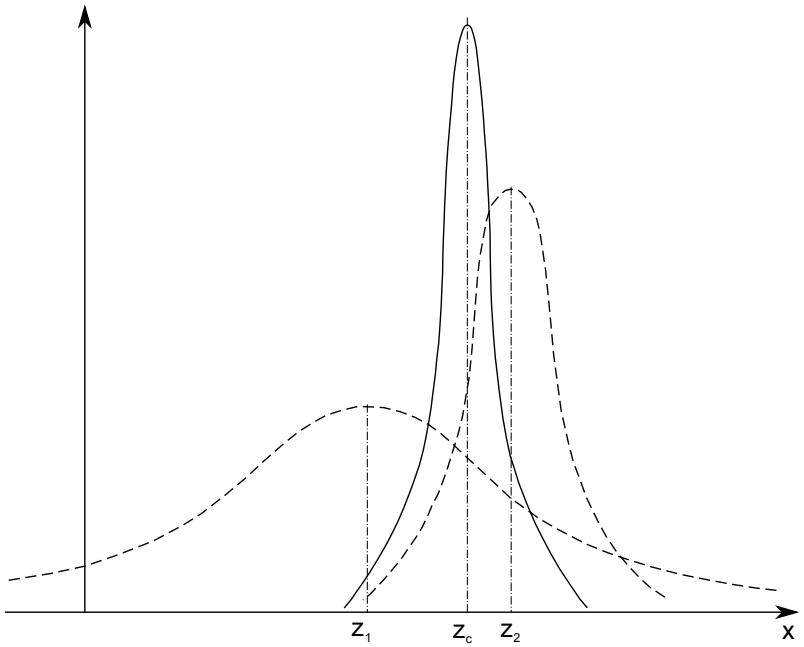

Figure 4.1.1: Conditional density of best estimate of a value based on two separate readings

If z_1 is now taken as a "prediction" of the system state based on a mathematical model of the system dynamics, for example a “dead reckoning” estimate based on a previous observation and known speed, instead of a second reading by a navigator of differing skill (or error characteristics) and z_2 is a measurement taken of the system state which is then used to "correct" your prediction then you have the beginnings of the "predictor-corrector" nature of the basic Kalman filter.

Thereafter the application of the static solution to that of a dynamic one demonstrating the effect of the weighting parameters is outlined and showing the analogy with the static derivation above. There is nothing to be gained by repeating any further as a specific implementation of the Kalman filter for the dynamic system of a floating body in a seaway whose motions are recorded by gyroscopes, accelerometers, tilt sensors and a GPS unit will now be developed.

The Kalman filter, as alluded to above, implements, at its core, a "predictor-corrector" iterative algorithm on a state variable, or more commonly, a vector of state variables. The filter operates on an iterative basis and employs the following steps (detailed implementation of each the matrices noted below may be seen in the later sections of this chapter):

1. Initialise state vector, $[x]_0$ with values representing state at the start of the simulation or calibration values while at rest.

2. Initialise the state transition matrix $[A]$ with the prediction function which represents the mathematical model of the theoretical propagation of system states from time step $k-1$ to k such that:

$$[x]_k = [A]\,[x]_{k-1} \tag{4.1.6}$$

3. Initialise the measurement vector, $[y]_0$ with the initial measurements from the system.

4. Initialise the measurement matrix, $[C]$ which maps the measurements against the state vector.

5. Initialise the measurement noise covariance matrix, $[S_z]$ with the characteristic noise covariances of the measurement instruments.

6. Initialise the process noise covariance matrix, $[S_w]$.

7. Initialise the simulation noise covariance matrix, $[P]$ as equal to the process noise covariance matrix, $[S_w]$.

8. Initialise the innovation vector, also known as the error vector, $[E]$ to zero. This vector is used, in each time step, to store the difference between the propagated or predicted state and the measured state and is then adjusted or weighted using the Kalman gain matrix to correct the propagated state to the latest "best estimate".

9. Commence loop for each time step where $t = 0$; step size dt; to T, where T is the total time of the process measured and subscript k represents the current time step:

   (a) Propagate initial state vector (for the first time through the loop) or the latest state estimate, through time step dt to get estimated state at $t+dt$ before correction using the equation below (this is known as the "a priori estimate" signified by the bar above the vector identifier):

   $$[\bar{x}]_k = [A]\,[x]_{k-1} \tag{4.1.7}$$

   (b) Store measurements in the measurement vector $[y]$

   (c) Update the innovation vector using:

   $$[E] = [y]_k - [C]\,[x]_k \tag{4.1.8}$$

   (d) Calculate the covariance of the innovation, $[S]$ where:

   $$[S] = [C]\,[P]\,[C]^T + [S_z] \tag{4.1.9}$$

   (e) Form the Kalman gain matrix, $[K]$ used to correct the state estimate based on measurements made, where:

   $$[K] = [A]\,[P]\,[C]^T\,inv\,[S] \tag{4.1.10}$$

   (f) Using the Kalman gain matrix and the "a priori" estimate above, update the state estimate:

   $$[x]_k = [\bar{x}]_k + [K]\,[E] \tag{4.1.11}$$

(g) Compute the covariance of the estimate error to be used in the next iteration through the loop:

$$[P] = [A]\,[P]\,[A]^T - [A]\,[P]\,[C]^T\,inv\,[S]\,[C]\,[P]\,[A]^T + [S_w] \tag{4.1.12}$$

(h) Save/log parameters, including the error estimate for storage and future use before continuing the loop.

As all data is available for post processing after the event, i.e. as opposed to measuring and adjusting "on the fly" as readings from the sensors come in, a number of options are available to us to extract the best solution and a linear Kalman filter was opted for on the basis of it offering reasonable mathematical rigour and robustness with simplicity of implementation. An option for future research may be to look at alternative solutions in a similar vein such as Kalman smoothing algorithms, such as [Movellan (2011)] or [Pnevmatikakis at al (2012)], which specifically take advantage of the fact that all data is available from the outset and the Kalman filter can be run on the data twice, both chronologically and in reverse order, before combining to get the best possible smoothed data. However the linear Kalman filter was deemed to perform adequately well for the purposes of this research without delving too deeply into the realms of electrical signal theory and away from ocean engineering cable dynamics.

In addition there are two principle options for tracking system states. The first tracks actual states where the state vector, which for our case, would store actual estimates of position and attitude.

Alternatively, for example in [Setoodeh et al (2004)], these values can be tracked outside the filter with the filter only keeping track of the error, or system bias which is then combined with the external state estimates to come up with the best estimate of the actual system state at any given point in time.

The implementation used for the research here employed a two stage filtering process coded in MatLab, see figure 4.1.2, whereby raw data recorded on the datalogging devices were processed as follows (Note: "vessel" could refer to the logger and data associated with either the tug or the barge).

A subroutine was built to execute the two stage filter process in series. This was then run from a controlling program which extracted the raw measurements from a series of large CSV (comma separated value) based text files and fed to the filter an hour at a time. The output was then saved as a series of vessel offsets against a global timeline. Therefore for each hour of the voyage, the cascade filters produced a pair of files, one for the tug and one for the barge containing the 3D positions of the towline end points ready for input into the lumped mass algorithm later.

A high level description for this routine is as follows:

- High frequency tilt sensor input of roll and pitch angles as well as low frequency data from the mean heading of the vessel obtained from GPS sensor were read in from the raw measurement files (one for the sensors and one for the GPS data).

– Overlap in data was checked for to ensure that a complete dataset of GPS readings and sensor readings was available for the hour in question (data outages and quality are reviewed in the next chapter). Where sporadic drop outs in the GPS data were found, these were filled by cubic interpolation.

– The origin for the hour long run was set as the first reading in the data series and the latitude and longitude readings were converted to positions in 3D space where the surface of the ocean area being traversed in any given hour was taken to be a flat plane (a reasonable assumption given that at a maximum towing speed of 8 knots, the greatest area covered would be a square with a diagonal of around 14.5km or a straight line of the same length). MatLab's internal cartographic functions were used for this with a WGS72 geodetic scheme.

– Scaling and conversion factors were set for converting the "as measured" voltages to real world, useable values. Bias values and tilt sensor non linear corrections were set depending if it was a tug or barge logger's data being imported and the resulting acceleration, angular velocity and orientation measurements loaded and converted to the correct axis system.

– Roll and pitch data vectors populated from the data loaded above at the higher sampling frequencies of the MEMS and tilt sensors. Yaw data interpolated and filled out from the lower frequency, GPS heading readings.

– Attitude transition, measurement, measurement noise covariance, process noise covariance matrices as well as state and error vectors initialised (see sections 4.1.2 through 4.1.4 for detailed implementation notes).

– First stage attitude filter run for all time steps producing a vector of system state estimates of roll, pitch, yaw, roll velocity, pitch velocity and yaw velocity at each time step.

– It was found that a significant amount of noise was still present in the attitude estimates at this stage and so a secondary low pass filter applied to reduce this noise.

– The physical offsets for each of the loggers from the CoG and towline connection points were loaded into memory.

– The estimates of vessel orientation were then used to correct the accelerations from the triaxial accelerometers by removing the gravity component inherent in the readings i.e. at rest and level, the z axis sensor records a negative acceleration of $-9.81m/s^2$ with x and y axis reading a theoretical zero acceleration (see section 4.1.5 for detailed implementation notes).

– Motions were then translated via rigid body dynamic assumptions to the vessel's assumed centre of rotation i.e. it's CoG.

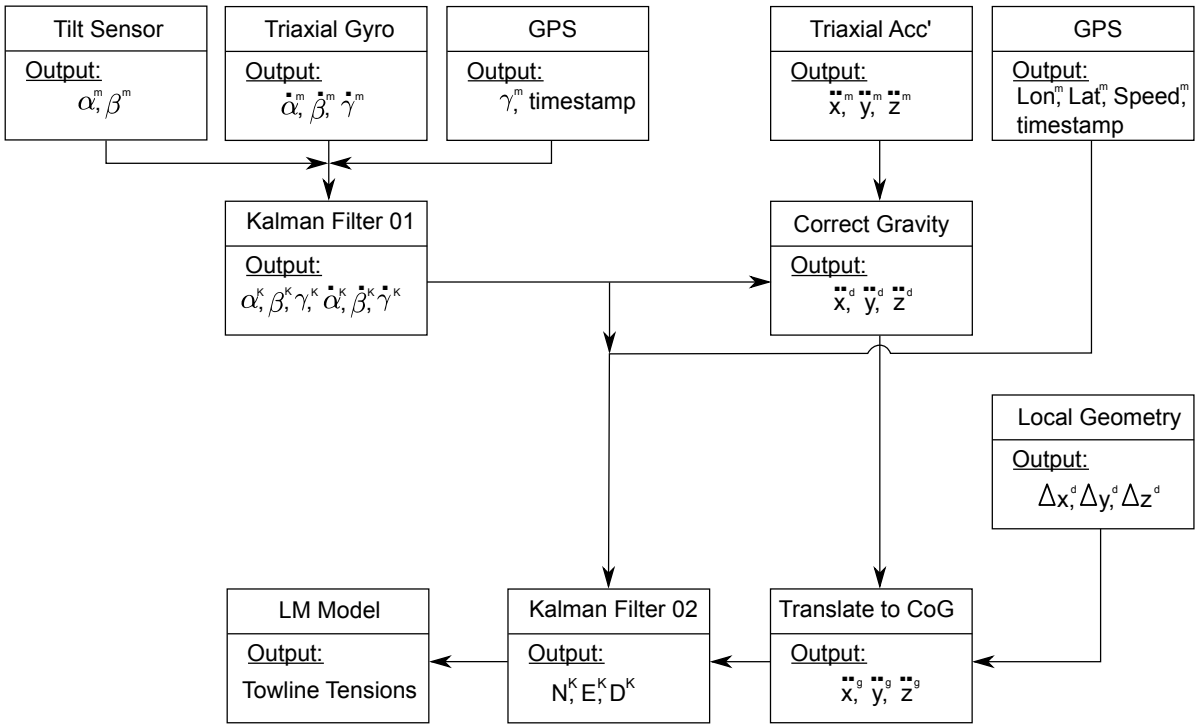

Figure 4.1.2: Multi-tier Kalman filter block diagram

- Thereafter the INS data was converted to a local inertial frame where East, North and Down are mapped to a flat earth local Cartesian frame.
- A second Kalman filter was then used to combine readings from the GPS sensors with the corrected/translated accelerations to give an estimate of the towline connection point's position in 3D space, with the GPS fixes used to correct any residual bias and errors in the integration of the accelerometer readings. This was a relatively "loose" coupling of the GPS and INS units. Tighter coupling was not feasible as the raw satellite data was not available through the firmware implementation used here.
- The output of the two Kalman filters was then combined using equations 4.1.22 through 4.1.24 to provide positions of the towline connection point to the vessel in global space ready for input into the lumped mass equations covered later in section 5.2.

4.1.2 Measurement noise covariance matrices

The measurement noise covariance matrix, as mentioned above, is a measure of the noise present in the measurement sensors of the system. This was simply found by taking the variance of the zero mean (after adjusting for static bias) white noise signal produced by each sensor during the soak test, the values of which are as reported in table 3.2.2 and table 3.2.9 and then entering these in the appropriate location within the diagonal on the measurement noise covariance matrix for either the attitude

Table 4.1.1: Process noise simulations - Attitude filter, amplitude and period ranges

	Minimum	Maximum	Step
Amplitude (deg)	5	45	5
Period (secs)	10	40	5

estimation filter or the position estimation filter. The assessment of the process noise covariance matrix is described in the respective of section for each of the filters.

4.1.3 Process noise covariance matrix

The process noise covariance matrix tells the filter essentially how much to trust the readings and how much to trust the model. During literature review a wide difference on viewpoints was noted as to how best to obtain relevant values for the process noise covariance matrix but a consistent finding was that for attitude and position filters used in navigation, low values of the order of between 1 $E^{-3}$to 1 E^{-2} where appropriate. In an attempt to verify this, for the orientation filter, a large number of simulated runs were executed across a range of amplitudes and periods of roll, pitch, and yaw oscillations onto which was superimposed white noise derived mathematically from the actual measurement noise covariance, obtained from soak test data on all sensors employed. For each of these runs a range of process noise covariance values were applied to obtain an estimate of the orientation or position, depending on the filter under review. This allowed the calculation of "true" values based on theoretical orientations and positions, which were in turn based on "perfect" readings superimposed with representative noise for each of the real world sensors in each of the loggers. These could then be compared with the estimates from the Kalman filters, outlined above and below, which resulted in an error between the two values. This error was then used to rank the process noise values used to obtain an optimum value for each channel in the orientation filter. In addition, as the theoretical noise was generated programmatically based on the characteristics from the soak data, several runs were made to understand if there was any sensitivity to small variations in the input data from disparately generated noise signals.

Process Noise Characteristics of the Attitude Filter

The range of amplitudes and periods across each of the roll, pitch and yaw axis were as per table 4.1.1 with corresponding theoretical data created for a 100 seconds run time against each data pair.

Initially a fairly course range of process noise covariance values was used to find the relevant inflection points on the error graphs and once this was identified a more refined search around any points was conducted to see the detail of the effect of varying the process noise covariance.

Once this point was found a series of runs were made for a number of discrete, single pairings of amplitude and period values and it was found that the results were stable. Figure 4.1.3 shows data for the roll angle estimate errors across 5 runs for an amplitude/period pairing of 25 deg/30 secs (sub-figure a) and 45 deg/30 secs (sub-figure b). It may be seen that despite the code creating new values for the noise data to be overlaid onto the theoretical "clean" oscillations, the variation in the errors reported are minimal. This was consistent across all readings however the overall magnitude of error increased as the magnitude of the amplitude of oscillations increased. The selection process, nevertheless allows for selection of values that ensure minimum error possible for the sensor quality and process employed.

Once satisfied that the process was relatively insensitive to the noise variations, the full range of runs could be carried out with data assessed against a single 100 sec run for each pairing. The results produced 32 traces for each degree of freedom. As noted above, it was observed that the error increase as the amplitude increased however the error was insensitive to the period employed. In addition it was found that across roll and pitch degrees of freedom, a consistent value for the process noise covariance which offered optimum error results while each degree of freedom exhibited identical behaviour. This was deemed a valid finding and demonstrated that the process noise coefficient was relatively insensitive to the small difference in the measurement noise signals. Even for yaw where the error characteristics and both source of the direct measurements and update method differed slightly the same process noise sensitivities were observed.

The error was relatively unaffected when the process noise covariance was in the range of 0.7 to 0.8 x $E^{-3}$and so a consistent value of 0.75 x E^{-3} was used for the orientation estimating filter against roll and pitch, reference figure 4.1.4 and for the position filter it was found that a value of 1 E^{-8} offered a stable solution.

4.1.4 Kalman filter for determining vessel orientation

When placed on board a vessel the axis of the logger are aligned with the principle axis of the vessel resulting in the following correlation between local logger axis and local ship axis as shown in figures 4.1.5 and 4.1.6.

With reference to figure 4.1.2 it may be seen that there are two Kalman filters operating in cascade. The first filter takes measurements of the pitch, roll and yaw and derives the best estimate of the vessel's actual orientation and, bearing in mind what was noted at the start of section 4.1.1, i.e. that it can never be absolutely known what the true orientation of the tug is at any given time, only the best possible fit of the data gathered can be sought. Given that the dataloggers in question use relatively low grade, as opposed to tactical grade, sensors, there was some concern over just how accurate a position estimate

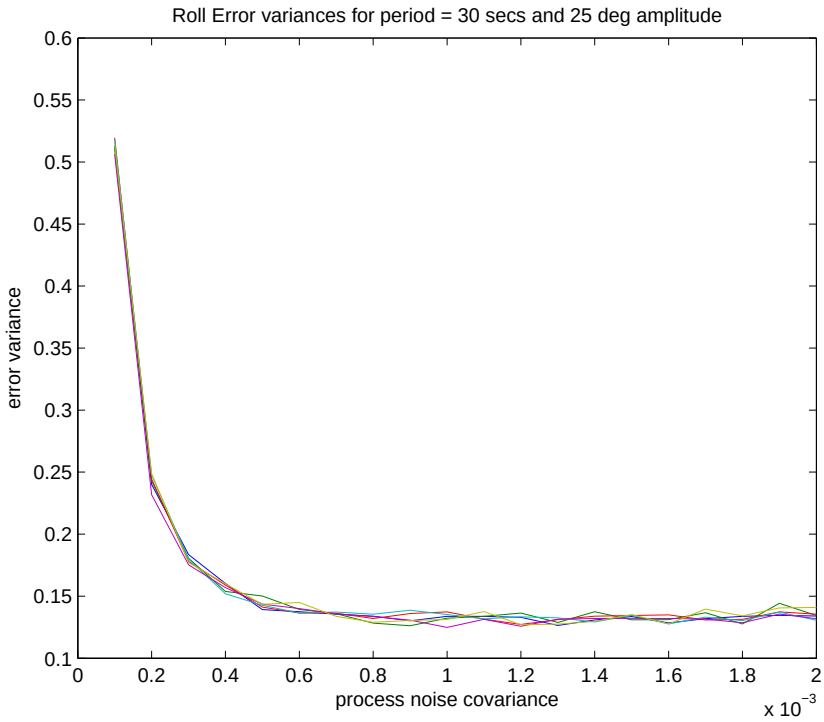

(a) Roll errors for 25 deg amplitude and 30 seconds period

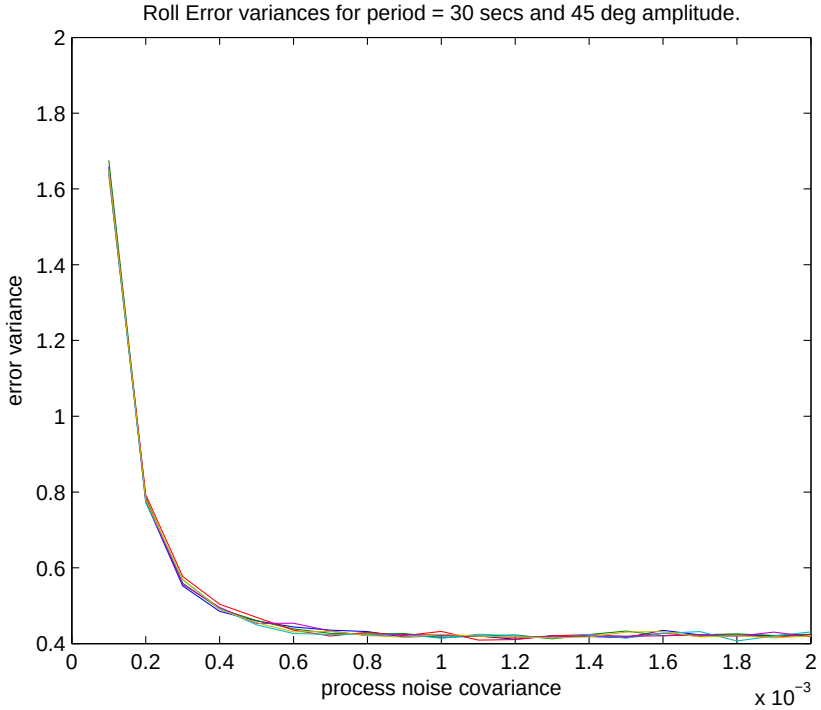

(b) Roll errors for 45 deg amplitude and 30 seconds period

Figure 4.1.3: Attitude process noise covariance sensitivities

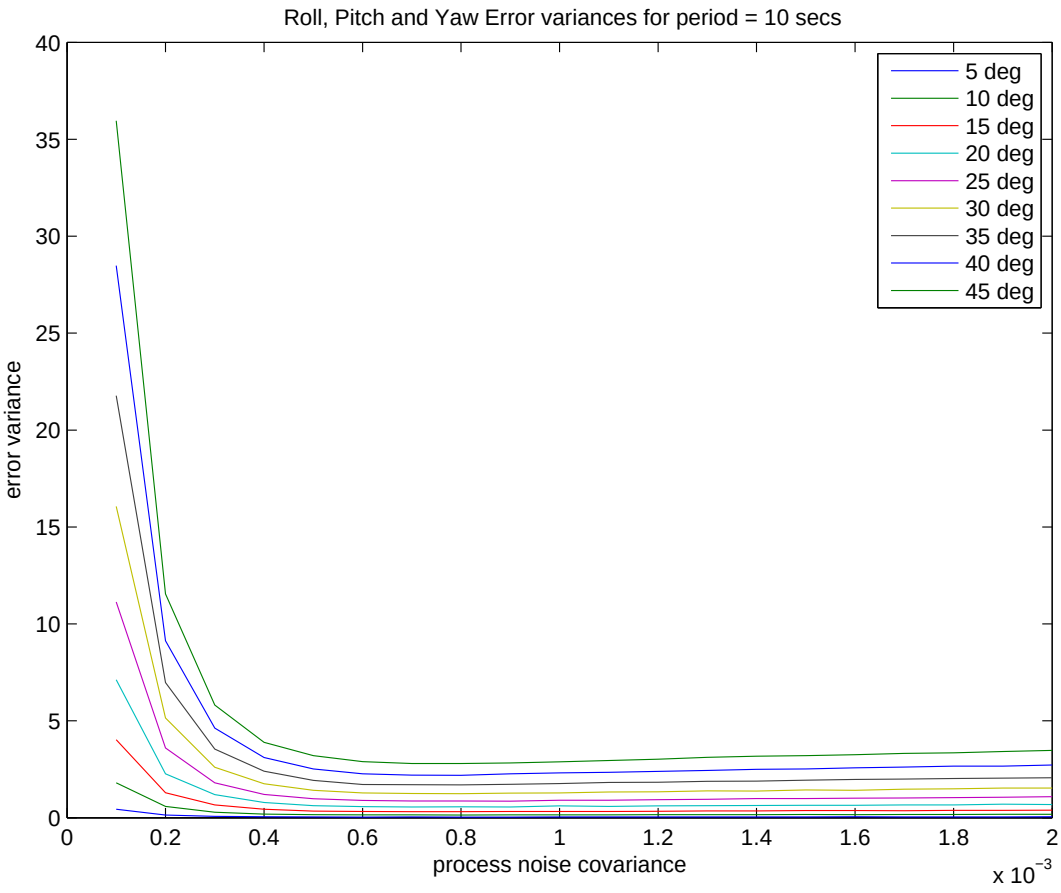

Figure 4.1.4: Process noise covariance sensitivity tests for range of amplitudes

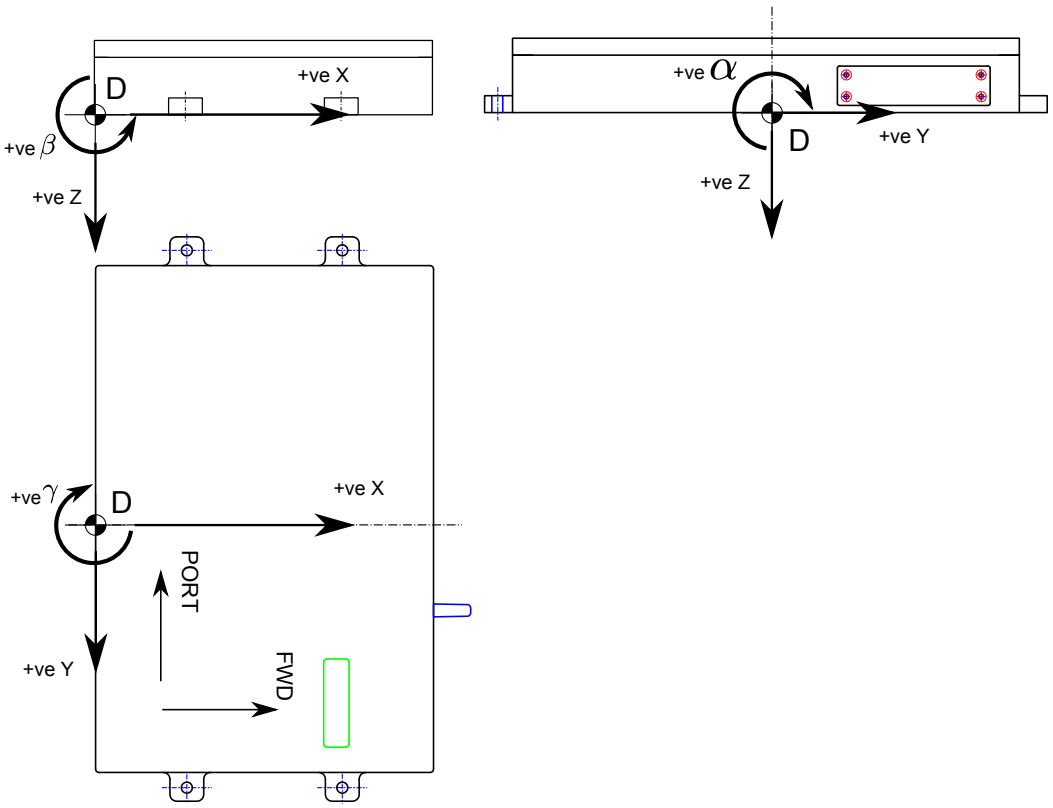

Figure 4.1.5: DLogg local axis definitions

could be achieved given the equipment available for the trials and so some initial experiments on the algorithm for the attitude estimate were made.

The attitude Kalman filter was coded in MatLab with the key matrices in the filter modeled as follows (applicable to tug and barge separately):

Attitude Estimation - State Propagation:

$$[x]_k = [A]\,[x]_{k-1} \tag{4.1.13}$$

$$\begin{bmatrix} \alpha^K \\ \beta^K \\ \gamma^K \\ \dot{\alpha^K} \\ \dot{\beta}^K \\ \dot{\gamma}^K \end{bmatrix}_k = \begin{bmatrix} 1 & 0 & 0 & dt & 0 & 0 \\ 0 & 1 & 0 & 0 & dt & 0 \\ 0 & 0 & 1 & 0 & 0 & dt \\ 0 & 0 & 0 & 1 & 0 & 0 \\ 0 & 0 & 0 & 0 & 1 & 0 \\ 0 & 0 & 0 & 0 & 0 & 1 \end{bmatrix} \begin{bmatrix} \alpha^K \\ \beta^K \\ \gamma^K \\ \dot{\alpha}^K \\ \dot{\beta}^K \\ \dot{\gamma}^K \end{bmatrix}_{k-1} \tag{4.1.14}$$

It is worth noting here that simple Euler angles are used to record roll, pitch and yaw. As the vessel will, hopefully, not find itself approach 90 degrees of roll or pitch then there should be no issues with “gimbal

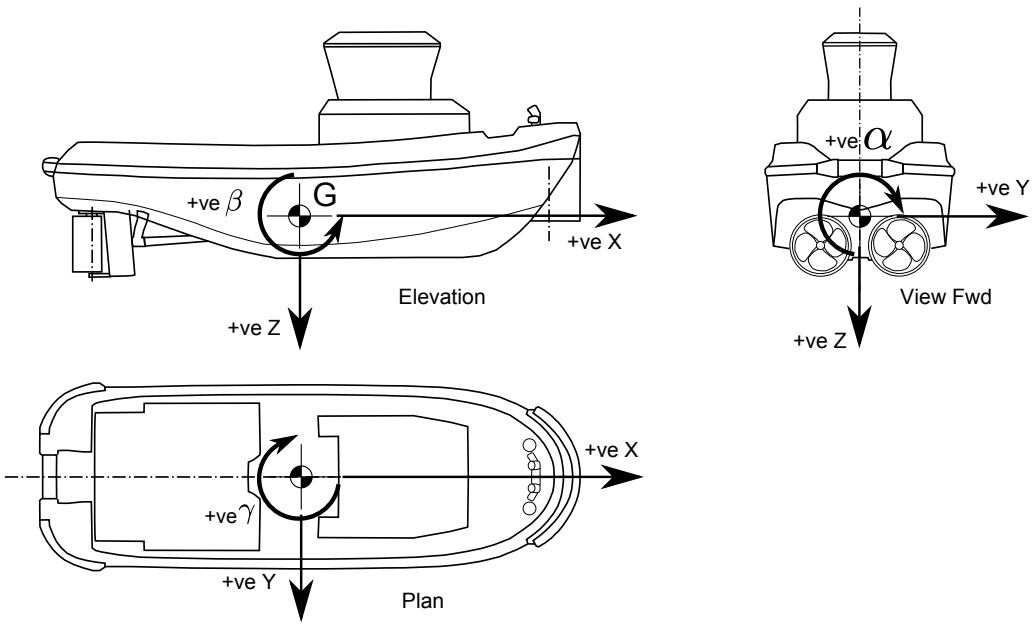

Figure 4.1.6: Vessel local axis definitions

lock" which is a concern with INS systems in aerospace applications.

In addition, for the propagation of angular velocity from one time step to the next, it was simply estimated to be equal to the last. As the model does not have access to rules that could govern the predictability of the motions of the vessel (excited by random sea state) and the filter does not allow for access to previous readings from which a projection could be made (i.e. $\dot{\beta^K}_{k-1}$ and $\dot{\beta^K}_{k-2}$ for a linear estimate or more for cubic/quadratic projections) this was all that was available. If this was found to be an issue, a more robust system could be possible using look-up tables which provided an estimate of the prediction based on the fact that the next value is available, due to the fact a complete time series of the data is ready for post processing at any one time. As it transpired, due to the long period of oscillations, an estimate of the next value being equal to the last was sufficient for the filter to stabilise.

Attitude Estimation - Measurement Matrix:

$$[E] = [y]_k - [C]\,[\bar{x}]_k \tag{4.1.15}$$

$$[E] = \begin{bmatrix} \alpha^m \\ \beta^m \\ \gamma^m \\ \dot{\alpha}^m \\ \dot{\beta}^m \\ \dot{\gamma}^m \end{bmatrix}_k - [C]\,[\bar{x}]_k \tag{4.1.16}$$

The measurement matrix is set as follows and note the assumption that all yaw measurements are available at the full data resolution as the 1 Hz GPS readings for heading have been upsampled to provide 10 Hz cover for the filter. It is worth noting that MatLab provides a very useful and little known function ("unwrap") for assisting interpolating radial angle data across the 360/0 degree boundary.

$$[C] = \begin{bmatrix} 1 & 0 & 0 & 0 & 0 & 0 \\ 0 & 1 & 0 & 0 & 0 & 0 \\ 0 & 0 & 1 & 0 & 0 & 0 \\ 0 & 0 & 0 & 1 & 0 & 0 \\ 0 & 0 & 0 & 0 & 1 & 0 \\ 0 & 0 & 0 & 0 & 0 & 1 \end{bmatrix} \tag{4.1.17}$$

Some simulated data was created to represent sinusoidal pitch readings from a very noisy tilt sensor in conjunction with some less noisy but variously biased readings from a gyro sensor. It is important to understand if the bias, in particular, had any effect on the long term stability of the filter's estimate of the oscillating pitch and roll values, i.e. didn't want to find that over time the barge was being shown to execute complete revolutions about the roll or pitch axis. The benefit of simulated datasets was that various scenarios could be created to examine the bounds of the filter's operability and highlight any areas of concern over its robustness.

The first two runs detailed in figures 4.1.7 and 4.1.8 show the results of the pitch channel of data only however results for other channels were similar. Here the improvement in the quality of data can clearly be seen. The trend of the integrated data to continue to deviate unbounded, due to small residual bias in the signal, can also be seen and the simulation time is extended to 500 seconds, as in figure 4.1.9, it may be seen that, irrespective of the deviation in integrated data (i.e. angular data derived from the gyroscope measurements), the best estimate continues to hold to a zero mean estimate. This is important as confidence in the ability of the filter to be relatively insensitive to bias errors is required due to the fact that, while estimated bias means are calculated, the logger may be susceptible to longer term bias drift or temperature induced fluctuations which this implementation does not take account of.

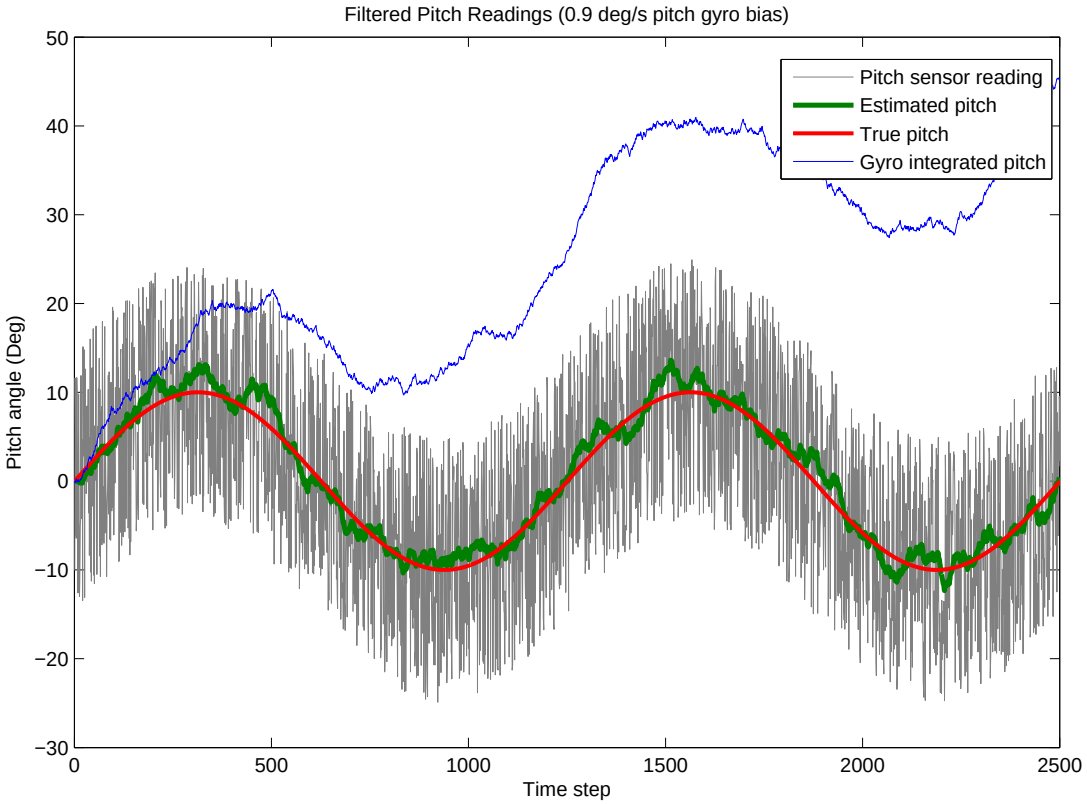

Figure 4.1.7: Example Kalman filtering of simulated pitch angle and gyro sensor suite (0.9 deg/s bias)

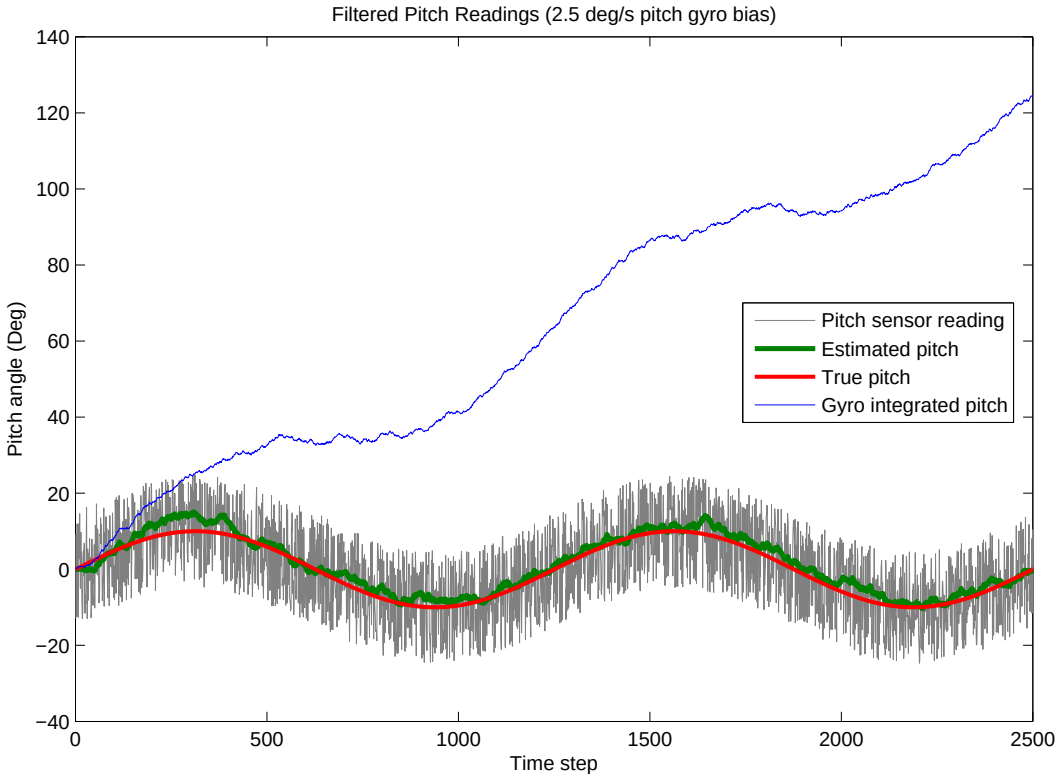

Figure 4.1.8: Example Kalman filtering of simulated pitch angle and gyro sensor suite (2.5 deg/s bias)

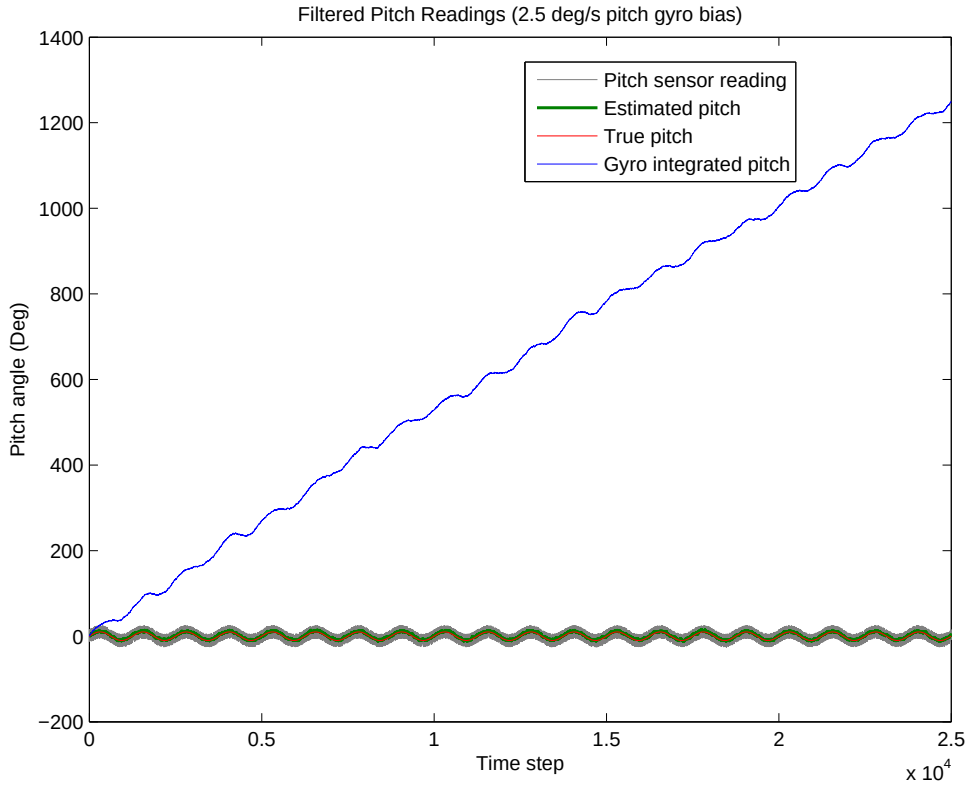

Figure 4.1.9: 500 second prolonged run of simulated pitch sensor data

4.1.5 Kalman filter for position

Over and above the requirements to filter the data to obtain best estimates of attitude and position there is also a requirement, due to the nature of the sensors employed, to edit sensor data to:

- Correct recorded accelerations to remove the gravity component.
- Translate accelerations from point of recording to assumed centre of gravity of the vessel (i.e. to remove any centripetal or tangential effects when combining with GPS data).
- Convert body accelerations and motions in RPY(Roll Pitch Yaw) coordinate system to a local planar NED (North East Down) coordinate system that is compatible with the data and low frequency position estimates obtained from the GPS unit. To ensure that the error characteristics are correctly applied to the accelerometer and velocity data, this step is carried out within the Kalman filter, after the integration of the accelerometer data.
- Translate rigid body motions at the CoG to the towline connection point on the vessel or barge for inputting into the lumped mass simulation routines.

Euler Rotation Matrices The rotation matrices employed in the transformations within the subsequent sections are defined as follows:

$$C_\alpha = \begin{bmatrix} 1 & 0 & 0 \\ 0 & \cos\alpha & \sin\alpha \\ 0 & -\sin\alpha & \cos\alpha \end{bmatrix} \tag{4.1.18}$$

$$C_\beta = \begin{bmatrix} \cos\beta & 0 & -\sin\beta \\ 0 & 1 & 0 \\ \sin\beta & 0 & \cos\beta \end{bmatrix} \tag{4.1.19}$$

$$C_\gamma = \begin{bmatrix} \cos\gamma & \sin\gamma & 0 \\ -\sin\gamma & \cos\gamma & 0 \\ 0 & 0 & 1 \end{bmatrix} \tag{4.1.20}$$

Removal of Gravity Component The accelerations recorded in the logger are zeroed, due to the fact that as they incline they will detect a component of the vertical gravity field and report this as a component of acceleration along the axis normal to the axis of rotation which required correction. These effects were removed as follows:

$$\begin{bmatrix} \ddot{x}^d \\ \ddot{y}^d \\ \ddot{z}^d \end{bmatrix} = \begin{bmatrix} \ddot{x}^m \\ \ddot{y}^m \\ \ddot{z}^m \end{bmatrix} - C_\alpha C_\beta C_\gamma \begin{bmatrix} 0 \\ 0 \\ g \end{bmatrix} \tag{4.1.21}$$

Translation from Data Logger Position to CoG Position Taking the data recorded and subsequently cleaned up at each datalogger station and resolving into a single dataset suitable for input into the catenary simulation involves translating the motions through several different reference frames.

Firstly, local to each body, the tug and barge are treated as separate rigid bodies rotating about their respective centres of mass. Given the fact that actual angular and linear displacements of each body are being measured, independently of each other, the effect of the towline on the two bodies is implicitly captured.

The next step therefore is to resolve the motions and accelerations recorded at the datalogging location to the vessel centre of gravity.

Translating from sensor position (d) to CoG (g) (note that the superscript “K” is left out below for ease of reading but the estimates for attitude used are those derived from the first stage filter):

$$\ddot{x}^g = \ddot{x}^d + \ddot{\beta}\triangle z^d - \dot{\beta}^2\triangle x^d - \ddot{\gamma}\triangle y^d - \dot{\gamma}^2\triangle x^d \tag{4.1.22}$$

$$\ddot{y}^g = \ddot{y}^d - \ddot{\alpha}\triangle z^d + \dot{\alpha}^2\triangle y^d - \ddot{\gamma}\triangle x^d + \dot{\gamma}^2\triangle y^d \tag{4.1.23}$$

$$\ddot{z}^g = \ddot{z}^d + \ddot{\alpha}\triangle y^d + \dot{\alpha}^2\triangle z^d + \ddot{\beta}\triangle x^d + \dot{\beta}^2\triangle z^d \tag{4.1.24}$$

Kalman filter for determining vessel position As above, with reference to figure 4.1.2 the second Kalman filter in the implementation used here is shown to be operating in cascade to the first taking best estimated attitude as input along with accelerometer, GPS timestamp, GPS velocity over ground and GPS heading information.

$$\begin{bmatrix} \ddot{x}^K \\ \ddot{y}^K \\ \ddot{z}^K \\ \dot{N}^K \\ \dot{E}^K \\ \dot{D}^K \\ N^K \\ E^K \\ D^K \end{bmatrix}_k = \begin{bmatrix} 1 & 0 & 0 & 0 & 0 & 0 & 0 & 0 & 0 \\ 0 & 1 & 0 & 0 & 0 & 0 & 0 & 0 & 0 \\ 0 & 0 & 1 & 0 & 0 & 0 & 0 & 0 & 0 \\ & & & 1 & 0 & 0 & 0 & 0 & 0 \\ [C_\alpha.C_\beta.C\gamma]\,dt & & & 0 & 1 & 0 & 0 & 0 & 0 \\ & & & 0 & 0 & 1 & 0 & 0 & 0 \\ & & & dt & 0 & 0 & 1 & 0 & 0 \\ [C_\alpha.C_\beta.C\gamma]\,\frac{dt^2}{2} & & & 0 & dt & 0 & 0 & 1 & 0 \\ & & & 0 & 0 & dt & 0 & 0 & 1 \end{bmatrix} \begin{bmatrix} \ddot{x}^K \\ \ddot{y}^K \\ \ddot{z}^K \\ \dot{N}^K \\ \dot{E}^K \\ \dot{D}^K \\ N^K \\ E^K \\ D^K \end{bmatrix}_{k-1} \tag{4.1.25}$$

Here offsets, velocities and accelerations are in the local body frame, converted to navigation frame later. As for the attitude estimator the accelerations from one step to the next are simply taken as equal to each other and again, this was found to be sufficient for the filter to stabilise. Future work could revolve around investigating means of improving the robustness of this with a more comprehensive treatment.

Position Estimation - Measurement Matrix: As before equation 4.1.15 is expanded however due to the differing update rates for the GPS, this only occurs when there is a GPS fix to process, otherwise the filter ignores updates and simply integrates the accelerometer data. For the vertical position and velocity measurements, this is estimated at a mean position of the deck above the water line and zero m/s respectively as the altitude data is not obtainable from the logger in its current implementation. This will smooth out the heave offsets and under report the true amplitude. Note the measurement matrix adjusts every 10 iterations through the loop (10 Hz MEMs data read rate). Where there are no data readings of position and speed form the GPS system, the measurement mapping matrix is:

$$[C] = \begin{bmatrix} 1 & 0 & 0 & 0 & 0 & 0 & 0 & 0 & 0 \\ 0 & 1 & 0 & 0 & 0 & 0 & 0 & 0 & 0 \\ 0 & 0 & 1 & 0 & 0 & 0 & 0 & 0 & 0 \\ 0 & 0 & 0 & 0 & 0 & 0 & 0 & 0 & 0 \\ 0 & 0 & 0 & 0 & 0 & 0 & 0 & 0 & 0 \\ 0 & 0 & 0 & 0 & 0 & 0 & 0 & 0 & 0 \\ 0 & 0 & 0 & 0 & 0 & 0 & 0 & 0 & 0 \\ 0 & 0 & 0 & 0 & 0 & 0 & 0 & 0 & 0 \\ 0 & 0 & 0 & 0 & 0 & 0 & 0 & 0 & 0 \end{bmatrix} \tag{4.1.26}$$

However when a reading from the GPS is available, the measurement matrix is updated to map these readings to the state a priori estimate as follows:

$$[C] = \begin{bmatrix} 1 & 0 & 0 & 0 & 0 & 0 & 0 & 0 & 0 \\ 0 & 1 & 0 & 0 & 0 & 0 & 0 & 0 & 0 \\ 0 & 0 & 1 & 0 & 0 & 0 & 0 & 0 & 0 \\ 0 & 0 & 0 & 1 & 0 & 0 & 0 & 0 & 0 \\ 0 & 0 & 0 & 0 & 1 & 0 & 0 & 0 & 0 \\ 0 & 0 & 0 & 0 & 0 & 1 & 0 & 0 & 0 \\ 0 & 0 & 0 & 0 & 0 & 0 & 1 & 0 & 0 \\ 0 & 0 & 0 & 0 & 0 & 0 & 0 & 1 & 0 \\ 0 & 0 & 0 & 0 & 0 & 0 & 0 & 0 & 1 \end{bmatrix} \tag{4.1.27}$$

$$[E] = \begin{bmatrix} \ddot{x}^g \\ \ddot{y}^g \\ \ddot{z}^g \\ \dot{N}^m \\ \dot{E}^m \\ \dot{D}^m \\ N^m \\ E^m \\ D^m \end{bmatrix}_k - [C]\,[\bar{x}]_k \tag{4.1.28}$$

Noise Covariance Matrices Measurement noise covariance matrix, which contains the characteristic noise covariances of the measurement instruments. This is was specified as a 9x9 matrix as follows, after tuning.

$$[S_z] = \begin{bmatrix} 1E^{-8} & 0 & 0 & 0 & 0 & 0 & 0 & 0 & 0 \\ 0 & 1E^{-8} & 0 & 0 & 0 & 0 & 0 & 0 & 0 \\ 0 & 0 & 2E^{-8} & 0 & 0 & 0 & 0 & 0 & \\ 0 & 0 & 0 & 1E^{-8} & 0 & 0 & 0 & 0 & 0 \\ 0 & 0 & 0 & 0 & 1E^{-8} & 0 & 0 & 0 & 0 \\ 0 & 0 & 0 & 0 & 0 & 0.0001 & 0 & 0 & 0 \\ 0 & 0 & 0 & 0 & 0 & 0 & 1E^{-3} & 0 & 0 \\ 0 & 0 & 0 & 0 & 0 & 0 & 0 & 1E^{-3} & 0 \\ 0 & 0 & 0 & 0 & 0 & 0 & 0 & 0 & 1E^{-3} \end{bmatrix} \tag{4.1.29}$$

Process noise covariance matrix, as discussed earlier in 4.1.3, was found to work well when set to a constant 0.001 which was consistent with findings in literature on position Kalman filters.

$$[S_w] = \begin{bmatrix} 0.001 & 0 & 0 & 0 & 0 & 0 & 0 & 0 & 0 \\ 0 & 0.001 & 0 & 0 & 0 & 0 & 0 & 0 & 0 \\ 0 & 0 & 0.001 & 0 & 0 & 0 & 0 & 0 & 0 \\ 0 & 0 & 0 & 0.001 & 0 & 0 & 0 & 0 & 0 \\ 0 & 0 & 0 & 0 & 0.001 & 0 & 0 & 0 & 0 \\ 0 & 0 & 0 & 0 & 0 & 0.001 & 0 & 0 & 0 \\ 0 & 0 & 0 & 0 & 0 & 0 & 0.001 & 0 & 0 \\ 0 & 0 & 0 & 0 & 0 & 0 & 0 & 0.001 & 0 \\ 0 & 0 & 0 & 0 & 0 & 0 & 0 & 0 & 0.001 \end{bmatrix} \tag{4.1.30}$$

Rigid Body Translations from CoG to Towline Connection Location Before progressing, it is worth considering the towline connection points themselves. In the case of the tug this is assumed to be at the aft edge of the working deck on the CL. Transverse slippage across the roller stern of the tug between the longitudinal buffers is not accounted for. However for a typical dataset in this study this unrecorded transverse movement represents between 1% and 2% of the spacing between the tug and barge and, as it is not acting along the surge axis (i.e. axis of greatest sensitivity to changes in relative position) it is deemed not significant.

For the barge, this connection point is represented by the intersection of the mid point between the two connection points of the tow bridle to the bow of the barge. The effect of the triangulation of the bridle, and therefore minor asymmetry as load is transferred from one leg to another during the yawing motion of the barge, is also ignored.

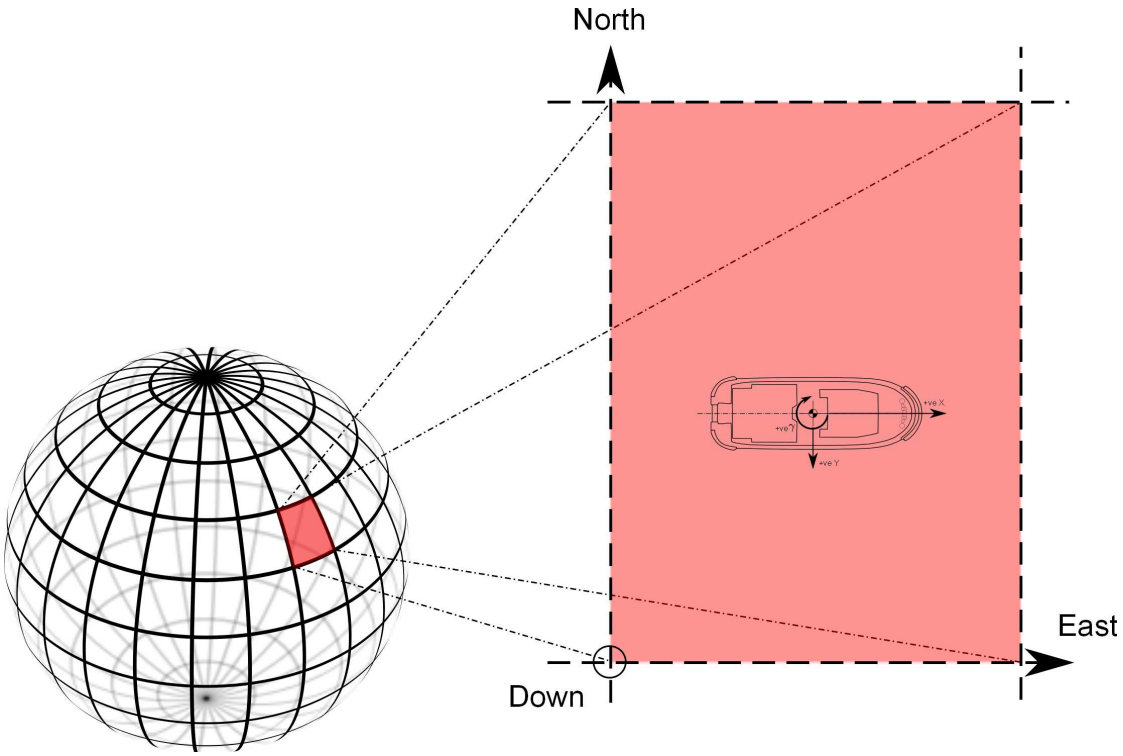

Figure 4.1.10: Local NED to body XYZ mapping

Following completion of the steps above there now exists a time series of global XYZ offsets of the vessels CoG position relative to a local navigation origin in the NED frame as well as a time series of roll, pitch and yaw angles. These can then be converted by combining with the knowledge of the position of interest in the vessel (i.e. the towline connection point) into a time series of XYZ offsets of this position of interest in the local navigation frame which, when repeated for both vessels, will give a paired XYZ time series which will form the input to the lumped mass numerical simulation covered in the next chapter.

Position Filter running test data As was done for the attitude filter, some clean simulated data representing roll, pitch, yaw, surge, sway and heave was created and corrupted with some representative noise. The clean signals were translated to the NED axis system and then integrated to create the true track of the vessel at sea. This true track was then used to create GPS signals every 1 second, again with representative noise from the GPS tests added to create a GPS signal.

This data was then run through the position Kalman filter to give confidence that all was working as expected. The sample plot in figure 4.1.11 shows how simply integrating the noisy acceleration readings quickly drifts to a solution that deviates considerably from the actual position. The estimated position from the filter tracks the actual position very closely with deviation reaching a maximum where the vessel velocity is at its lowest. The filter was found to be stable and effectively removed the drifting of the estimated position from the actual position as a result of the double integration of acceleration while maintaining the high frequency of position estimates made possible by the accelerometer readings.

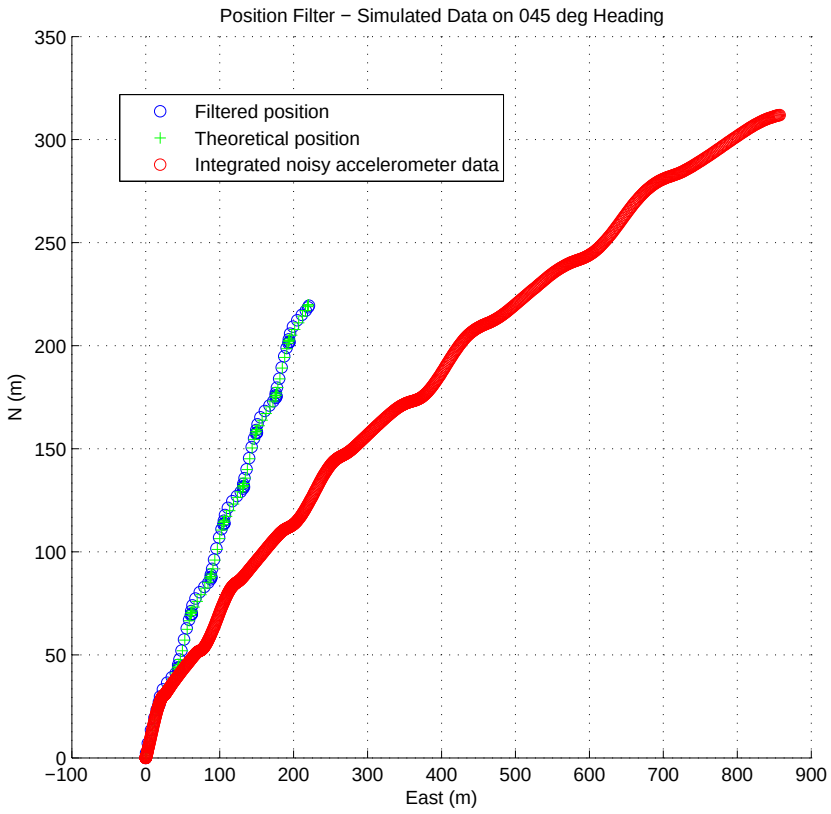

Figure 4.1.11: Position filter sample run at heading of 45 deg

4.2 Chapter Summary

In the preceding chapter an optimal state estimation scheme was proposed and detailed which would take data recorded in a datalogger rigidly attached to a floating body and translate this into useable information in the time domain that could then be fed into a numerical lump mass simulation. Some test data was fed through the filters to demonstrate the effect of removing any bias and drift in the system.

The limits of the system implemented here is acknowledged and suggestions for future research is covered in chapters 7.1 and 8 later.

Chapter 5

Numerical Model Description and Validation

5.1 Tug and Barge Towage

5.1.1 Towline General Arrangements

As this research is primarily interested in the numerical simulation of towlines of deep sea tows typically employing tugs of between 50 Te and 150 Te bollard pull, the towlines employed are all wire rope towlines attached to the towed barge by a bridle arrangement, figure 5.1.3 shows a view from the bow of a “300x90” class “north sea barge” looking out towards the stern of a 90 Te BP tug with the towline, delta plate and bridle legs clearly shown.

For deep sea towages the general makeup of the towing bridle arrangement on the barge is similar to that shown in figure 5.4.3. Key components are the main towline spooled from the winch on the aft deck of the towing tug, figure 5.1.1, and typically terminated in a spelter socket or other similar pin jointed interface, thereafter connected to a short, intermediate wire rope pennant also known as a “pigtail” or “forerunner”. This intermediate section is primarily used for handling and the retrieval of the heavy bridle onto the aft deck of the tug, allowing the towline to be connected to the tow.

In addition some tug masters like to introduce a short intermediate polypropylene pennant between their main towline and the wire pennant on the triplate known as a “stretcher”. These stretchers typically have a lower MBL (Minimum Breaking Load) and a significantly lower stiffness than the main towline. This allows it to serve two purposes namely:

– Act as a “fuse” which, should the towline experience significant shock loadings, will break before the main towline does. This allows the tug to circle, pickup the trailing emergency retrieval buoy and deploy the emergency towline without having to utilise the secondary towline which all tugs on high value tows should have on board.

– Act as a “spring” element which reduces the overall stiffness of the system allowing for damping of high frequency shock loading into the system which can cause overload and breakage.

These “stretcher” type arrangements also work well when towlines have been “shortened up” for inshore towing and the catenary effect of the main towline cannot be relied upon to provide some absorption of uneven peak impulse loads on the mooring line. In [van den Boom (1986)] it was shown via two dimensional lumped mass simulations that the introduction of an element into the towline arrangement which has a weaker MBL and has a lesser stiffness than the main towline could serve to increase “safety” “by reducing the diameter and increasing the length of the nylon or polypropylene/polyester spring. This” “increases the elasticity and thus reduces the dynamic effects in the line tension”. The author here shows a beneficial effect of stretchers up to 75m in length, however the practical use of which is not discussed in any detail as pennants are typically 10-15m in length for ease of handling. Modern guidelines, [DNVGL (2016)] and [ISO 19901-6 (2009)], permit the use of stretchers and also permit the use of “fuse” links but in special circumstances only and subject to special considerations. For shortened tows where the catenary of the main towline cannot be relied upon, the use of “surge chains” is suggested, reference 11.13.9.65 of [GL Noble Denton (2013), DNVGL (2016)], but the use and handling of these in close quarters can also be problematic.

Thereafter the pennant is attached to the apex of the wire bridle via heavy triangular plate, known as a tri-plate or “monkey’s face” with holes drilled to suit 3 large shackles of appropriate size. Each of the bridle legs have a capacity, stipulated by the regulations (for example 11.13.6, 11.13.7 and 11.13.8 of [DNVGL (2016)]), equal to each other and greater than that of the main towline, and are connected to the tri-plate and the barge towage point. These bridle legs consist of either all chain construction or wire/chain composite. The composite bridle setup offers greater ease of handling as only a relatively short length of chain is required as chafe protection immediately adjacent to the barge deck connection but sacrifices the shock absorbing capability offered when lines have been “shortened up”.

Finally, the termination on the barge is typically a quick release, high capacity shear connection known as a SMIT bracket. In figure 5.1.2 the detail of the SMIT bracket itself may be seen along with a photograph from above on a large semisubmersible barge showing the starboard SMIT bracket, the centreline emergency towing line SMIT bracket and the bridle retrieval A-frame.

Figure 5.1.1: Typical aft deck of towing tug showing main and secondary towing winches

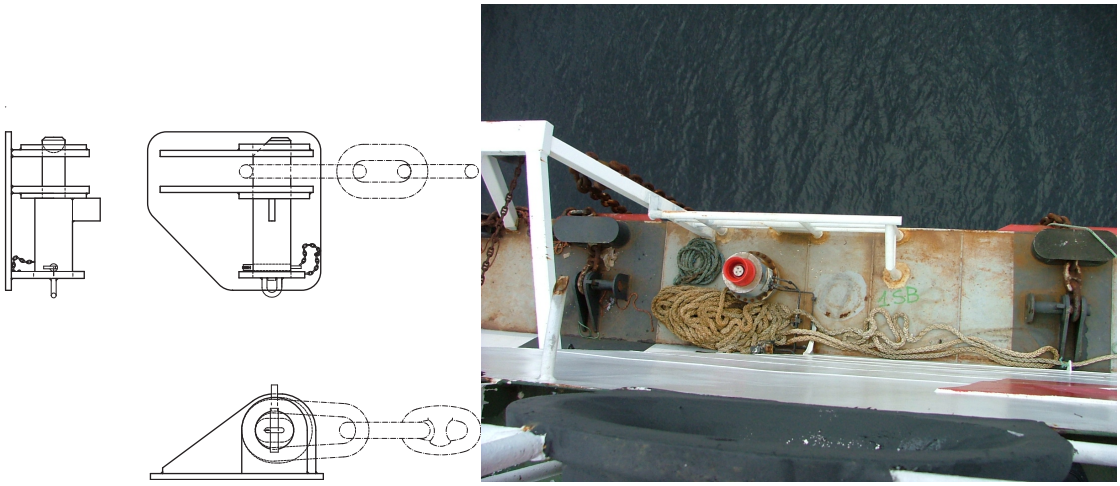

Figure 5.1.2: SMIT bracket detail and typical deck connection layout

5.1.2 Specific Properties of Towline Components

The numerical model employed requires a detailed description of the towline from end to end, including unit weights, drag characteristics and stiffness of each component including shackles, delta plate, bridle legs, pennants/pigtails and spelter sockets in order for it to correctly simulate the dynamic response of the system.

The key relationship for specifying the equipment on a tug is the one between is published Bollard Pull and the minimum breaking load of its towline. Generally this relationship takes into account the area the tow will be operating in as well. Example guidelines from the two principle operational references in use at the time of writing, namely [DNVGL (2016)] and [ISO 19901-6 (2009)] are shown in tables 5.1.1 and 5.1.2. Reviewing these it is immediately obvious there has been a harmonisation and a general industry consensus on the relationship between towline MBL and a tug's static bollard pull, something which was not the case 5 years ago. It is worth noting that as the tug capacity increases so too does the capacity of the gear required for towing resulting in equipment that is very difficult to handle by the crews working the aft deck of the tug and special allowances are made for "very large tugs" in the DNVGL regulations where the certified bollard pull is greater than 280 Te.

From these two tables it may be seen that given a stated range of tug capacities of interest to this work of 50 to 150 Te BP there are a range of towline MBLs based on the referenced range of principle industry guidelines outlined in the tables below as between 140 Te and 330 Te.

Table 5.1.1: BS/ISO Towline MBL Requirements [ISO 19901-6 (2009)]

Tug Bollard Pull Force, F_{BP} (kN)	Towline MBL - Benign Areas (kN)	Towline MBL - Other Areas (kN)
BP $\leq$400	2.0 x F_{BP}	3.0 x F_{BP}
400 $<$ BP $\leq$900	2.0 x F_{BP}	$F_{BP}\left(3.8 - \frac{BP}{500}\right)$
BP $>$ 900	2.0 x F_{BP}	2.0 x F_{BP}

Table 5.1.2: DNVGL Towline MBL Requirements [DNVGL (2016)]

Tug Bollard Pull Force, BP (Te)	Towline MBL - Benign Areas (Te)	Towline MBL - Other Areas (Te)
BP $\leq$40	2.0 x F_{BP}	3.0 x F_{BP}
40 $<$ BP $\leq$90	2.0 x F_{BP}	$\frac{F_{BP}(220-F_{BP})}{60}$
BP $>$ 90	2.0 x F_{BP}	2.0 x F_{BP}

Once this correlation between towline MBL and tug bollard pull has been made, the safe working load (SWL) of each of the constituent elements can be assessed. Principle industry guidelines state the following:

[ISO 19901-6 (2009)], 12.3.3 states for both towline connection points and bridle components:

> The design strength of the towline connections to the tow, including bridle legs, chain pennants and fairleads, where fitted, shall not be less than 1,3 times the MBS of the towline. The

design strengths of shackles or other mooring components can be applied for towing.

[DNVGL (2016)], 11.13.3.4 states:

> The Ultimate Load Capacity (ULC), in tonnes, of towline connections to the tow, including each bridle leg, connectors (apart from shackles and bridle apex which are covered in [11.13.8]), chain pennants, and fairleads, where fitted, shall be not less than:

- ULC = 1.25 x required towline MBL for the actual tug (for MBL less than or equal to 160 tonnes) or
- ULC = required towline MBL for the actual tug + 40 (for MBL greater than 160 tonnes).

Note that for the sizing of shackles in the towline, these are often taken as the ones with the correct fit for the triplate in question and as Green Pin shackles (referenced here from [Van Beest (2008)]) typically have a safety factor of 6 then capacity of shackles used, especially around the triplate leg connections, is general much greater than the rules require.

5.2 Model Description

5.2.1 Lumped Mass Numerical Model

The lumped mass system was selected for this study due to its maturity, robustness and ability to handle composite lines, i.e. lines made up of a large number of elements with different strength, mass, stiffness and drag properties. The method also lends itself well to time domain simulation, an essential feature due to the nature of the datasets generated during towages monitored with the data loggers used. The method utilised for this study was that proposed in [Huang (1994)] where the numerical solution for the governing equation is presented as follows (derived from the finite difference method in [Huang (1994)] and repeated in equation 5.2.1 here due to small error in the formula displayed in the original paper):

Figure 5.1.3: View on Towing Tug and Bridle at Sea

$$\frac{\mathbf{A_i}}{\Delta t^2}\begin{bmatrix} x_i \\ y_i \\ z_i \end{bmatrix}^{j+1} + \mathbf{BC_i}\begin{bmatrix} x_{i-1} \\ y_{i-1} \\ z_{i-1} \\ x_i \\ y_i \\ z_i \\ x_{i+1} \\ y_{i+1} \\ z_{i+1} \end{bmatrix}^{j+1} = \begin{bmatrix} f_{ix} \\ f_{iy} \\ f_{iz} \end{bmatrix}^{j} - \frac{\mathbf{A_i}}{\Delta t^2}\begin{bmatrix} x_i \\ y_i \\ z_i \end{bmatrix}^{j-1} + \frac{2\mathbf{A_i}}{\Delta t^2}\begin{bmatrix} x_i \\ y_i \\ z_i \end{bmatrix}^{j} + \mathbf{B_i}\begin{bmatrix} A_{C(i-\frac{1}{2})}E \\ A_{C(i+\frac{1}{2})}E \end{bmatrix} \tag{5.2.1}$$

This method was developed and shown to be effective for modeling the towage of a subsea unit, i.e. simulating the situation where the motions of the upper end of the towline as well as the drag and mass characteristics of the lower subsea module were known, and a time domain simulation run to determine the 3 dimensional path of the subsea unit when subjected to a variety of turning manoeuvres. A by product of this analysis is the calculation of the towline tensions themselves and as this is principally what is of interest to this research. For implementation here, the method was modified slightly to allow for simulation of a system where the motions of both ends of the towline catenary were known and the end tensions plotted and saved against a known timeline.

The numerical method employed in this research therefore is typical of the lumped mass method in its principle features in that:

- The cable is represented by a finite series of lumped masses separated by massless spring elements.
- Full three dimensional and large displacement motion is allowed for.
- Weight, buoyancy, drag and added mass is accounted for.
- Weight, drag, buoyancy and mass properties of the cable segments are amortised equally between adjoining point mass nodes.
- Method is capable of accounting for non-uniform or composite cables, i.e. can simulate cables constructed from a variety of segments each with different lengths, mass, drag and buoyancy characteristics.

An isometric and plan layout of the implementation of the scheme for this work showing overview and axis conventions as well as node numbering of the lumped mass spring may be seen in figures 5.2.1 and 5.2.2.

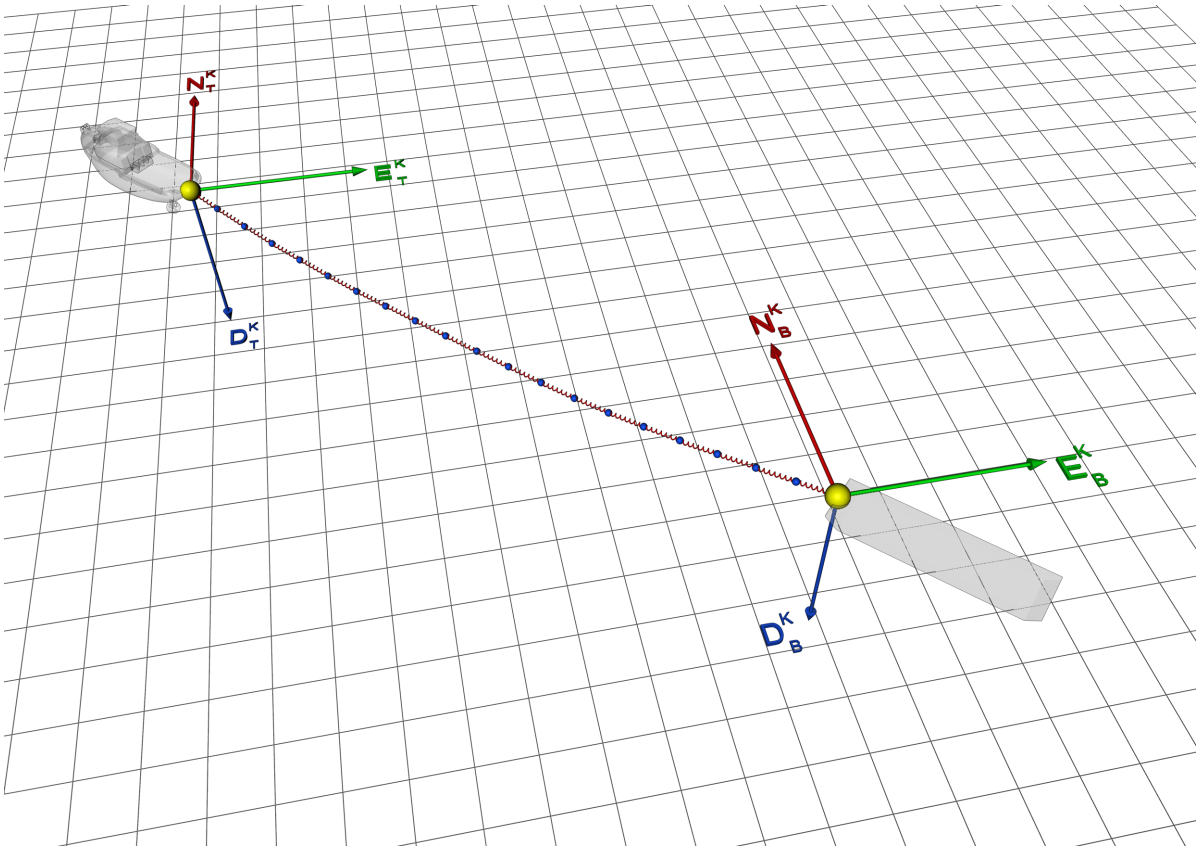

Figure 5.2.1: Lumped Mass Overview

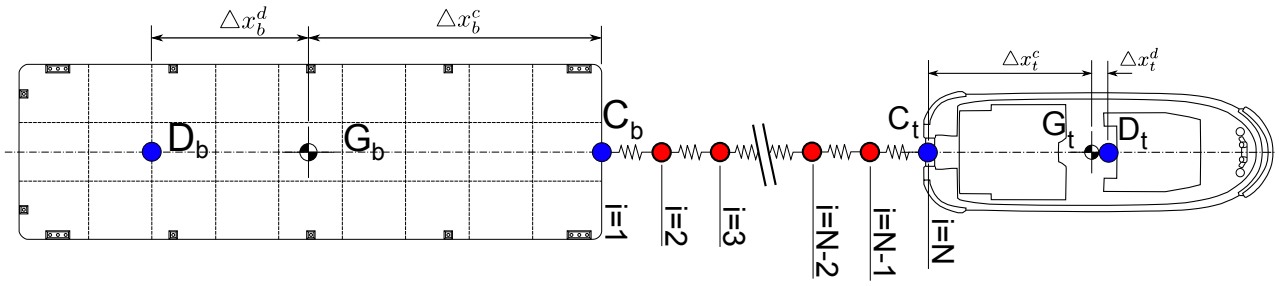

Figure 5.2.2: Towline index numbering convention

The full derivation of this method, is clearly laid out in the original paper however key features and assumptions of the internal workings of the method are worth discussing here with a review of how they were implemented and made to fit the specifics of the problem in question along with any changes to the methodology to suit a more accurate implementation of the problem at hand, see psuedocode in section 5.3.1. In addition a fully commented and simplified version of the MatLab code is given in Appendix A for completeness and ease of future reproduction of results.

First, as noted above, the original method stipulated boundary conditions where the upper end motions and the characteristics of the towed module were known. For the upper boundary condition, i.e. at the stern of the tug, this is simply:

$$x_N(t) = E_T^K(t) \tag{5.2.2}$$

$$y_N(t) = N_T^K(t) \tag{5.2.3}$$

$$z_N(t) = D_T^K(t) \tag{5.2.4}$$

Where index "N" represents the end node in the lumped mass formulation and N_T^K, E_T^K, and D_T^K represent filtered motions in the global North, East and Down directions of the connection point. For the lower boundary condition [Huang (1994)] invoked Newton's law of motion in 3 dimensions to solve the motion of the module as follows:

$$\begin{bmatrix} a_{11} & a_{12} & a_{13} \\ a_{21} & a_{22} & a_{23} \\ a_{31} & a_{32} & a_{33} \end{bmatrix} \begin{bmatrix} \ddot{x}_0 \\ \ddot{y}_0 \\ \ddot{z}_0 \end{bmatrix} = \begin{bmatrix} F_{x0} \\ F_{y0} \\ F_{z0} \end{bmatrix} \tag{5.2.5}$$

This was simply swapped in the numerical implementation here for the equivalent of equations 5.2.2, 5.2.3, and 5.2.4 at node 0, i.e. the barge end of the line as follows:

$$x_0(t) = E_B^K(t) \tag{5.2.6}$$

$$y_0(t) = N_B^K(t) \tag{5.2.7}$$

$$z_0(t) = D_B^K(t) \tag{5.2.8}$$

5.2.2 Towline Properties

The tensions of the towline are calculated for in [Huang (1994)] by assessing the extensions of each segments utilising Hooke's law where the tensions in either side of node "i" are denoted $T_{i+\frac{1}{2}}$ and $T_{i-\frac{1}{2}}$ and given by:

$$T_{i+\frac{1}{2}} = A_{C(i+\frac{1}{2})}E\left(\frac{\sqrt{(x_{i+1}-x_i)^2+(y_{i+1}-y_i)^2+(z_{i+1}-z_i)^2}}{l_{i+\frac{1}{2}}}-1\right) \tag{5.2.9}$$

$$T_{i-\frac{1}{2}} = A_{C(i-\frac{1}{2})}E\left(\frac{\sqrt{(x_i-x_{i-1})^2+(y_i-y_{i-1})^2+(z_i-z_{i-1})^2}}{l_{i-\frac{1}{2}}}-1\right) \tag{5.2.10}$$

Where E is the Young's modulas of the segment, A_C is the cross sectional area and l is the length, of the segment denoted by the subscripted index.

Note that the convention used in [Huang (1994)] as applies to nodal positions in the global space using x, y, and z naming conventions and later, the use of matrix naming conventions $[A]$, $[B]$, and $[C]$ which have been maintained for ease of cross reference with the technical paper from which they have been derived. The latter are not to be confused for example, with the measurement matrix $[C]$ in the Kalman filter implementation described earlier in this thesis and the use of x, y, and z maintained rather than using N_i, E_i, and Z_i again for ease of cross reference. It is hoped more is gained in legibility than is lost in following convention here.

It may be seen then that stiffness of the towline is purely a function of elastic elongation of the segment based, principally of the strain function, $\frac{EA}{l}$. This methodology is valid where there are only elements where stiffness is a linear function cross sectional area. In the formulation and use of the above this was assumed to be the case i.e. age of rope, non linear stretching properties of the rope, tension induced torque due to the particular combination of "wrap" of the wire, are all ignored, however this assumption warrants further investigation before adoption in the analysis here.

The form of multistrand mostly used in towing is of 6x36 construction. This construction consists of 6 separate helically wound strands, each consisting of 36 separate strands wrapped in an opposite lay round a central wire rope or fibre core (see figure 5.2.3). The static and dynamic response of such wire rope in both tension and bending, when viewed on the micro scale (i.e. strand against strand)

is an extremely complex one and has been the subject of much research over the years. Excellent summaries of this research can be found, earlier, in [Hobbs (1996)] and [HSE (1991)] with updated reviews in [Prawoto (2012)] among others.

The manner in which ropes are laid up, with each layer wound in alternating directions, or “lays”, serves to minimise the torsional effects when loaded axially and so the effects of this are not expected to significantly affect the outcome of the results presented here. Due to the nature of this construction therefore, as load is placed upon a spiral strand rope, tension in the individual strands cause a tightening in the individual outer strands groups as well as a tightening around the core, or king wire. This interlayer friction acts on adjoining wire strands either via long parallel contact areas, or “line contacts”, where stands run aligned with each other, or as a pattern of more concentrated contact areas, or “trellis contacts” where ropes of different lays on adjoining layers pass over each other. Friction is a result of force normal to the contact area, which in this case, is a function of the wire geometry and tension loads applied. Matters are further complicated by the fact that as the tensile load increases, a point is reached whereby the strands “slip” against each other therefore stiffness for a line segment is in fact much higher for smaller loads than it is as loads increase as small strains may not be enough to introduce inter-wire slippages.

Bending of wire rope is also discussed in the aforementioned references and this too changes as a function of tension however less so as local slippages can be forced at lower tensions by the magnifying effect of any radius of curvature. For towages, the bending radius is relatively large and the model employed here ignores any local bending in the wire towline.

An interesting exception that is noted in the research is where the wire rope is sheathed in a fully watertight shell, for corrosion protection purposes, in which case the hydrostatic pressure serves to increase the clamping force applied to the outer strands thereby increasing the interlayer friction forces and rendering the tension and bending stiffness a function of water depth also. This type of rope is not generally used in towages and so these effects can be ignored but modifying the code base shown in Appendix A would be trivial to include such effects if required.

Therefore the situation is such that the axial stiffness of the wire rope is highly non linear when looked at in a macro sense and a function of the applied tension and bending.

The treatment of towline tensile stiffness varies in the literature. Much research typically derive towline stiffness from the cross sectional area and length of the towline, with Young’s modulas of steel [Desroches (1997)] as follows:

$$k_{towline} = \frac{E_s A_{towline}}{L_{towline}} \tag{5.2.11}$$

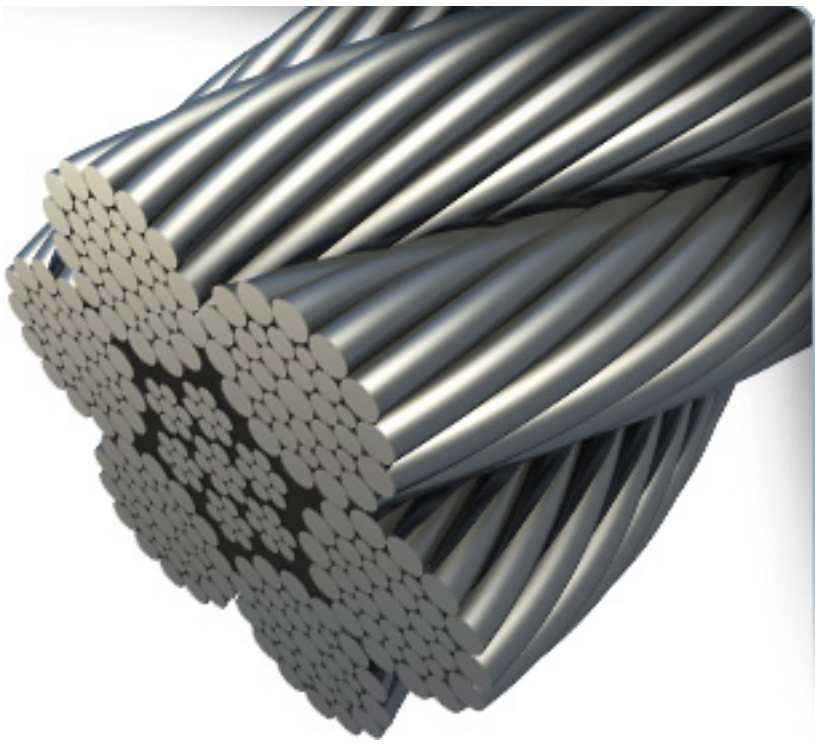

Figure 5.2.3: 6x36 wire rope section (source www.bridon.com)

Typically, for this calculation, the area of the towline is marked down by a factor which is representative of the true metallic cross sectional area. Values for this markdown vary in the literature but with reference to the data from [Bridon Ropes (2009)] and [Viking Moorings (2010)] the cross sectional area of a 6x36 steel core towing line as a function of diameter is as follows:

$$A_{towline} = \frac{C_{6x36}\pi D_{towline}^2}{4} \tag{5.2.12}$$

Where $C_{6x36}$is calculated as 0.593 from the aforementioned references and collates very closely with the figure of 0.586 from [Wichers (2013)].

While the modulas of elasticity of a wire rope varies throughout its life and typically rises as ropes age and initially “set in”, an excellent summary of properties again may be found in [Wichers (2013)] who notes that for steel core, 6x36 lay wire rope, a value of 105 kN/mm^2 is noted for the effective Young’s Modulas. For the final real world runs presented here, the values from [Wichers (2013)] will be adopted.

5.2.3 Bridle Modeling Assumptions

Turning our attention to the bridle arrangement, this portion of the towline requires consideration as to how to effectively model it as a significant portion of the overall towline’s mass is concentrated in this, relatively, short section. For example taking the case of a 100 Te bollard pull tug towing on a

700m long, 56mm diameter main towline the mass of the tug's towline itself would be circa. 8,960 kg. Commercial norms dictate that the tow comes with its own bridle pre-installed, however if it is assumed that the equipment is the minimum required for connection to a tug of such power then a bridle with 30m legs, consisting of 55 Te triplate, 55Te shackles and 70mm stud-link chain would have a weight of approximately 6,960 kg. Setting aside, for now, the larger drag resistance of the chain and tri-plate arrangement we can see that, based on the figures above, for a fairly representative system, the full tow arrangement has approximately 45% of its mass concentrated in only 2% of its length. Bearing this in mind, it is obvious how the catenary effect of such a heavy segment of the towline can assist to dampen out shock loadings on the towline, especially when main towline from the tug's drum has been "shortened up" for inshore or harbour manoeuvres.

With reference to figure 5.2.4, it may be seen that the bridle connection to the barge is constructed of two legs however the scheme employed is for single, continuous towlines only. It was not felt necessary to alter the scheme and try and model, accurately, both of the legs and the following points/assumptions were made:

- The applicable rules and regulations reviewed, and most commonly used in the towage industry, namely [DNVGL (2016)] and [ISO 19901-6 (2009)] all stipulate that each leg of the bridle must be capable of taking the full load of the tow. This is due to the fact that rarely will the tow be perfectly aligned with the tug and therefore, at any one time, only one leg of the bridle will see any load. This can in fact be seen in figure 5.1.3 where the left hand leg of the wire bridle is dragging in the water while the right hand leg, as it leaves the image, is under load.
- With reference to figure 5.2.4 the bridle was combined into a single series of segmentations that represented the twin legs.
- Springs and nodes associated with the bridle only were given stiffness and mass, respectively, equivalent to only one leg of the bridle as well as drag characteristics equivalent to twice that of a single leg to simulate the drag effect the second bridle leg would have on the tri-plate, the ultimate connection to the towline from the tug. A simplified treatment of the bridle springs was made to account for the fact that it was acting at a varying angle offset from the centreline of the main towline itself.
- Springs and nodes associate with the towline only were given stiffness and mass, respectively, associated with the towline only (and intermediate shackles/connections point modeled at their respective locations on the towline).
- The node corresponding to the tri-plate (delta plate node) was assigned mass under the numerical scheme associated with 50% of the mass of the bridle and tow wire segments bounding it.

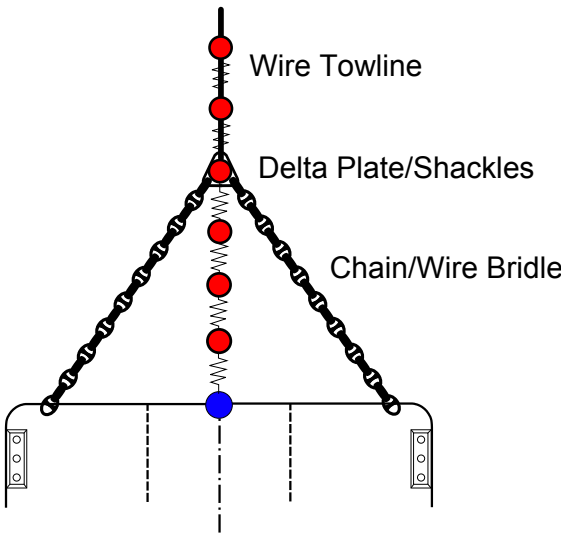

Figure 5.2.4: Bridle segmentation

- The tri-plate node was then assigned additional mass associated with the mass of the delta plate itself and that of the three adjoining shackles.
- The tri-plate node was also assigned mass equivalent to a portion of both bridle legs and pennant on either side of it as the leg not under tension would still be exerting a force on the tri-plate due to gravity (with drag effects accounted for in an earlier assumption above).
- The single line of mass and springs were connected to the barge at the centreline and fed end motions resolved from the logger to this location.
- The full bridle arrangement is assumed to be in the water at all time (i.e. buoyancy and drag effects based on immersion in sea is assumed to be in effect during the entirety of the simulation runs).

For completeness, the effect of load on elements where stiffness is a function of bending rather than linear stretching should also be verified to ensure no effects which could have a bearing on the analysis methodology used are ignored, for example verification of shackle, triplate and stud link chain global stiffness properties.

In order to do this a range of applicable equipment was selected and modeled firstly in a 3D CAD package (Rhino) to ensure geometric accuracy and thereafter exported in IGES format for importing and solid meshing in an FEA package (Strand7). Nominal unit loads were applied and the deflection noted to assess the equivalent spring stiffness. A simple linear analysis was used therefore changes in deflection shape, altered contact bearing areas etc were all ignored however the simplification was deemed acceptable for the load range applied.

By assessing the distortion of discrete components these can then be translated into the equivalent spring stiffness which can then, in turn, be combined with the stiffness of multiple elements to offer up equivalent stiffness of the bridle as a whole.

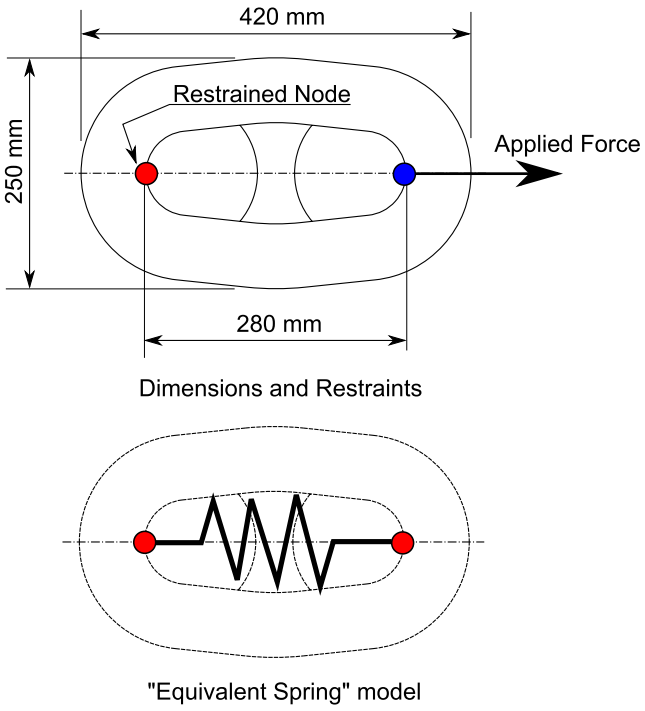

Figure 5.2.5: 70mm studlink chain link key dimensions and FEA restraints

Studlink Chain FEA Stiffness Check Taking the studlink chain element of the bridle first, a series of 56mm, 70mm and 92mm chain links (representing matching specifications for 35Te, 55Te and 85 Te triplate/shackle pairings), were assessed. A single link for each size was modeled, restrained (see example arrangement for the 70mm link shown in figure 5.2.5), and had a unit force of 1,250 kN applied equally over 5 nodes aligned to the x axis. An additional restraint was applied to a node at the extreme end of the link restricting movement along the axis normal to the link's centreline to ensure stability by avoiding rotations about the pinned nodes on the inside face. The displacement of the five loaded nodes were noted for each model run and the average used to calculate the effective tensile stiffness by treating the studlink element as a discrete spring and employing equation 5.2.13 below. A summary of these equivalent stiffness's may be found in table 5.2.1.

$$k_{stud} = \frac{F_{applied}}{\delta_x} \tag{5.2.13}$$

Tri-plate FEA Stiffness Check Applying a similar approach as used for the studlink chain element, a series of FEA model were built covering 35Te, 55Te and 85 Te standard design tri-plates. These were restrained and loaded with 1,260 kN along the x axis (variation in actual load applied required to provide round numbers when spreading across either 6 or 7 nodes which in turn was determined by the discretisation in the FEA mesh following import and meshing). Figure 5.2.7 shows the overall dimensions and restraints placed upon the 55Te tri-plate FEA model with other models adopting a similar philosophy. Note that the line of action of the force applied assumes that only one leg of the bridle is acting at any

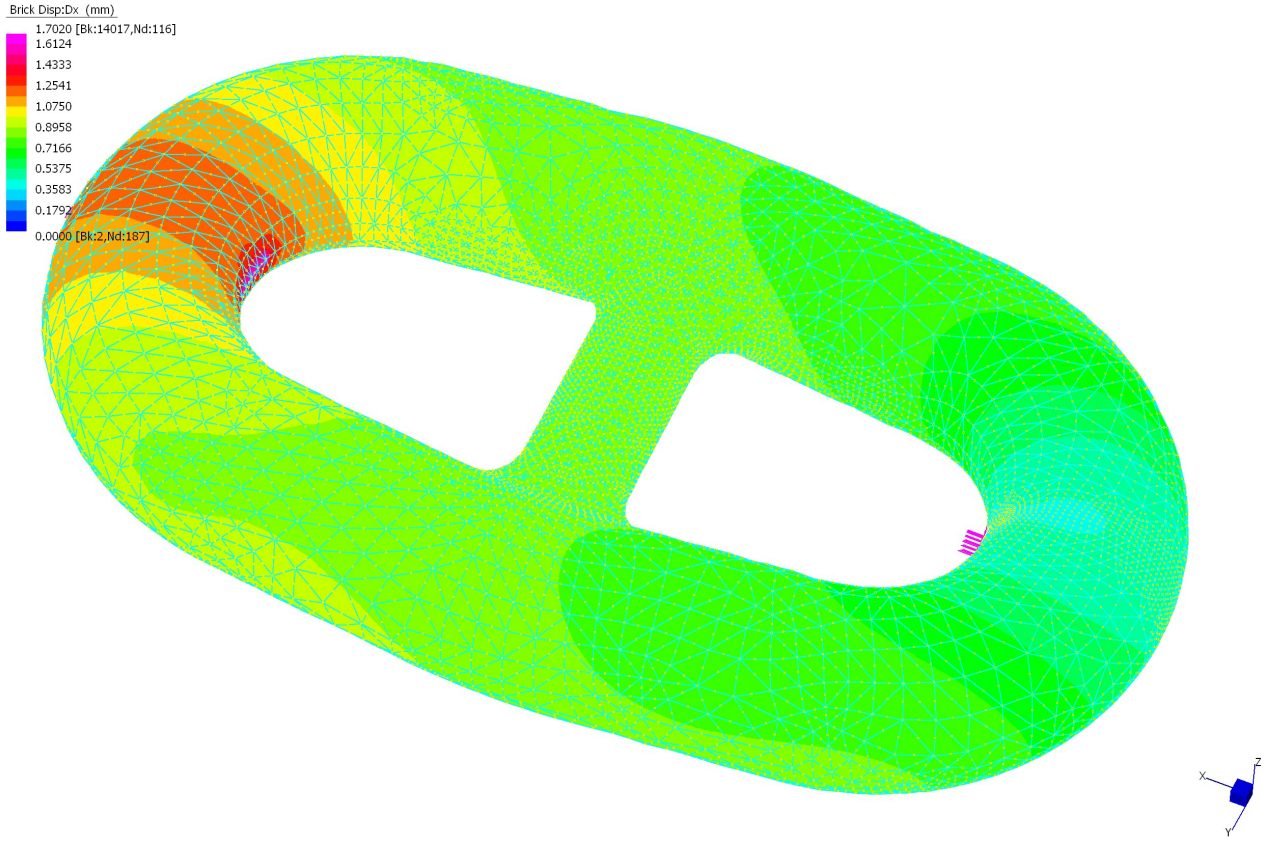

Figure 5.2.6: 70mm studlink chain link FEA plot

Table 5.2.1: Average nodal displacement on studlink FEA models and calculated stiffness

Node	Ux (mm)	Average Disp' (mm)	Force (kN)	Stiffness (kN/mm)	Stiffness (Te/mm)
56mm Studlink					
118	2.1134				
117	2.0827				
116	2.1275	2.1008	1,250	595.000	60.65
115	2.0733				
114	2.1073				
70mm Studlink					
118	1.6907				
117	1.6661				
116	1.7020	1.6807	1,250	743.755	75.82
115	1.6586				
114	1.6859				
92mm Studlink					
118	1.2864				
117	1.2677				
116	1.2950	1.2788	1,250	977.509	99.64
115	1.2620				
114	1.2827				

Note: Ux represents the longitudinal displacement of the nodes along the x axis.

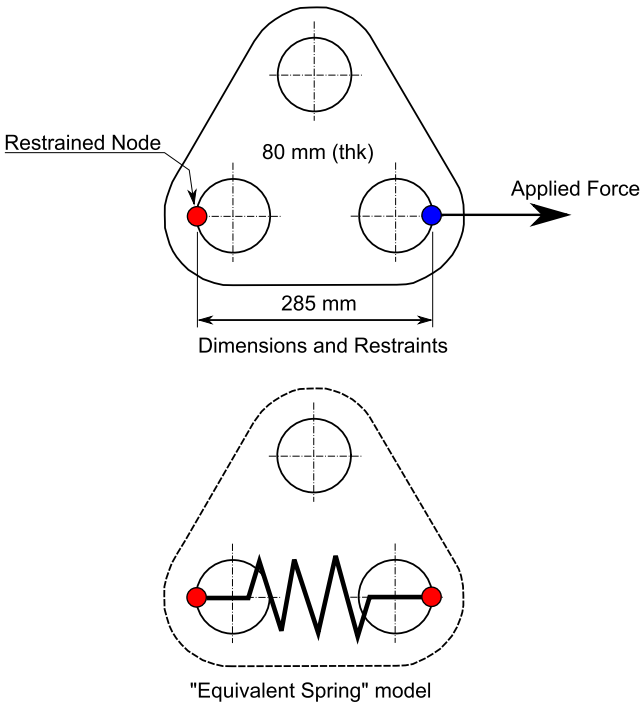

Figure 5.2.7: 55 Te tri-plate key dimensions and FEA restraints

one time. This is consistent with class/industry guidelines when specifying the capacity of bridles as well as being, intuitively, what occurs during towing (i.e. full weight of the bridle hangs of the tri-plate but only one leg effectively providing transmission of towage forces to the towed object) as the bridle will rarely ever act fully equally on both legs other than at particular points in time as the barges yaws about the effective mean direction of the towing force. The displacements across a nominal bearing strip inside the pin hole were not even due to the fact that the unsupported edge displaced further than the node located at the mid plane. An approximation of the net displacement was made by averaging across the loaded nodes, reference table 5.2.2. This effect may be seen in the scaled FEA plot shown in figure 5.2.9.

Referring to the same equation used for stud link above was employed to ascertain the stiffness for each of the tri-plate models and reported in table 5.2.2.

Shackle FEA Stiffness Check Finally a series of FEA model of 35Te, 55Te and 85 Te wide bodied shackles were created (based on geometry for “Green Pin” model produced by Van Beest [Van Beest (2008)]). The shackle was typically restrained and loaded as shown in figure 5.2.10. The body of the shackle was modelled using solid elements however to simplify the pin detail and avoid any requirement for large numbers of contact elements, a solid beam was used. This was restrained via pinned connections (represented by red dots in the aforementioned figure) set at an offset from the shackle centreline to simulate bearing points of the pin on a tri-plate. In the case shown for a 55 Te shackle the plate thickness of the corresponding 55 Te tri-plate is 80mm, and this offset altered according to the specific shackle and tri-plate pairing of each configuration.

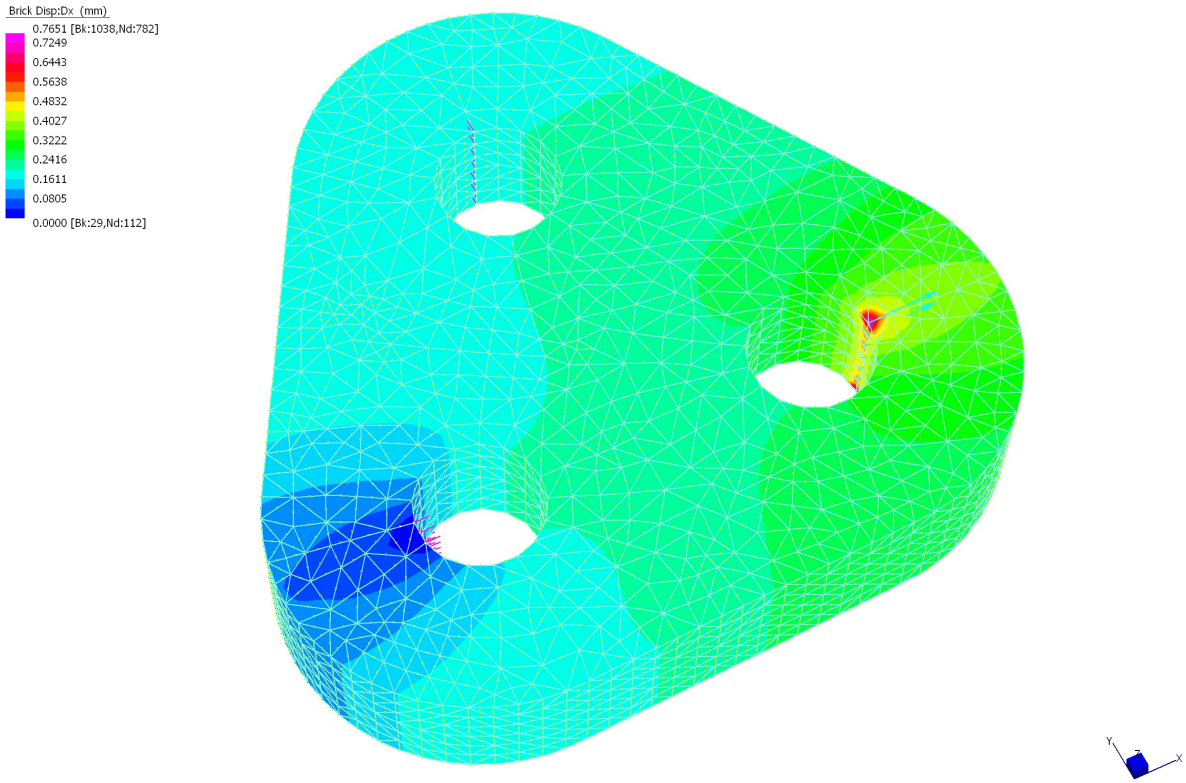

Figure 5.2.8: 55 Te Tri-plate FEA plot

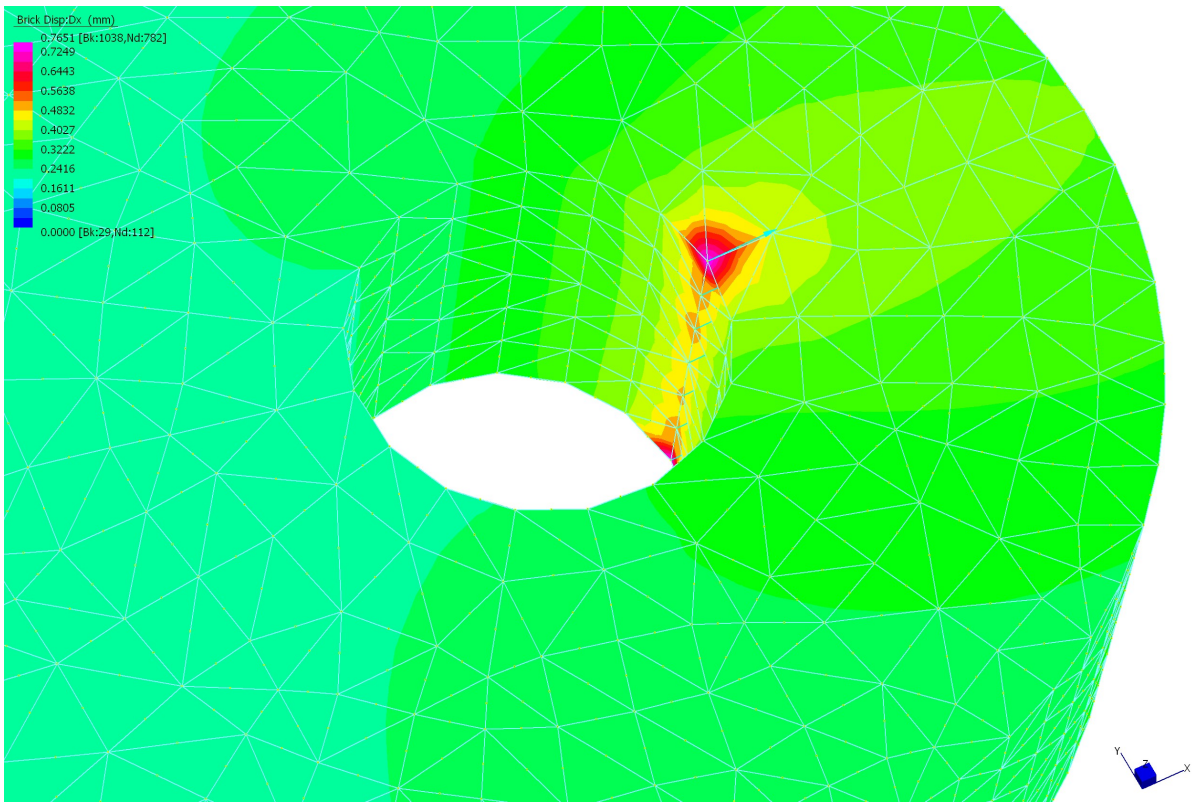

Figure 5.2.9: 55 Te Tri-plate detailed displacements in way of shackle pin hole

Table 5.2.2: Average nodal displacement on tri-plate FEA models and calculated stiffness

Node	Ux (mm)	Average Disp' (mm)	Force (kN)	Stiffness (kN/mm)	Stiffness (Te/mm)
35 Te Tri-plate					
821	1.0978				
2048	0.7689				
2047	0.7504				
2046	0.7471	0.8464	1,260	1,488.635	151.75
2045	0.7529				
2044	0.7077				
140	1.1001				
55 Te Tri-plate					
782	0.7651				
2004	0.5194				
2003	0.5199				
2002	0.485	0.5801	1,260	2,171.879	221.39
2001	0.497				
2000	0.5141				
138	0.7605				
85 Te Tri-plate					
865	0.6515				
2006	0.4604				
2005	0.4554				
2004	0.4565	0.5226	1260	2410.875	245.76
2003	0.4602				
138	0.6517				

Note: Ux represents the longitudinal displacement of the nodes along the x axis.

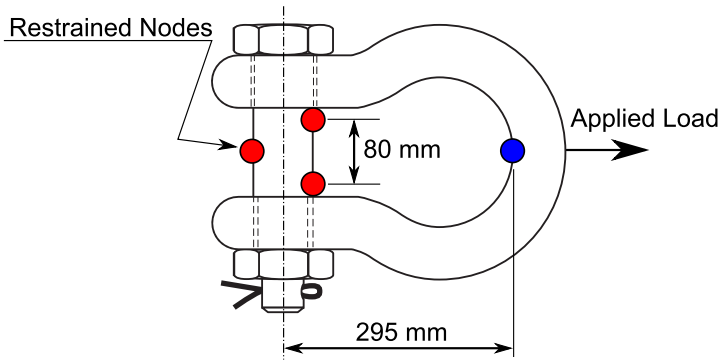

Dimensions and Restraints

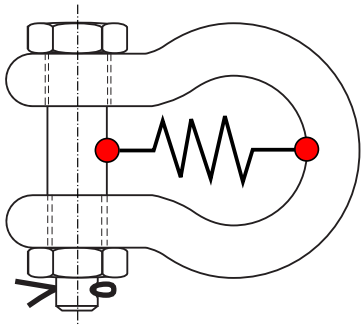

"Equivalent Spring" model

Figure 5.2.10: 55 Te wide body shackle key dimensions and FEA restraints

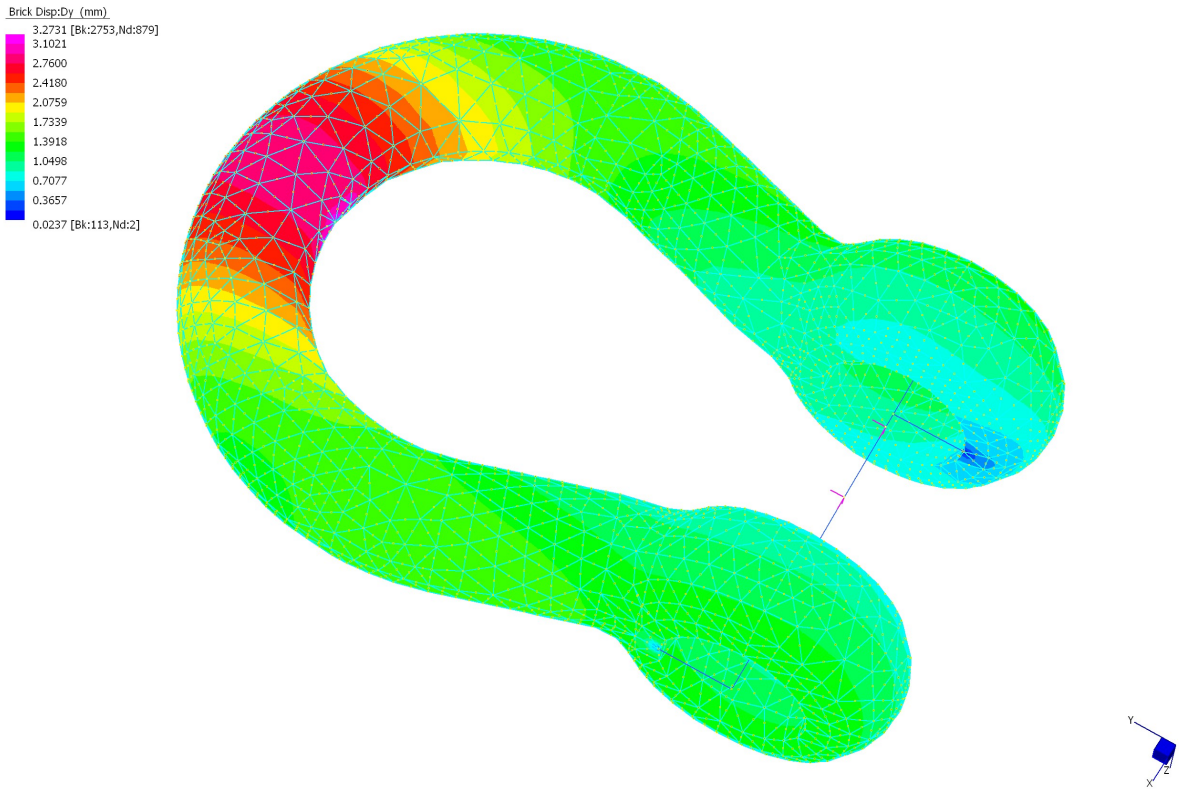

Figure 5.2.11: 55 Te wide body shackle FEA plot

Table 5.2.3: Nodal displacement on shackle FEA models and calculated stiffness

Node	Uy (mm)	Average Disp' (mm)	Force (kN)	Stiffness (kN/mm)	Stiffness (Te/mm)
35Te Green Pin Shackle					
665	4.0512				
664	4.1231	4.0799	1,245	305.157	31.11
663	4.0653				
55Te Green Pin Shackle					
878	3.2365				
879	3.2731	3.2345	1245	384.913	39.24
880	3.1939				
85Te Green Pin Shackle					
2079	3.0103				
2078	3.0325	3.0218	1245	412.010	42.00
2077	3.0225				

Note: Uy represents the longitudinal displacement of the nodes along the y axis.

Discussion on FEA and CSA stiffness methodologies It is worth taking a moment to compare the different approaches outlined here of assessing the stiffness of any given component of the towline.

It is normal practice to assess stiffness using Hooke's Law, as per the main tow line, based on the metallic cross sectional area of the component in question. This is open to interpretation with regards to where exactly the cross section is taken. For the purposes of the summary in table 5.2.4, figure 5.2.12 shows the assumptions made here for assessing conventional stiffness properties based on (where A_{CS} represents the cross sectional area of the element in question):

$$k = \frac{EA_{CS}}{L} \tag{5.2.14}$$

In addition to this, a methodology for assessing the axial stiffness of studlink chain is offered in [Wichers (2013)] the results of this for the sample here is also shown in table 5.2.4:

$$k = 1.01 \times 10^8 \times D^2 \tag{5.2.15}$$

Where k is returned in kN and the studlink bar diameter, D, is entered in metres.

Note that the tri-plate stiffness based on Hooke's law has not been reported simply due to the fact that its geometry leaves it very much open to a varied interpretation of its applicable cross sectional area.

Table 5.2.4 shows that the stiffness as calculated by FEA for studlink chain is between 41% and 67% of that reported by Hooke's law and, interestingly enough, a consistent 63% of that reported by the methodology from [Wichers (2013)]. No reference can be found for the original source of this approach but the consistent linear relationship between the two values, even in as small a dataset as this, is compelling. For the relationship between the FEA assessment of shackle stiffness to that of Hooke's, the difference is even greater ranging as it does between 26% and 43%, although conversely, the effect here of the potential discrepancy in shackle stiffness's in most mooring and cable dynamic problems is less significant since such elements would usually make up a very small percentage of the overall line length.

Given that chain and wire will make up the majority of a towline, it is interesting to compare the properties of a unit length of each and table 5.2.5 does just this. The specifications have been grouped by tug capacity and so each row represents what you may be likely to see together on an idealised towage (not taking into account that most towages are ones of opportunity, i.e. based on what towing tonnage is available at the time of the proposed movement). Here the circa 30% to 50% gains in stiffness over a 80% to 90% reduction in weight are striking.

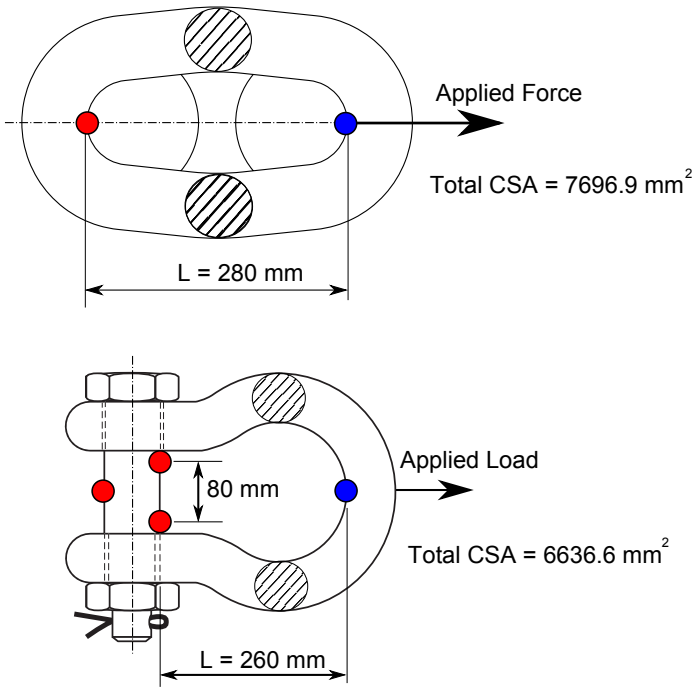

Figure 5.2.12: Assumed cross section cuts for stiffness calculations (55Te equipment shown)

Table 5.2.4: Summary of component stiffness values by FEA and CSA method

Item	FEA Stiffness (Te/mm)	CSA/Hooke's Stiffness (Te/mm)	Stiffness [Wichers (2013)] (Te/mm)
Studlink			
56 mm	60.65	89.67	96.09
70 mm	75.82	140.11	120.12
92 mm	99.64	242.01	157.87
Shackle			
35 Te	31.11	71.48	-
55 Te	39.24	120.81	-
85 Te	42.00	160.84	-

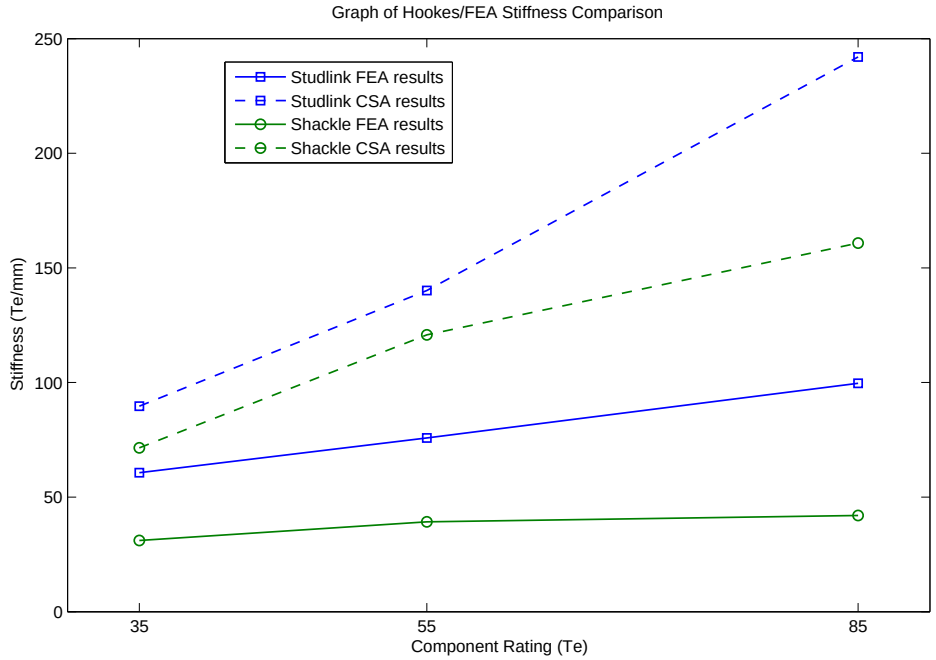

Figure 5.2.13: Graph of component stiffness values by FEA and CSA method

Table 5.2.5: Wire/studlink chain stiffness comparisons

	Chain Properties			Wire Properties		
Tug BP (Te)	Chain Size (mm)	Stiffness (FEA) (Te/mm)	Weight in air (kg/mm)	Wire Size (mm)	Stiffness (Te/mm)	Weight in air (kg/m)
~45	56	60.65	70.76	44	81.10	7.92
~100	70	75.82	112.62	56	105.09	12.80
~165	92	99.64	195.82	74	139.63	22.70

Composite Bridle Stiffness Taking what has been outlined above and now applying to a typical bridle arrangement as shown in figure 5.2.4, the following methodology for the segment stiffness between towline connection point and the bow of the tow can be derived as follows:

The net stiffness of a series of spring elements in series is defined as, [Thomson (1993)]:

$$k_T = \frac{1}{\frac{1}{k_1} + \frac{1}{k_2} + \dots} \tag{5.2.16}$$

For ease of modeling it is advantageous to derive the values of a series of equivalent springs that can be substituted to avoid modeling each of the bridle components individually so the total stiffness of bridle chain, connecting shackles and tri-plate is:

$$k_{bridle} = \left[\frac{1}{k_c \cos\theta_{bl}} + \frac{1}{k_s \cos\theta_{bl}} + \frac{1}{k_t} + \frac{1}{k_s}\right]^{-1} \tag{5.2.17}$$

Expanding to obtain the stiffness of the chain section, of length l_c, to allow for direct use of the stiffness values of the individual stud link elements, of length l_{sc}, from the FEA results, the following may be seen:

$$k_c = \left[\frac{\left(\frac{l_c}{l_{sl}}\right)}{k_{sl}}\right]^{-1} = \frac{k_{sl} l_{sl}}{l_c} \tag{5.2.18}$$

Taking the total stiffness of the bridle if it were represented as a single element, k_{bridle}, and separating into a number, n, of individual segments of stiffness k_b it may also be seen:

$$k_{bridle} = \frac{1}{\left(\frac{n}{k_b}\right)} = \frac{k_b}{n} \tag{5.2.19}$$

Combining 5.2.17, 5.2.18 and 5.2.19 the following expression for each element in the simplified representation bridle is as follows:

$$k_b = n\left[\frac{l_c}{k_{sl} l_{sl} \cos\theta_{bl}} + \frac{1}{k_s \cos\theta_{bl}} + \frac{1}{k_t} + \frac{1}{k_s}\right]^{-1} \tag{5.2.20}$$

Note: Unit mass and drag handled as per the discussion at the beginning of this section.

5.3 Model Implementation and Validation

5.3.1 Lump Mass Model Implementation

The theoretical procedure as described in [Huang (1994)] was modified slightly to accept forced motions at each end of the towline and implemented in MatLab as per the following pseudo-code:

1. Define simulation time and time step and run in time. Run in time is a simulation period where the model was run without end motions to allow the catenary to settle to the catenary shape under whatever current and environmental conditions the user specifies.
2. Data specifying the end motions is loaded from the Kalman routines.
3. Towline discretisation is defined, each lumped mass element assigned mass and drag (tangential and longitudinal), spring elements assigned length and stiffness values. Note the routine is coded in such a manner that these need not be constant, i.e. different mass, stiffness and drag may be specified for each element (see section 5.4.1 for details of how the line drag has been determined), including buoyant lumped elements.
4. Plotting and storage vectors setup.
5. Loop for each time step j:
   (a) Loop through each node and calculate the internal segment tensions from the 3D geometry of each node positions, and towline stiffness values.
   (b) Break each segment down and calculate the projected lengths onto each of the 3 Cartesian planes.
   (c) Create empty matrices to hold the final assembly of equations in the form of: $\left\{[A_{Full}]_{3(n-2)\times 3(n-2)} + [BC_{Full}]_{3(n-2)\times 3(n-2)}\right\}[X]_{3(n-2)\times 1} = [F]_{3(n-2)\times 1}$, where $[X]$ represents the unknown node positions in 3 dimensions at time step $j+1$.
   (d) Create LHS of equation above by looping for each node, i, on the towline between $i = 2$ and $i = n-1$:
      i. Populate local matrix $[A]_{3\times 3}$ for each node.
      ii. Populate local matrix $[B]_{3\times 2}$ for each node.
      iii. Calculate coefficients q_1 and q_2 for each node.
      iv. Populate local matrix $[C]_{2\times 9}$ for each node.
      v. Create local matrix $[BC]_{3\times 9}$ for each node.
      vi. Create $\begin{bmatrix} A_{C(i-\frac{1}{2})}E \\ A_{C(i+\frac{1}{2})}E \end{bmatrix}$ for each node.

(e) Assemble the above into the full matrices and divide $[A_{Full}]$ by $\frac{1}{\Delta t^2}$.

(f) Create RHS of equation above by looping for each node, i, on the towline between $i = 2$ and $i = n - 1$ to populate $[F]$:

i. Calculate relative velocities of fluid over each segment taking account of any local or global 3 dimensional fluid velocity field specified.

ii. Calculate tangential and longitudinal drag over each segment based on segment specific values for drag in each direction and local velocities calculated above.

iii. Calculate buoyancy and vertical weight of each segment.

iv. Using $[A]$ calculated above, and node positions at the previous two time steps, i.e. j and $j - 1$ and calculate the accelerating force on each node.

(g) Sum node drag vector based on the distribution of segment drag calculated above (half of the drag on a segment immediately to either side of a node aggregated to that node's position in the same manner that mass is attributed to a specific node), gravitational acceleration, local acceleration and buoyancy for each node into complete force vector.

(h) Solve equation for 3D dimensional position of nodes at the next time step $j + 1$.

(i) Store node positions and line tensions for post processing

6. Plot and report data as required.

5.3.1.1 Typical process for lumping technique as applied to the drag forces

For the concentration of forces on line elements at nodes on the line, see figure 5.3.1 for graphical representations of the drag cases. Taking the normal drag, therefore, the force on the towline segments on either side of node i would be concentrated into the lumped mass as follows (see lines 548 to 550 for implementation in MatLab code in appendix A):

$$F_{DN(i)} = 0.5\rho(V^2_{N(i-\frac{1}{2})}C_{N(i-\frac{1}{2})}l_{(i-\frac{1}{2})}D_{(i-\frac{1}{2})}) + 0.5\rho(V^2_{N(i+\frac{1}{2})}C_{N(i+\frac{1}{2})}l_{(i+\frac{1}{2})}D_{(i+\frac{1}{2})}) \tag{5.3.1}$$

Note: See appendix A for example MatLab implementation of the above.

5.3.2 Numerical Run Initialisation

Before commencing a simulation a practical method of positioning the nodes in their initial, ideal catenary shape was required. A number of approaches were looked at and initially it was the intention to

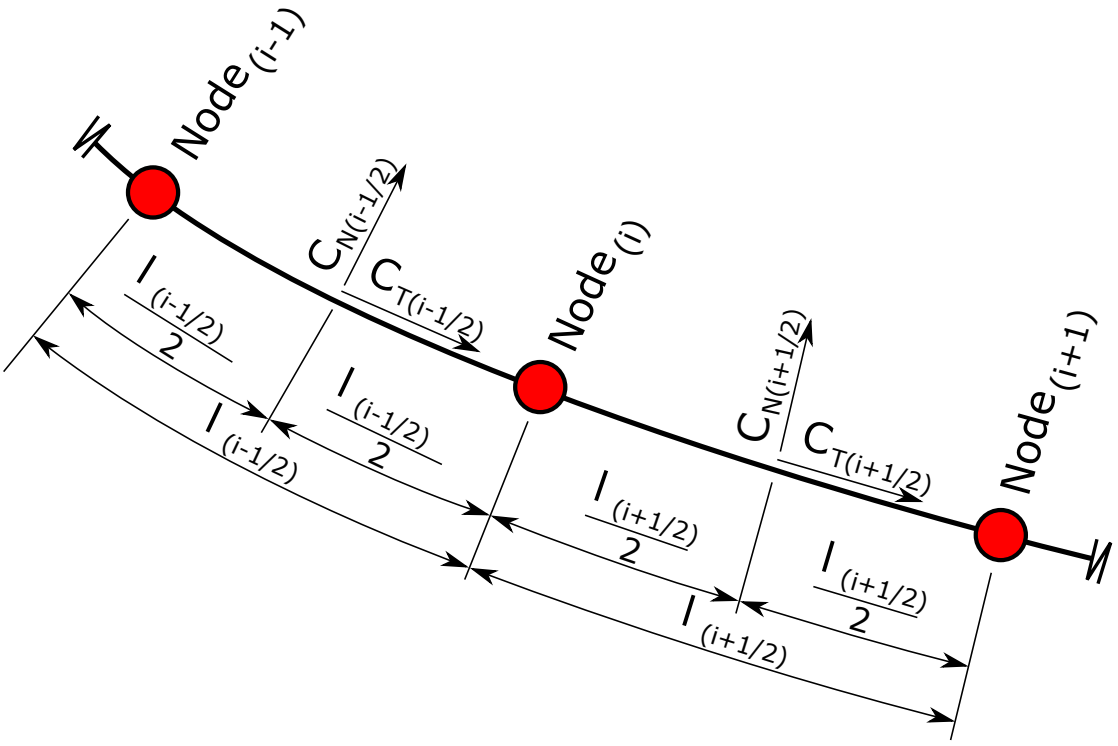

Figure 5.3.1: Line segment drag

simply calculate the theoretical positions based on the ideal catenary shape and segment lengths however this was quickly dismissed over concerns of accurately calculating the node positions for a wide variety of complex catenaries and towline configurations and any discrepancies would be evident by local snapping tensions in segments as differences in the theoretical and ideal settled positions tried to assert themselves at the commencement of the simulations. This then set up high frequency vibrations that took considerable simulation time to settle.

It is obvious that the tug and barge points for the cases considered here, will always be closer to each other than the total length of towline deployed at all stages during the simulation, i.e. the towline never goes fully "bar tight" or the elastic stretch is never enough to have more than the total geographic distance between tug and tow exceed the deployed, unstretched, towline length. Therefore simply setting start positions for each and letting the towline catenary fall into shape leaves a large amount of kinetic energy in the system as it drops into its catenary shape. This is clearly demonstrated in a sample case shown in figure 5.3.2 for a 250m wire towline modeled using 20 lumped mass nodes and hung off between a tug and tow 230m apart on the x axis and 0m apart on the y and z axis. With reference to figure 5.3.3 it can be seen that it takes around 70 seconds of simulation time for the towline to settle to a mean oscillation of amplitude less than 3% of the mean tension (internal target to be met prior to commencing simulation runs of forced excitation of the towline end points). 70 seconds was felt to be too long and some time was spent looking at reducing this without overly complicating the numerical code base.

Much of the jitter in the towline as it settles, it was felt, was due to the fact the code base does not allow for positive compressive forces in the towline nor does it allow for bending stiffness across the segment

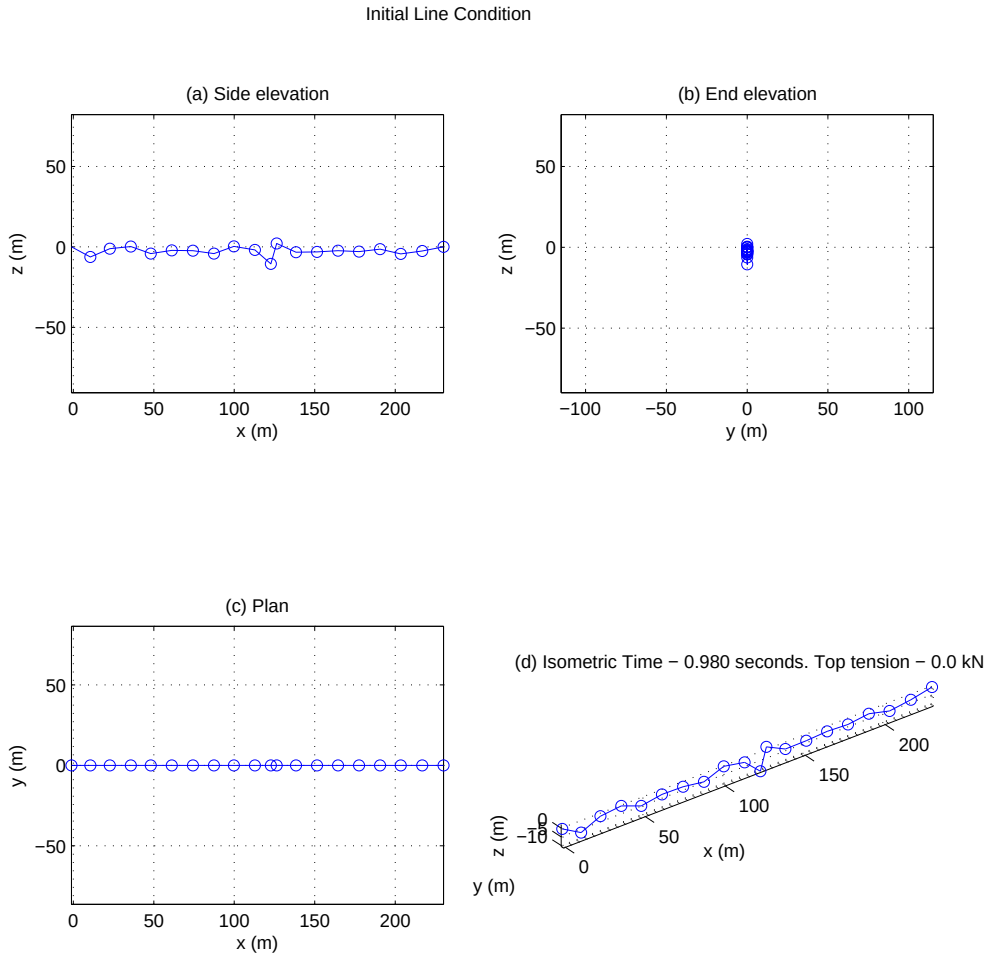

Figure 5.3.2: Initial condition for 250m towline on simulation start

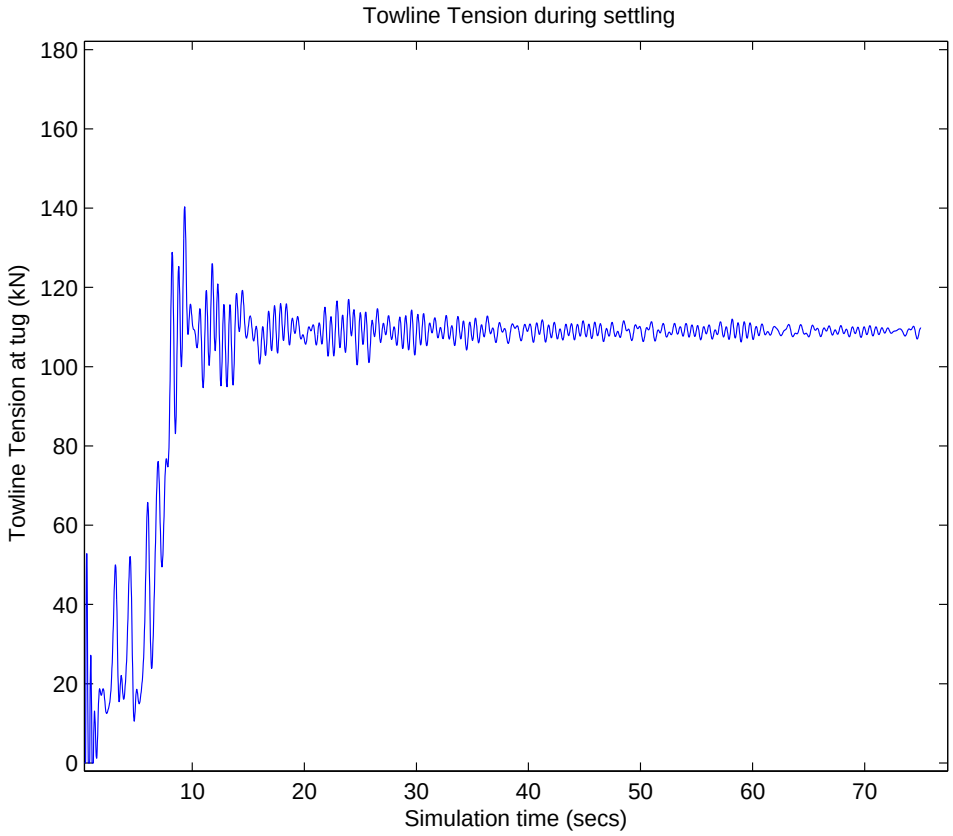

Figure 5.3.3: Towline tension during settling with no aiding techniques

joints, therefore not accurately simulating the damping both would have on settling the towline. Given that once the line settles, the code was found to perform acceptably it was not felt worth the extra effort to change the code base to incorporate these additional numerical features simply to shorten settling and therefore the batch simulation times.

To resolve this, it was found that a simple "run in" methodology was effective in gradually bringing the towline to a settled position whereby the towline end points were extrapolated through the actual start points to provide a straight 3 dimensional line of true length equal to the towline length. The code base was allowed to provide for a number of run_in_time steps which then brought the ends into position usually over a period of around 20 seconds simulation time, see figure 5.3.4 for graphic representation of the process in 2D. In this way the towline was brought to its rest state in a controlled manner. A direct, real world, interpretation of this would not be feasible but it is analogous to a pair of positions being set and then the towline being slowly paid out to form the catenary and this alternative implementation could also be easily implemented in the code base as it allows for dynamic changing of all variables, both geometrical (such as segment length, masses, buoyancy, segment modulas) and environmental (such as current local to each segment on 3 axis, water density, pressure), from one time step to the next.

By adopting this methodology it was found that the run in time had to be selected with a little care to

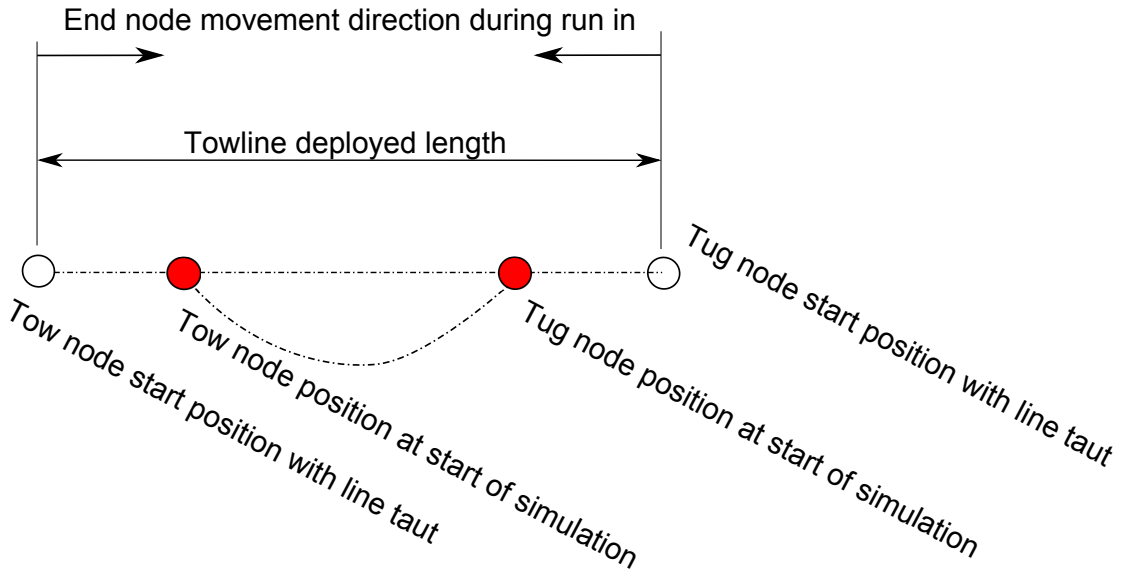

Figure 5.3.4: Simulation "run in" methodology

ensure there was no "bellying" of the towline as the transverse drag on the middle segments was such that a critical or terminal velocity was reached which was lower than that of the segments nearer the ends of the line which were more sharply angled and whose motion and corresponding node speed was more strongly governed by the, lower, longitudinal drag coefficient of the local segments.

At this stage a simple check was carried out to understand what a target settling time could be and so several runs were carried out to see what effect the run in time and discretisation of the towline had on the settling to a steady state condition (or close enough approximation such that forced excitation simulation could begin). The effect of discretisation on tension settling can be seen in figure 5.3.6. For a consistent run in time, the variation in amplitude of residual tension oscillations can be seen to be fairly consistent across several discretisation schemes. The only significant difference is the frequency of these residual oscillations which appears to be a linear function of the segment length.

Effect of run in time on settling time Reference figure 5.3.5 one can see that for run in times of 10 seconds and above the improvement in settling time is significantly reduced and 20 seconds appears to offer best compromise. This will be used in the main simulations and data quality checked to ensure the assessment remains true for other towline variations with local run in times tweaked to improve performance as required.

Effect of towline discretisation on settling time Reference figure 5.3.6 the effect of discretisation has little effect on the actual settling times in simulated time but does have a effect on the actual run times of the numerical code base. It may also be seen that the settled towline mean tensions trends towards the ideal theoretical value as the number of nodes increases, reference figure 5.3.7. It was

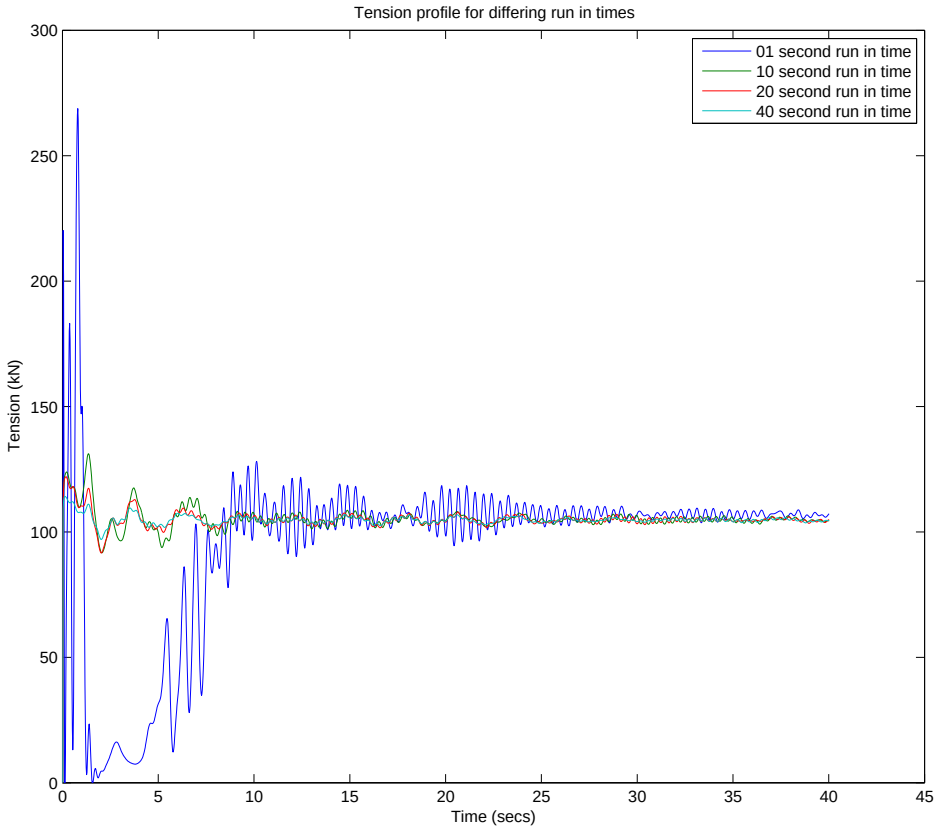

(a) Overview of tension fluctuations and settling time

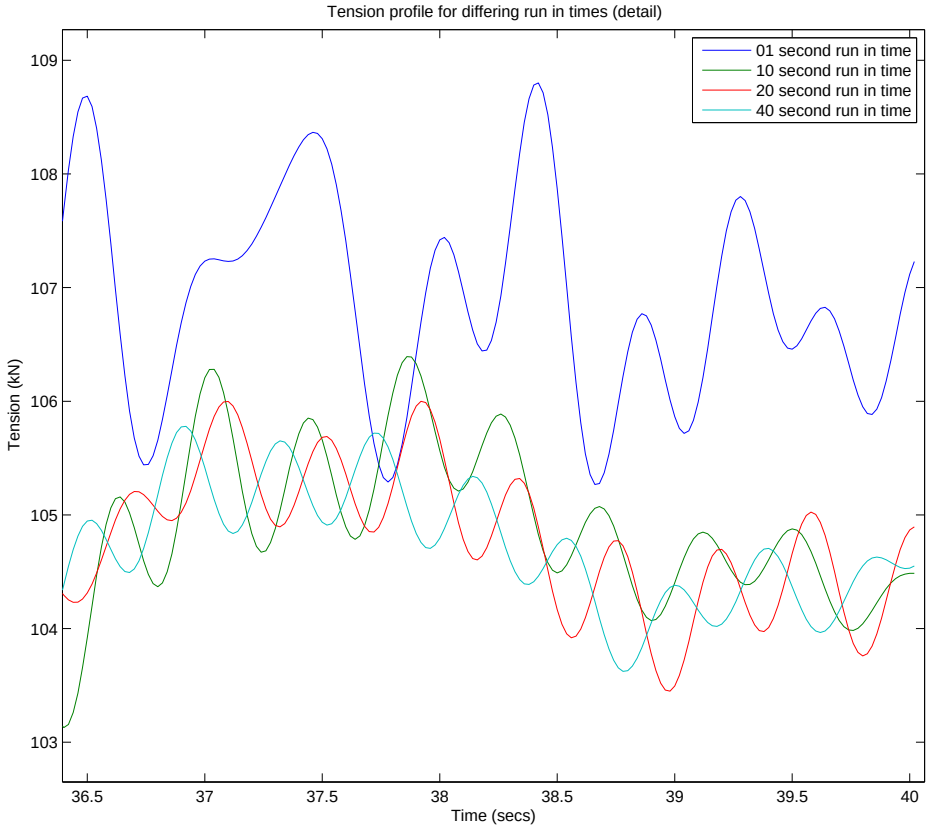

(b) Detail on towline tension fluctuations

Figure 5.3.5: Towline tensions for differing “run in” times

found that, generally, a towline segment length of between 2% and 5% of the overall deployed towline length was sufficient.

One final method employed to increase the speed at which the line settled to an adequate starting position and energy state, was to adjust the line drag and, therefore, damping during the periods of free fall, thereby allowing the line to settle through the fluid as the end points were adjusted to their initial starting position and then "turning on" or increasing drag as the settling period started. This served to further improve settling time and was used on a case by case basis with values always returning to their default states prior to the actual simulation starting.

Finally the code was profiled to highlight areas where run time was concentrated and further improvements made by pre-calculating interpolated values and allocating space for storage arrays outside the main simulation loop. The end result of all code and numerical routine improvements was a drop of the average run time for a simulation of one hour of captured logger data from circa. 3 hours to just under 5 minutes.

5.3.3 Lump Mass Model Dynamic Verification

Comparison was made between the code base developed for this research with data from other accepted numerical code bases and some experimental results. In [Low and Langley (2006)] some experimental data based on riser analysis is presented. Whereas this research is primarily concerned with data for cables of diameter ~0.060m in diameter, experimental data in [Low and Langley (2006)] was for risers of 0.396m in diameter. In addition different heights for the end locations were specified and the length of the catenary was shorter than that applied for this research. Some differences were expected due to the combined effects of these differences with the fact that the code base here notably does not take into account bending stiffness of the cable.

The model and environment data used were as presented in table 5.3.1. Both static and dynamic cases were available for verification and both are presented here for comparison. In the static results, table 5.3.2 and figure 5.3.8, a difference in the end tensions may be noted, especially at the lower end. This has been attributed to the increased effect bending stiffness has on the geometry. A comparison with a steady state dynamic case from [Low and Langley (2006)] may also be seen in figure 5.3.9. While the shape is similar there is a difference in the values at peaks and troughs of the graph which again are attributed to bending stiffness effects.

To ascertain the code's effectiveness for cable like structures a number of simple harmonic motion simulation runs were made in OrcaFlex (OF) and compared with MatLab (ML) results. These results are shown in in figure 5.3.10 with input data outlined in table 5.3.3 where much closer correlation between

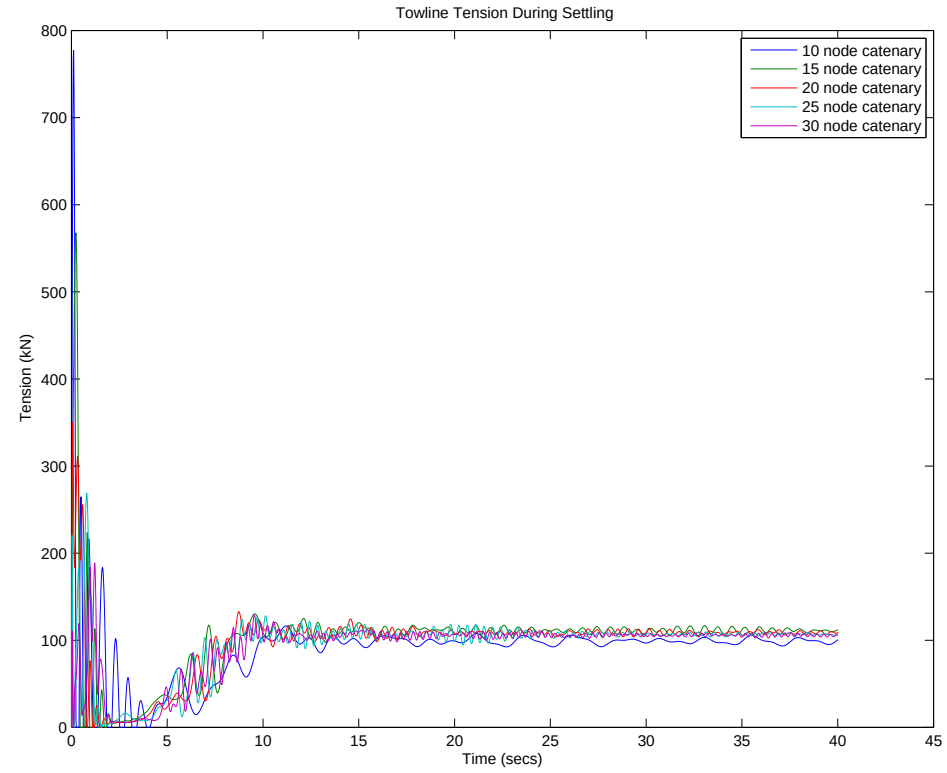

(a) Overview of tension fluctuations and settling time

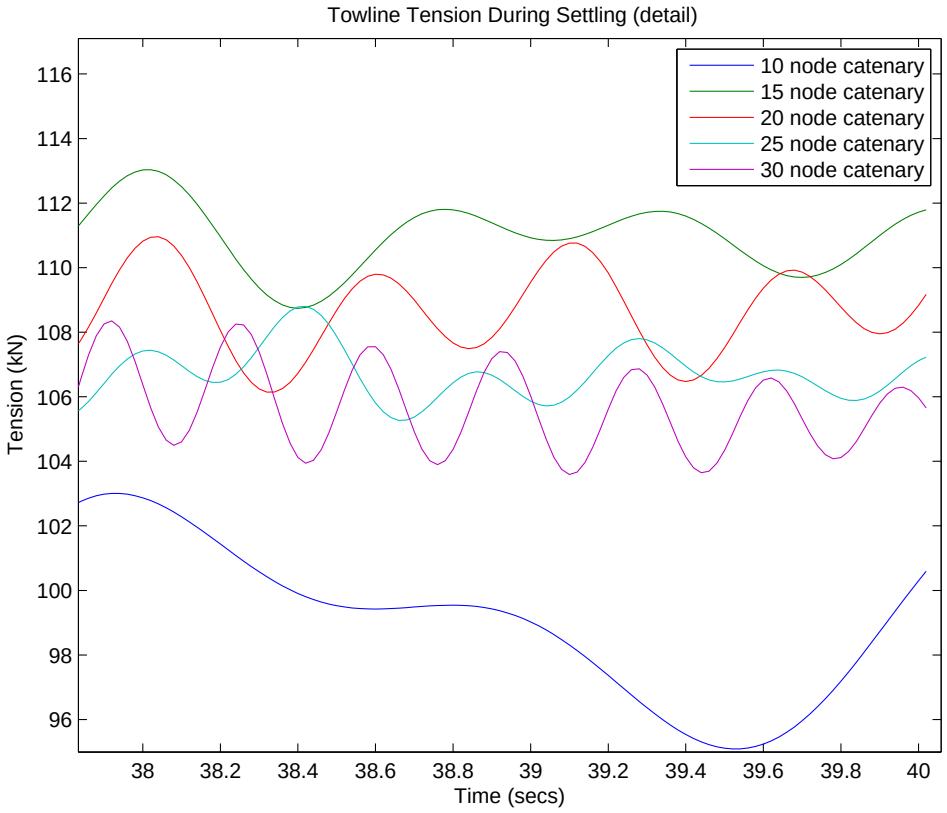

(b) Detail on towline tension fluctuations

Figure 5.3.6: Towline tensions for differing levels of line discretisation

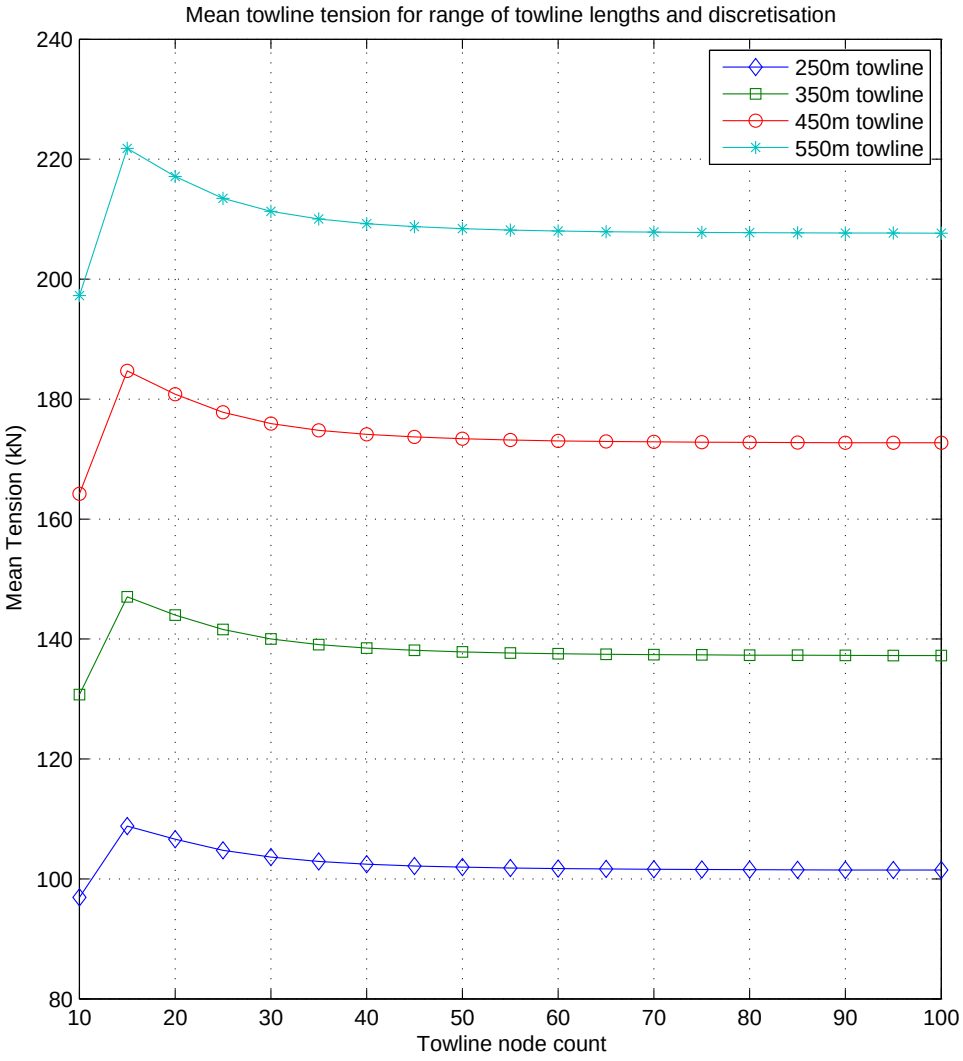

Figure 5.3.7: Mean, settled towline tensions for varying discretisation schemes

Table 5.3.1: Test data from [Low and Langley (2006)]

Property	Value
Total, unstretched, deployed line length	170 m
Cable Dia	0.396 m
Cable Mass (in air)	165 $kg.m^{-1}$
Modulas of Elasticity (E)	4.06 x 109 $N.mm^{-2}$
Water Density (ρ)	1000 $kg.m^{-3}$
Gravitational Acceleration (g)	9.807 $m.s^{-2}$
Drag Coefficient - C_N	1.00
C_τ	0.00
Added Mass Coefficient	1.00
Number of Cable Segments	68
Segment Size	2.5 m

Table 5.3.2: Static Riser test results

Description	Numerical Model Employed	
	Low and Langley (2006)	Huang (1994)
Top Tension	47.11 kN	46.90 kN
Bottom Tension	26.60 kN	28.42 kN

the code bases may be seen. AS the purposes was to compare code bases, the input data into the orcaflex model was matched with that used in the numerical system written for this research. OrcaFlex cable element was employed with matching discretisation.

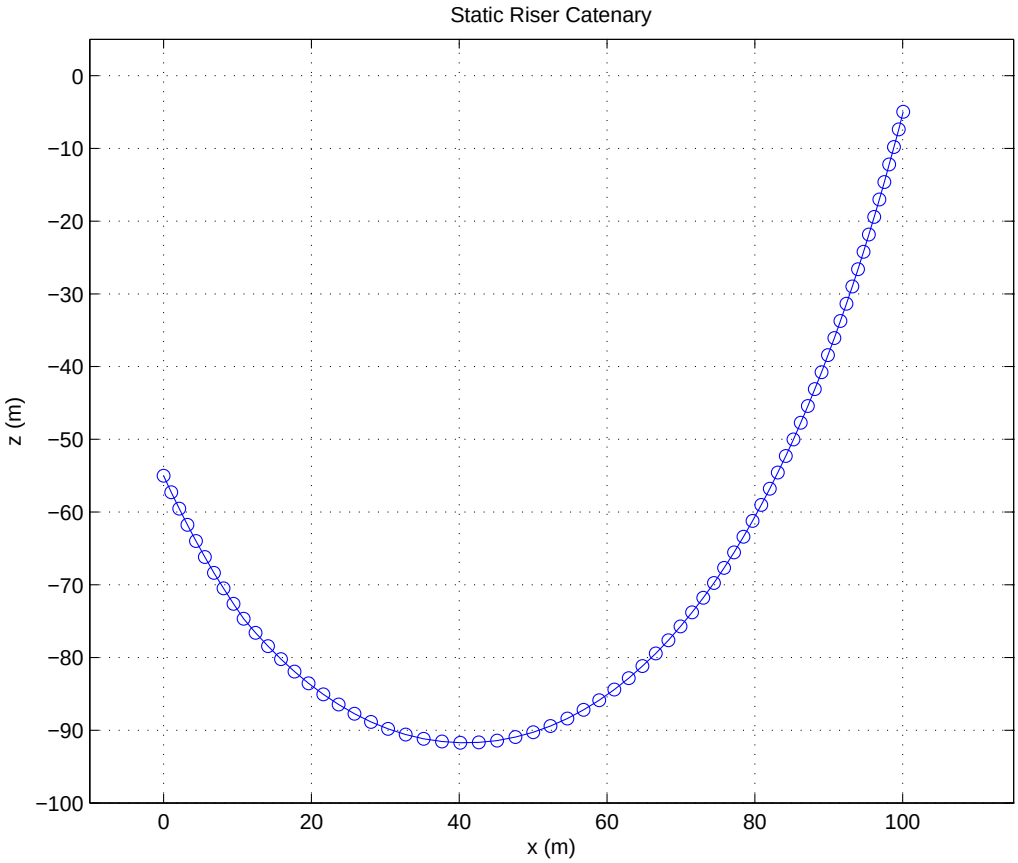

Note: In this assessment the z axis represents the water depth below a waterline set at z=0m.

Figure 5.3.8: Static test case plot based on model data from [Low and Langley (2006)]

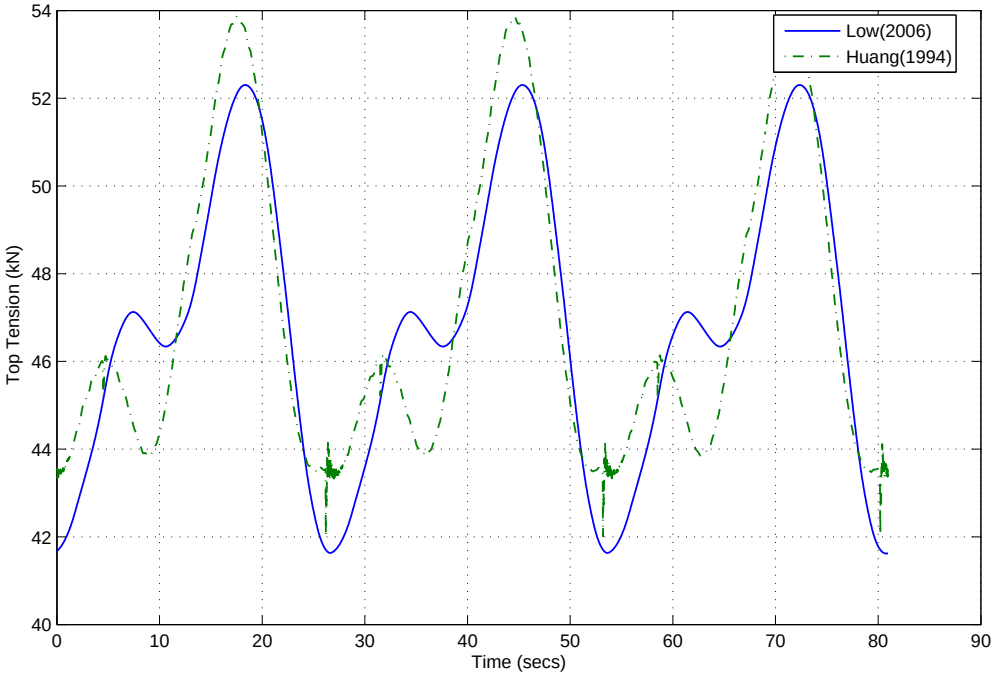

Note: the curves represent tensions reported in the original paper by Low and the output from the numerical method employed here based on the methodology outlined in the paper by Huang.

Figure 5.3.9: Dynamic test case plot based on model data from [Low and Langley (2006)]

Table 5.3.3: Simple harmonic motion test cases run in Matlab and Orcaflex

Cable length		310 m
Cable Dia		0.052 m
Load case 1	Direction	Surge
	Period	20 sec
	Amplitude	10 m
Load case 2	Direction	Sway
	Period	20 sec
	Amplitude	10 m
Load case 3	Direction	Heave
	Period	20 sec
	Amplitude	10 m
Drag coefficient	C_N	1.00
	C_τ	0.01
Added Mass coefficient	k	1.00
Number of cable segments		19 (20 nodes)
Segment size		16.3158 m

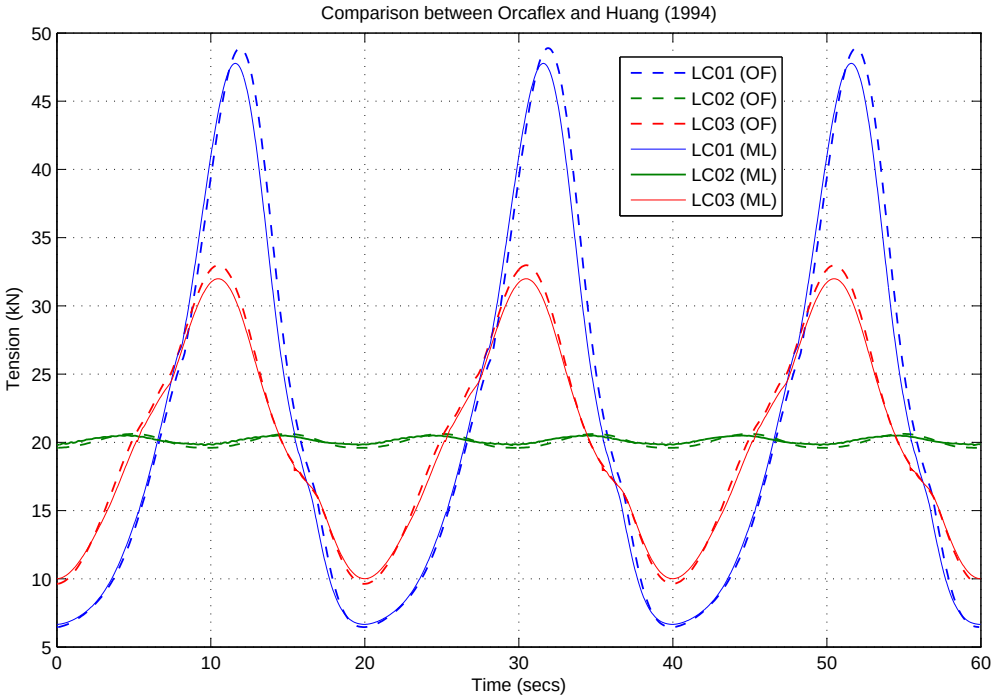

Note: the curves represent tensions reported in the Orcaflex model and the output from the numerical method employed here based on the methodology outlined in the paper by Huang.

Figure 5.3.10: Matlab/Orcaflex simple harmonic motion comparison runs

5.4 Examination of the effect of GPS Noise on full scale numerical model

With reference to the discussion on GPS noise and corresponding soak tests in section 3.2.3 it is interesting to isolate and examine what the effect these random movements may have on the calculated towline tensions under the numerical modeling scheme employed here. For this the towline as used in the full scale trials was modelled and the effect of stimulating the ends of these lines with recorded GPS traces from a datalogger left at rest were assessed.

5.4.1 Towline and bridle drag characteristics

For this numerical run the best possible estimates of the towline properties have been implemented, rather than the more generic ones used above. It will be these that will be carried forward to the final numerical runs on the actual tow considered in chapter 6.

When considering the final hydrodynamic drag properties of wire rope and chain to be employed in the full scale runs, a literature search revealed a study, [Yang (2007)], where a series of dynamic free and forced oscillation tests were carried out, albeit on chains of considerably lower sizes than those considered here. This study looked to derive curves of drag and added mass for chains operating at a range or Reynold numbers. Reference was also found in [DNV (2010)] where by a static range of values for different mooring equipment was published and are repeated in table 5.4.1 for convenience.

[DNV (2010)] also notes that longitudinal/tangential drag coefficients “can often be neglected”, however where it is to be considered it makes reference to [DNV (2007)] which offers a mechanism for calculating the longitudinal drag on inclined cylinders which itself is based on research published in [Eames (1968)]. Here the longitudinal drag coefficient for 6-stranded wire is derived from:

$$C_\tau = C_N \left(m + n \cdot \sin \alpha_i\right) \cos \alpha_i \tag{5.4.1}$$

Where m = 0.03, n = 0.06 (for 6-stranded wire, [DNV (2007)]) and α_i is the angle of attack of the segment of wire under analysis. If this is run for a range of angles of attack between 0 degrees and 90 degrees a range of drag coefficients as shown in figure 5.4.1 may be seen.

The mean of the longitudinal drag coefficient between angles of attack of 0 degrees and 40 degrees (assumed as representative of the core range of angles of attack of a towline in normal towing circumstances) is 0.085 which will be adopted for the balance of runs in this research.

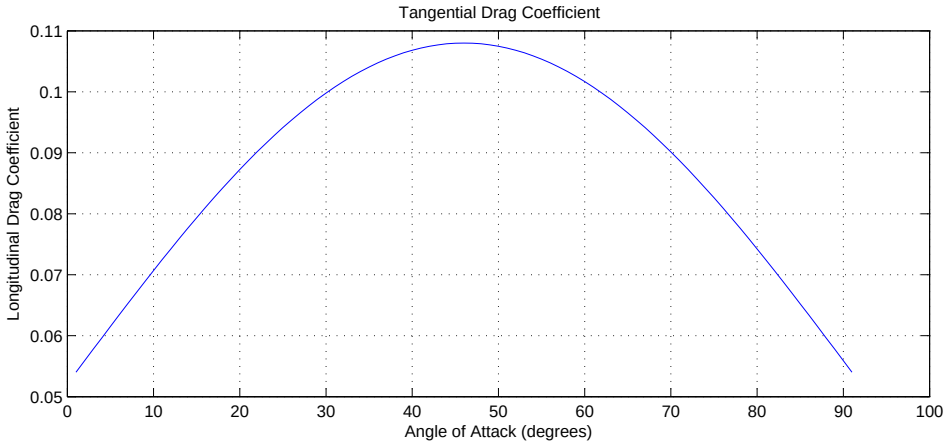

Figure 5.4.1: Tangential drag coefficient from [DNV (2007)]

Table 5.4.1: Mooring equipment drag coefficients with no marine growth (ref section B701 in [DNV (2010)] and section 6.3 in [DNV (2007)])

Item	C_N	C_τ
Stud chain	2.6	1.4
Studless chain	2.4	1.15
Stranded rope	1.8	0.085 *
Spiral rope without plastic sheathing	1.6	-
Spiral rope with plastic sheathing	1.2	-
Fibre rope	1.6	-

(*) Longitudinal drag from [DNV (2007)]

5.4.2 Numerical Run setup

The code employed for these runs is identical to that verified and discussed in 5.3.3. GPS readings from a datalogger at rest were applied to the towline ends. The same 21hr soak test data outlined earlier was employed and the first 3600 second extract taken and applied to the tow end. The final dataset is to be post processed as 1 hour segments hence the selection of 3600 seconds for these runs.

The same data extract was reversed in order and then applied to the tug end of the towline. This then ensured there was no artificial synchronisation of end motions. For this reduced dataset the measured error margin was reduced as may be seen from the reduced standard deviations on the x and y axis of 0.8002m and 1.0159m respectively. The graph in figure 5.4.2 also shows a reduced CEP of 1.0715m for the single hour of data used.

5.4.3 Towline test on generic single component towline

The effect of the GPS random walk movements as applied to a full scale towline configuration as outlined in table 5.4.2 was explored. For the case of the towline at rest, i.e. without forward speed, it may be seen that the GPS jitter noise introduces oscillations into the towline of a relatively low amplitude and

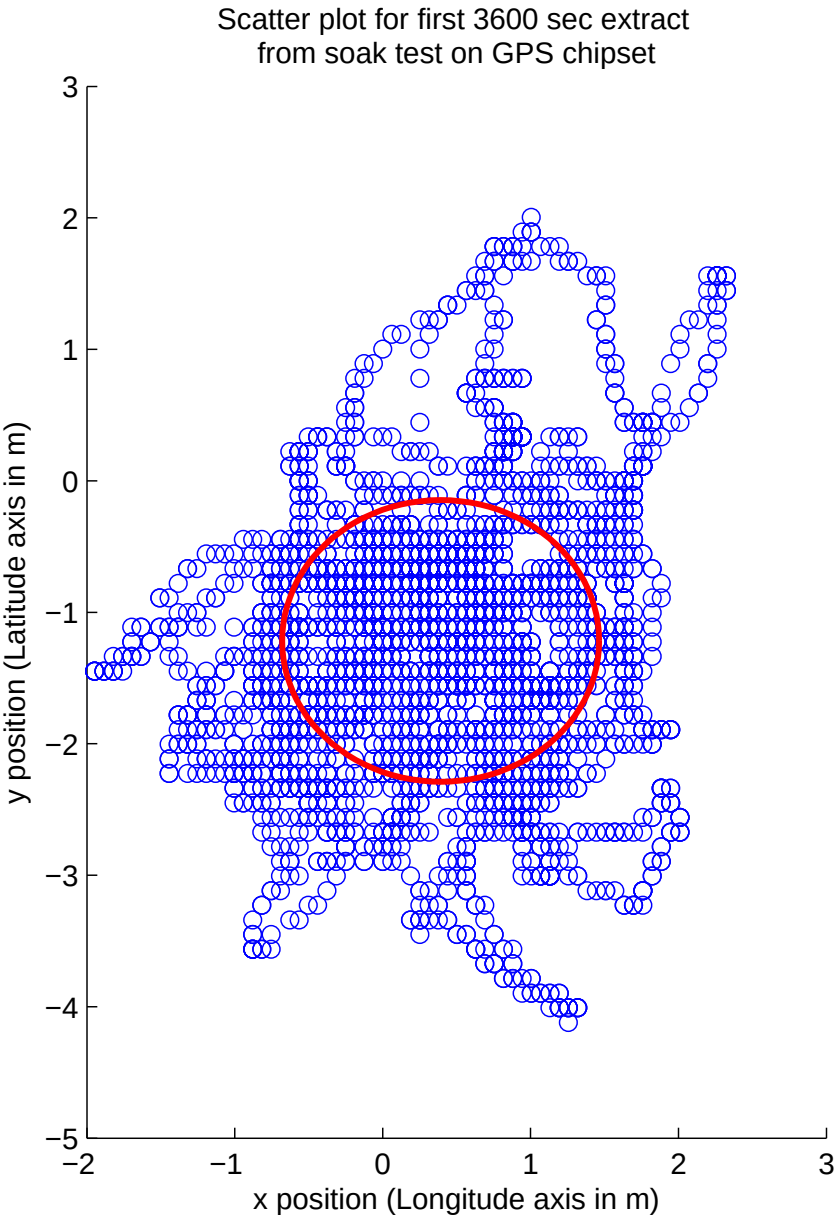

Figure 5.4.2: 3600 seconds GPS jitter sensitivity soak extract

Table 5.4.2: GPS Random walk tests on full scale representative towline configuration

Cable lengths		250 m, 350 m, 450 m, 550m, & 650 m
Towline Dia		0.060 m
Towline unit mass		15.1 kg/m
Bridle Dia		0.066m (studlink)
Bridle unit mass		99.71 kg/m/leg
Mass shackle		53.6 kg x 3 (off)
Mass triplate		118.69 kg x 1 (off)
Length “forerunner”		9.00 m
Unit mass “forerunner”		99.71 kg
Load cases	Direction	X and Y axis
	Duration	3600 secs
	Amplitude	GPS Random walk
	Separation	95 % of towline length
Drag coefficients - Towline	C_N	1.800
	C_τ	0.085
Drag coefficients - Bridle	C_N	2.600
	C_τ	1.400
Added Mass coefficient	k	1.000
Number of cable segments		26 (27 nodes)

Table 5.4.3: GPS Noise driven tension variances

Towline Length (m)	Tension variance
250	87.5964
350	45.7402
450	29.2305
550	20.8606
650	16.5041

the maximum offsets represented by the +/- 2m in the N and E directions will be significantly less than any surge and sway induced motions of interest in the final simulations.

With reference the FEA stiffness models created, the properties of 66mm studlink chain have been used for both the bridle legs and “forerunner” pennant leg with the shackles modeled as 120 Te SWL green pin shackles and the triplate modeled as an 120 Te SWL variant with stiffness properties of each extrapolated from the FEA studies reported earlier. Another lumped mass representing an 120 Te SWL shackle has been assumed at the junction between the 60 mm Dia towline and the 9m long 66mm studlink chain pennant. For a detailed layout sketch of the bridle arrangement see figure 5.4.3.

The bridle model was simplified to a representative composite line, as proposed in equations 5.2.17 through 5.2.20 in section 5.2.3. The MatLab plot of the 250m system is shown in figure 5.4.5.

The observed variations across the runs were as shown in table 5.4.3 and follow the expected pattern of increasing variance in tensions as the ratio of maximum end motions to total towline length increases (i.e. any given end motions have tendancy to make shorter lines work the elastic stiffness more than the catenary action itself). For the full scale deployed towline length of around 450m a variance of around 30kN is noted.

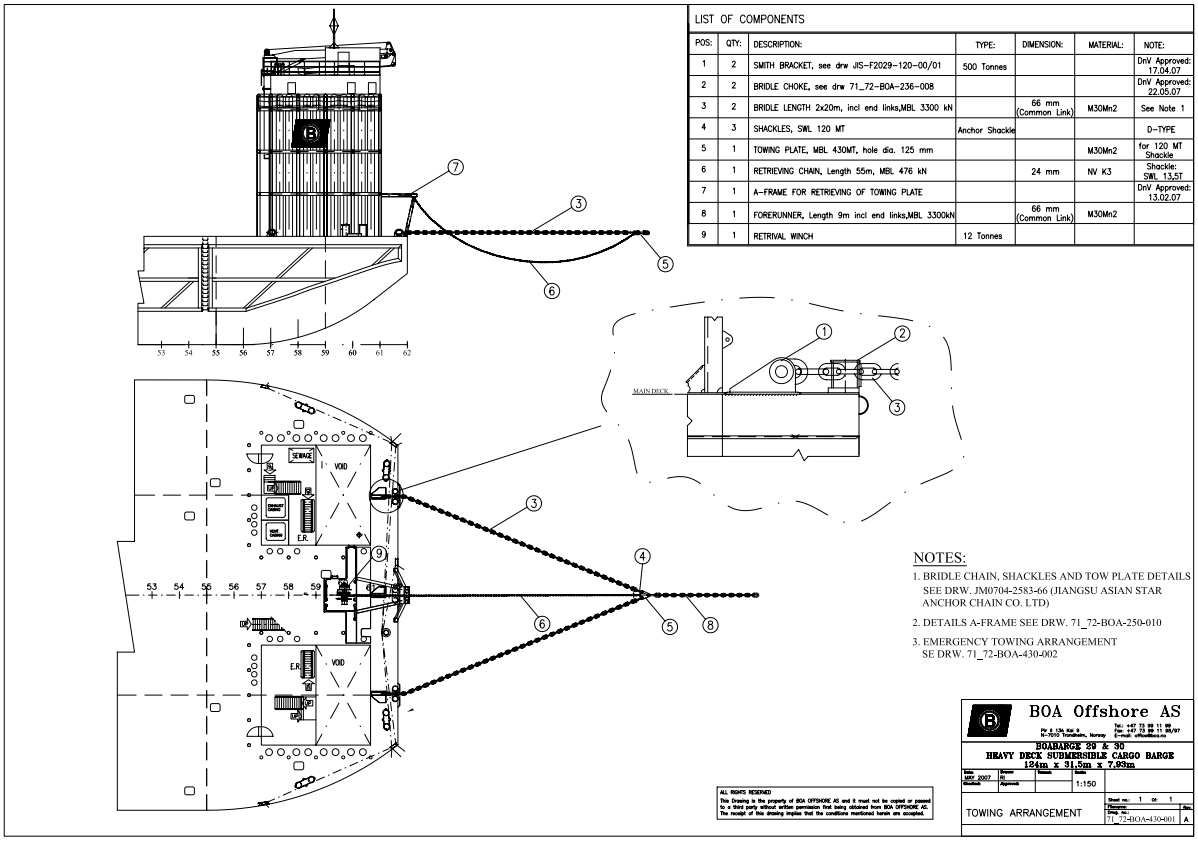

Figure 5.4.3: BOA 35 Towing Bridle Construction

5.5 Chapter Summary

In the preceding chapter a summary of the industry standards for towage equipment, the means by which it is connected to the tow and the range of equipment typically used for different classes of tug as specified by principle industry guidelines has been presented. Thereafter an outline was given of the different means of modelling towline stiffness with reference to the complications associated with accurately assessing the stiffness of helically wound wire strand ropes as well as modeling key components in an FEA package to better understand their true stiffness properties. In doing so some interesting comparisons with chain and wire rope could be made. This was then used to provide a stiffness model for the two leg bridle typically found on towed barges which could be resolved into a series of stiffness elements providing largely equivalent stiffness and weight properties, both of which are critical to the response of the towline catenary under excitation. Furthermore, a summary of tangential and normal drag coefficients options was made and a methodology selected for the final full scale runs.

Finally, the numerical lumped mass model was presented with detailed pseudo-code for the numerical routines as coded in MatLab, to be read in conjunction with the theory outlined in [Huang (1994)]. This was then verified against published data and against an existing industry accepted code base (OrcaFlex) and the code developed here was shown to be robust and therefore acceptable for use in post processing the full scale data trials.

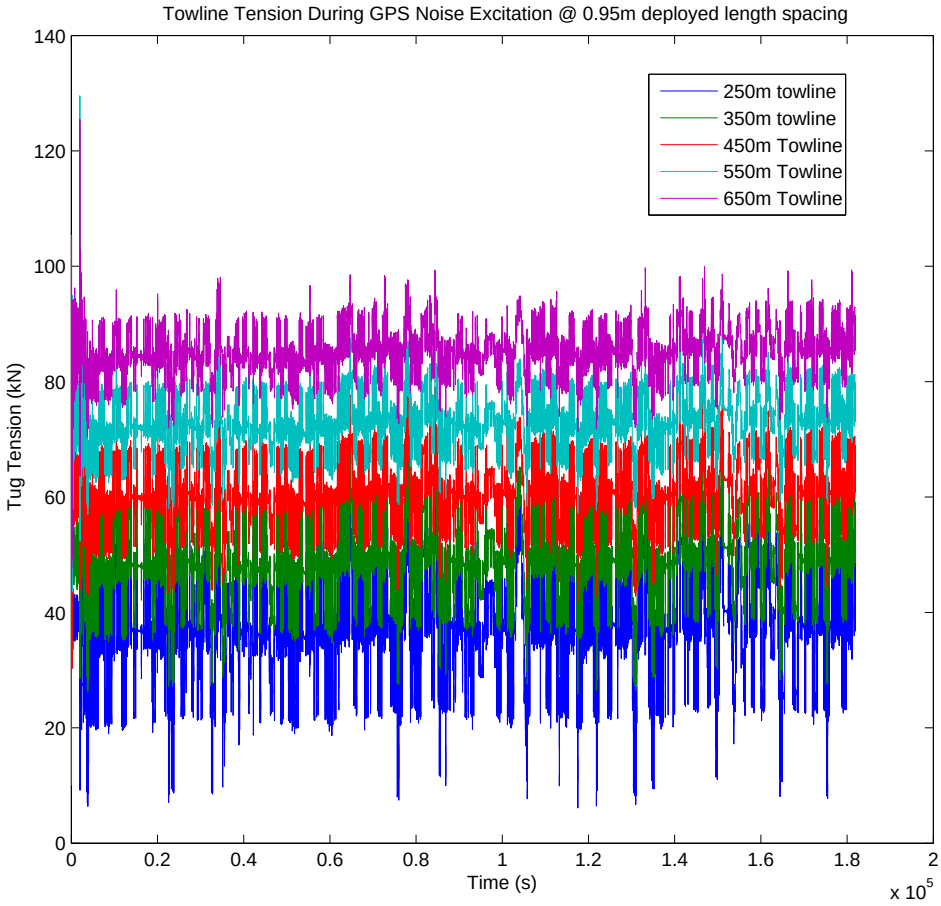

Figure 5.4.4: GPS Noise Driven Towline Tensions @ 95% separation

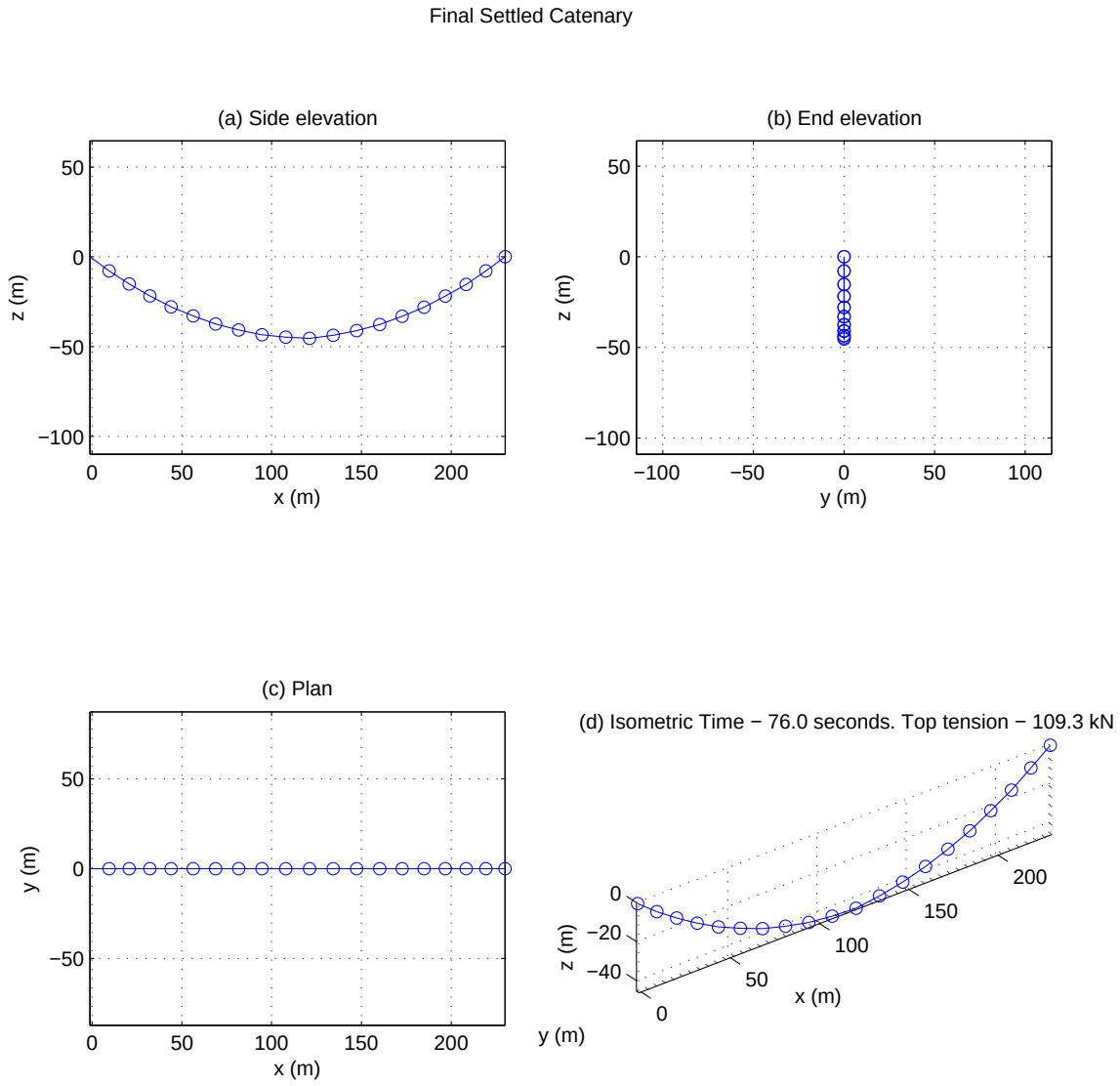

Figure 5.4.5: MatLab plot of composite towline showing chain bridle concentrated nodes and wire towline nodes

Chapter 6

Full Scale Trials

6.1 Legacy Data and Datalogging Issues

The original plan for data collection was to run data gathering on voyages of opportunity in tandem with the development of the methodology and numerical routines. The author, through his company, had access to a large number of tug and barge charters of various sizes which would, ideally, allow for the post processing of a wide range of data towards the end of the research period. Unfortunately the technology for the data gathering was also under continuous development during this period with its main focus being its intended commercial application, the end result being that almost all of the early data contained flaws of such magnitude that it precluded its use in any meaningful context for this research. Such issues included:

- PCB design issues resulting in significant noise pollution of accelerometers and tilt sensor signals. Data adequate for sensing significant shock loads to cargo but not for sensing vessel motions.
- Version 01 of PCB incorporated multiple accelerometers paired and aligned to detect and derive angular motions via differences in the recorded linear accelerations perpendicular to any one axis. Issues associated with the signal noise problems noted above was further compounded by the relatively small levers between sensors all located within a single housing meaning that angular acceleration data was of extremely limited accuracy and any meaningful signal was swamped by system and signal noise.
- GPS chipset was only designed to be woken up to record longitude and latitude fixes when subject to accelerations or angles of tilt above defined “trigger” values. A workaround within the limit of the original firmware was found which set the alarm levels to triggers that essentially had the GPS

always on. This caused issues with continuity of GPS readings as the firmware would lock and result in GPS readings frequency that were too low (circa 0.2 Hz or less).

- This manner of working the system resulted in non-optimum power consumption and premature shutdown on certain towages.
- The flexible design, i.e. allowing for remote transmitting of data over GPRS network, sensor trigger levels, high and low frequency datalogging etc, when coupled with the relative immaturity of the firmware resulted in buggy and unstable on board software manifesting in GPS outages and signal data not recorded for long period on the voyages for no discernible reason (remote debugging during voyages being practically impossible).

As the 3rd anniversary of the project approached and the post processing and algorithm verification stage imminent, with little useable data available, the decision was made to re-code a temporary version of the firmware with the sole remit of reliably recording sensor data and GPS at defined intervals (variable via simple “ini” file stored on the memory card). Low power, reliability and simplicity were the design features required for this “research only” build of the firmware. This was done in time for the last scheduled voyage of the batch of voyages of interest.

6.2 Full Scale Voyage Details

6.2.1 Project Background

The voyages of opportunity that were earmarked for this research were primarily those associated with the transportation of large ship sections for the UK’s next generation “Queen Elizabeth Class” of Aircraft Carriers.

The attractiveness here was that a wide range of barge, tugs and cargo masses/geometry were to be transported ranging from multiple sections of up to 350 Te each through to larger single loads of significant portions of the hull up to 12,000 Te in weight, see figures 6.2.1 through 6.2.4 for examples.

6.2.2 Voyage Particulars

It was on the voyage depicted by figure 6.2.1 that a pair of data loggers, one on the barge and one on the tug, were most successfully deployed.

Figure 6.2.1: Lower block 02 @ ~6,500 Te on semisubmersible barge

Figure 6.2.2: Forward flight deck sections, 5 off @ ~850 Te each

Figure 6.2.3: Transom sections, 2 off @ ~800 Te each

Figure 6.2.4: Bridge section @ ~850 Te

The voyage for which the data presented here covers the towage of Lower Block 02 on board a large semisubmersible barge around the south coast of the UK sailing from Portsmouth to Rosyth between the 26th and 30th August 2014.

Extracts from the voyage log notes the following relevant times (adjusted to GMT):

- 26/08/14 - Barge enters C Lock at Portsmouth @ 0840 hrs
- 26/08/14 - Bow of barge at West Gate of C Lock at Portsmouth @ 1008 hrs
- 26/08/14 - Barge berthed at North west wall @ 1050 hrs
- 26/08/14 - Seagoing tug MT Eraclea presented to bow of barge and tow bridle connected @ 1200 hrs
- 26/08/14 - Tug and barge departs north west wall for sea @ 1645 hrs
- 26/08/14 - Tug and barge clear into main channel and departs to sea @ 1800 hrs
- 30/08/14 - Tug and barge arrive Fairway Buoy (pilot station), Firth of Forth @ 1220 hrs
- 30/08/14 - Tug and barge arrive Inverkeithing Bay, Firth of Forth for handover to harbour tugs @ 1455 hrs
- 30/08/14 - Barge and harbour tugs pass under Forth Rail Bridge @ 1555 hrs
- 30/08/14 - Barge all fast, Middle Jetty, Rosyth @ 1700 hrs

These timings can be compared with the detailed GPS traces (approximately one GPS fix recorded every second for the full voyage, any localised data outages excepted) as seen in figures 6.2.5 and 6.2.6 where excellent correlation with the manually recorded timings may be observed. The resolution of the GPS is also sufficient to make out operationally significant details such as the towing tug departing its layby berth in Portsmouth to make fast to the bow of the barge on the north west wall. Also, in Rosyth on arrival, the tracks for tug and barge may be seen running in parallel until the handover to harbour tugs is complete whereupon the red track departs due west for the bridges while the barge continues due east a short while before being spun west and following the tug in towards the discharge location.

From the summary above, and for the purposes of this analysis, the simulation will be run on data between 2000 hrs on the 26th and 1200 hrs on the 30th.

The route from Portsmouth to Rosyth was “southabout” i.e. via the English Channel and up the east coast of the UK. A plot of the full route may be seen in figure 6.2.7 on page 142.

The data gathered on the loggers were initially analysed for dropouts and coverage. Tables6.2.1 and 6.2.2 summarise the results of this for the GPS records at 1 Hz and sensor readings at 10 Hz for

(a) Departure detail at Portsmouth

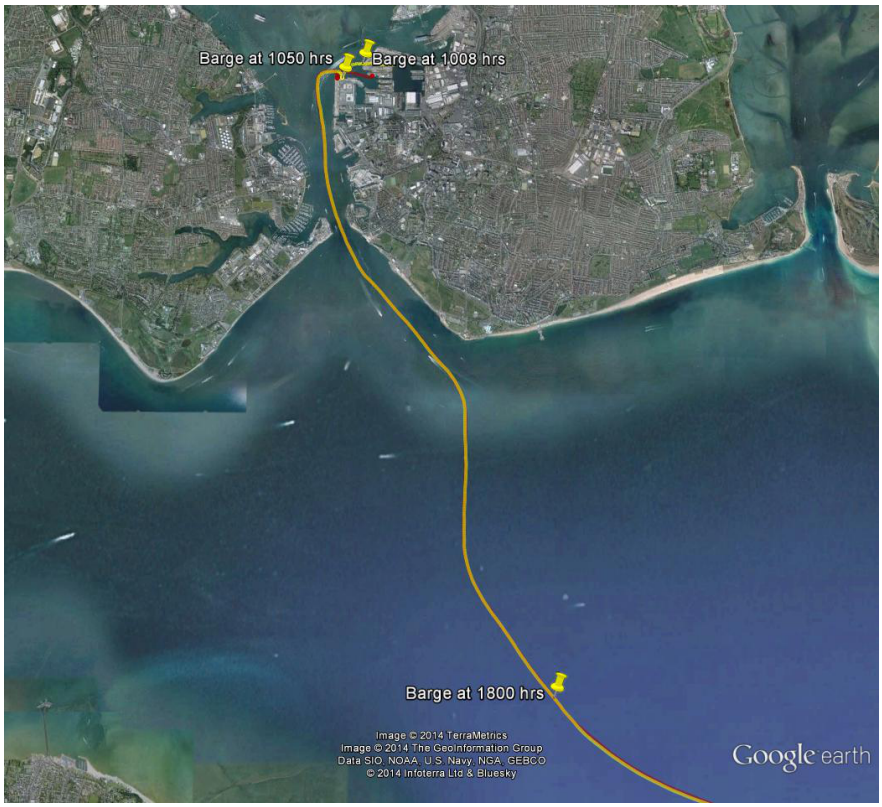

(b) Departure Portsmouth

Figure 6.2.5: Detailed, annotated GPS trace of departure of tug (red) and tow (yellow) at Portsmouth (satellite image (c) Google, 2014 - Infoterra Ltd and Bluesky & 2014 - The GeoInformation Group)

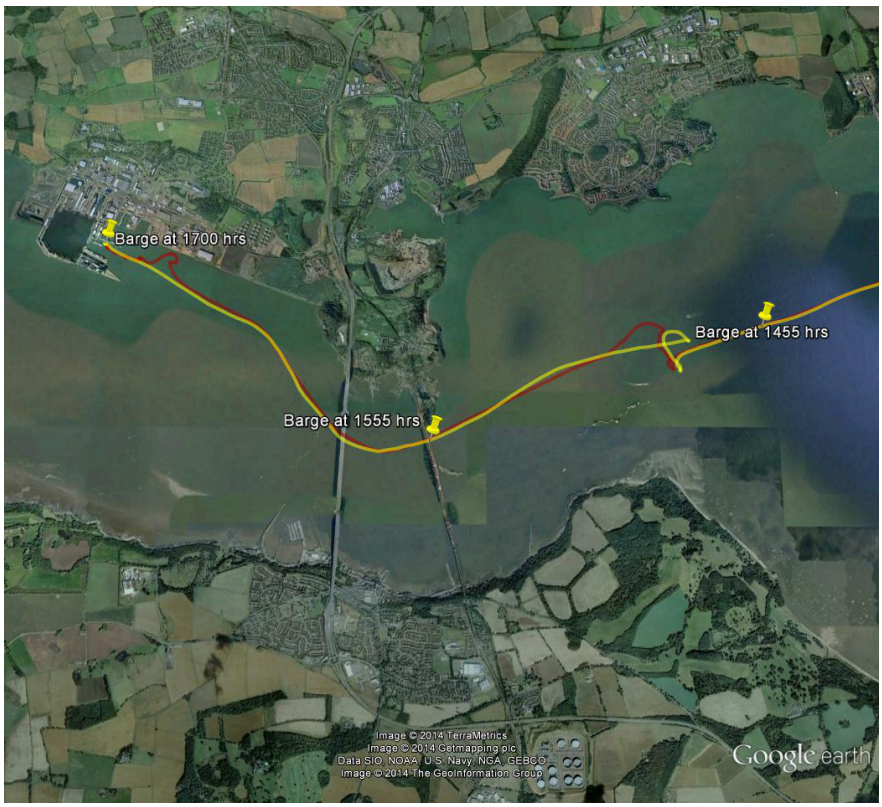

Figure 6.2.6: Detailed, annotated GPS trace of arrival of tug (red) and tow (yellow) at Rosyth (satellite image (c) Google, 2014 - Terrametrics, 2014 - Getmapping plc and 2014 - The GeoInformation Group)

complete 24 hr periods between the 26th and 30th inclusive. Note that for the dates of the 26th and the 30th, some of the readings noted in the summary tables will represent readings while the barge and tug are at layby alongside the quay. The quality of the data gathered will be discussed in more detail in section 6.2.5 later.

6.2.3 Barge Particulars and Logger position

The barge employed for the tow was the BOA35 (reference table 6.2.3 for main particulars).

The barge logger was located and clamped firmly to the forward handrail of the main access walkway spanning between the two forward caissons of the barge (reference figure 6.2.8 on page 144).

The barge's sailing stability condition, overall CoG and draughts are as recorded in the official documentation and an extract from this may be seen in figure 6.2.9. Combining this condition with the recorded logger location and the barge and bridle geometry one has the relative location of the logger to barge CoG and towline connection point as detailed in figure 6.2.10 and table 6.2.4.

Figure 6.2.7: GPS trace for barge over full route 26/8/14 to 30/8/14 (satellite image (c) Google 2014)

Table 6.2.1: Barge Data coverage

(a) Barge GPS data coverage

Date	Dataset coverage (hrs)	Total readings	Total dropped readings	Average dropped readings per hour	Max. gap (secs)	Distance traveled (km)
26th	24	69890	16510	687.9	7561	109
27th	22.6	75026	6334	280.3	8	329
28th	24	73565	12835	534.8	6956	286
29th	24	69501	16899	704.1	10330	193
30th	24	77112	9288	387.0	9	115

(b) Barge Sensor data coverage

Date	Dataset coverage (hrs)	Total readings	Total dropped readings	Average dropped readings per hour	Max. gap (secs)
26th	24	862138	1862	77.6	1.1
27th	24	863871	129	5.4	1.1
28th	24	863787	213	8.9	1.1
29th	24	863802	198	8.3	1.1
30th	24	863757	243	10.1	1.1

Table 6.2.2: Tug Data coverage

(a) Tug GPS data coverage

Date	Dataset coverage (hrs)	Total readings	Total dropped readings	Average dropped readings per hour	Max. gap (secs)	Distance traveled (km)
26th	24	81466	4934	205.6	3	106.7
27th	24	80962	5438	226.6	3	338.1
28th	24	79939	6461	269.2	4	292.5
29th	24	79391	7009	292.0	9	205.3
30th	24	77535	8865	369.4	10	117.3

(b) Tug Sensor data coverage

Date	Dataset coverage (hrs)	Total readings	Total dropped readings	Average dropped readings per hour	Max. gap (secs)
26th	24	863834	166	6.9	1.1
27th	24	863783	217	9.0	1.1
28th	24	863834	166	6.9	1.1
29th	24	863854	146	6.1	1.1
30th	24	863754	246	10.3	1.1

Table 6.2.3: BOA barge 35 Main Particulars

Item	Value
Length (oa)	124.00m
Breadth (mld)	31.50m
Depth (mld)	7.93m
Draught (max)	6.08m

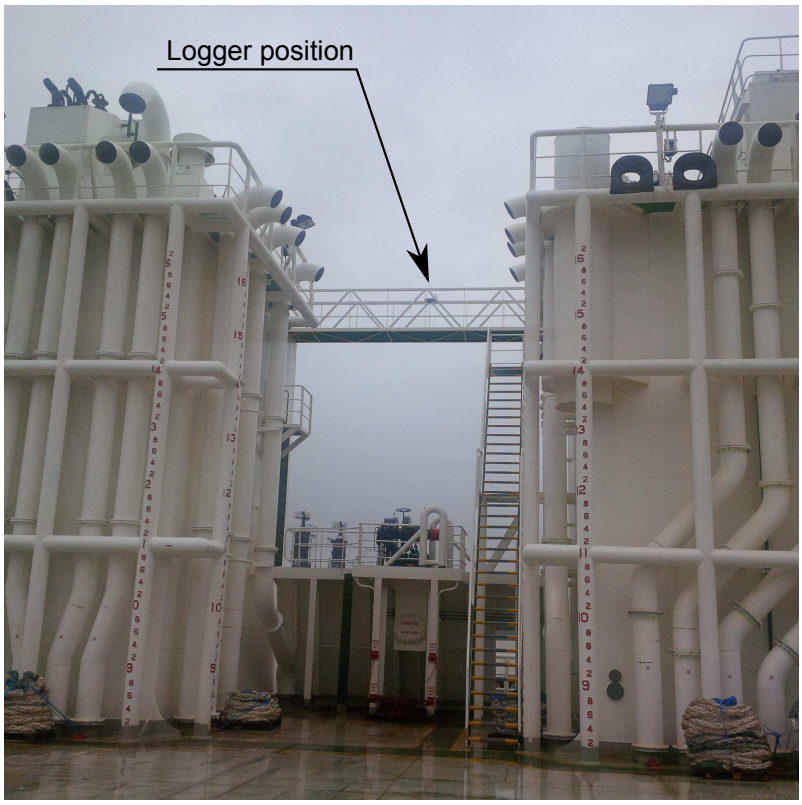

(a) View on logger position from main deck

(b) View on logger position from walkway

Figure 6.2.8: Lower Block 02 section and logger position on transportation barge

4.0 Stability Calculations

4.1 Stability Results Weight CoG (LCG&TCG as weighed - VCG Max)

4.1.1 Ballast Arrangement

The ballast arrangement for the BOA Barge 35 with the cargo was chosen to give the barge a level heel and a trim in the region of 0.25-0.50m by the stern to allow for trim due to towing. The barge is equipped with skegs and therefore does not need to trim further by the stern to improve the directional stability of the barge as suggested by Noble Denton. The tanks chosen allowed for further adjustments to overcome the effects of the movement of the CoG within the envelope provided and maintain the trim and heel. It has been assumed that all tanks will contain a minimum of 2% of their capacity to account for ballast trapped between stiffeners.

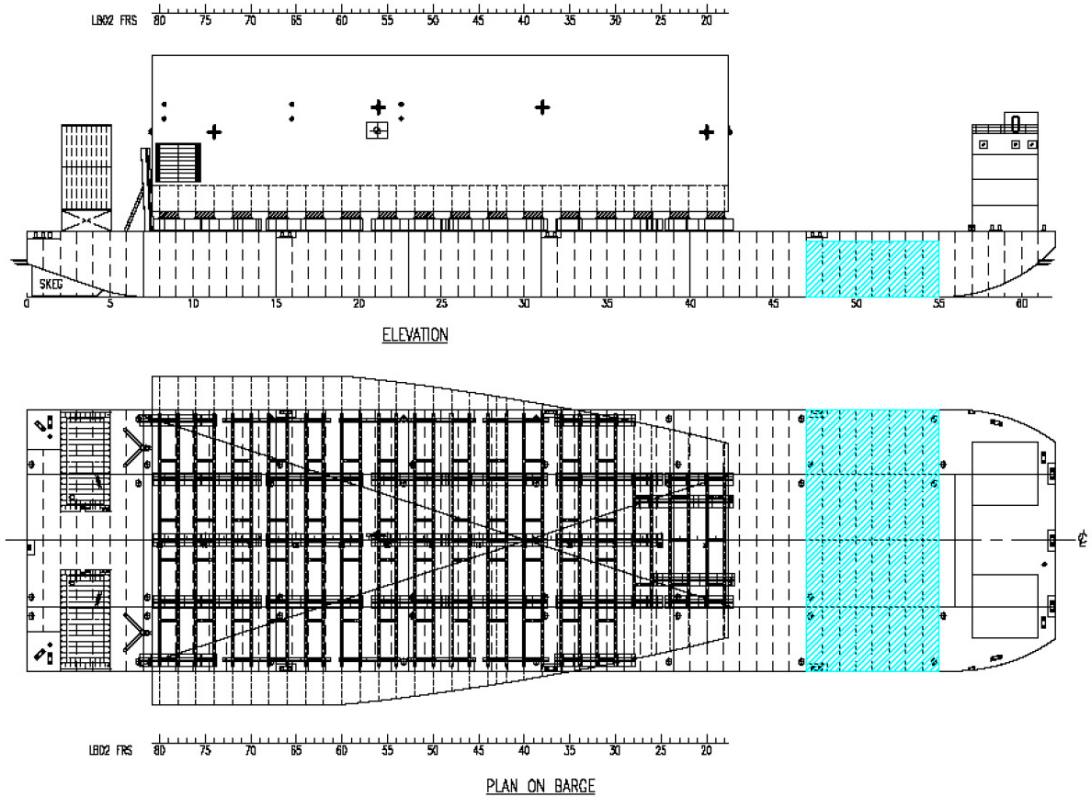

Figure 5: Ballast Arrangement - Elevation and Plan on BOA35

Floating Status

Draft FP	4.263 m	Heel	port 0.09 deg.	GM(Solid)	11.928 m
Draft MS	4.306 m	Equil	Yes	F/S Corr.	2.363 m
Draft AP	4.348 m	Wind	Off	GM(Fluid)	9.566 m
Trim	0.04 deg.	Wave	No	KMt	22.677 m
LCG	62.516f m	VCG	10.749 m	TPcm	38.76
Displacement	15,460.32 MT	WaterSpgr	1.025		

Figure 6.2.9: Barge Sailing Condition

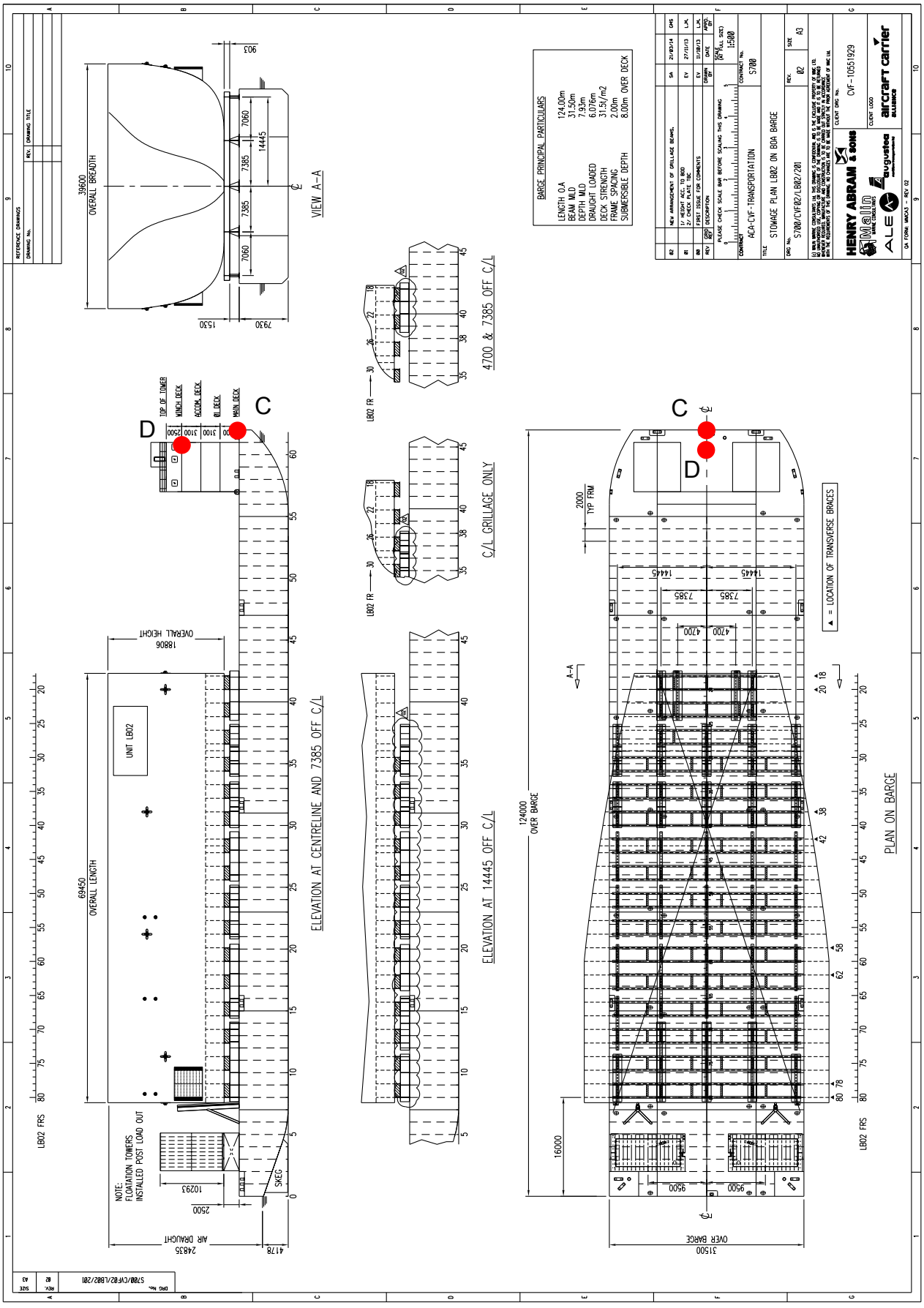

Figure 6.2.10: Barge logger position (D) relative to CoG of the system and the towline connection point (C)

Table 6.2.4: Barge Centroids

Item	X m (fwd)	Y m (stbd)	Z m (down)	Notes
AP	0.000	0.000	0.000	From AP/BL/CL
CoG	62.515	0.000	-10.749	From AP/BL/CL
Logger	122.000	0.000	-18.430	From AP/BL/CL
Connection Point	124.000	0.000	-7.930	From AP/BL/CL
Logger	59.485	0.000	-7.681	From CoG
Connection Point	61.485	0.000	2.819	From CoG

Table 6.2.5: AHT “Eraclea” Main Particulars

Item	Value
Length (oa)	50.00m
Breadth (mld)	15.50m
Depth (mld)	6.55m
Bollard Pull	120.00Te

6.2.4 Tug Particulars and Logger position

The tug employed for the main tow was the AHT “Eraclea” owned and operated by the Augustea Group (reference table 6.2.5 for main particulars).

6.2.5 Dataset Coverage

With reference to the high level summaries of data volume gathered, outlined in tables 6.2.1 and 6.2.2, it may be seen that there is a marked difference between the quality and coverage of the data logged on the tug and the barge. The tug data is of a reasonably high quality with low rates of dropped data which are reflected in histograms of data entries against each hour in the day. However the barge logger’s GPS sensor has experienced several long periods of data outage. This may be seen in the corresponding histograms of data readings shown in figure 6.2.13. Here the data outages may be clearly seen and therefore the following hours will be excluded from the simulations:

- 26th - hours 20, 21, and 22
- 28th - hours 20, 21, and 22

Table 6.2.6: Tug Centroids

Item	X m (fwd)	Y m (stbd)	Z m (down)	Notes
AP	0.000	0.000	0.000	From AP/BL/CL
CoG	21.692	0.000	-4.698	From AP/BL/CL
Logger	27.600	0.000	-19.185	From AP/BL/CL
Connection Point	-2.750	0.000	-6.700	From AP/BL/CL
Logger	5.908	0.000	-14.487	From CoG
Connection Point	-24.442	0.000	-2.002	From CoG

(a) View on logger position over aft deck of tug from quay

(b) View on logger from island over bridge deckhead

Figure 6.2.11: Lower Block 02 towage tug logger position

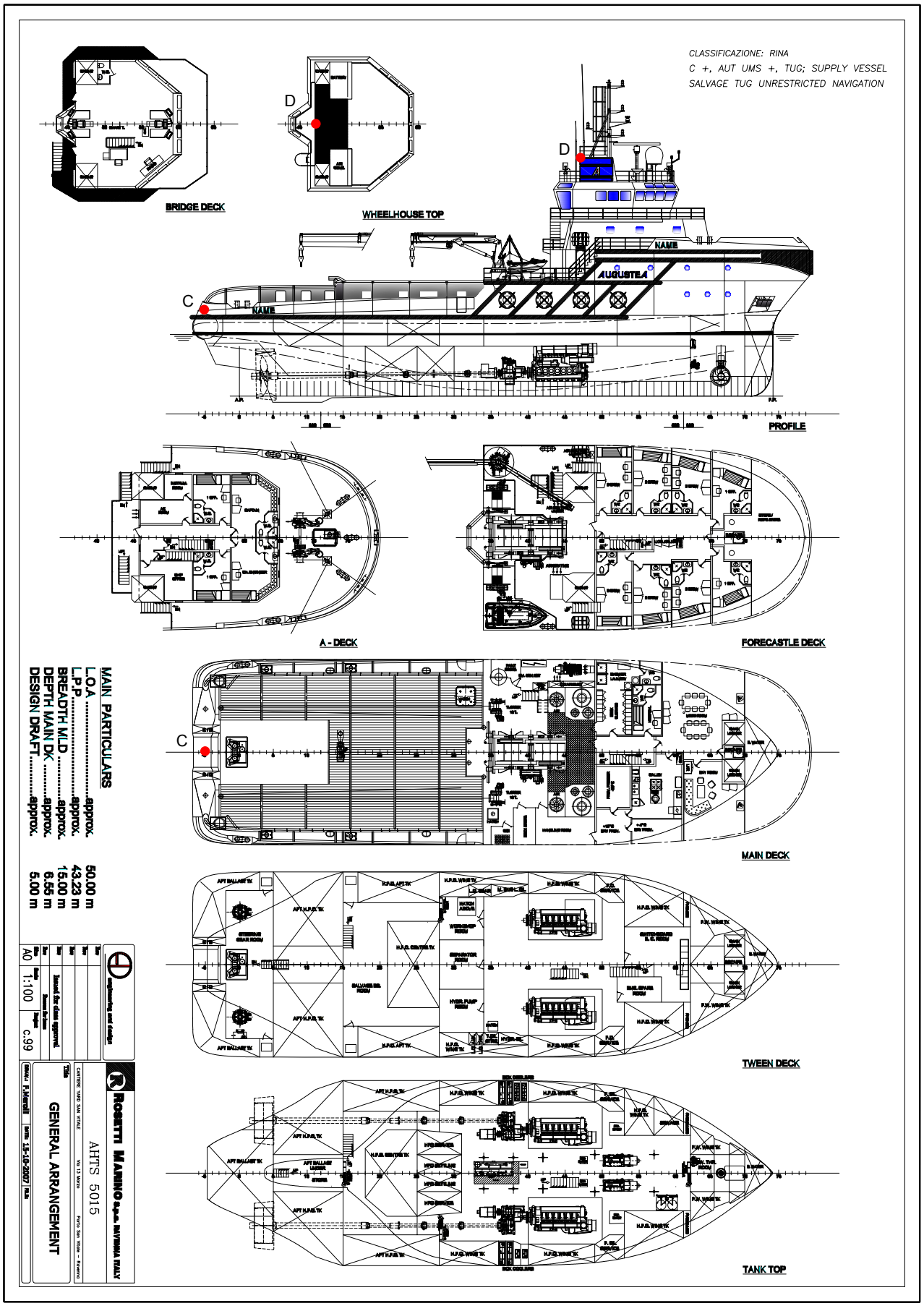

Figure 6.2.12: Tug logger position (D) relative to CoG of the system and the towline connection point (C)

Table 6.2.7: Tabulated Voyage Log

Time	Date	Deployed length of towline (m)	Seastate	Hs (m)	Wave Direction	Average Towline Tension (Te)
2400	26/08/2014	450	4	1.5	E	20-30
0400	27/08/2014	450	3	>1.0	ENE	20-30
0800	27/08/2014	450	4	>1.0	ENE	20-30
1200	27/08/2014	450	3	<1.0	ENE	20-30
1600	27/08/2014	450	3/2	0.5	NE	20-30
2000	27/08/2014	450	2	0.5	NE	20-30
2400	27/08/2014	450	2	0.5	SE	20-30
0400	28/08/2014	450	2	0.5	SE	20-30
0800	28/08/2014	450	4	1.0	SSE	20-30
1200	28/08/2014	250	3	1.0	SSE	10-15
1600	28/08/2014	250	3	1.0	SSE	10-15
2000	28/08/2014	250	2	<1.0	SSW	10-15
2400	28/08/2014	250	2	>0.5	SSW	10-15
0400	29/08/2014	250	2	>0.5	SSW	10-15
0800	29/08/2014	250	3/4	1.5	SSW	10-15
1200	29/08/2014	250	3/4	1.5	SSW	10-15
1600	29/08/2014	250	3/2	<1.0	SSW	10-15
2000	29/08/2014	250	3	1.0	SW	10-15
2400	29/08/2014	250	3	<1.0	SW	10-15
0400	30/08/2014	250	2	>0.5	SW	10-15
0800	30/08/2014	250	3	>0.5	W	10-15
1200	30/08/2014	150	3	>0.5	W	10-15

- 29th - hours 2, 3, 4, and 5

While the hours dropped for the 26th and 28th are the same, it is thought that this is coincidental. No reason was found for these dropouts but it is worth noting that the Siemens chipset on board the logger streams the readings to the logger for recording and so reliability is wholly dependent on the integration and the implied reliability of this closed subsystem.

Tug voyage records are shown in table 6.2.7 and scans of the originals may be seen in Appendix B. It shows a fairly benign voyage and while ideal from an operational point of view, it is less interesting from a perspective of wishing to explore methods of modeling extreme towline tensions from field gathered data.

From the voyage log it is not apparent when, exactly, the towline was shortened as the detail was only recorded every four hours. Therefore, as a cross check of the records kept by the tug crew, the GPS output from the tug and barge loggers was processed and the raw distance between the loggers second by second for the voyage was plotted. This allowed identification of the points in the tow where the mean distance changed and by how much thereby allowing a degree of verification of the timeline prior to running the time domain simulations. This cross check raised some concerns over the accuracy of the measure of towline deployed and record of same which was borne out by the simulations themselves.

With reference to figure 6.2.15 one can see key events played out in the calculated distance between

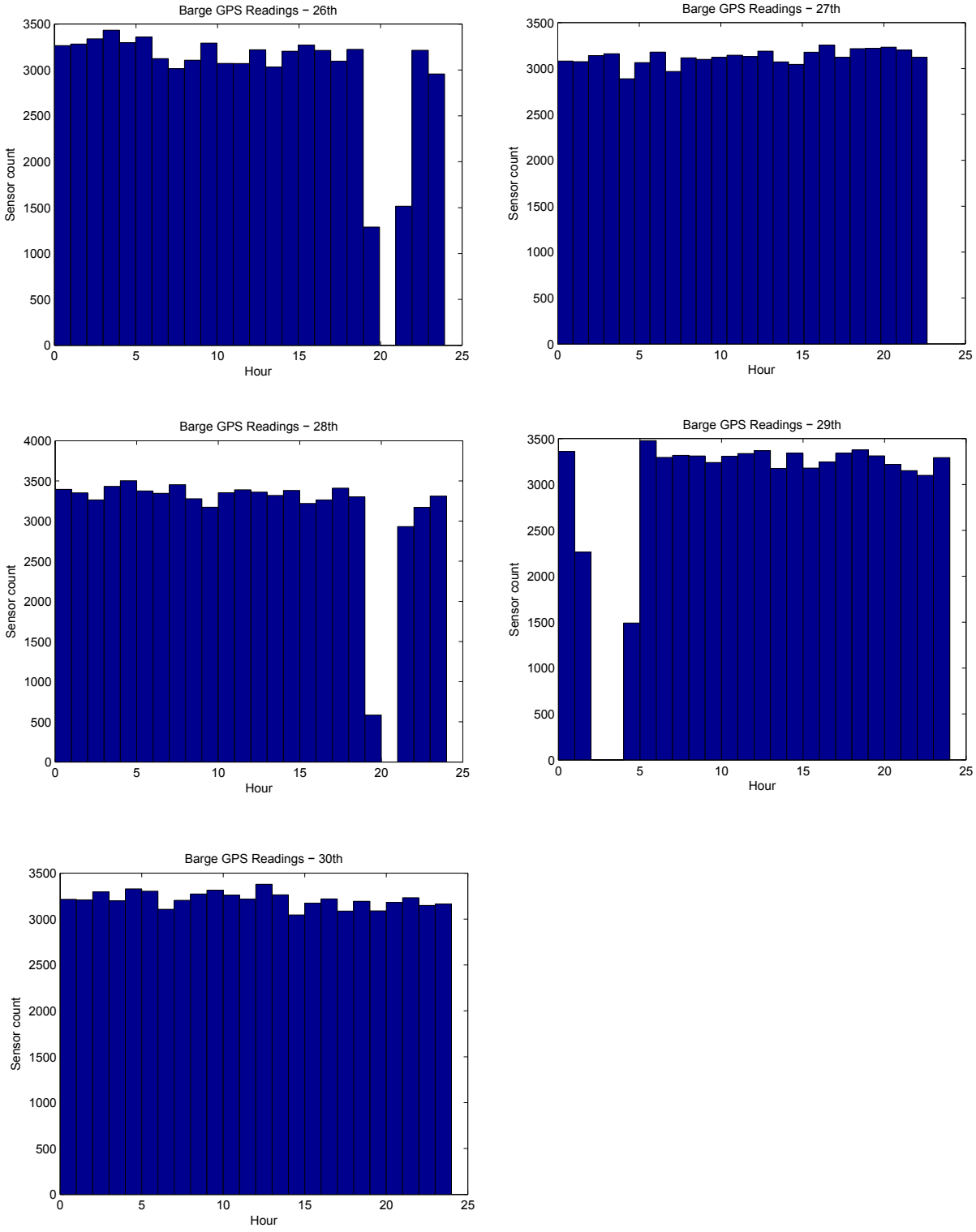

Figure 6.2.13: Histograms of Barge GPS readings

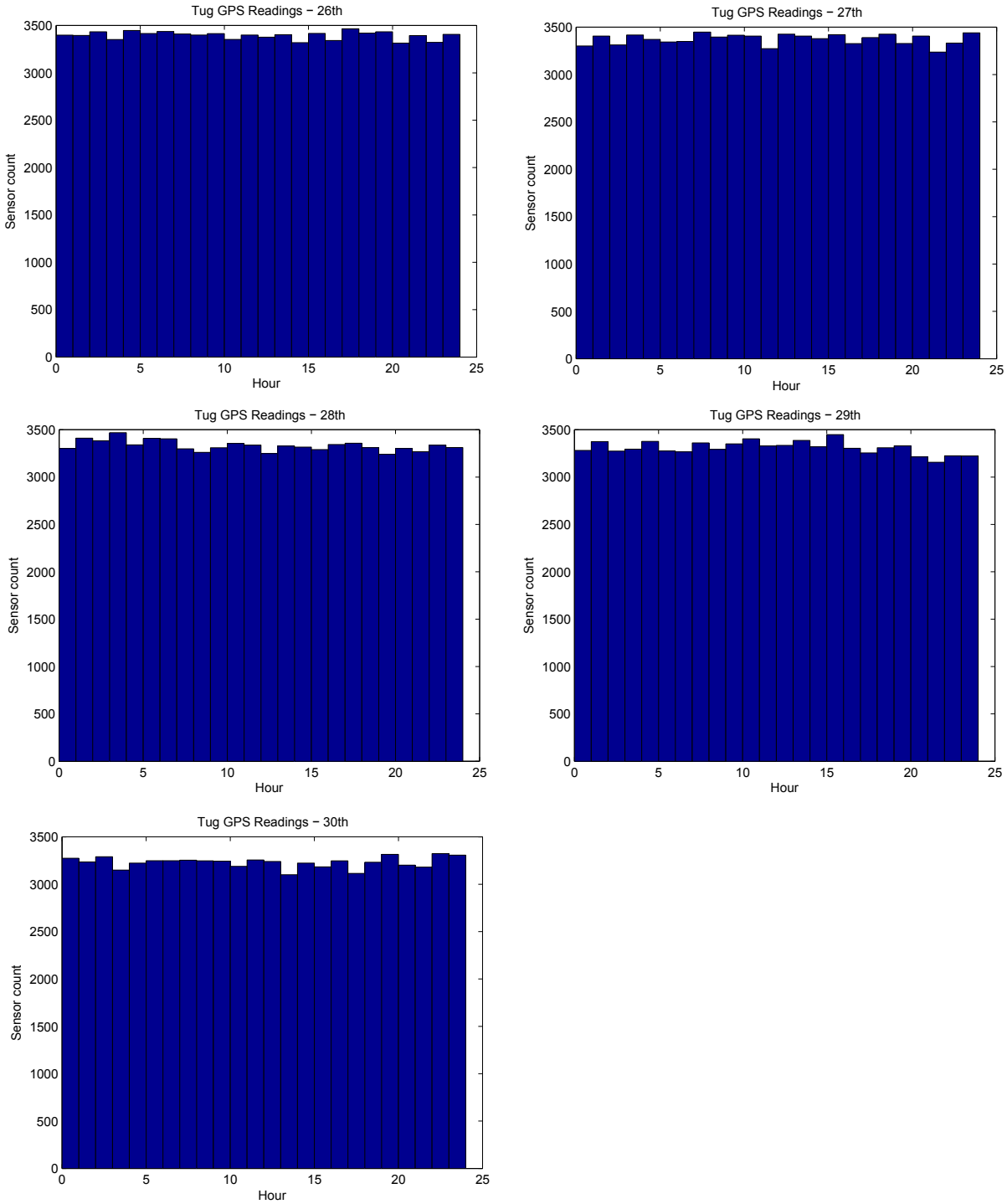

Figure 6.2.14: Histograms of Tug GPS readings

the two GPS loggers and these are noted as follows:

- On day 1 (26th), it may be seen that the tug and barge were sitting at around 600 m apart whereupon they moved alongside each other at around 1100 hours. Here they remained for a time then distance between them varies as they made their way to open sea with steady increases of the towline payout. The spike in distances noted at around 2000 hours is a data outage on the barge GPS as the towline would not be expected to be lengthened by this amount in such close proximity to the shoreline (verified by the histograms in figure 6.2.13). Valid data is assumed to be collected from 2200 hours onwards, ref figure 6.2.16)
- On day 2 (27th), a fairly benign tow is noted where the distance between the tug and barge was maintained at around 420m (note this is the distance between the GPS loggers and not the bow and stern of the barge and tug respectively). Here valid data assumed from 0000 hrs on the 27th to 2200 hrs with data dropping out at around 2240 hrs (ref figure). This too appears to be borne out by the histograms in figure 6.2.13.
- On day 3 (28th), the recorded towline shortening between 0900 and 1000 hours may be seen as well as a couple of data dropouts around 2000 hours, again captured in the histograms of barge GPS readings seen in figure 6.2.13. Examining the detail of the towline shortening event and comparing with the voyage log (reference figure 6.2.7 and the originals in section B) a limitation of the granularity of data the crew were asked to record may be observed. They have noted that towline length as at 1200 hours was 250m, whereas the actual event occurred just before 1000 hours. This failure of recording was entirely due to the request made of them by the author, in that he asked that the situation be recorded every four hours. This is discussed further in section 8 as an area for improvement should this research be built upon by others in the future. Furthermore, it should be obvious that the shortening of the towline is not an instantaneous event and this too is borne out by the data shown in figure 6.2.18 where the time taken to reel in 200m of towline was around 15 minutes between 0945 and 1000 hrs (the take up speed was not wholly linear during this period). This was not captured in the simulation data and although the shortening event could be handled by the code base developed (i.e. dynamic line lengths can be accounted for) it was not simulated as the event was outwith the scope of the study. Therefore for the purposes of valid data extracts, 0900 to 1000 hrs as well as 1900 hrs to 2200 hrs will be excluded (reference figure 6.2.19).
- During the early hours of Day 4 (29th), another GPS outage was noted, again verified by the barge GPS data count histograms, reference figure 6.2.13. For the rest of the day, however, the data and distance between the tug and barge was consistent at approximately 220m. Therefore data between 0100 hrs and 0500 hrs will be excluded (reference figure 6.2.20).

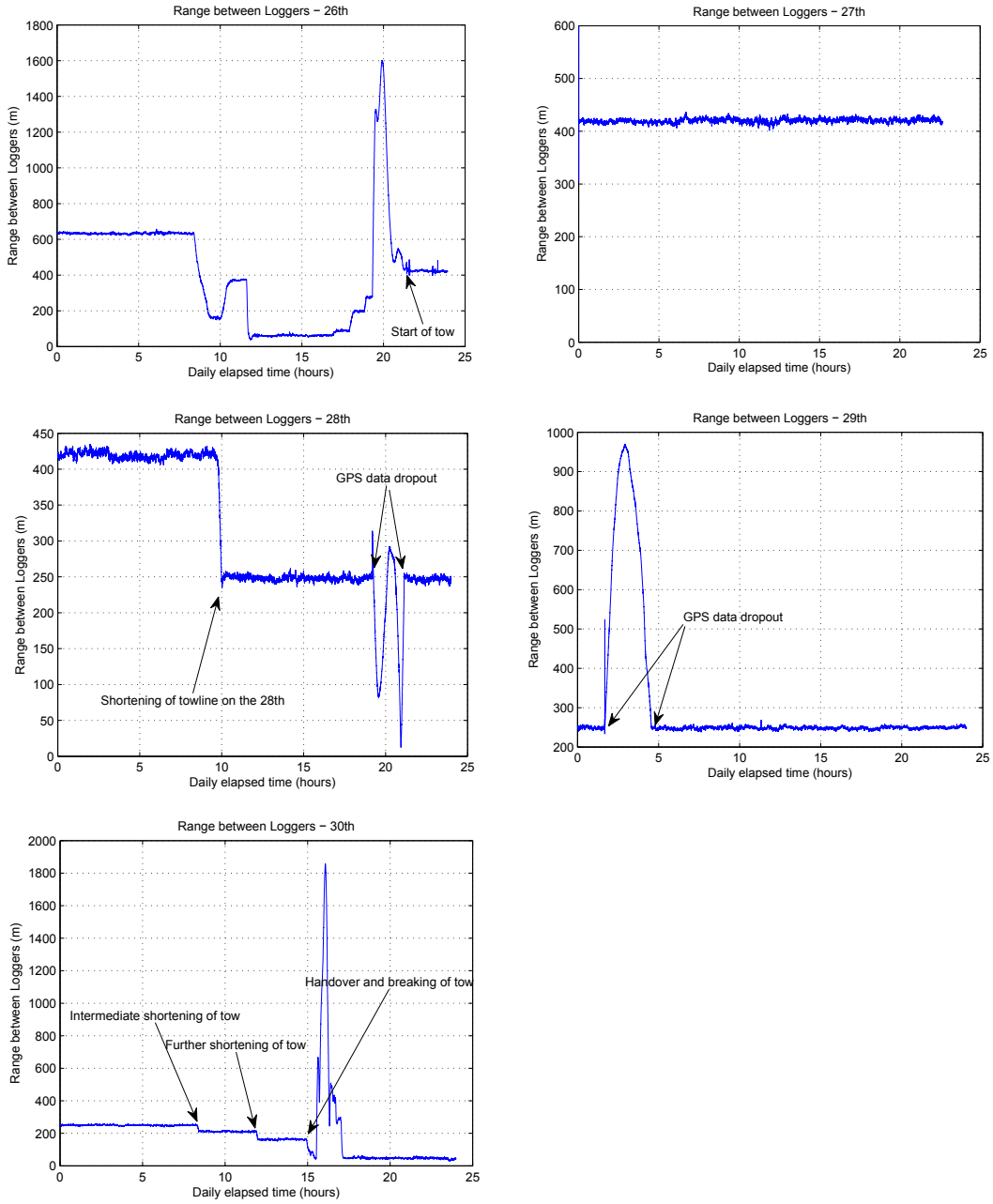

Figure 6.2.15: Range between loggers on voyage

– On the final day, Day 5 (30th), a number of phenomenon may be observed. Although the masters log shows the tow line at a consistent 250m until 1200 hrs where it is noted as shortening to 150m, the range between GPS loggers seems to register an intermittent shortening of the tow by around 40m between 0818 and 0824 hrs (reference figure 6.2.21). Thereafter a second shortening of the tow by around 50m occurs between 1154 and 1200 hrs (ref figure 6.2.22). This then remains the case until the final shortening up, at around 1500 hrs prior to breaking the tow and handing over to harbour tugs (reference figure 6.2.23). The effect of the intermediate shortening of the towline will be reviewed in the post processing later. The valid data set for this final day will be taken as between 0000 hrs and 1500 hrs.

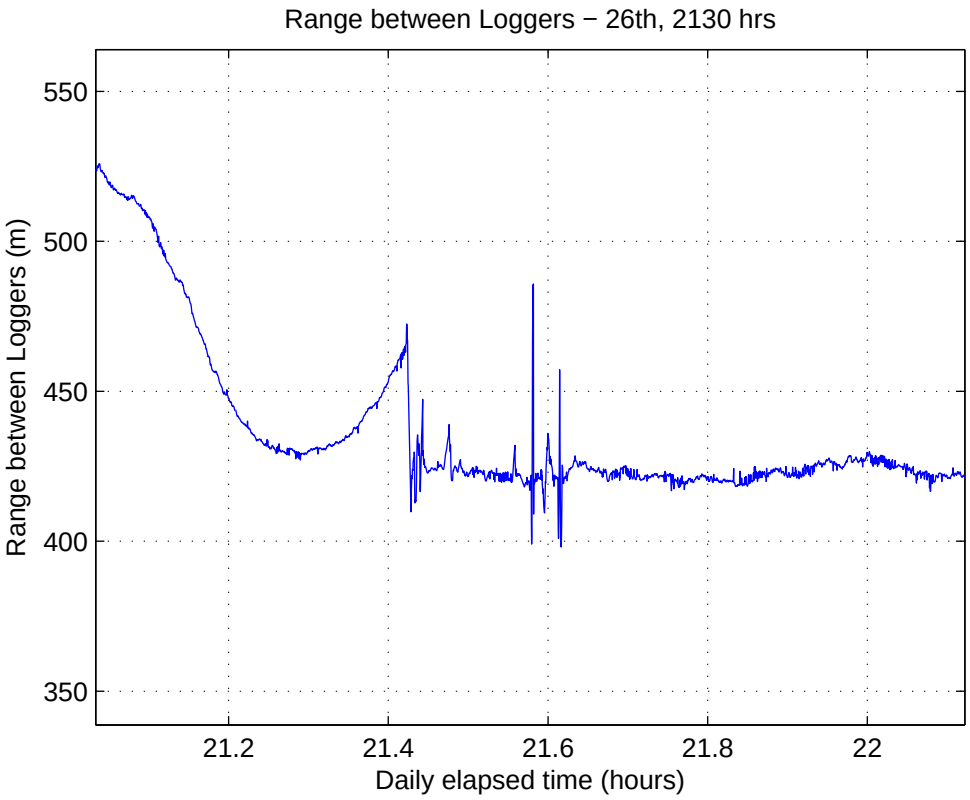

Figure 6.2.16: Detail of tug and barge GPS pitch at 2130 hours on the 26th

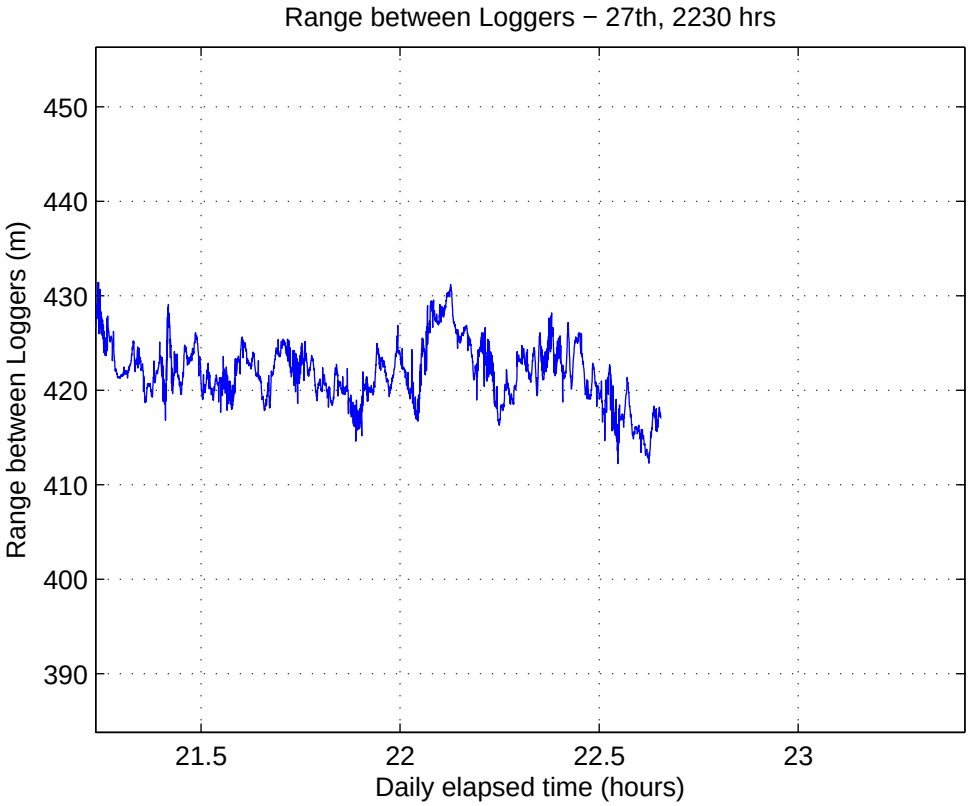

Figure 6.2.17: Detail of tug and barge GPS pitch at 2230 hours on the 27th

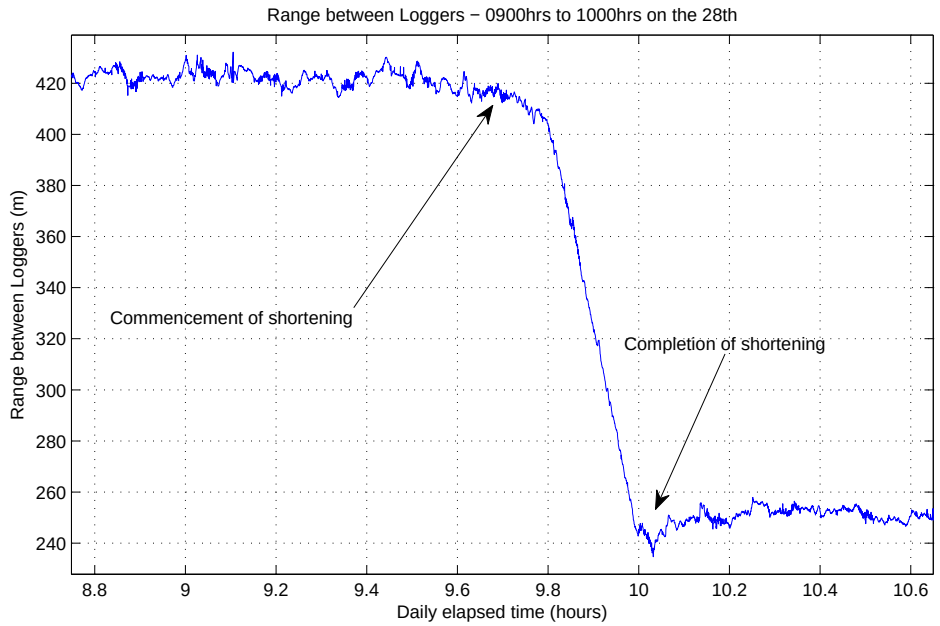

Figure 6.2.18: Detail of range between loggers on tug and barge during shortening of towline on day 3

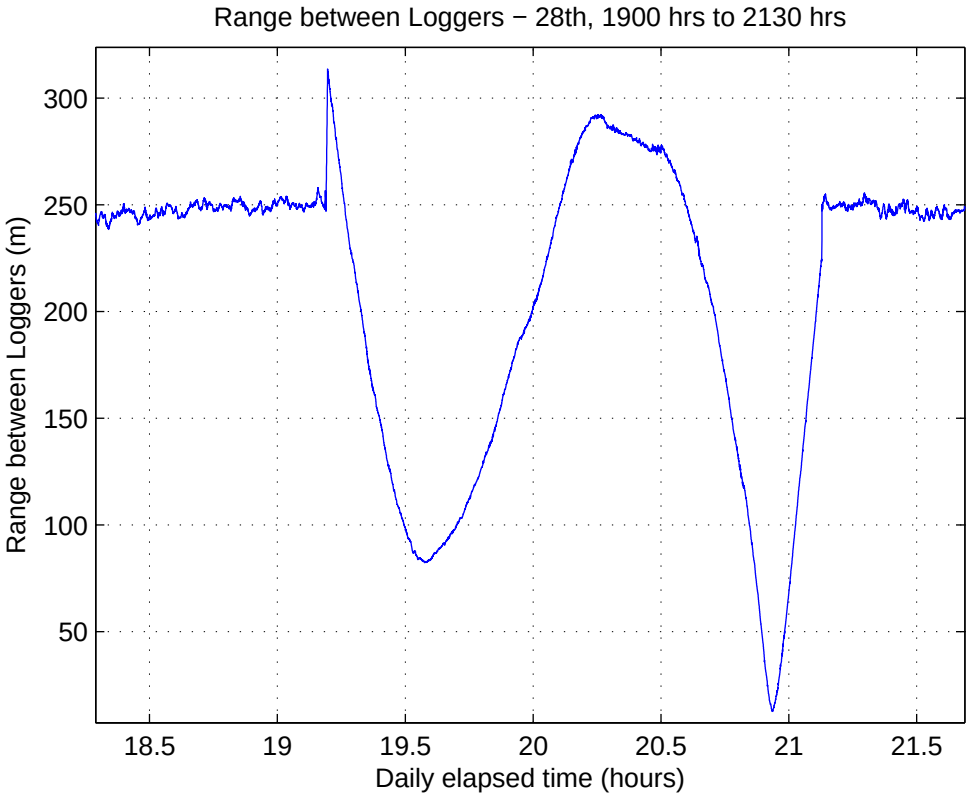

Figure 6.2.19: Detail of range between loggers on tug and barge around 2000 hrs on the 28th

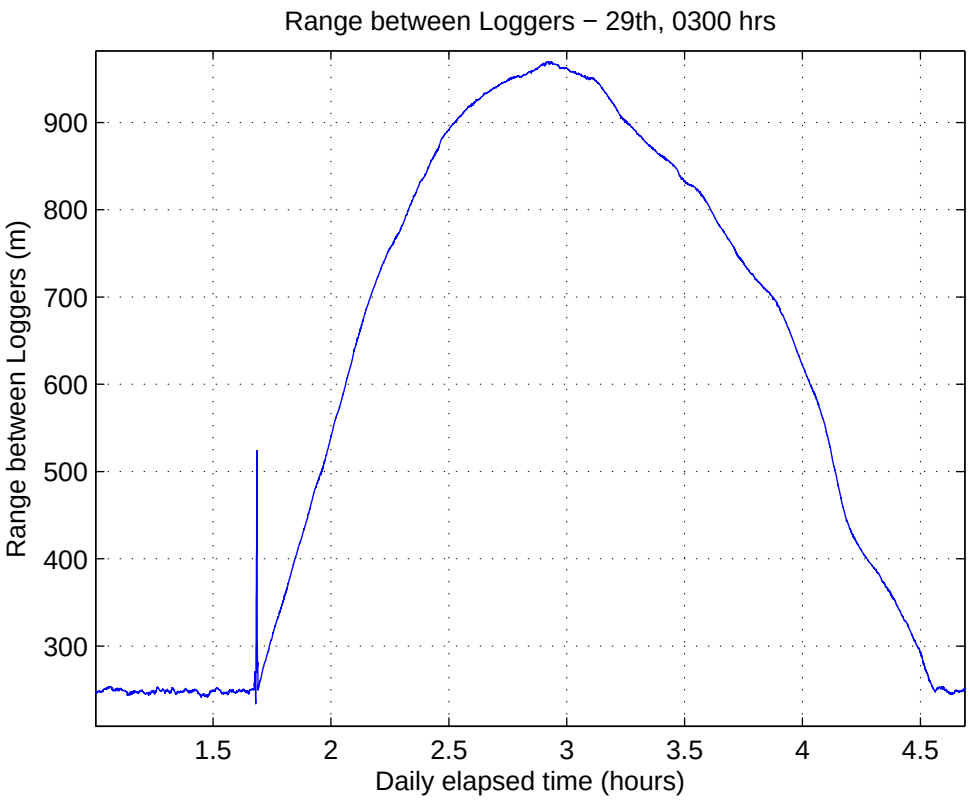

Figure 6.2.20: Detail of range between loggers on tug and barge around 0300 hrs on the 29th

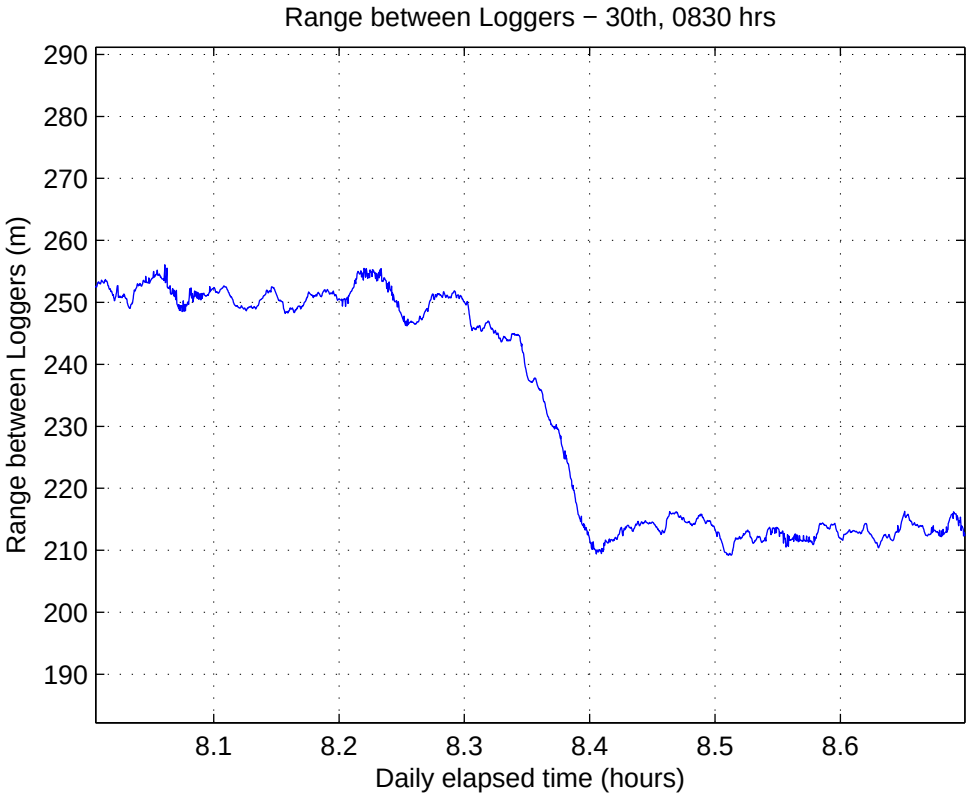

Figure 6.2.21: Detail of range between loggers on tug and barge around 0830 hrs on the 30th

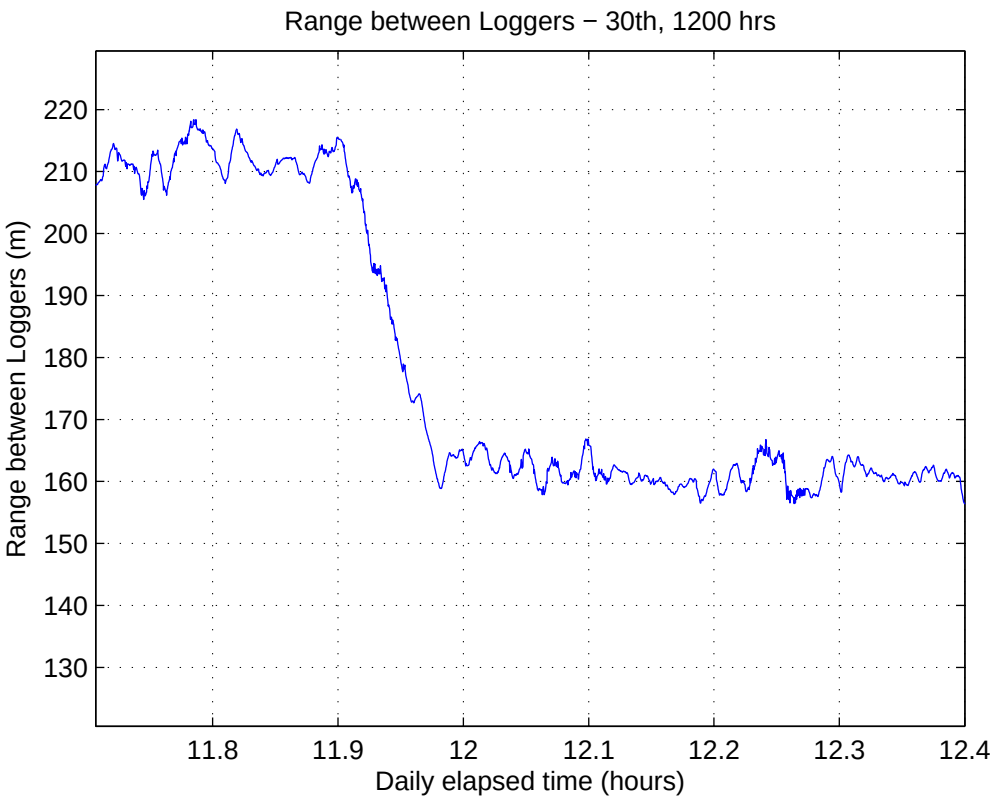

Figure 6.2.22: Detail of range between loggers on tug and barge around 1200 hrs on the 30th

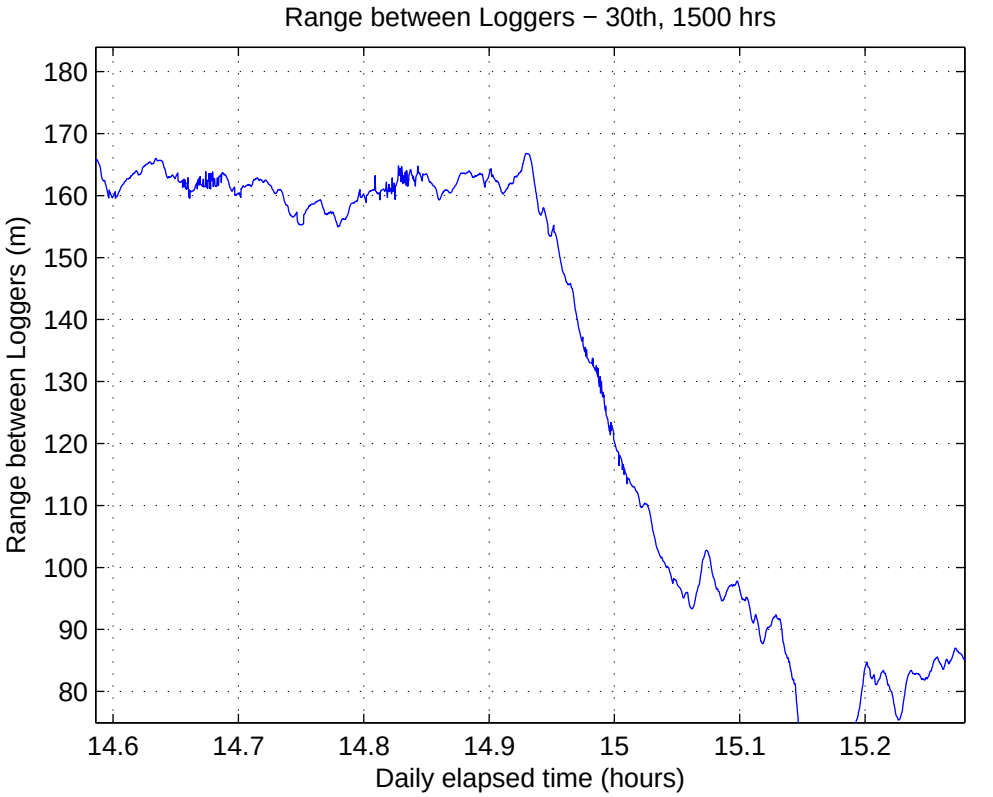

Figure 6.2.23: Detail of range between loggers on tug and barge around 1500 hrs on the 30th

If a summary of this data is looked at and comparing the key events along the towage timeline several points where the record logs do not tie in with what the GPS data appears to be telling us on the averaged readings may be seen. Furthermore if the GPS range is adjusted by the logger offsets from the towline offsets as recorded in tables 6.2.4 and 6.2.6 and adjust the deployed towline length by the offset of the winch from the aft roller (23.15m fwd) and add the length of the bridle, shackles, triplate and pennant (28.4m) a rough comparison between the GPS range and deployed towline catenary length as show in table 6.2.8 is obtained. It may also be seen that there are some issues with the apparent changes in the reported catenary sag which has a significant effect on the simulated tensions. This will be discussed in detail later in section 6.3.

The pitch between readings in the barge and tug GPS data was looked at for a more granular assessment of missing data. The files for each day were analysed and the number of instances where there were readings on consecutive seconds, i.e. the pitch between readings was one second, every two seconds and where there was three seconds or more between the readings was recorded. Tables 6.2.9 and 6.2.10 show the results of this data quality assessment. It is interesting to note that as the tow progressed north the quality of the GPS data degraded with greater frequency of large spaces between readings occurring (defined as gaps of 3 seconds or more).

In addition to the data dropouts, issues were found on the tilt sensors readings for the tug logger. Spurious long term variations in the output were noticed and these may be seen when comparing the raw output for the 26th for both the tug and barge loggers in figure 6.2.24. The reason for this variance was not determined and is peculiar to the tug logger on this voyage. To obtain useful data that would not corrupt the Kalman filter process, this output was adjusted on the assumption that the mean roll and trim recorded at the outset was likely to continue to represent the mean roll and trim angle. Therefore the rolling average over a window length of 100 samples was adjusted to represent this starting mean. This would cause some local issues where the boundary of the rolling average window spanned a point in the data where the was this step change but the Kalman filter is designed specifically to handle these large but very localised spurious data points. An example of the effect of this data modification may be seen in figure 6.2.25.

6.3 Lumped Mass Simulations

The simulations were run using the same towline properties and bridle setup as shown in table 5.4.2 with the exception that the simulated towline lengths deployed were adjusted based on the following observation:

- With reference to the comparison between towlines lengths recorded and GPS ranges logged

Table 6.2.8: Summary of GPS range data

Event	Day	Date	Hour	Recorded Towline deployed (m)	GPS Range (m)	(a) Towline/bridle over tug stern deployed (m)	(b) Adjusted Range (m)	(a-b) Difference (m)	% Difference
Tow commence	1	26th	2130	450	425	455.25	392.65	62.60	14%
Commence tow shortening up	3	28th	0945	450	425	455.25	392.65	62.60	14%
Complete tow shortening up	3	28th	1000	250	255	255.25	222.65	32.60	13%
Commence tow shortening up	5	30th	0818	250	255	255.25	222.65	32.60	13%
Complete tow shortening up	5	30th	0824	250	210	255.25	177.65	77.60	30%
Commence tow shortening up	5	30th	1154	250	210	255.25	177.65	77.60	30%
Complete tow shortening up	5	30th	1200	150	160	155.25	127.65	27.60	18%
Final shortening for disconnection	5	30th	1456	150	160	155.25	127.65	27.60	18%

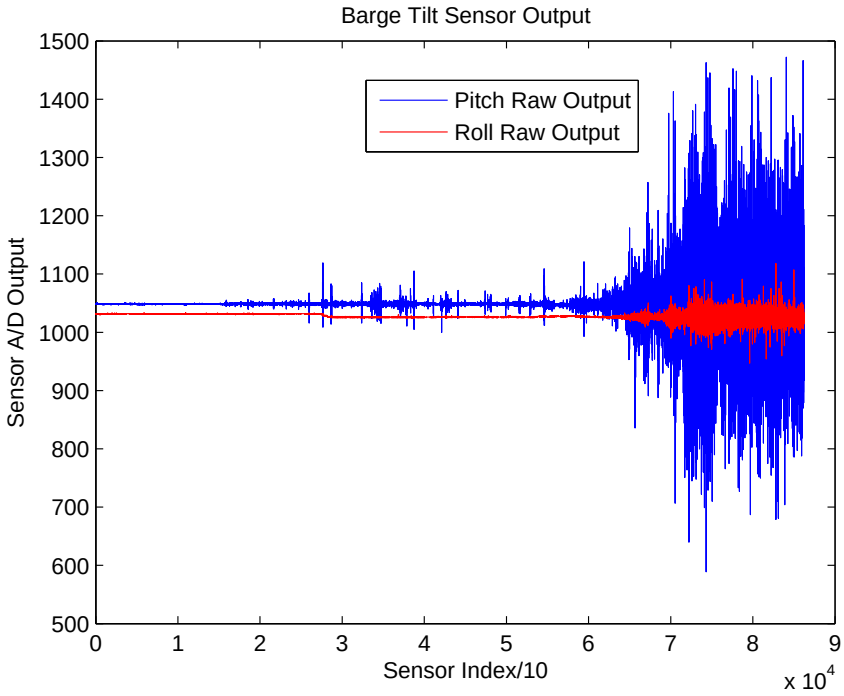

(a) Barge tilt sensor data for 26th

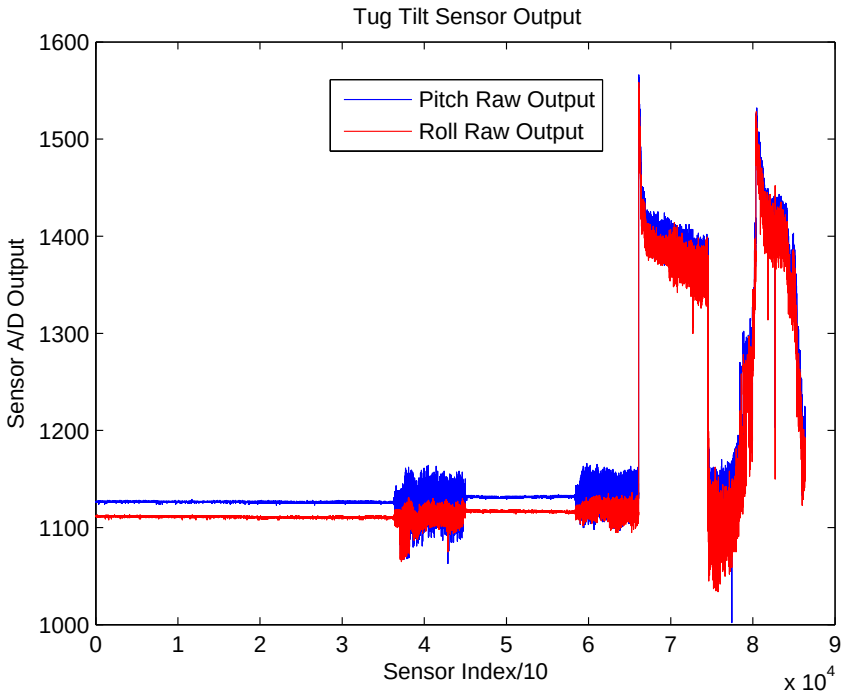

(b) Tug tilt sensor data for 26th

Figure 6.2.24: Tug and barge tilt sensor raw output

Table 6.2.9: Pitch in seconds between GPS readings for the tug logger

Day	1 sec	2 sec	≧3 sec	Total	1 sec as % of total	2 sec as % of total	3 sec as % of total
1	76568	4845	52	81465	93.99%	5.95%	0.06%
2	75583	5307	71	80961	93.36%	6.56%	0.09%
3	73688	6028	222	79938	92.18%	7.54%	0.28%
4	73158	5770	462	79390	92.15%	7.27%	0.58%
5	71844	5186	504	77534	92.66%	6.69%	0.65%

Table 6.2.10: Pitch in seconds between GPS readings for the barge logger

Day	1 sec	2 sec	≧3 sec	Total	1 sec as % of total	2 sec as % of total	3 sec as % of total
1	61651	8162	76	69889	88.21%	11.68%	0.11%
2	68544	6442	39	75025	91.36%	8.59%	0.05%
3	67850	5584	130	73564	92.23%	7.59%	0.18%
4	63695	5463	342	69500	91.65%	7.86%	0.49%
5	70351	6280	480	77111	91.23%	8.14%	0.62%

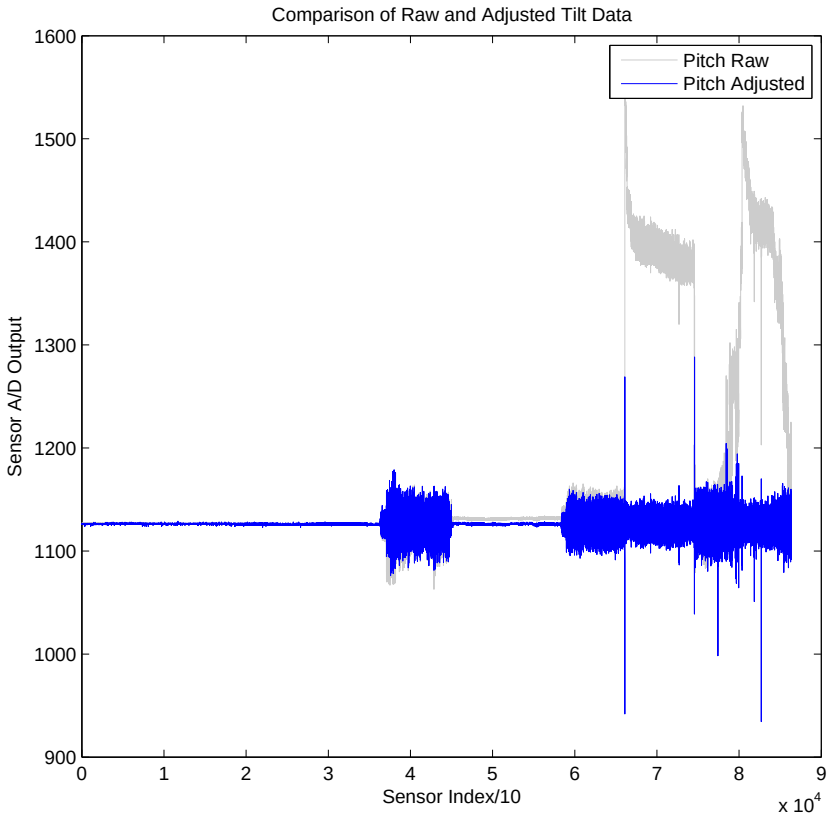

Figure 6.2.25: Example of adjusted tug pitch tilt sensor output

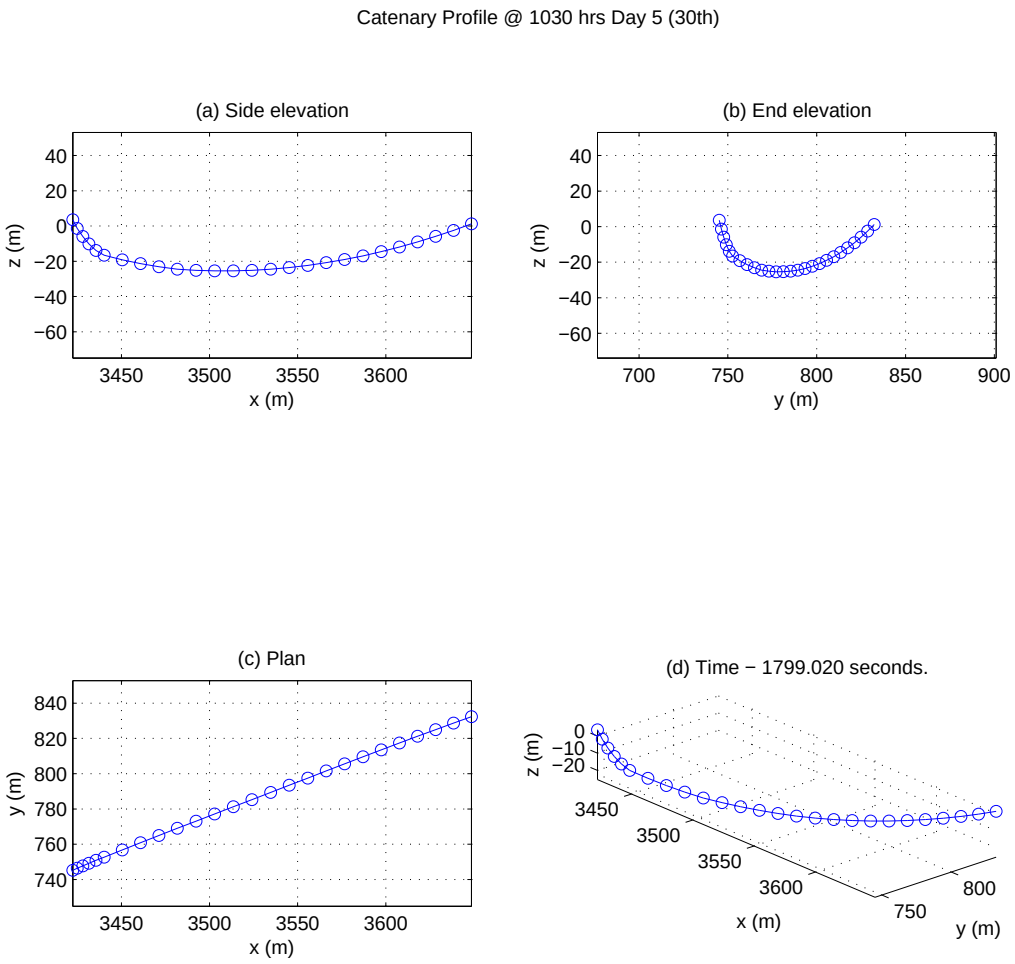

Figure 6.3.1: Example plot of towline shape under forward speed for 255.25m towline and bridle length ~1030 hrs 30th August

detailed in table 6.2.8 there is an issue with the towline lengths recorded in the crew log between 0818 hours on the 30th August and 1100 hours the same day. The recorded towline paid out between connection points is noted as unchanged in the crew log but the GPS recording show that there was an intermediate shortening, closing the distance by around 45m. The simulations will account for this with a notional reduction of towline paid out over this period by 40m to bring the % difference between GPS range and towline deployed in line with the other simulations. Runs carried out with this original length bore this assumption out in that the towline was simply far too slack, see sample extract plots, mid-simulation shown in figure 6.3.1.

With regards to table 6.3.1 please consider the following guidance notes when studying this table and bear in mind in any future references to hours of data run:

– The first hour of the day is noted as hour 0 (i.e. representing the hour starting at 0000 hours and

ending at 0059 hours).

- The last hour of the day is noted as hour 23 (i.e. representing the hour starting at 2300 hours and ending at 2359 hours).
- The start and end hours noted below are inclusive of the hour mentioned (i.e. start hour of 1 and end hour of 5 refers to simulations running in one hour blocks between 0100 hours and 0559 hours).
- Day 1 represents, as before, data gathered on the 26th of August (towage commencement date from Portsmouth) with day 5 representing data gathered on the 30th of August (towage arrival date at Rosyth).
- Towline length is the length of the towline as recorded in the voyage logs (subject to modification noted below).
- Towline deployed length is the noted length minus 23.15m representing the distance between the towage winch and the aft deck of the tug (simulation connection point on tug, see figure 6.2.12).
- GPS range is the approximate, adjusted GPS range between connection points as reported in table 6.2.8.
- Delta towline/range is the difference between the GPS adjusted range and the towline deployed, where a positive value represents the spare line length that contributes to the sag in the catenary shape.

6.3.1 Attitude Data Quality

A major factor in creating stable INS systems is the quality of the sensors employed. Reviewing some randomly selected, sample plots extracted from the tow for tug and barge loggers, figures 6.3.2 through 6.3.6, clearly show several things:

1. The ability of the Kalman filter to reduce the noise in the roll and pitch readings.
2. The lack of any major events on the voyage.
3. The ability of the filter to smooth out the heading readings from the GPS sensor by supplementing the data with the yaw gyroscope readings.
4. The fact that the tug motions were, marginally, more pronounced that the barge motions.
5. The ability to extract, from noisy data, both high and low frequency features of the response.

Table 6.3.1: Simulated towline lengths

Day	Start hour	End hour	Simulated Towline Length (m)	Towline deployed (m)	* GPS Range (m)	Delta towline/range
1	22	23	450	426.85	392.65	34.20
2	0	23	450	426.85	392.65	34.20
3	0	8	450	426.85	392.65	34.20
3	9	23	250	226.85	222.65	4.20
4	0	23	250	226.85	222.65	4.20
5	0	7	250	226.85	222.65	4.20
5	8	10	*210	186.85	177.65	9.20
5	11	13	*190	166.85	127.65	39.20

Examples in 6.3.2 show the removal of spikes in the sensor data and detail in figure 6.3.6 show the smoothing effect the filter has on the yaw readings. While adequate as a proof of concept, the sensor data quality could be much improved and further comment will be made on this in chapter 8 later.

6.3.2 Position Data Quality

The combination of GPS data with data from the accelerometers produced varying results. On a macro scale the differences in data are often hard to detect (figure 6.3.7 is typical) where the tug and barge track overlay each other closely (in the case of steady towage in a straight line). In others where weather conditions or maneuvering cause the mean paths to diverge (such as in figures 6.3.8 and 6.3.9) the differences in the raw GPS tracks and the filtered positions are more evident.

There were occasions where the supplemental data from the filter captured detail at a resolution that the GPS readings alone would miss such as the example in figure 6.3.10.

There were also situations where the filter struggled with either rapid maneuvers or highly anomalous data from the accelerometers and examples of this may be seen in figures 6.3.11 and 6.3.12 respectively.

The accelerometer data (see figure 6.3.13 for a typical example) was of relatively low quality yet despite this, the filter managed to combine these with the GPS readings to a surprising degree. Suggestions for future work and how this could be significantly improved are made in chapter 8 later.

It should be noted that as the Kalman filter reports the position and attitude at a frequency of 1 Hz, derived from 10 Hz sensor data, and this is subsequently upsampled for input into the numerical cable simulation, further filtering will be effected by this process.

There are a number of other conventional filters which could have been employed which would have removed some of the higher frequency readings, but other than the high level tests carried out and noted in section 6.3.9 later, these were deliberately avoided so as to understand better the capabilities offered by the Kalman filter and have a true understanding of the limitations of the sensors employed so as to better guide subsequent work.

6.3.3 Summary of Lumped Mass Results - Day 1

The first day of the towage was short and only one hour of useable data was gathered and this is shown in figure 6.3.14. The average range between the towline end points was circa 405m against a deployed towline and bridle length of 455.25m. The reported average tension in the towline at the tug end was 85.3kN which was well below the reported tension of 20Te to 30Te. Referring to the catenary plot in figure 6.3.15 taken from around 2330 hours it is obvious that the line is excessively slack.

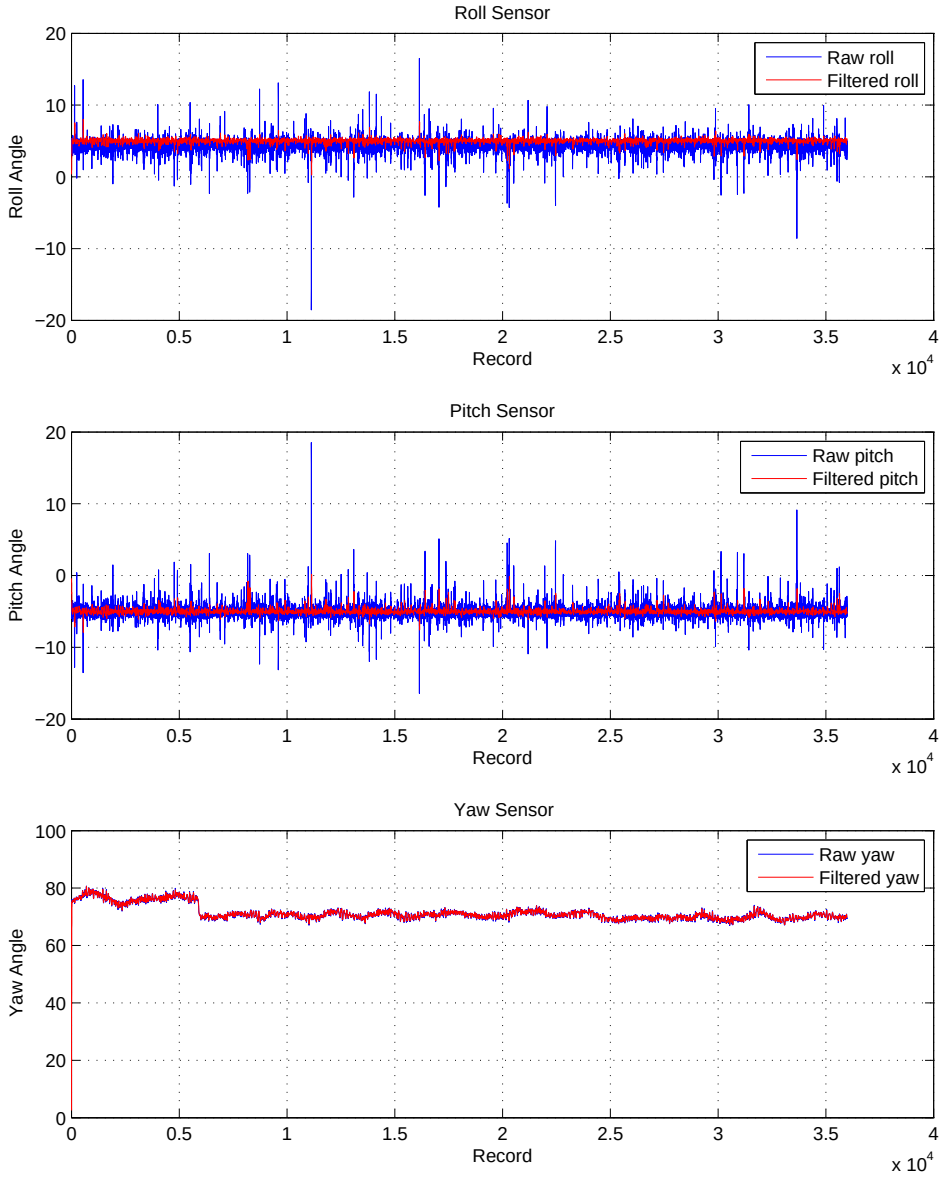

Figure 6.3.2: Barge sensor output for 0300 hours on day 2

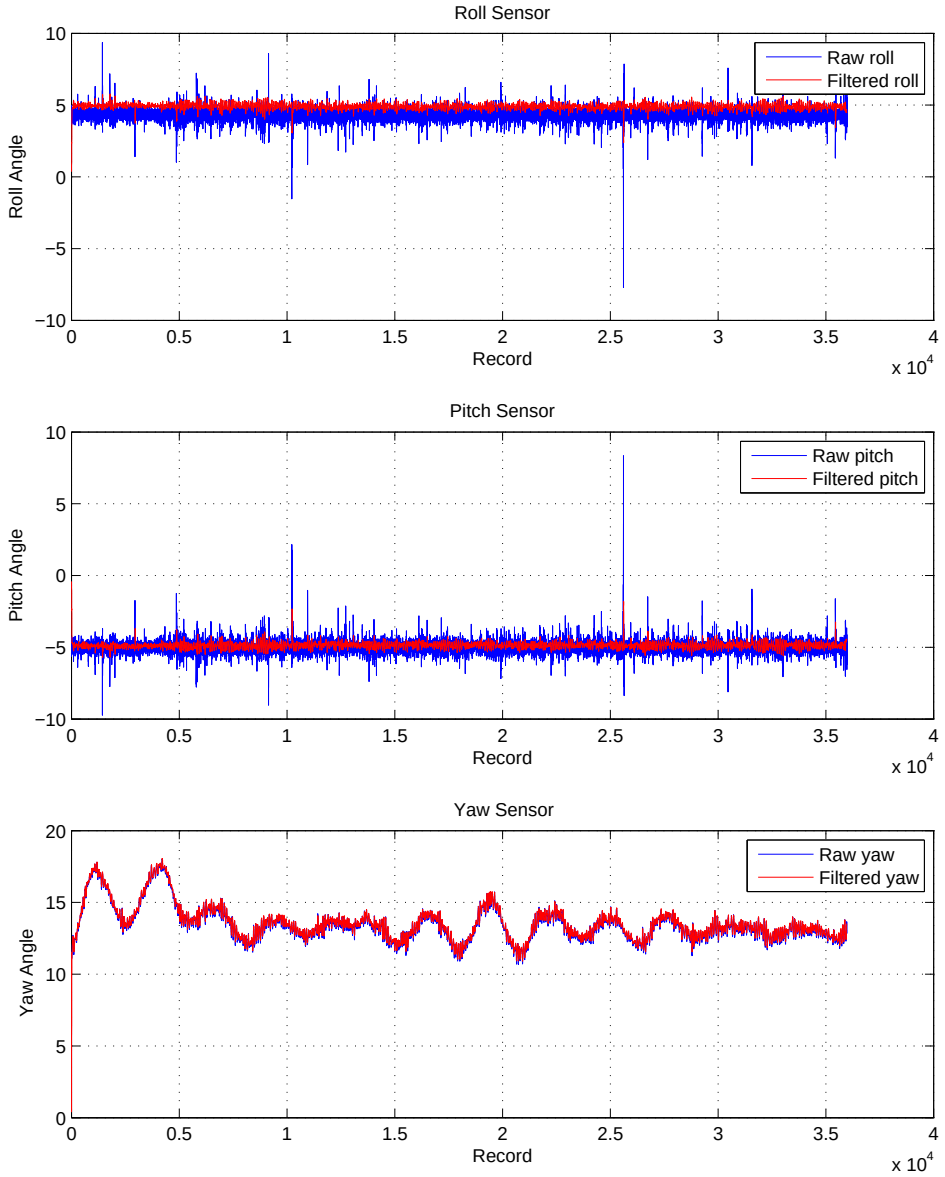

Figure 6.3.3: Barge sensor output for 1000 hours on day 2

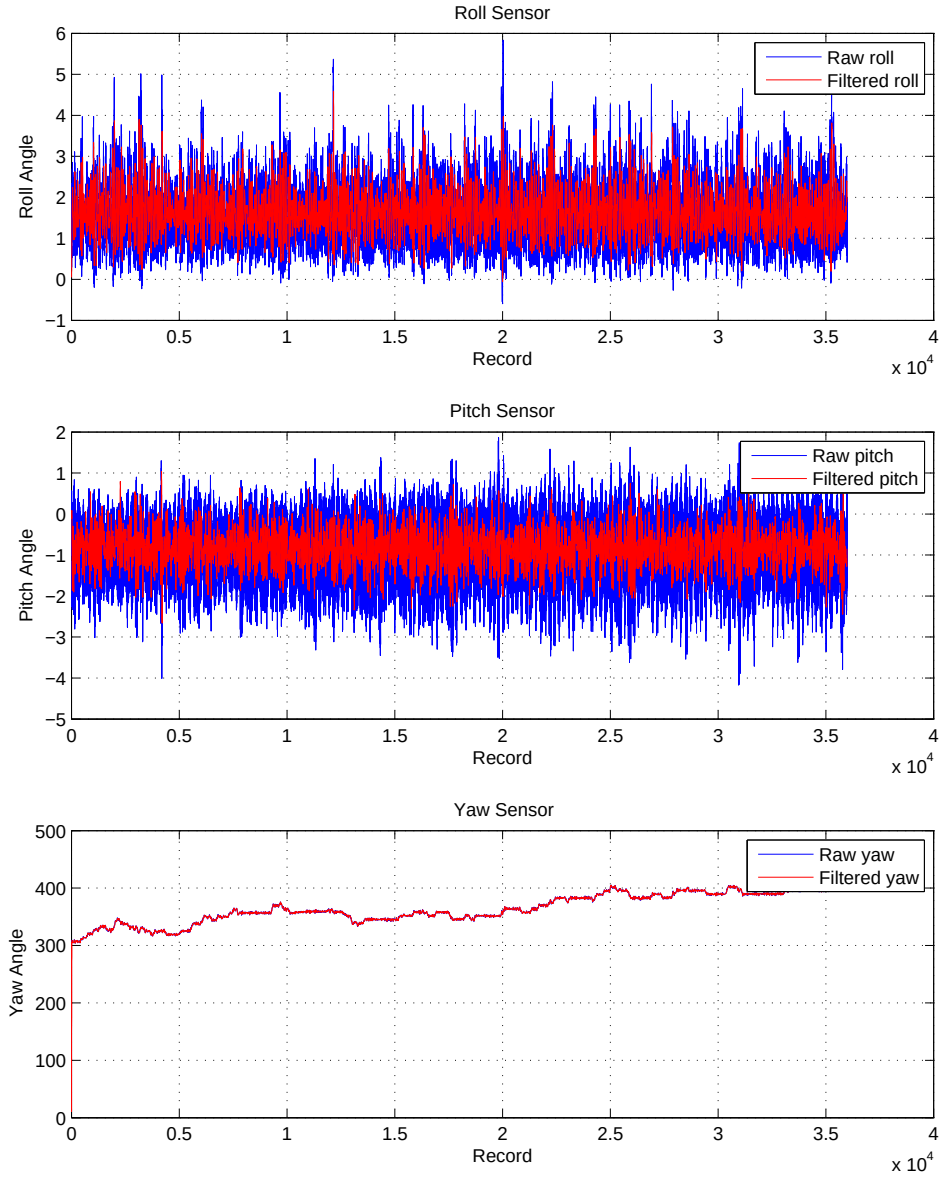

Figure 6.3.4: Tug sensor output for 0800 hours on day 3

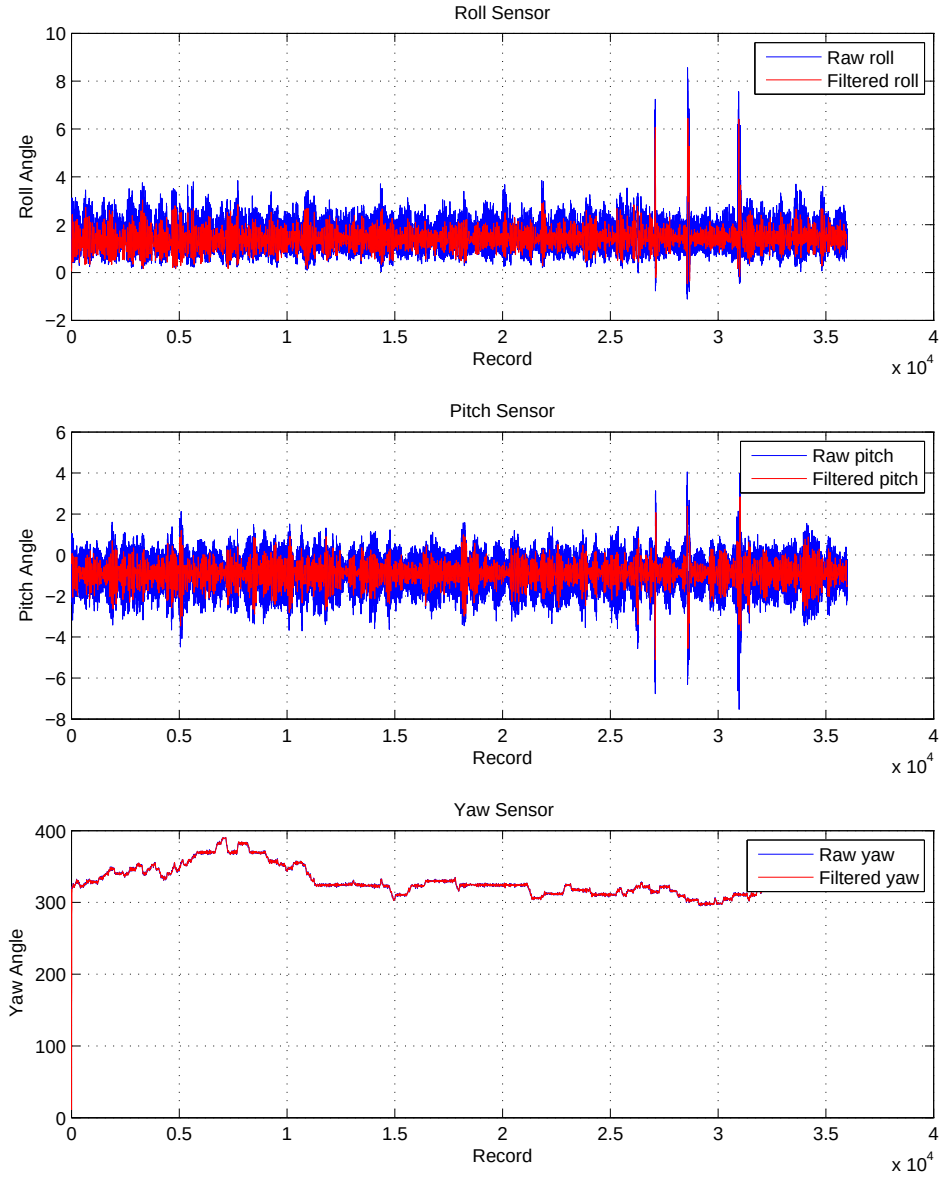

Figure 6.3.5: Tug sensor output for 1300 hours on day 4

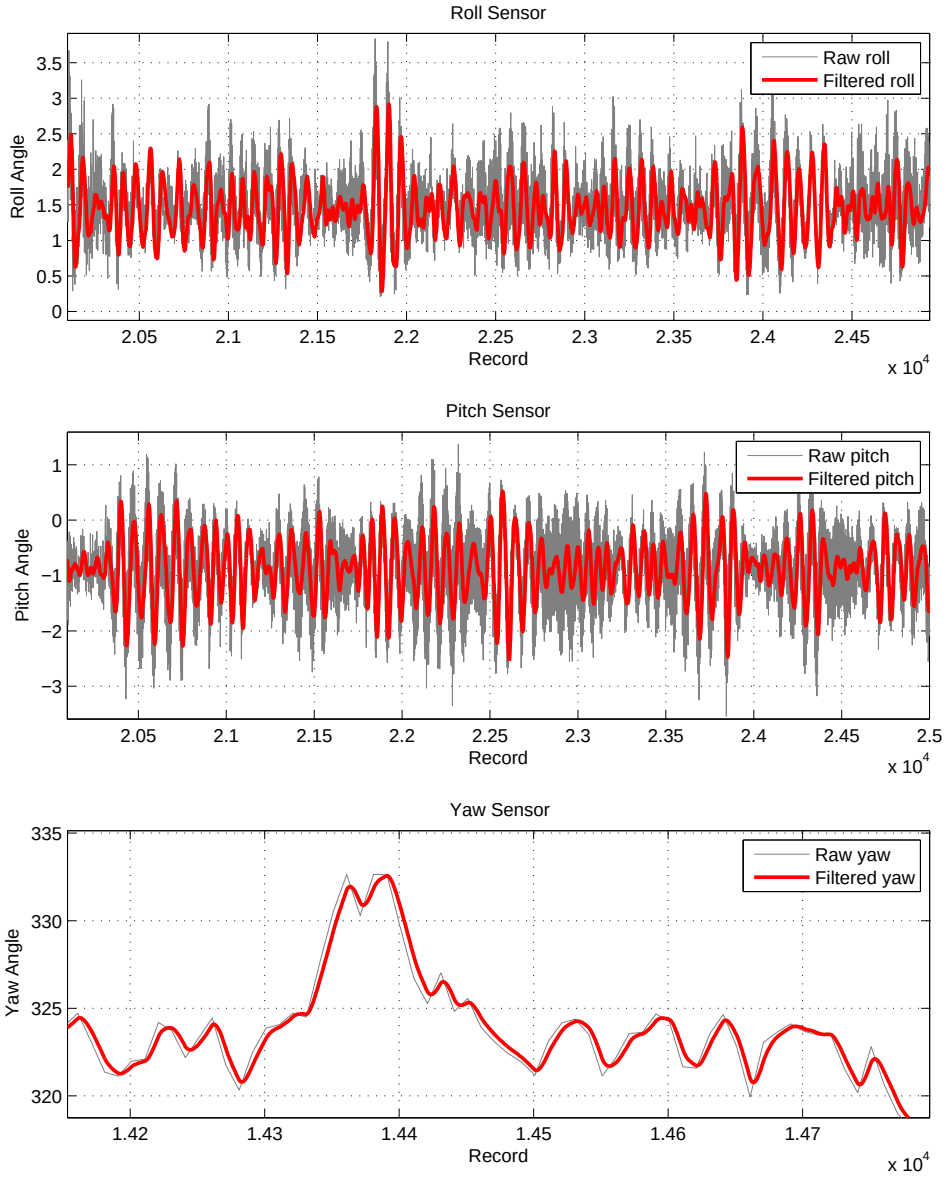

Figure 6.3.6: Detail on tug sensor output for 1300 hours on day 4

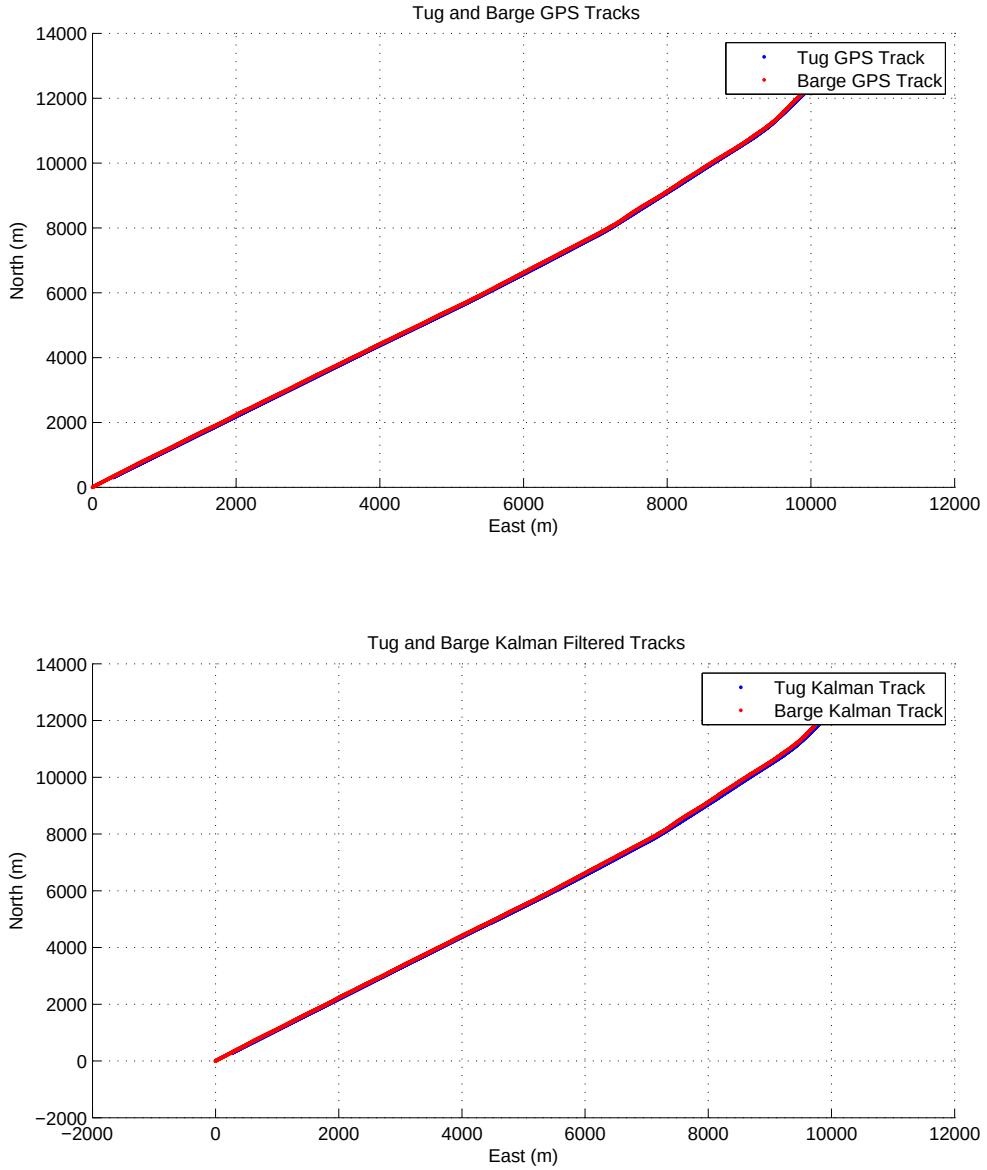

Figure 6.3.7: GPS/Filtered Position Estimates for 1700 hours on day 2

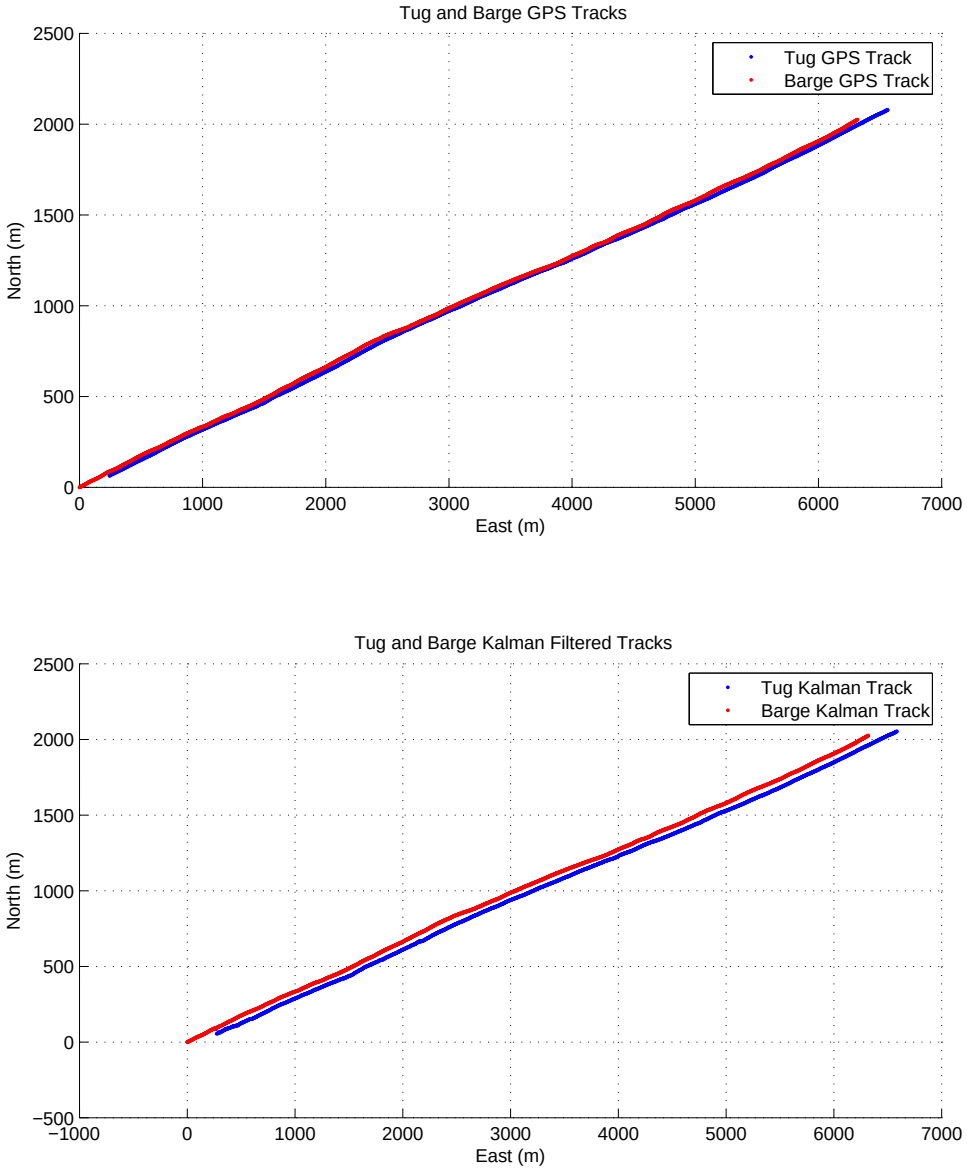

Figure 6.3.8: Barge steady drift from mean towing path, 0500, day 5

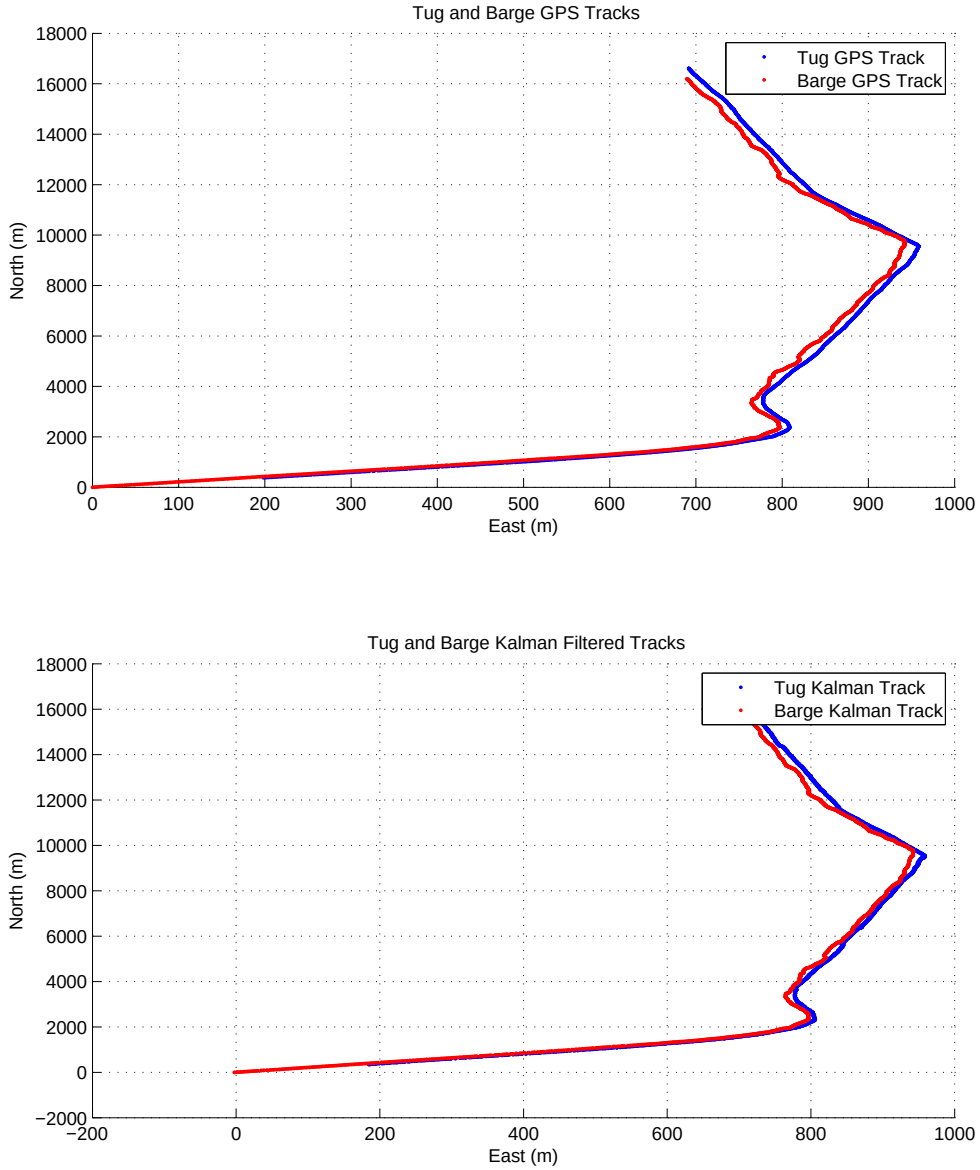

Figure 6.3.9: Barge drift from mean towing path due to maneuvering, 1800 hours, day 2

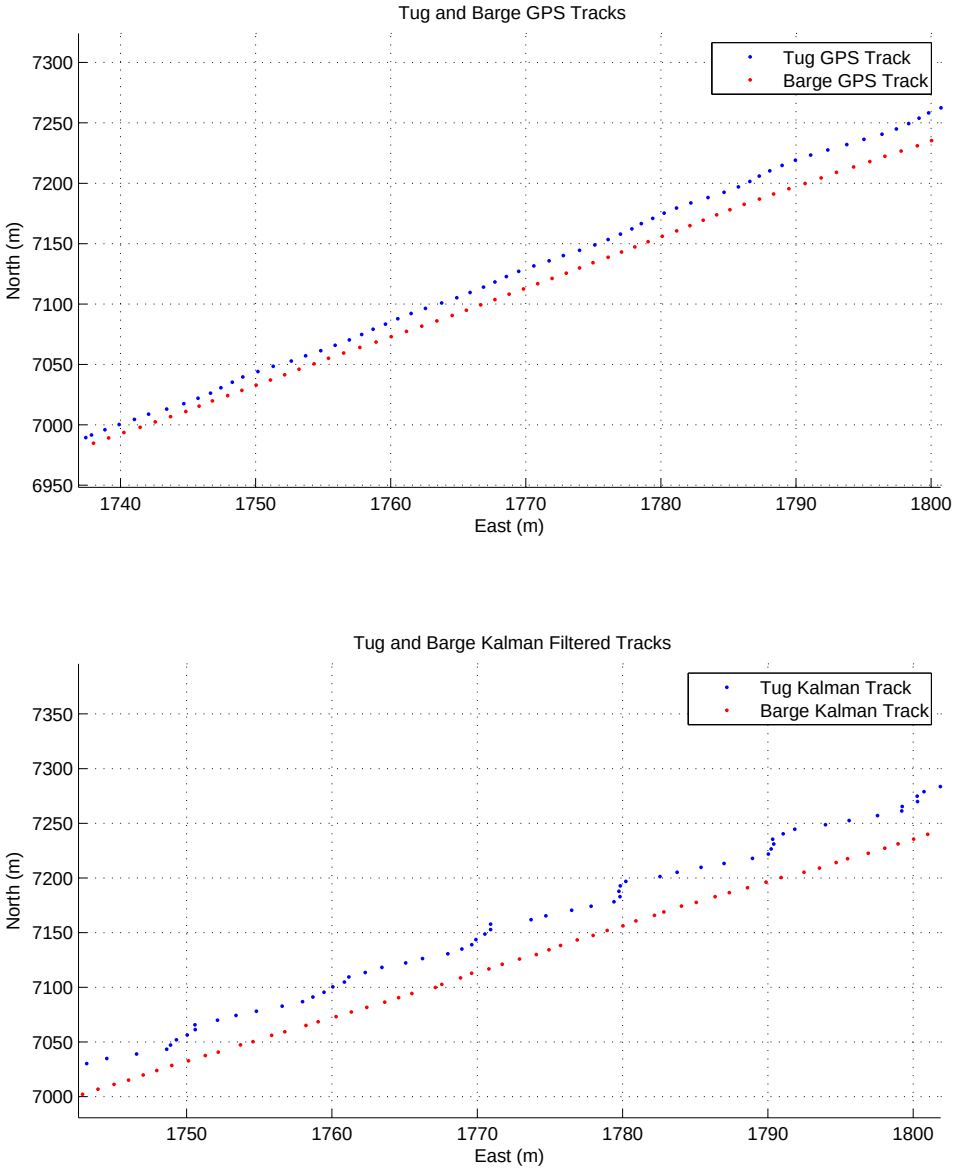

Figure 6.3.10: Tug and barge position detail increased by Kalman filter, 1000 hours, day 2

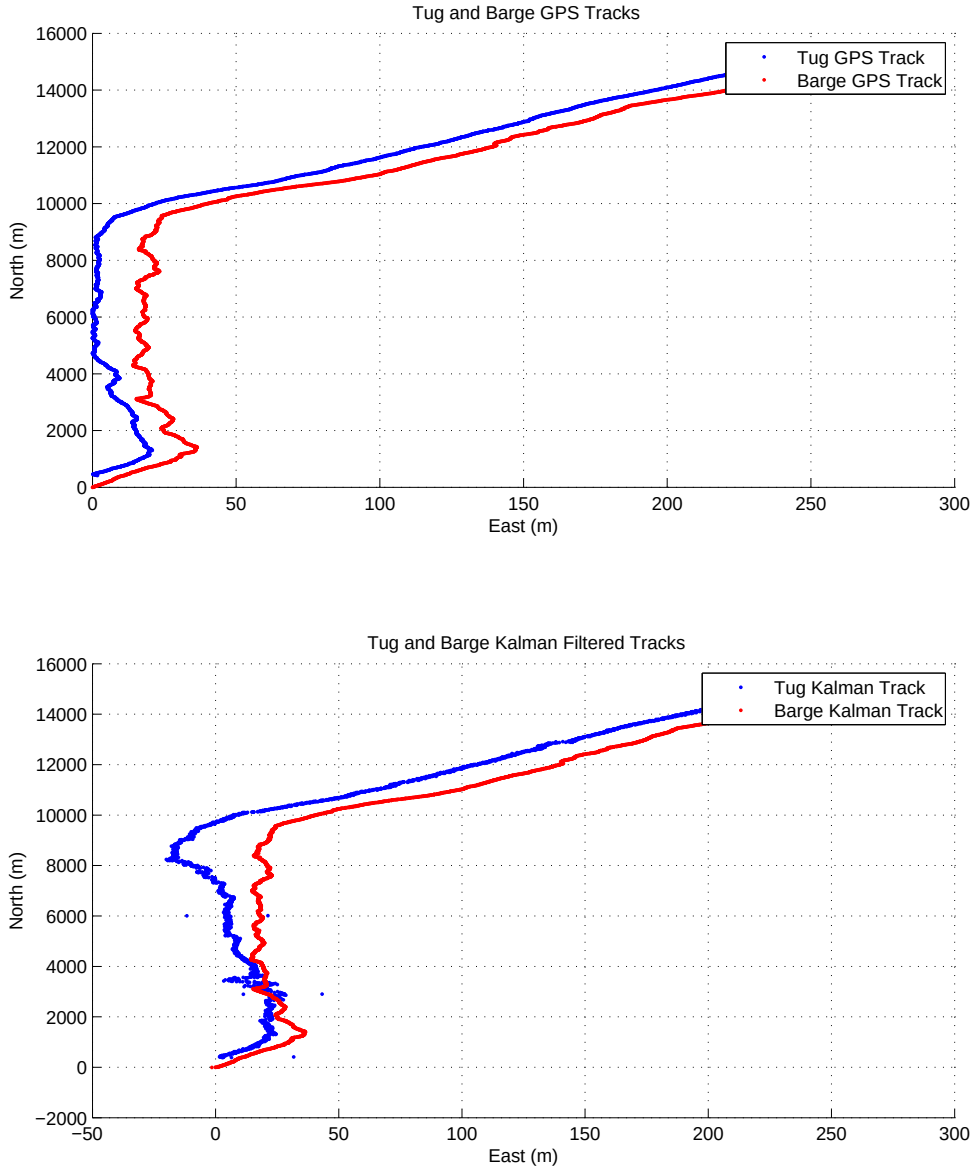

Figure 6.3.11: Example where filter struggles with high maneuvers, 1900 hours, day 2

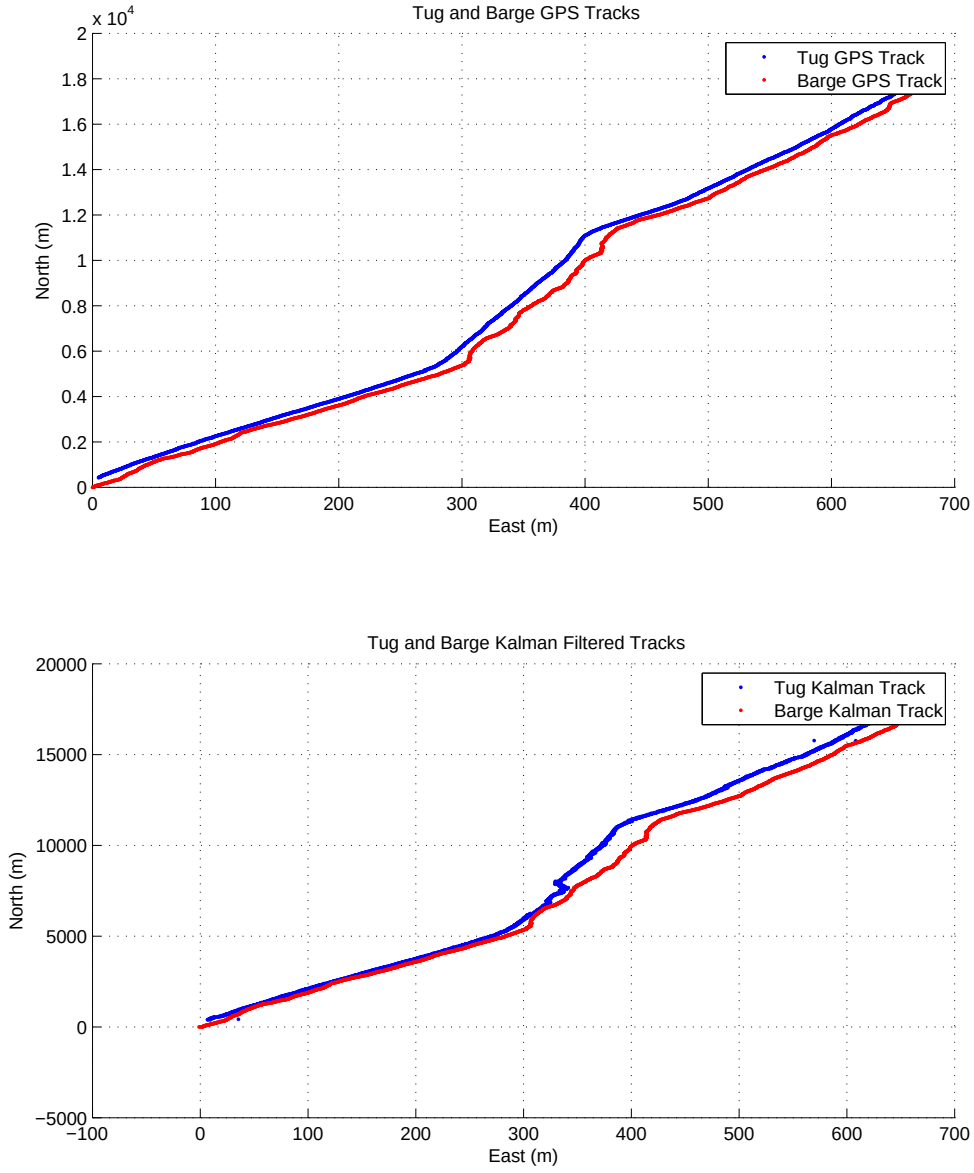

Figure 6.3.12: Example where filter struggles with highly anomalous data points

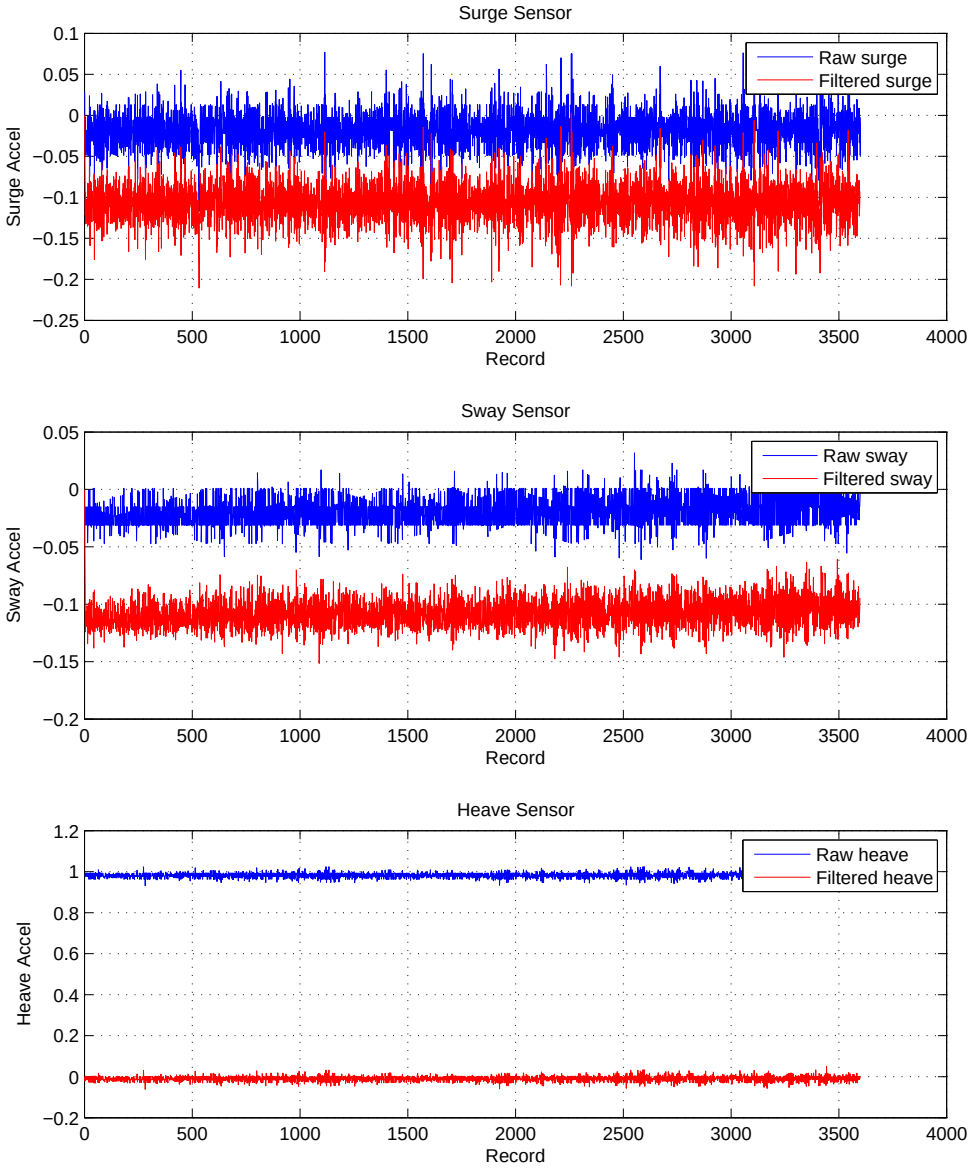

Figure 6.3.13: Sample accelerometer data, 0800 hours, day 4

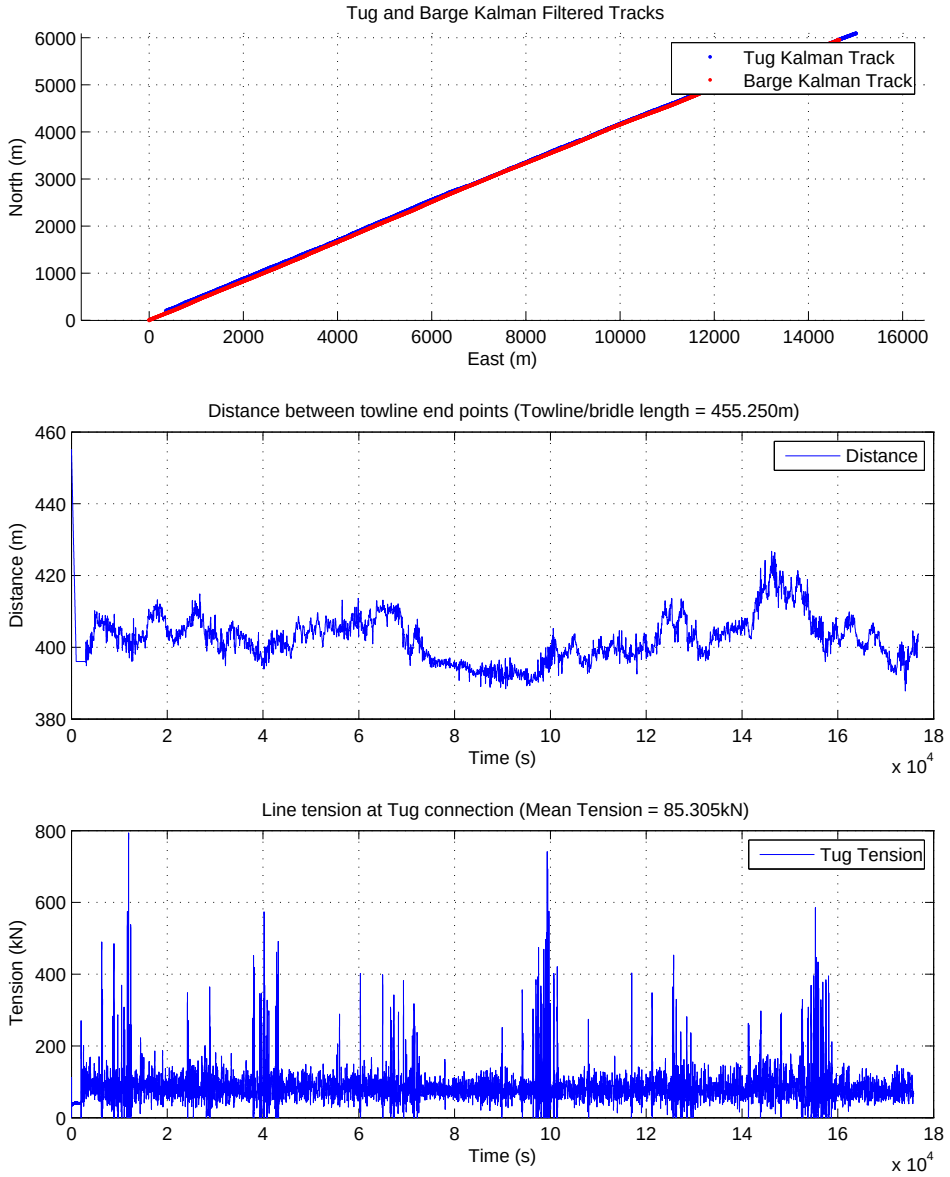

Figure 6.3.14: Towline tensions and tug/barge ranges, 2300 hours, day 1

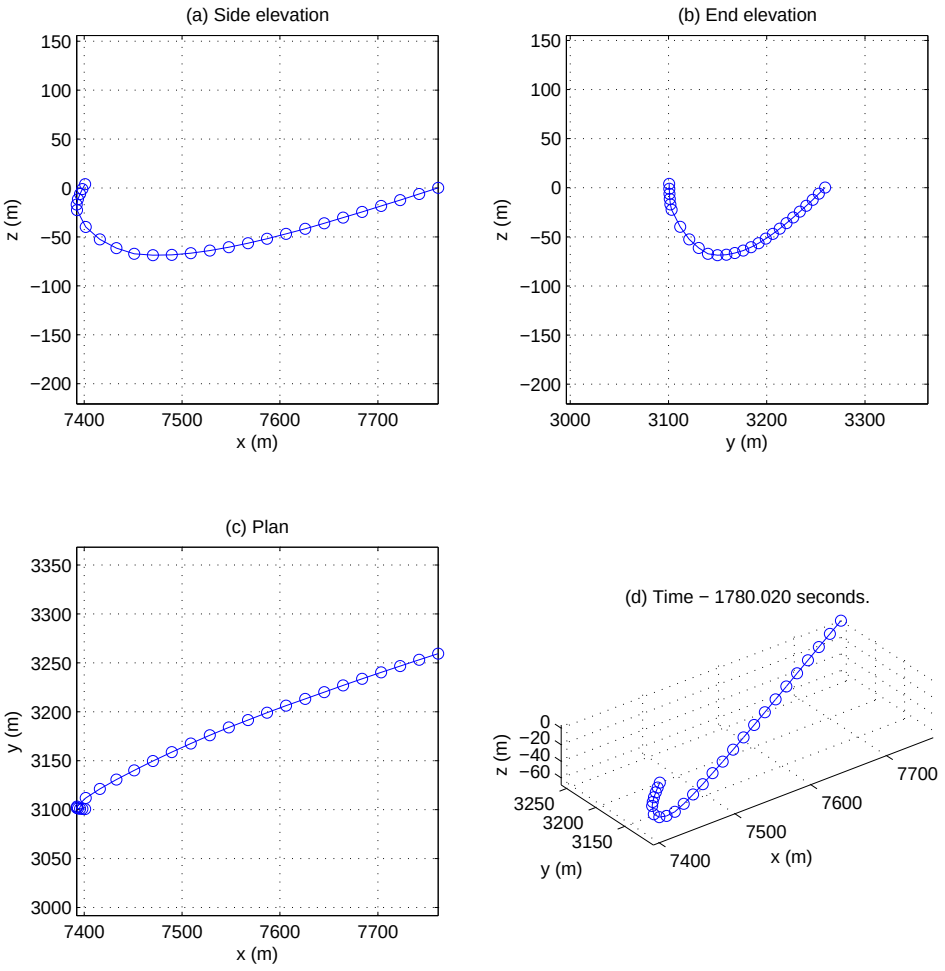

Figure 6.3.15: Catenary plot, 2330 hours, day 1

6.3.4 Summary of Lumped Mass Results - Day 2

The second day of the towage provided much more useable data. A sample of data gathered is shown in figure 6.3.16. The average range between the towline end points was circa 390m against a deployed towline and bridle length of 455.25m and the reported average tension in the towline at the tug end was 72.36kN which, again, was well below the reported tension of 20Te to 30Te. Referring to the catenary plot in figure 6.3.17 taken from around 1430 hours it is obvious that the line is, again, excessively slack.

There were peaks of line tensions at 0200 hours and 1900 hours but it is thought that these were due to anomalous filtered position data and the tension time trace in figure 6.3.18 confirms this where peaks in tensions are abnormally high where they coincide with excessive movements between the towline end points. These excessive movements are likely due to drift in the estimated position where the sensor fusion between low grade accelerometers and the GPS signals were not optimum.

With reference figure 6.3.18, a significant increase in tension variation may be seen. With reference to figure 6.2.15 where it may seen that the GPS readings show consistent mean range and so the only explanation for this tension variance is poor solid state sensor readings causing the filter to briefly diverge.

6.3.5 Summary of Lumped Mass Results - Day 3

The third day of the towage provided limited useable data. A sample of data gathered is shown in figure 6.3.19. The average range between the towline end points was circa 430m against a deployed towline and bridle length of 455.25m. The reported average tension in the towline at the tug end was 112.5kN (excluding hours where the predicted end points were incompatible with the towline length). Again this is below the reported tension of 20Te to 30Te but closer than was noted for days 1 and 2. Referring to the catenary plot in figure 6.3.20 taken from around 0630 hours it may be seen that the towline still appears slack but of a better form than found earlier. However as for day 02, there are several cases where tensions peaked such that the model stability was degraded.

6.3.6 Summary of Lumped Mass Results - Day 4

Day four of the towage provided much useable data however there were several discrete points where the towline tensions peaked abnormally, again due to drift in the estimated end position. A sample of data gathered is shown in figure 6.3.21. The average range between the towline end points was circa 230m against a deployed towline and bridle length of 255.25m. The reported average tension in the towline at the tug end was 93.08kN which is much closer to the reported tension of 10Te to 15Te.

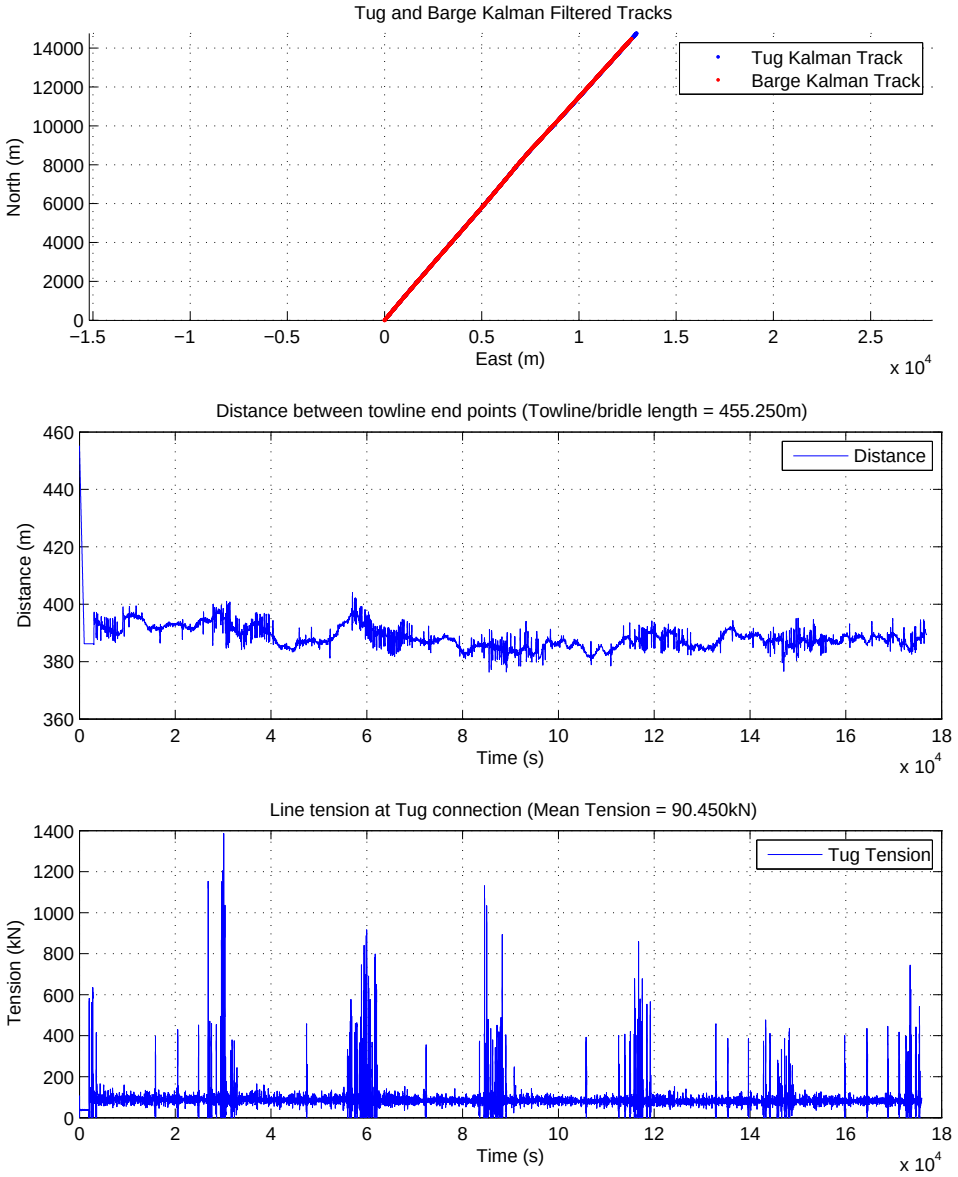

Figure 6.3.16: Towline tensions and tug/barge ranges, 1400 hours, day 2

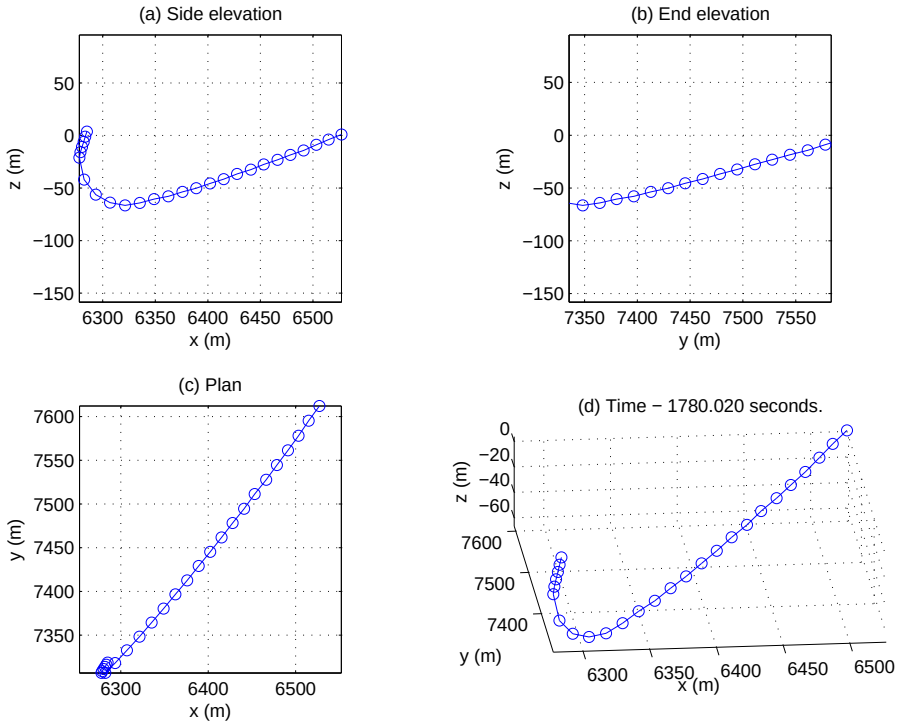

Figure 6.3.17: Catenary plot, 1430 hours, day 02

Referring to the catenary plot in figure 6.3.22 taken from around 1830 hours the line shows reasonable catenary profile. However as for day 02 and 03 previously, there are many examples where the towline was specified as too short resulting in unstable solutions.

6.3.7 Summary of Lumped Mass Results - Day 5

The final day of the towage was a conflicted a morass of mixed data due to the issues with recorded towline length and the fact there appeared to be an unreported shortening of the line requiring estimates of the deployed towline length. A sample of data gathered is shown in figure 6.3.23 and is representative of simulations ran on this final day. Numerical stability was an issue as the towline lengths reported were simply too short to offer any form of a stable solution. In the case cited, the average range between the towline end points was circa 260m against a deployed towline and bridle length of 255.25m which raises obvious questions. The reported average tension in the towline at the tug end was over 300kN which significantly in excess of the reported tension of 10Te to 15Te however it is suggested that comparisons are not of any practical use. Due to the issue of resolving the towline tensions in a lumped mass simulation no catenary plot is presented in this section.

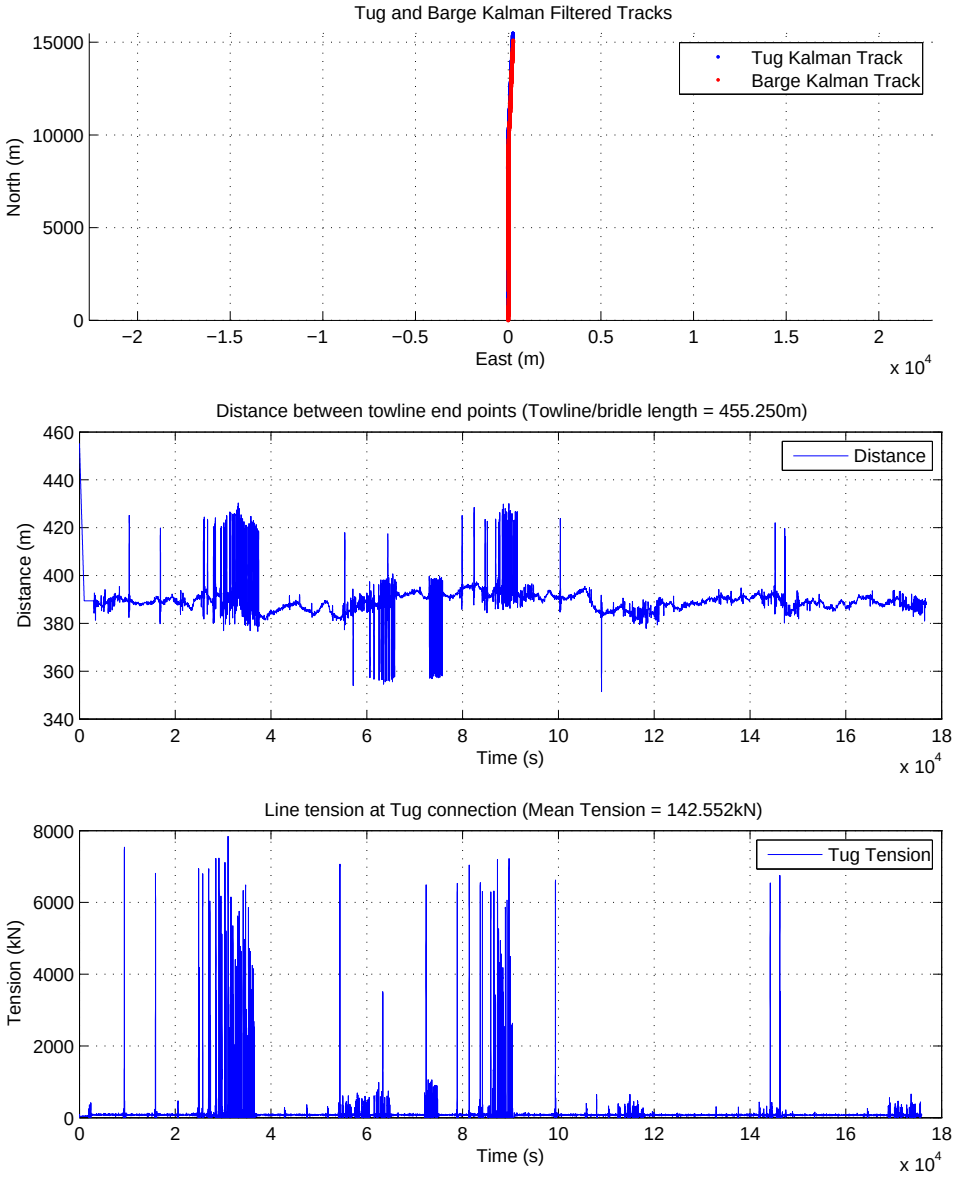

Figure 6.3.18: Towline tensions and tug/barge ranges, 1900 hours, day 2

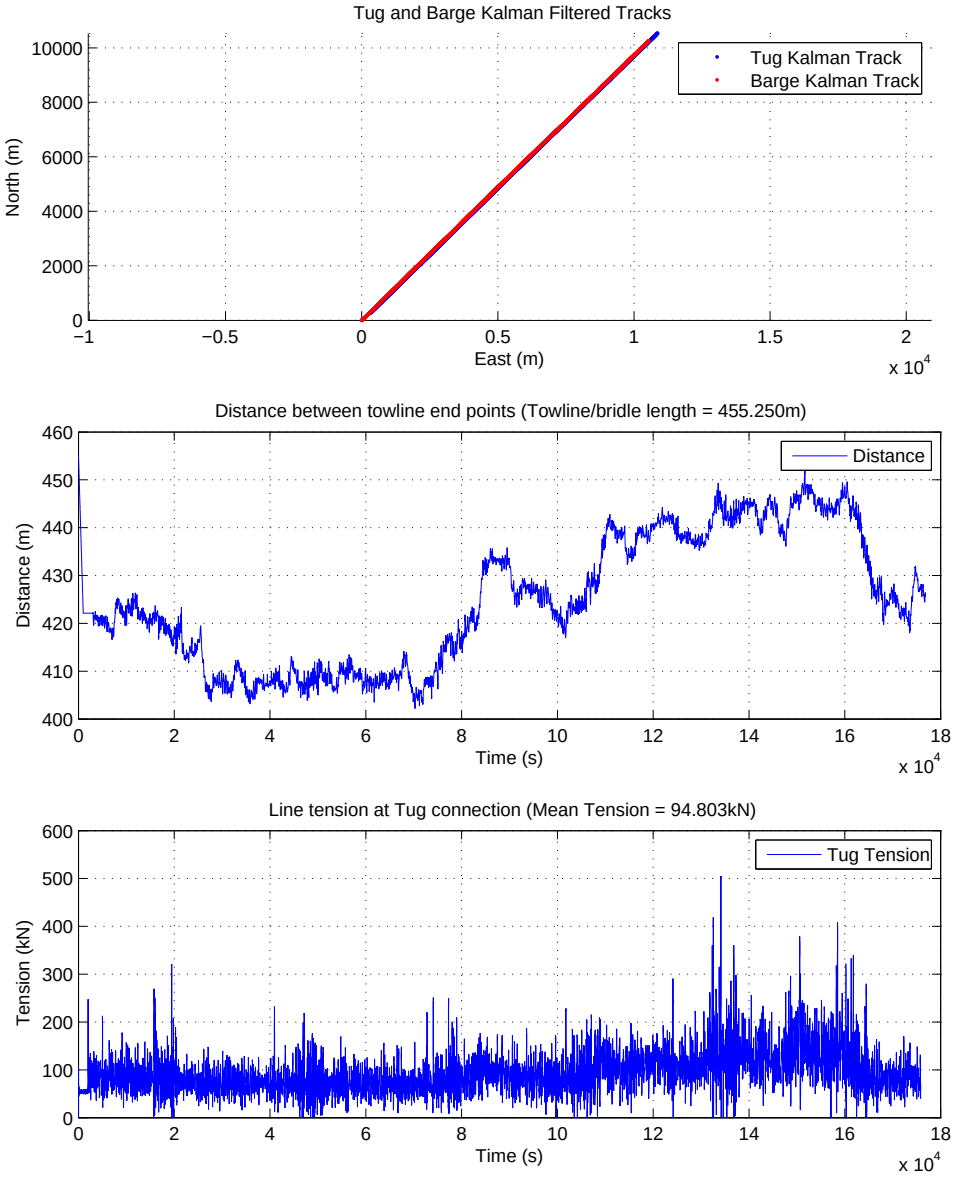

Figure 6.3.19: Towline tensions and tug/barge ranges, 0600 hours, day 3

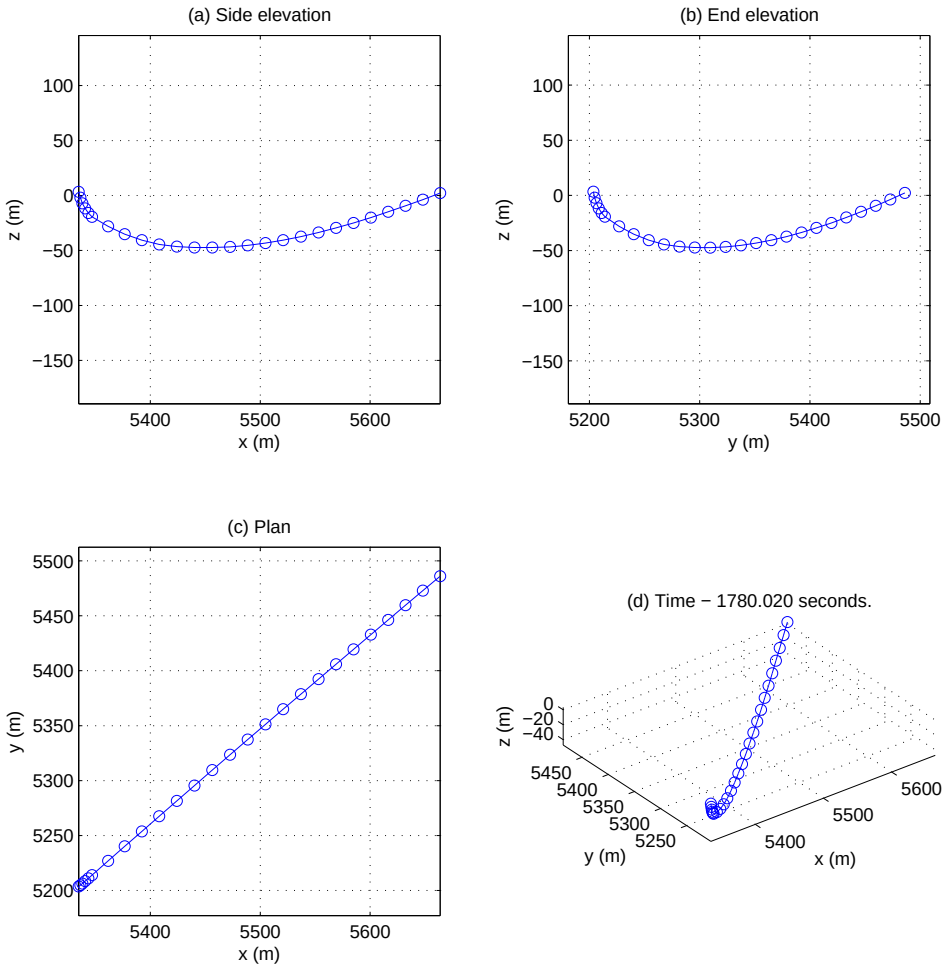

Figure 6.3.20: Catenary plot, 0630 hours, day 03

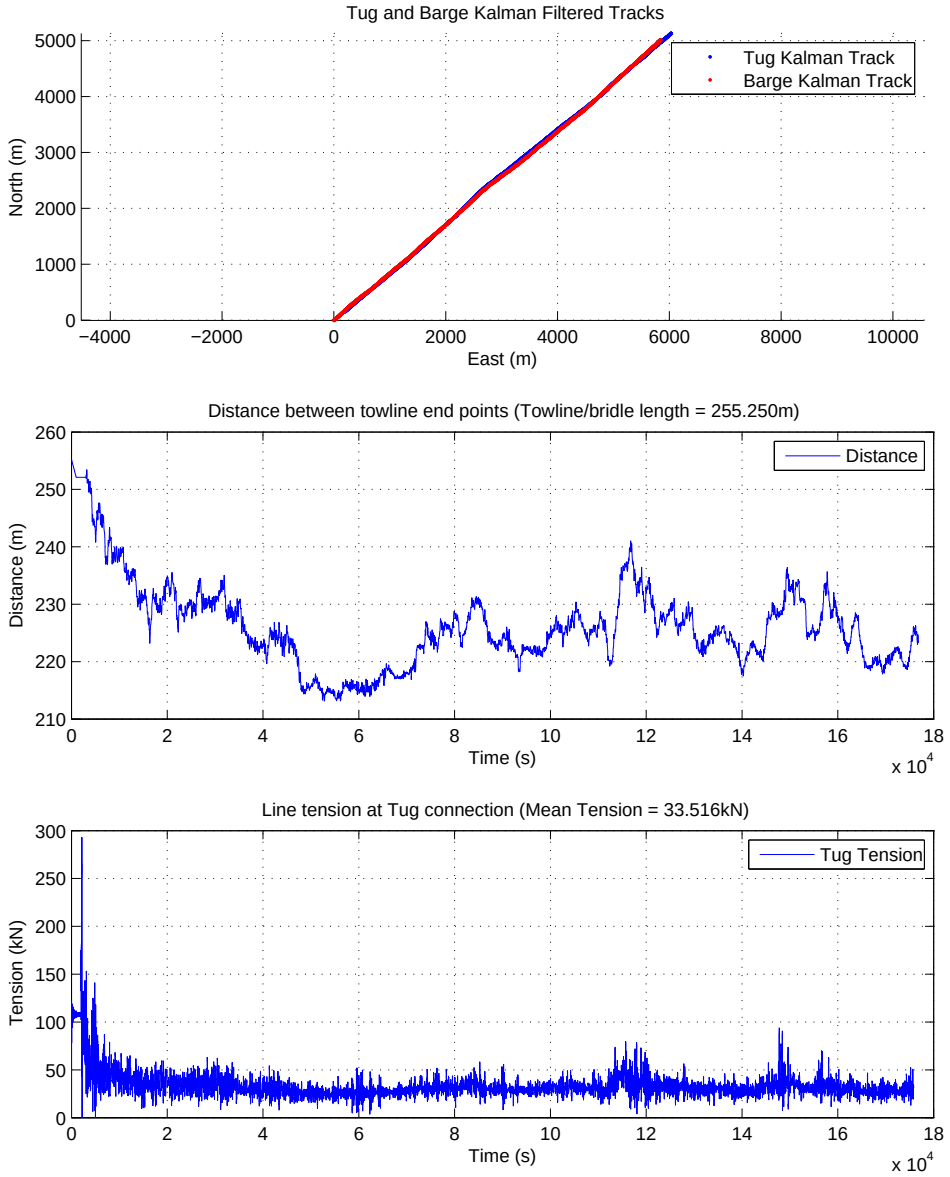

Figure 6.3.21: Towline tensions and tug/barge ranges, 1800 hours, day 4

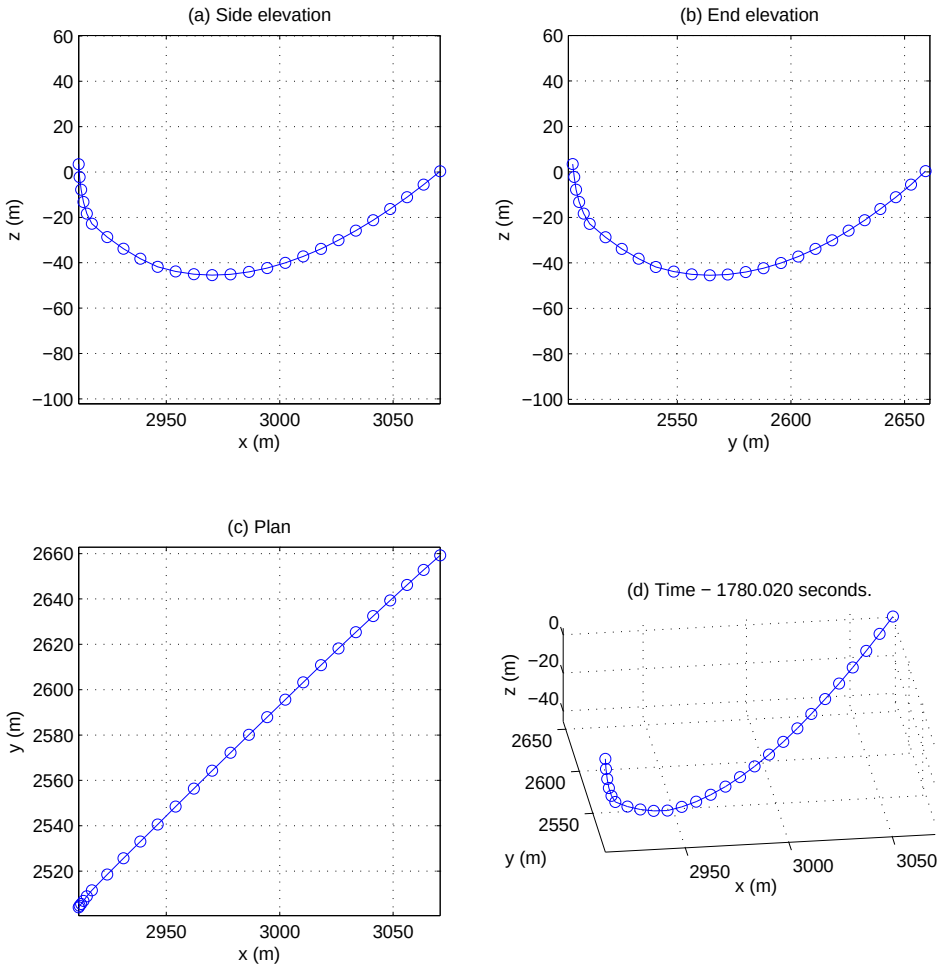

Figure 6.3.22: Catenary plot, 1830 hours, day 04

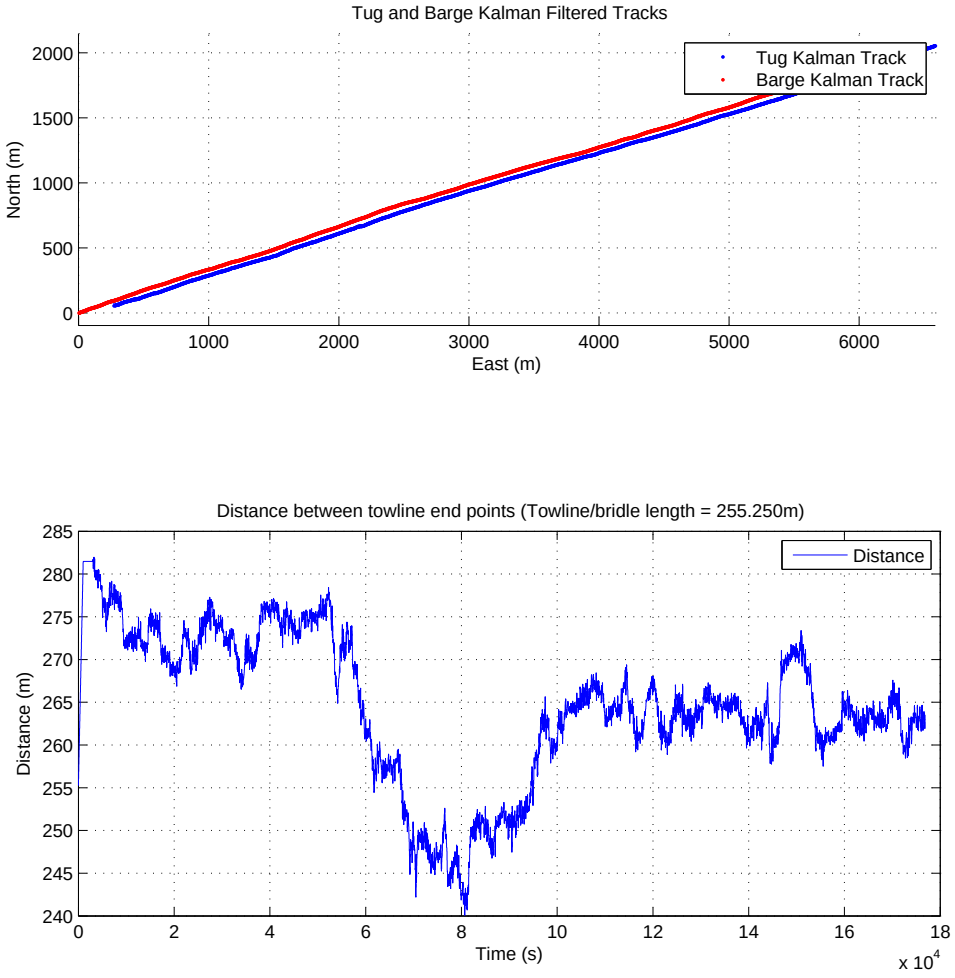

Figure 6.3.23: Towline tensions and tug/barge ranges, 0500 hours, day 5

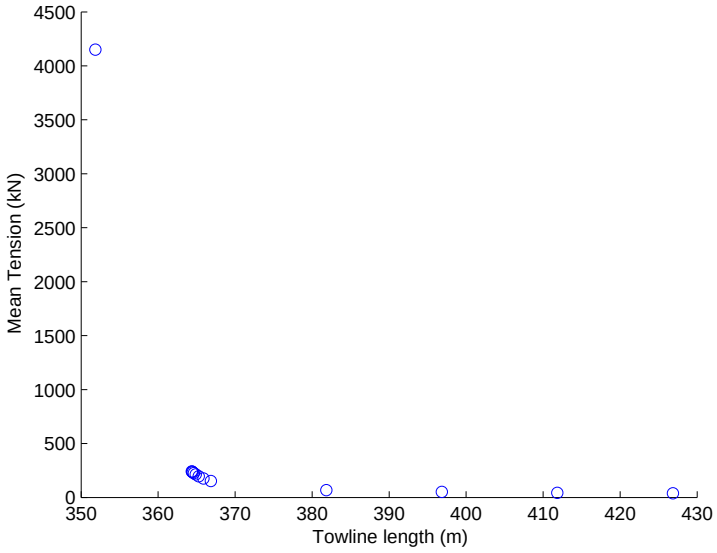

Figure 6.3.24: Balancing simulation to find optimum towline length

6.3.8 Simulated vs Recorded Towline Tensions

It was apparent that the combination of sensor quality and issues with reported towline deployed lengths from the vessel's crew caused issues in getting adequate simulation results. To verify this a series of runs were carried where the towline lengths were adjusted to find an optimum length whereby the reported mean tensions coincided with that reported by the vessel's crew.

A 12 hour segment of the second day was considered to see if consistent results could be found whereby the actual towline deployed could be estimated.

A target of 2.5% tolerance from a mean reported tension of 25Te was set. As the simulation is highly non linear anything between 5 and 15 runs were required to balance each hours worth of data (a sample of the algorithm's goal seeking may be seen in figure 6.3.24. The sensitivity of the final solution to small changes in towline length can be seen whereby there are only a few metres difference in the towline length between the solution and asymptotic increases in tension, which reinforces one of the conclusions of the research summarised later.

For the balancing runs between 0400 hours and 1600 hours on day two the balancing towline lengths were as reported in table 6.3.2. Here a distinct pattern can be seen whereby the deployed towline required to average to the mean reported towline tensions is around 365m. Now of course this conclusion is subject to the adequacy of the sensor data itself.

Table 6.3.2: Day 02, balanced towline lengths

Hour	Mean Tug Tension (kN)	Towline Length (m)
0400	245.58	390.08
0500	250.76	372.98
0600	240.62	366.43
0700	248.97	386.33
0800	239.45	364.79
0900	241.21	364.34
1000	239.86	365.80
1100	241.77	362.15
1200	241.09	362.07
1300	239.60	361.31
1400	239.15	365.17
1500	241.54	364.92
1600	239.97	364.96

6.3.9 Effect of high frequency sensor noise on tensions

There is a concern that the relatively poor sensor quality would have a significant effect on the quality of towline tensions recorded. To test this, a simple moving average filter with a span of five data point was applied to a sample data set of position estimates for the tug and barge. Taking the data previously shown for 0600 hours on day 3, figure 6.3.19 refers, it may be seen that the tensions in the towline peak at around 500 kN. The smoothed results however reduce this significantly by around 50% while maintaining the detail overall, represented by the mean tension dropping from 94.80kN in the unsmoothed case to 92.06 kN in the smoothed case, figure 6.3.25 refers.

Furthermore, by examining sample detail on both simulations, as shown in figures 6.3.26 and 6.3.27 for the smoothed and unsmoothed cases respectively it may be seen that the “jitter” in the towline tensions has been reduced significantly without loss of detail or magnitude of tensions predicted. The position estimate trace as well notes that the detail of the tug and barge tracks is not overly affected.

This was found to be the case in all simulation runs examined with the exception of those where the towline tension was unresolvable without adjusting the length of towline simulated from that reported in the voyage logs.

This indicates only marginal improvements in the sensor technology employed is required to result in dramatic improvements in the quality of data gathered through reduced noise.

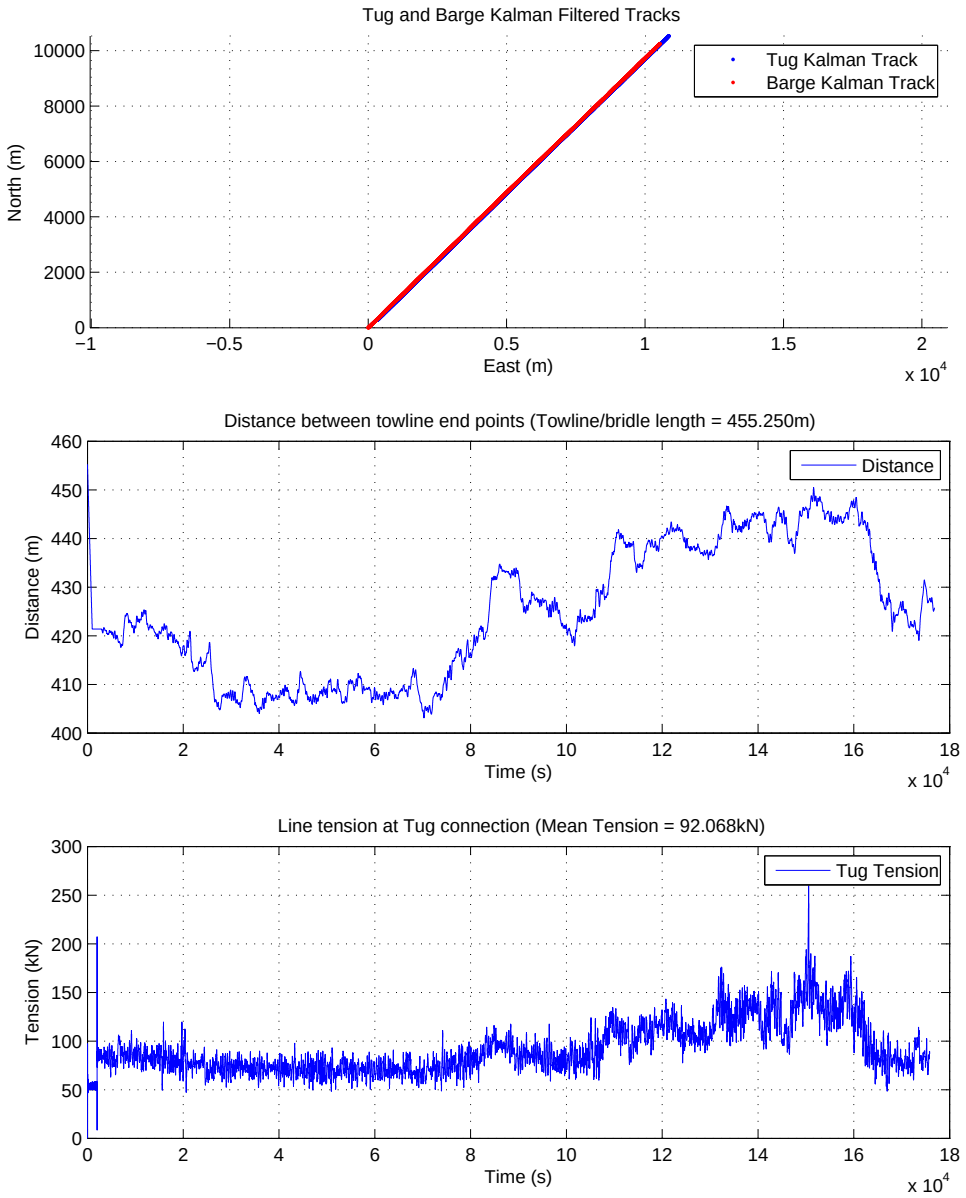

Figure 6.3.25: Smoothed position estimates and resulting towline tenons, 0600 hours, day 03

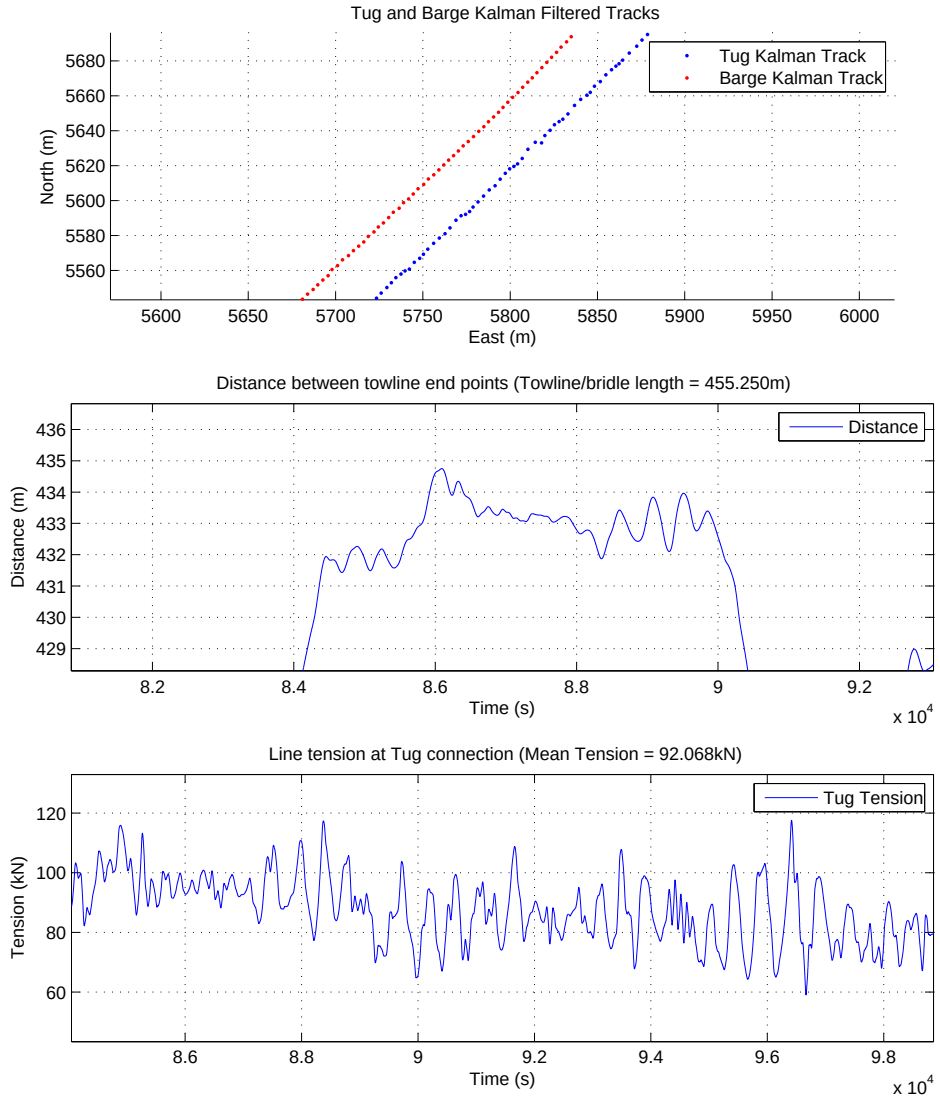

Figure 6.3.26: Detail on smoothed results, ~0630 hours, day 3

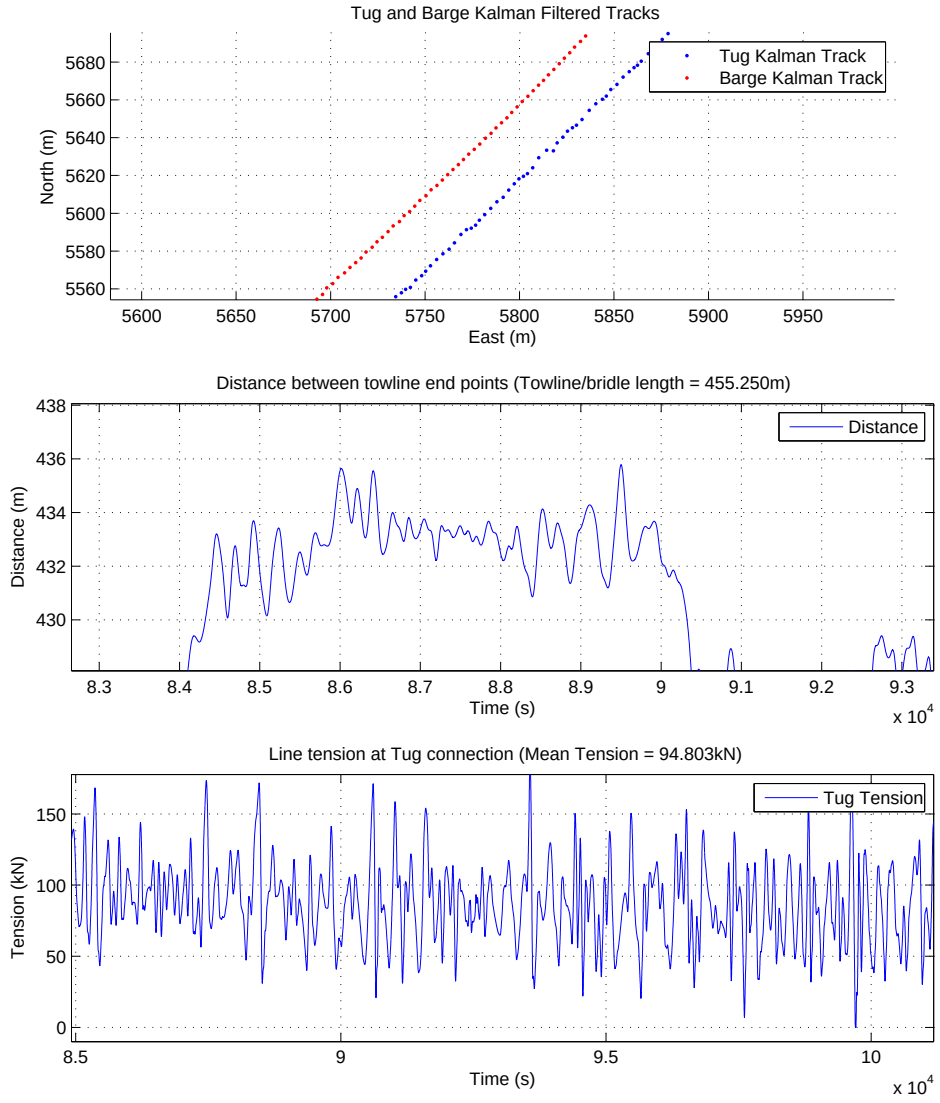

Figure 6.3.27: Detail on unsmoothed results, ~0630 hours, day 06

6.4 Chapter Summary

The results of the numerical solution was presented and the issues associated with the quality of the sensor data highlighted. It was noted that the data quality refers not just to the sensors within the data loggers but also the quality of the data gathered on the towline deployment as the simulations were particularly sensitive to this, especially in low tension and shortened towline towage regimes.

The feasibility of the methodology is apparent subject to close control of these key issues and recommendations for this are made in chapter 8 later.

Chapter 7

Conclusions

The aim of this research was to understand, using limited and simple technology, the feasibility of developing a system whereby the difficulties in gathering useful data on real world commercial towages could be overcome.

A system has been developed whereby this is now achievable. Furthermore, the ubiquitous development of sensor technology and integration of these into ever smaller, cheaper and more efficient chipsets is such that the restriction in data quality found here will only improve at a tremendous rate meaning what was state of the art 5-10 years ago in terms of the grade of sensor quality is likely to become almost disposable technology found in items such as consumer drones or mobile phones in the next 10 years.

While the restrictions in the data gathered here due to the quality of sensors employed has been clearly shown, this is not a barrier to the development of the methodology itself and in fact had the research been started 5 years later and the loggers developed specifically for the purpose, then the dramatic improvements in components available, alluded to above, would have resulted in a higher quality of data gathered. Suggestions for alternative equipment suppliers at the time of final write up are made in chapter 8 later.

Furthermore the publishing of the full source code for the methodology will, it is hoped, speed up subsequent improvements in the research, avoiding any “reinventing of wheels”.

7.1 Critical assessment of own work

The literature review found little evidence of work whereby the full 6DOF datasets for a tug and tow were gathered. Furthermore a single body of work that looked to span both the numerical implementation of the towline simulation (ocean engineering) and review the issues associated with the merging of differing datasets (electronic engineering) was not found.

In addition, interesting observations were made around industry norms for assessing the stiffness of key mooring components and areas worthy of further investigation were found.

However the implementation of the Kalman filter here was a rudimentary one. Furthermore the quality of the sensors employed was such that the data output was often polluted with considerable noise and suggestions for improving this are made in the next chapter.

7.2 Summary

The principle aim of this research was to understand the feasibility of accurately determining, by simulation, the full time history of a towline on voyages of opportunity with a quickly deployed, non invasive system. This has been demonstrated as feasible. In addition, areas of focus for future research in this field have been highlighted, including recommendations for equipment selection, suggestions for improvements in the methodology as well as providing a versatile and flexible, validated, code base for ease of continuing the work started here.

It is the belief of the author that a comprehensive review of actual tug utilisation on open sea towages is overdue. The current rules for matching tugs to their tow is based on empirical rules of thumb that have changed little over the years. This is down to limited real world data gathering, due to the difficulties in gathering the large datasets required.

The research here paves the way for leveraging the significant improvements in sensor technology both in terms of quality and cost made even over the life of this research programme to quickly, and easily gather rigorous data to drive this conversation forward on tug and tow response in the real world over a large number of voyages.

It would not be difficult, to follow this research with a programme partnering only two or three large tug owners and having each of their tugs fitted with unobtrusive loggers designed specifically for the task (costing only a few hundred dollars each). This coupled with secondary loggers that the Master can simply clamp in place on the tow and switch on during his survey prior to departure would allow a wealth of data to fuel this discussion.

This would also provide an incredible data source for other areas of research given these datasets provide, as natural by-product, motion response data which when coupled with the both vessels hydrodynamic characteristics, paves the way for much wider opportunities.

Chapter 8

Further Work

There are several areas worthy of further development as highlighted in this research and key areas are outlined as follows:

8.1 Voyage Logs

The sensitivity of the simulations to the length of towline deployed was evident throughout the post processing. A device was developed which could attach to the side of the winch drum magnetically and count the revolutions of the drum in a clockwise and counter clockwise fashion but space restrictions in most commercial, deepsea tugs around the towline drum rendered installation impractical. An alternative system whereby a time lapse camera mounted over the drum with some simple markers on the inside face of the drum walls would allow for an effective indicator of the wire wrap count on the drum. This combined with knowledge of the drum geometry would allow for a verifiable measure of the towline paid out and in itself be an interesting research project in image recognition and learning.

A more robust means of gathering the mean towline tensions (to allow simulation verification) would be required and a time lapse camera trained on the drum, open sea aft of the tug and the digital readout of the towline tension meter would serve to capture both as well as visual indicators of the sea state at the same time.

It is important to ensure the mean tensions marry up for simulation verification on a voyage by voyage basis permitting the numerical model to locate and report on peak tensions (reference [van den Boom (1986)]).

8.2 Implementation of the Kalman Filter

The filter implemented here could be significantly improved. Avenues for further research include implementing a multipass filter which looks to take advantage of the fact that the entire dataset is available at the outset and estimates are not required in realtime.

The implementation here is a loosely coupled variant and significant improvements in data quality may be made by designing the hardware such that it permits a tightly coupled implementation of the GPS raw data stream and the on board MEMs sensors.

8.3 Hardware implementation

It would be the recommendation of the author to any subsequent research in this field, or any other involved in datalogging, to ensure that the code base and the implementation of the loggers themselves be available. Much time was lost early on with debugging the firmware of the loggers, made worse by the fact that this was done by a third party who owned the code base. While they were always helpful and responsiveness, nevertheless delays were inevitable and perhaps avoidable if a bespoke device were built in house.

The quality of the sensors employed were a limiting factor in the quality of data gathered. For developing a replacement system, components such as that found in XSens range (www.xsens.com) would be highly recommended. The support offered with additional tools and post processing software would greatly speed up the future development of the simulation methodology.

8.4 Operational

The implementation of multiple loggers on a single vessel would also greatly improve the quality of data gathered. It would be simple to evolve the system described here to take input from a pair of loggers mounted at different locations on the host vessel, preferably at opposite ends. The data improvement in terms of quality and redundancy would be significant.

For the voyage of opportunity mentioned here it is a possibility that the choice of location for mounting the loggers had an effect on the data quality retrieved. The barge logger was mounted to a walkway between flotation towers (reference figure 6.2.8) and the tug logger mounted to the mast above the wheelhouse (reference figure 6.2.11). Both of these structures would be possible subject to vibrations while underway and the effect of this was not quantified.

8.5 Future cooperation

Subsequent research that would complement this work might look to partner with tug owners keen to understand the response and applicability of their tonnage to larger towages previously not open to them that a rigorous programme of research may permit. The author certainly found, through his discussions with owners both as part of this research and then commercially as charterer of such tonnage, that this is something they would likely be open to discussing.

This could be achieved by attaching the unobtrusive devices designed here to their tugs and providing a number of free standing variants that they could then place, as a matter of course, on board tows they undertake thereby routinely gathering large datasets that can be batch processed looking for longer term trends. This closer coupling with owners would allow exploration of other issues such as tug, towline and tow response in heavy weather. Tug performance in differing sea states and headings, even probabilities of propeller emergence due to the fact that both sea state and vessel attitude can all be derived from the datasets gathered.

8.6 Numerical Model

The numerical model implemented here allows for the simulation of a single line. It could be adapted to allow for correct modelling of the bridle. In addition, non linear drag coefficients where the tangential and normal drags are adjusted depending on the Reynolds number of the regime the segment finds itself in from one time step to the next. With the availability of better non linear stiffness data on the towline, this too could be implemented in the form of a lookup table or fitted curve with the stiffness adjusted dependent on water depth (for sheathed lines) or tension.

8.7 FEA of towline connections

The limited FEA analysis carried out here on chain links and other mooring components seemed to indicate that the conventional approach to assessing their stiffness results in over estimated values. There are numerous examples of FEA review and analysis of chain response and failure but these focus largely on other important issues such as fatigue, residual stresses and strength in bending or bearing and not global stiffness and dynamic response. The most common values in use in industry today when carrying out mooring analysis in commercial software such as OrcaFlex and Ariane use empirical values based around cross sectional area. A new approach which modifies the values produced by [Wichers (2013)] proposed in section 5.2.3 would be worth exploring further to understand the potential

for improvement in methodologies in fields where mooring chain represents a significant component of systems.

Bibliography

[Aalbers et al (1996)] A B Aalbers, C E J Leenars and F H H A Qauadvlieg, “Voyage Acceleration Climate: A Comprehensive Statistical Method for Evaluation of Design Loads for Offshore Transport”, Offshore Technology Conference, 1996

[Amahah (2009)] Justice Amahah, “The design of an Unmanned Aerial Vehicle Based on the ArduPilot”, Georgian Electronic Scientific Journal: Computer Science and Telecommunications, No. 5 (22), 2009

[Arden (2007)] Dale Arden, “MEMs/GPS Kalman Filter”, Defence Research and Development Canada - Ottawa, Contract report DRDC Ottawa CR 2007-093, May 2007

[Banks (2008)] John Banks, “Special Report - Heavy-lift”. Lloyd’s List, pp.11-14, 05/02/08

[Beegle (2007)] Robert Beegle, “An Overview of Trends in the Tug Market”, Marcon International Report, May 2007

[Bijker et al (2008)] Johan Bijker and Willem Steyn, “Kalman filter configurations for a low-cost loosely integrated inertial navigation system on an airship”, Control Engineering Practice 16, pp.1509 - 1518, 2008

[Balchen et al (1976)] J. G. Balchen, N. A. Jensen, and S. Saelid, “Dynamic positioning using Kalman filtering and optimal control theory”, Proceedings IFAC/IFIP Symposium Automation in Offshore Oil Field Operations, Bergen, Norway, 1976, pp.183-186

[Boeing (1966)] Boeing Company, Aerospace Group, “Final Report - Development of High Speed Towing Cables/Underwater Towed Body - Parts I and II, US Navy Electronics Laboratory, Reports D2-89924-1 and D289924-2, AD804190 (part II), 1966

[Bos (2008)] A. J. Bos, “Measurement Campaign for Validating the Motion Response Calculations of Heavy Transport Vessels and Fatigue Monitoring”, RINA Marine Heavy Transport and Lift II, February 2008

[Bridon Ropes (2009)] Bridon Ropes, “Specialist fibre and steel ropes solutions for the oil and gas industry”, Bridon ropes, http://www.bridon.com/site/brochures/, 2009

[Buckham and Nahon (2001)] B. J. Buckham and M. Nahon, “Formulation and Validation of a Lumped Mass Model for Low Tension ROV Tethers”, International Journal of Offshore and Polar Engineering, Volume 11, No. 4, ISSN 1053-5381, December 2001

[Cadet (2003)] Olivier Cadet, “Introduction to Kalman filter and its use in dynamic positioning systems”, Dynamic Positioning Conference, DP Design and Control Systems 1, September 16-17, 2003

[Cannon and Genin (1972)] T. C. Cannon and J. Genin, “Three Dimensional Dynamical Behavious of a Flexible Towed Cable”, Aeronautical Journal 23(3) pp.201-210, 1972

[Chen et al (1994)] Jeng-Heng Chan, Sou-Chen Lee, Daniel D. DeBra, "Gyroscope free strapdown inertial measurement unit by six linear accelerometers", Journal of Guidance, Control and Dynamics, Vol 17, No 2, pp.286-292, March-April 1994

[Choo and Casarella (1972)] Y. Choo and M. J. Casarella, “Configuration of a Towline Attached to a Vehicle Moving in a Circular Path”, Journal of Hydrodynamics 6(1), pp.213-220, 1972

[Christensen (1989)] Erik Niels Christensen, “Plans and Specifications for a Full-Scale Towing Model Validation Experiment”, MSc Thesis, Massachusetts Institute of Technology, 1989

[Desroches (1997)] Alexander S. Desroches, “Calculation of Extreme Towline Tension During Open Ocean Towing”, MSc Thesis, Massachusetts Institute of Technology, 1997

[DIYDrones.com] www.diydrones.com

[DNV (1996)] Det Norske Veritas, “Rules for the planning and execution of marine operations”, First Issued 1996, Amended 2000

[DNV (2007)] Det Norske Veritas, “Environmental Conditions and Environmental Loads”, Recommended Practice DNV-RP-C205, April 2007

[DNV (2010)] Det Norske Veritas, “Position Mooring”, Offshore Standard, DNV-OS-E301, October 2010

[DNV (2011)] Det Norske Veritas, “Marine Operations, General”, Offshore Standard, DNV-OS-H101, October 2011

[DNV (2011-2)] Det Norske Veritas, “Modelling and Analysis of Marine Operations”, Recommended Practice DNV-RP-H103, April 2011

[DNV (2012)] Det Norske Veritas, “Load Transfer Operations”, Offshore Standard, DNV-OS-H201, April 2012

[DNV (2015)] Det Norske Veritas, “Sea Transport Operations”, Offshore Standard, DNV-OS-H202, October 2015

[DNVGL (2016)] DNV.GL, “Marine operations and marine warranty”, DNVGL-ST-N001, November 2016

[Dougherty et al (1994)] John J. Dougherty, Hossny El-Sherief, and David S. Hohman, “Use of the Global Positioning System for Evaluating Inertial Measurement Unit Errors”, Journal of Guidance, Control and Dynamics, Vol. 17, No 3, pp.435-441, 1994

[Eames (1968)] Eames, M.C., “Steady state theory of towing cables”, Transactions of the Royal Institution of Naval Architects 110, pp. 185-206, 1968

[Fernandez et al (2009)] Vicente I. Fernandez, Stephen M. Hou, Franz S. Hover, Jeffrey H. Lang, Michael S. Triantafyllou, “Development and application of distributed MEMs pressure sensor array for AUV object avoidance”, Massachusetts Institute of Technology, July 23, 2009

[Fitriadhy et al. (2013)] A. Fitriadhy, H. Yasukawa, K. K. Koh, "Course stability of a ship towing system in wind", Ocean Engineering 64, pp.135-145, 2013

[Fossen and Perez (2009)] Thor I. Fossen and Tristan Perez, “Kalman Filtering for positioning and heading control of ships and offshore rigs”, IEE Control Systems Magazine, pp.32-46, December 2009

[Freescale (2008)] “MMA7361L Technical Data Sheet: +/ 1.5g, +/- 6g Three axis low-g Michromachined Accelerometer”, Freescale Semiconductor Document Number MMA7361L Rev 0, April 2008

[Fredericks (2011)] “0717-4304-99 Data Sheet Dual Axis Wide Angle Electrolytic Tilt Sensor”, The Fredericks Company, 0717-4304-99 data sheet revicion A, 2011

[Frimm (1987)] Fernando de Cavalho Frimm, “Non-Linear Extreme Tension Statistics of Towing Hawsers”, PhD Thesis, Massachusetts Institute of Technology, 1987

[Frimm and Milgram (1991)] F. C. Frimm and J. H. Milgram, “Towline Measurements at Sea”, Document submitted to the Naval Sea Systems Command (NAVSEA OOC), 1991

[GL Noble Denton (2010)] GL Noble Denton, “Technical Policy Board - Guidelines for Marine Transportation”, 0030/ND Rev 04, 31/03/2010

[GL Noble Denton (2013)] GL Noble Denton, “Technical Policy Board - Guidelines for Marine Transportation”, 0030/ND Rev 05, 22/06/2013

[Hara et al (2004)] Shoichi Hara, Kenji Yamakawa, Kunihiro Hoshino and Kazuhiro Yukawa, “At-sea towing of a Mega-Float unit”, Journal of Marine Science and Technology, pp.138-146, 2004

[Hide et al (2006)] Chris Hide, Terry Moore, Chris Hill and David Park, “Low cost, high accuracy positioning in urban environments”, The Journal of Navigation Vol 59, pp.365-379, September 2006

[Hide et al (2007)] Chris Hide, Terry Moore, Chris Hill, "A Multi-Sensor Navigation Filter for High Accuracy Positioning in all Environments", The Journal of Navigation, 60, pp.409-425, 2007

[Hobbs (1996)] R. E. Hobbs and M. Raoof, “Behavious of Cables under Dynamic or Repeated Loading”, Journal of Construction Steel Res. Vol 39, No 1, pp.31-50, 1996

[Hou (2004)] Haiying Hou, "Modelling Sensor Errors using Allan Variance", UCLE Reports No 20201, University of Calgary, September 2004.

[HSE (1991)] C. Richard Chaplin and Andrew E. Potts, “Wire Rope Offshore - A Critical Review of Wire Rope Endurance Research Affecting Offshore Applications”, UK Health and Safety Executive Report OTH 91 341, 1991.

[Huang (1994)] Shan Huang, “Dynamic Analysis of Three-Dimensional Marine Cables”, Ocean Engineering Vol 21, No6, pp.587-605, 1994

[Inoue et al (1994)] Y. Inoue, S. Surendran and T. Shimizu, “Dynamic Tension Analysis of Surface Towing System”, Journal of the Society of Naval Architects of Japan, v 175, pp.241-250 , 1994

[ISO 19901-6 (2009)] British Standard, “Petroleum and natural gas industries - Specific requirements for offshore structures. Part 6: Marine operations”, BS EN ISO 19901-6:2009, 2009

[Jazar (2010)] R. N. Jazar, “Theory of Applied Robotics”, 2nd Edition, DOI 10.1007/978-1-4419-1750-8_2, Springer Science+Business Media, LLC 2010

[Kalman (1960)] Kalman, R.E., “A new approach to linear filtering and prediction problems”, Transactions of the ASME-Journal of Basic Engineering, 82 (Series D), pp.35-45, 1960

[Koks (2007)] Don Koks, “Numerical calculations for passive geolocation scenarios”, Electronic Warfare and Radar Division, Defence Science and Tecehnology Organisation, Australian Government Department of Defense, DSTO-RR-0319, 2007

[Leonard and Nath (1980)] John W. Leonard and John H. Nath, “Comparison of Finite Element and Lumped Parameter Methods for Oceanic Cables”, Engineering Structures Volume 3, pp.153-167, 1981

[Li et al (2003)] Xiaojing Li, Gang-Ding Peng, Chris Rizos, Linlin Ge, Yukio Tamura and Akihito Yoshida, “Integration of GPS, Accelerometer and Optical Fibre Sensors for Structural Deformation Monitoring”, University of New South Wales Report, 2003

[Lloyd (1998)] Adrian R. J. M.Lloyd, Seakeeping: Ship Behaviour in Rough Weather”, 2nd Revised Edition, May 1998.

[LOC (1999)] London Offshore Consultants, “Guidelines for Marine Operations”, Oilfield Publications Ltd, May 1997

[Long and Jia-han (2006)] YU Long and TAN Jia-han, "Numerical investigation of seabed interaction in time domain analysis of mooring cables", Journal of Hydrodynamics Ser.B, 18(4), pp.424-430, 2006

[Low and Langley (2006)] Y.M. Low and R. S. Langley, “Time and frequency domain coupled analysis of deepwater floating production systems”, Applied Ocean Research, Vol 28, pp.371-385, 2006

[MacSween (2011)] John A. MacSween, “Examination of the Effectiveness of Modelling Towline Response using GPS and Strapdown INS Data Gathering Techniques”, ISOPE 2011.

[Maklouf et al (2012)] Othman Maklouf, Abdurazag Ghila and Ahmed Abdulla, “Cascade Kalman filter configuration for low cost IMU/GPS integration in car navigation like robot”, Wolrd Academy of Science, Engineering and Technology Vol 66, pp.602 - 607, 2012

[Maung et al (2011)] Htoo Maung Maung, Zaw Min Naing and Hla Myo Tun, “Implementation of PIC based vehicle’s attitude estimation system using MEMS inertial sensors and Kalman filter”, Proceedings of The First International Conference on Interdisciplinary Research and Development, Thailand, pp.70.1 - 70.6, 2011

[Maybeck (1979)] Peter S. Maybeck, "Stochastic Modles, Estimation, and Control", Volume 1, 1979

[Milgram et al (1988)] J.H. Milgram, M. S. Triantafyllou, F. C. Frimm and G. Angostou, “Seakeeping and Extreme Tensions in Offshore Towing”, Paper presented at Annual Meeting of the Society of Naval Architects and Marine Engineers, New York, 1993

[MOD (2002)] Ministry of Defence, “Requirements for Anchoring, Berthing, Towing and Securing to a Buoy”, Defence Standard 02-117 Issue 02, 1st May 2002

[Moore et al (2008)] Terry Moore, Chris Hill, Andy Norris, Chris Hide, David Park and Nick Ward, “The potential impact of GNSS/INS intergration on maritime navigation”, The Journal of Navigation Vol 61, pp.221 - 237, 2008

[Mostov et al (1997)] Kirill S. Mostov, Andrey A. Soloviev & T.-K. John Koo, “Accelerometer Based Gyro-Free Multi-Sensor Generic Inertial Device for Automotive Applications”, IEEE Conference on Intelligent Transportation System, pp.1047-1052, 1997

[Motwani et al (2012)] A Motwani, SK Sharma, R Sutton and P Culverhouse, “Interval Kalman filtering applied to uninhabited surface vehicle navigation”, Marine and Industrial Dynamic Analysis, School of Marine Science and Engineering, Plymouth University, Technical Report MIDAS.SMSE.2012.TR.003, June 2012

[Movellan (2011)] J. R. Movellan, “Discrete time Kalman filters and smoothers”, MPLab Tutorials, University of California, San Diego, 2011

[Nevalainen (2008)] Eero Nevalainen, “Accelerometer configurations for a gyroscope free inertial navigation system", Helsinki University of Technology, 2008

[Omerbashich (2002)] Mensur Omerbashich, "Integrated INS/GPS navigation from a popular perspective", Journal of Air Transportation, Vol. 7, No. 1, 2002

[Pfau et al (2005)] Thilo Pfau, Thomas H. Witte and Alan M. Wilson, “A method for deriving displacement data during cyclical movement using an inertial sensor”, The Journal of Experimental Biology, pp.2503-2514, 2005

[Pnevmatikakis at al (2012)] Eftychios A. Pnevmatikakis, Kamiar Rahnama Rad, Jonathan Higgins, Liam Paninski, “Fast Kalman filtering and forward-backward smoothing via a low rank perturbative approach”, Department of Statistics and Center for Theoretical Neuroscience, columbia University, New York, October 15th, 2012, (http://www.stat.columbia.edu/~liam/research/pubs/fast-low-rank-kalman.pdf)

[Prawoto (2012)] Yunan Prawoto and Raimee B. Mazlan, “Wire Ropes: Computational, mechanical and metallurgical properties under tension loading”, Computational Materials Science 56, pp.174-178, 2012

[Sanders (1982)] Joel Sanders, “A Three Dimensional Dynamic Analysis of a Towed System”, Ocean Engineering Volume 9 Numner 5, pp.483-499, 1982

[Sazdovski et al (2005)] Vasko Sazdovski, Tatjana Kolemishevska-Gugulovska, Mike Stankovski, "Kalman Filter Implementation for Unmanned Aerial Vehicles Navigation Developed within a Graduate Course", Insitute of ASE at Faculty of EE, St Cyril and Methodius University, MK-1000, Skopje, Republic of Macedonia, 2005

[Schmidt (2003)] George T. Schmidt, “INS/GPS Technology Trends”, The Charles Stark Draper Laboratory, NATO/OTAN Report RTO-EN-SET-064, 2003

[Schram and Reyle (1968)] J. W. Schram and S. P. Reyle, “A Three Dimensional Analysis of a Towed System”, Journal of Hydrodynamics 2(4), pp.213-220, 1968

[Setoodeh et al (2004)] Peyman Setoodeh, Alireza Khayatian and Ebrahim Farjah, “Attitude estimation by seperate-bias Kalman filter-based data fusion”, The Journal of Navigation, Vol 57, pp.261-273, 2004

[Siemens (2007)] “XT75 Celluler Engine - Hardware Interface Description”, Siemens AG, Document ID XT65_XT75_HD_v01.001, January 2007

[Sotak (2009)] Milos Sotak, “Determining stochastic parameters using an unified method”, Acta Electrotechnica et Informatica, Vol. 9, No. 2, 2009, pp.59-63

[ST (2009-1)] “LY503ALH - MEMs motion sensor: high performance +/- 30 deg/s analog yaw rate gyroscope”, ST Microelectronics Document ID 15799 Rev 2, July 2009

[ST (2009-2)] “LPR503AL - MEMs motion sensor: dual axis pitch and roll +/- 30 deg/s analog gyroscope”, ST Microelectronics Document ID 15810 Rev 2, July 2009

[Stewart (2012)] Ian Stewart, “First Among Equals”, NewScientist, pp 35 - 38, 11th February, 2012

[Stockwell] Dr Walter Stockwell, “Angle Random Walk”, Crossbow Technology, Technical Note, www.xbow.com

[Strandhagen and Thomas (1963)] A. G. Strandhagen and C. F. Thomas, “Dynamics of Towed Underwater Vehicles”, US Navy Mine Defense Laboratory, Report 219, AD425731, 1963

[Thomas (1994)] Gregory Robert Thomas, “Comparison of Predicted and Measured Towline Tensions”, Masters Thesis, Massachusetts Institute of Technology, 1994

[Thomson (1993)] William T. Thomson, "Theory of vibrations with applications - Fourth edition", Nelson Thornes

[Titterton et al (2004)] David Titterton and John Weston, “Strapdown Inertial Technology”, Institution of Engineering and Technology, 2004

[US Navy (2002)] U.S. Navy, “ U.S. Navy Towing Manual”, SL740-AA-MAN-010, Revision 3, 1st July 2002

[Van Beest (2008)] Van Beest, “Equipment Catalogue - 2008”, www.vanbeest.nl

[van den Boom (1985)] H. J. J. van den Boom, “Dynamic Behavior of Mooring Lines”, Behavior of Offshore Structures, pp.359-368, 1985

[van den Boom (1986)] H. J. J. van den Boom, “Dynamic Forces in Tow Lines”, Transactions of The Royal Institution of Naval Architects Vol. 129, pp.115-126, 1986

[van den Boom and Walenkamp (1986)] H. J. J. van den Boom and H. J. G. Walenkamp, “Theory and Practice in Tow Line Loading”, 9th International Tug Convention, pp.153-162, 1986

[Van Hoorn (2008)] Frank van Hoorn, “Heavy-lift Transport Ships - Overview of Existing Fleet and Future Developments”, Proceedings of the Marine Operations Speciality Symposium 2008

[Viking Moorings (2010)] Viking Moorings, “Viking Moorings - Marine Equipment Handbook, 2010 Edition”, www.viking-moorings.com, 2010

[Vukmirica et ak (2010)] Vladimir Vukmirica, Ivana Trajkovski, and Nada Asanovic, “Two methods for the determination of inertial sensor parameters”, Scientific Technical Review, Vol. 6, No. 3-4, 2010, pp.27-33

[Wagner and Kasties (2004)] Jorg F. Wagner and Gunther Kasties, “Applying the principle of integrated navigation systems to estimating the motion of large vehicles”, Aerospace Science and Technology 8, pp.155-166, 2004

[Walton and Polachek (1959)] Thomas S. Walton and Harry Polachek, “Calculation of Transient Motion of Submerged Cables”, David Taylor Model Basin Report 1279, 1959

[Wichers (2013)] Dr Ir. Johan Wichers, “Guide to Single Point Moorings”, WMooring, July 2013.

[World Meteorological Organisation (1998)] World Meteorological Organization, E. Bouws (Editor), “Guide to Wave Analysis and Forecasting”, WMO-No. 702, 1998

[Woodman (2007)] Oliver J. Woodman, “An Introduction to inertial navigation”, Technical Report Number 696, UCAM-CL-TR-696, ISSN 1476-2986, University of Cambridge, August 2007

[Yang (2007)] Woo Seuk Yang, “Hydrodynamic analysis of mooring lines based on optical tracking experiments”, PhD Thesis, Texas A&M UUniversity, December 2007

Appendix A

MatLab sample lumped mass code implementation

```
1  %-------------------------------------------------------------------
2  %-- Lumped mass solution for cable
3  %-- based on huang 94
4  %--
5  %-- John A. MacSween
6  %-- Rev 00 Jan '11 - base case run to get steady state
7  %-- condition for verification against Low-2006.
8  %--
9  %-- Example 01 - Clump weight on cable
10 %-- Released under GPL License (www.gnu.org)
11 %-------------------------------------------------------------------
12
13 %-------------------------------------------------------------------
14 % Setup global contants and variables
15 %-------------------------------------------------------------------
16 %-------------------------------------------------------------------
17
18 %-------------------------------------------------------------------
19 % Setup global contants and variables
20 %-------------------------------------------------------------------
21 % number of simulations required...
22  clear;
```

```
23
24 run_count = 1;
25 Run_Max_Tension = 0;
26 Freqs = 0;
27
28
29 for r=1: run_count, % this allows multiple runs to be executed...
30
31
32     % here we change whatever initial data we want for each simulation
33     % based on changing index of r...
34
35     % for this run I am looking at seeing if harmonic frequencies can be
36     % found by simply oscillating the ends at different frequecies and
37     % record maximum inline tension...
38     % note no check done to ensure line has settled before starting clock
           ...
39
40      amplitude = 2; % m...
41      freq = 0.01; % inital frequency in hertz...
42      freq_step = 0.01; % step change in frequency for each run...
43      current_freq = freq+ (r-1)*freq_step;
44
45     delta_t = 1/50;
46
47     simulation_time = 10; % secs
48     run_in_time = 10; % secs
49     run_time = simulation_time + run_in_time; %secs
50
51     % the towline end points are scaled into the start positions over the
52     % the run in time steps...
53     run_in_time steps=run_in_time/delta_t;
54
55     time steps = run_time/delta_t;
56
57     node_count = 20;
```

```
58
59      deployed_cable_length=150; % m
60
61      %-------------------------------------------------------------------
62      % Setup intial conditions
63      %-------------------------------------------------------------------
64      % reference indices starting at 1 for matlab debugging. in c++ can
65      % use base 0 which ties in with reference paper...
66
67      % setup unit vectors for ease of data entry. U_L for cable elements and
            U_M
68      % for mass elements...
69
70      U_L= ones(1,node_count-1);
71
72      U_M= ones(1,node_count);
73
74          % Vectors for buoyancy and clump weight elements...
75      Buoys = zeros(1,node_count);
76      Clumps = zeros (1, node_count);
77
78      % unstretched lengths...
79      % unit length...
80      ul=deployed_cable_length/(node_count-1);
81      l=U_L*ul;
82
83      % set up starting coordinates....
84
85      x = zeros(node_count,1);
86      y = zeros(node_count,1);
87      z = zeros(node_count,1);
88
89      % end motions of tug and barge, in format t1,x1,y1,z1; t2,x2,y2,z2 etc
            ...
90      % must be at least two entries...
91
```

```
92      % for this run tow end is submerged end and tug end is upper end...
93
94          % NOTE...
95          % For running dynamic cases here, you would populate each of these
                matrices
96          % with the motions of the end points as x,y,z triplets for each
                time step...
97
98      Tug_Motions = [0,100,0,-5; 15,0,175,0]; % static case only...
99      Tow_Motions = [0,0,0,-55; 15,0,0,0]; % static case only...
100
101         % This next section is the run in methodology for settling the
                towline. It
102         % is accepted that it is a little convoluted and better
                implementations are
103         % possible...!
104
105     x_Tow_start = Tow_Motions(1,2);
106     y_Tow_start = Tow_Motions(1,3);
107     z_Tow_start = Tow_Motions(1,4);
108
109     % set the end position of the tug node afer run in time cmplete...
110     x_Tug_end = Tug_Motions(1,2);
111     y_Tug_end = Tug_Motions(1,3);
112     z_Tug_end = Tug_Motions(1,4);
113
114     x_range = x_Tug_end - x_Tow_start;
115     y_range = y_Tug_end - y_Tow_start;
116     z_range = z_Tug_end - z_Tow_start;
117
118     % calc full towline length...
119     Full_L = sum(l);
120
121     % calc initial range from tow to tug...
122     Initial_L = sqrt(x_range^2 + y_range^2 + z_range^2);
123
```

```
124     % work out end of towline would be if stretched out in line betwen tow
125     % position thrgouh tug position...
126     tmp_tug_x = x_Tow_start + Full_L*x_range/Initial_L;
127     tmp_tug_y = y_Tow_start + Full_L*y_range/Initial_L;
128     tmp_tug_z = z_Tow_start + Full_L*z_range/Initial_L;
129
130     run_in_dx=(tmp_tug_x-x_Tug_end)/run_in_time steps;
131     run_in_dy=(tmp_tug_y-y_Tug_end)/run_in_time steps;
132     run_in_dz=(tmp_tug_z-z_Tug_end)/run_in_time steps;
133
134     % work out x, y and z step sizes for intial set of nodal positions...
135     delta_x = (tmp_tug_x - x_Tow_start)/(node_count-1);
136     delta_y = (tmp_tug_y - y_Tow_start)/(node_count-1);
137     delta_z = (tmp_tug_z - z_Tow_start)/(node_count-1);
138
139     x(1) = x_Tow_start;
140     y(1) = y_Tow_start;
141     z(1) = z_Tow_start;
142
143     % set the x, y and z coords...
144     for i=2:node_count,
145         x(i)=x(i-1) + delta_x;
146         y(i)=y(i-1) + delta_y;
147         z(i)=z(i-1) + delta_z;
148     end;
149
150     % for use in setting graph axis limits...
151     x_max=max(x)+0.2;
152     x_min=min(x)-0.2;
153     y_max=max(y)+1;
154     y_min=min(y)-1;
155     z_max=max(z)+0.5;
156     z_min=min(z)-50;
157
158     % set up starting velocities
159     xv = zeros(node_count,1);
```

```
160     yv = zeros(node_count,1);
161     zv = zeros(node_count,1);
162
163     % set up starting accelerations
164     xa = zeros(node_count,1);
165     ya = zeros(node_count,1);
166     za = zeros(node_count,1);
167
168
169     % setup diameter in metres...
170     % wire rope dia...
171         % NOTE... Each segment can have different properties, just access
                the individual
172         % elements of "d" below and set each up in turn. Same applies to "k
                ", "m", "E"
173         % and "sigma" below...
174     wr_dia = 0.055;
175     d=U_L*wr_dia;
176
177     % setup mass
178     um = 55; %unit mass in kg/m...
179     m = um * ul * U_M;
180
181     %add 250 kg clump weight at node 10...
182     %m(10) = m(10) + 250;
183
184     % setup added mass
185     k = 1 * U_M;
186
187     % setup cross sectional area (sigma), density (mu), gravitational
            acceleration (g)
188     % and Youngs Modulas (E) for cable elements
189     sigma = U_L*(wr_dia/2)^2*pi;
190
191     g = 9.807;
192     mu = 1339.7 * U_L;
```

```
193     % allow for E to vary along length - future addition...
194     % E = 2.10E9 * U_L
195     % stiffness...
196     E = 4.0597E9 * U_L;
197
198     % setup density of fluid as 1025 kg/m^3
199     rho = 1000;
200     % normal and tangential drag coefficients
201     C_N = 1.00 * U_L;
202     C_T = 0.01 * U_L;
203     % setup simple current profile for now. option to vary this with time
            and
204     % position later... specified as x, y, and z velocity in m/s...
205     U_C = [0.0; 0.0; 0.0];
206
207     % calculate added mass factors for each of the cable elements.
208     e=[];
209     for i=1:node_count-1,
210         e(i)= rho * k(i) * sigma(i) * l(i);
211     end;
212     % show e
213      e;
214
215     % set up arrays for storing data position, velocity and acceleration
216     % data as the numerical run progresses...
217     x_data = [];
218     y_data = [];
219     z_data= [];
220
221     xv_data = [];
222     yv_data = [];
223     zv_data= [];
224
225     xa_data = [];
226     ya_data = [];
227     za_data= [];
```

```
228
229     % add intial coordinates to starting conditions (twice as we require
            two
230     % time steps to get the solver started due to finite difference
231     % equations)... transpose to store rows for each time step...
232     % set first two time steps to be stationary...starting condition...
233     x_data = [x_data; x'; x'];
234     y_data = [y_data; y'; y'];
235     z_data = [z_data; z'; z'];
236
237
238     xv_data = [xv_data; xv'; xv'];
239     yv_data = [yv_data; yv'; yv'];
240     zv_data = [zv_data; zv'; zv'];
241
242     xa_data = [xa_data; xa'; xa'];
243     ya_data = [ya_data; ya'; ya'];
244     za_data = [za_data; za'; za'];
245
246     % tension storage array...
247     Max_Tension = 0;
248     Tow_Tension = 0;
249     Tug_Tension = 0;
250
251
252     for j=3: time steps,
253         % setup known values of x,y,z @ i=1 and i=10...
254         % TODO with real values...
255         % here we set the new end values, then we run through the time step
                and
256         % store the other values by "pushing back" in c++ speak to the
              storage
257         % arrays...
258
259         % EXAMPLE CODE... This code can be used to drive the end points
              using
```

```
260             % user specified harmonic motions. Left in for guidance...
261
262         %if j>run_in_time steps
263         %    current_time=run_time*j/time steps; % current time in secs
                from start of run...
264         %    offset = sin(2*3.1415*current_time*current_freq)*amplitude-sin
                (2*3.1415*(current_time-delta_t)*current_freq)*amplitude;;
265         %    y(node_count)=y(node_count) + offset;
266         %    y(1)=y(1) - offset;
267         %end;
268
269         %z(node_count)=z(node_count) + sin(j/50)*0.005;
270         %z(1)=z(1) + sin(j/50)*(0.005);
271
272
273         if j<run_in_time steps
274             x(node_count)=x(node_count)-run_in_dx;
275             y(node_count)=y(node_count)-run_in_dy;
276             z(node_count)=z(node_count)-run_in_dz;
277         end;
278
279             % EXAMPLE CODE... Here an example is shown how to add
                    weights and change current
280             % velocity at specific points in the simulation...
281         if j==run_in_time steps
282             U_C = [0; 2.5; 0];
283             Buoys(6) = 25000;
284         end;
285
286         % calculate Tensions...
287         T=[];
288         for i=1:(node_count-1),
289             T(i)=sigma(i) * E(i) * ((sqrt((x(i+1)-x(i))^2 + (y(i+1)-y(i))^2
                    + (z(i+1)-z(i))^2)) / l(i) - 1);
290             % check if compression and if so set to zero...
291             if T(i)<0
```

```
292                 T(i) = 0;
293             end;
294         end;
295         % show T
296         T;
297
298         % create 3d triangle lengths required for calculating angles for
                each
299         % segment. Inefficient but good for debugging for now...
300         L=[];
301         L1=[];
302         L2=[];
303         L3=[];
304         L4=[];
305
306         for i=1:(node_count-1),
307             L(i)=sqrt((x(i+1)-x(i))^2 + (y(i+1)-y(i))^2 + (z(i+1)-z(i))^2);
308             L1(i)=sqrt((x(i+1)-x(i))^2 + (y(i+1)-y(i))^2);
309             L4(i)=z(i+1)-z(i);
310             L2(i)=x(i+1)-x(i);
311             L3(i)=y(i+1)-y(i);
312         end;
313
314
315         % calculate trig identities. vectorised, would need to break up in
                c++...
316         sin_phi=L4 ./ L;
317         sin_theta=L2 ./ L1;
318         cos_phi=L1 ./ L;
319         cos_theta=L3 ./ L1;
320
321
322         % we know the motions at each end so we need to loop through each
                node from
323         % i=2 to i=nodecount-1. This means there are 3*(node_count-2)
                unknowns.
```

```
324         % create std matrices that are refreshed every time step
325         % goal is to create the following form for each time step to solve:
326         %       [LHS_Full].[X] = [RHS_Full]
327         % where:
328         %       [LHS_Full] = [A_Full]+[BC_Full]
329
330         A_Full=zeros(3*(node_count-2), 3*(node_count-2));
331         BC_Full=zeros(3*(node_count-2), 3*(node_count-2));
332         B_Full=zeros(3*(node_count-2), 2*(node_count-2));
333         sigma_E=zeros(2*(node_count-2), 1);
334         RHS_Full=zeros(3*(node_count-2), 1);
335
336         % for each value of i between 2 and end -1 create the set of three
337         % simultaneous equations as per eq 18 from [Huang94]...
338
339         % do ends first...
340         % i=2...
341         A= zeros(3,3);
342         B= zeros(3,2);
343         C= zeros(2,9);
344
345         % setup position on line...
346         i=2;
347
348         % populate A...
349         % row 1...
350         A(1,1) = m(i) + (e(i)*(1-sin_theta(i)^2*cos_phi(i)^2) + (e(i-1)*(1-
                sin_theta(i-1)^2*cos_phi(i-1)^2))); %A(1,1)
351         A(1,2) = -0.5*(e(i)*sin_theta(i)*cos_theta(i)*cos_phi(i)^2 + e(i-1)
                *sin_theta(i-1)*cos_theta(i-1)*cos_phi(i-1)^2) ; % A(1,2)
352         A(1,3) = -0.5*(e(i)*sin_theta(i)*sin_phi(i)*cos_phi(i) + e(i-1)*
                sin_theta(i-1)*sin_phi(i-1)*cos_phi(i-1)); % A(1,3)
353
354         % row 2...
355         A(2,1) = A(1,2); % A(2,1) = A(1,2)
356         A(2,2) = m(i) + 0.5*(e(i)*(1-cos_theta(i)^2*cos_phi(i)^2) + e(i-1)
```

```
        *(1-cos_theta(i-1)^2*cos_phi(i-1)^2)); % A(2,2)
357     A(2,3) = -0.5*(e(i)*cos_theta(i)*sin_phi(i)*cos_phi(i) + e(i-1)*
            cos_theta(i-1)*sin_phi(i-1)*cos_phi(i-1)); % A(2,3)
358
359     % row 3...
360     A(3,1) = A(1,3); % A(3,1)=A(1,3)
361     A(3,2) = A(2,3); % A(3,2) = A(2,3)
362     A(3,3) = m(i) + 0.5*(e(i)*cos_phi(i)^2 + e(i-1)*cos_phi(i-1)^2); %
            A(3,3)
363
364     % populate B...
365     B(1,1) = sin_theta(i-1)*cos_phi(i-1);
366     B(2,1) = cos_theta(i-1)*cos_phi(i-1);
367     B(3,1) = sin_phi(i-1);
368     B(1,2) = -sin_theta(i)*cos_phi(i);
369     B(2,2) = -cos_theta(i)*cos_phi(i);
370     B(3,2) = -sin_phi(i);
371
372     %create C
373     q1 = l(i-1)^2 * ((T(i-1)/(sigma(i-1)*E(i-1)))+1);
374     q2 = l(i)^2 * ((T(i)/(sigma(i)*E(i)))+1);
375     C(1,1) = -sigma(i-1)*E(i-1)*(x(i)-x(i-1))/q1;
376     C(1,2) = -sigma(i-1)*E(i-1)*(y(i)-y(i-1))/q1;
377     C(1,3) = -sigma(i-1)*E(i-1)*(z(i)-z(i-1))/q1;
378     C(1,4) = -C(1,1);
379     C(1,5) = -C(1,2);
380     C(1,6) = -C(1,3);
381     C(2,4) = -sigma(i)*E(i)*(x(i+1)-x(i))/q2;
382     C(2,5) = -sigma(i)*E(i)*(y(i+1)-y(i))/q2;
383     C(2,6) = -sigma(i)*E(i)*(z(i+1)-z(i))/q2;
384     C(2,7) = -C(2,4);
385     C(2,8) = -C(2,5);
386     C(2,9) = -C(2,6);
387
388     %create temp storage for sigma_E pair for this node...
389     tmp_Sigma_E = [sigma(i-1)*E(i-1) sigma(i)*E(i)]';
```

```
390
391         % at each end we must break off a section of the BC matrix for
                moving
392         % across to the right hand side, reference appendix A of thesis...
393         BC_tmp=B*C;
394         BC_Full(1:3, 1:6)=BC_tmp(1:3, 4:9);
395
396         % top left boundary condition 3x1 and just move to RHS now. note we
397         % will build RHS by adding elements to it as they are calculated...
398         temp_vec=(BC_tmp(1:3, 1:3)*[x(1); y(1); z(1)]);
399         RHS_Full(1:3, 1)=RHS_Full(1:3, 1)-temp_vec;
400
401         % move A to A_Full matrix...
402         A_Full(1:3, 1:3)=A;
403
404         % move B to B_Full matrix...
405         B_Full(1:3, 1:2)=B;
406
407         % create sigma_E stiffness element...
408         sigma_E(1:2,1)=tmp_Sigma_E;
409
410         %-----------------------------------
411         % bottom right now...
412         %-----------------------------------
413
414         % i=node_count-1...
415         A= zeros(3,3);
416         B= zeros(3,2);
417         C= zeros(2,9);
418
419         % setup position on line...
420         i=node_count-1;
421
422         % populate A...
423         % row 1...
424         A(1,1) = m(i) + (e(i)*(1-sin_theta(i)^2*cos_phi(i)^2) + (e(i-1)*(1-
```

```
        sin_theta(i-1)^2*cos_phi(i-1)^2))); %A(1,1)
425     A(1,2) = -0.5*(e(i)*sin_theta(i)*cos_theta(i)*cos_phi(i)^2 + e(i-1)
        *sin_theta(i-1)*cos_theta(i-1)*cos_phi(i-1)^2) ; % A(1,2)
426     A(1,3) = -0.5*(e(i)*sin_theta(i)*sin_phi(i)*cos_phi(i) + e(i-1)*
        sin_theta(i-1)*sin_phi(i-1)*cos_phi(i-1)); % A(1,3)
427
428     % row 2...
429     A(2,1) = A(1,2); % A(2,1) = A(1,2)
430     A(2,2) = m(i) + 0.5*(e(i)*(1-cos_theta(i)^2*cos_phi(i)^2) + e(i-1)
        *(1-cos_theta(i-1)^2*cos_phi(i-1)^2)); % A(2,2)
431     A(2,3) = -0.5*(e(i)*cos_theta(i)*sin_phi(i)*cos_phi(i) + e(i-1)*
        cos_theta(i-1)*sin_phi(i-1)*cos_phi(i-1)); % A(2,3)
432
433     % row 3...
434     A(3,1) = A(1,3); % A(3,1)=A(1,3)
435     A(3,2) = A(2,3); % A(3,2) = A(2,3)
436     A(3,3) = m(i) + 0.5*(e(i)*cos_phi(i)^2 + e(i-1)*cos_phi(i-1)^2); %
        A(3,3)
437
438     % populate B...
439     B(1,1) = sin_theta(i-1)*cos_phi(i-1);
440     B(2,1) = cos_theta(i-1)*cos_phi(i-1);
441     B(3,1) = sin_phi(i-1);
442     B(1,2) = -sin_theta(i)*cos_phi(i);
443     B(2,2) = -cos_theta(i)*cos_phi(i);
444     B(3,2) = -sin_phi(i);
445
446     %create C
447     q1 = l(i-1)^2 * ((T(i-1)/(sigma(i-1)*E(i-1)))+1);
448     q2 = l(i)^2 * ((T(i)/(sigma(i)*E(i)))+1);
449     C(1,1) = -sigma(i-1)*E(i-1)*(x(i)-x(i-1))/q1;
450     C(1,2) = -sigma(i-1)*E(i-1)*(y(i)-y(i-1))/q1;
451     C(1,3) = -sigma(i-1)*E(i-1)*(z(i)-z(i-1))/q1;
452     C(1,4) = -C(1,1);
453     C(1,5) = -C(1,2);
454     C(1,6) = -C(1,3);
```

```
455         C(2,4) = -sigma(i)*E(i)*(x(i+1)-x(i))/q2;
456         C(2,5) = -sigma(i)*E(i)*(y(i+1)-y(i))/q2;
457         C(2,6) = -sigma(i)*E(i)*(z(i+1)-z(i))/q2;
458         C(2,7) = -C(2,4);
459         C(2,8) = -C(2,5);
460         C(2,9) = -C(2,6);
461
462         % Create BC at i=node_count-1 move last portion of BC_tmp & x(
                node_count),
463         % y(node_count), & z(node_count) to RHS and add whats left to btm
                right
464         % slot of BC_Full...
465         BC_tmp=B*C;
466         start_row=3*(node_count-2)-2;
467         end_row=3*(node_count-2);
468         start_col=3*(node_count-2)-5;
469         end_col=3*(node_count-2);
470         B_start_col=2*(node_count-2)-1;
471         temp_vec = BC_tmp(1:3, 7:9)*[x(node_count); y(node_count); z(
                node_count)];
472         BC_Full(start_row:end_row, start_col:end_col)=BC_tmp(1:3, 1:6);
473
474         % btm right boundary condition 3x1 and just move to RHS now...
475         RHS_Full(start_row:end_row, 1)=RHS_Full(start_row:end_row, 1)-
                temp_vec;
476
477         % move A to A_Full matrix...note same rows and cols used as opposed
                 to
478         % BC matrix where rows and columns are staggered due to overlapping
479         % terms...
480         A_Full(start_row:end_row, start_row:end_row)=A ;
481
482         B_Full(start_row:start_row+2, B_start_col:B_start_col+1)=B ;
483
484         tmp_Sigma_E = [sigma(i-1)*E(i-1) sigma(i)*E(i)]';
485         % strt col etc used here as this is pair of matrix multiplication
```

```
                that
486         % produces single column vector and therefore row count must match
                col
487         % count in B matrix...
488         sigma_E(B_start_col:B_start_col+1,1)=tmp_Sigma_E;
489
490         % create vector of "f"
491         % assemble force vector in rhs of system of equations
492         % first calculate values for each length segment. then combine to
                column
493         % for drag at each node
494         FDSeg = [];
495         FDN= zeros(3*node_count-1,1); % stored in triplets of FDNx1, FDNy1,
                FDNz1, FDNx2 etc etc
496
497             % relative segment velocities based on average values for
                    each bounding node
498         % these are the velocities of water over each segemtnt taking into
499         % account current velicity and direction
500
501         for i=1:(node_count-1),
502             % calculate segment velocities
503             V_Cx = 0.5 * (xv_data(j-1,i)+xv_data(j-1,i+1));
504             V_Cy = 0.5 * (yv_data(j-1,i)+yv_data(j-1,i+1));
505             V_Cz = 0.5 * (zv_data(j-1,i)+zv_data(j-1,i+1));
506             V_Ctemp = [V_Cx; V_Cy; V_Cz];
507             % subtract current velocities from segement velocities to get
                    relative
508             % velocities for drag calculation
509             V = V_Ctemp - U_C;
510
511             % calculate drag at each segment
512             P11 = 1-sin_theta(i)^2*cos_phi(i)^2;
513             P12 = -sin_theta(i)*cos_theta(i)*cos_phi(i)^2;
514             P13 = -sin_theta(i)*sin_phi(i)*cos_phi(i);
515             P21 = P12;
```

```
516             P22 = 1-cos_theta(i)^2*cos_phi(i)^2;
517             P23 = -cos_theta(i)*sin_phi(i)*cos_phi(i);
518             P31 = -sin_theta(i)*sin_phi(i)*cos_phi(i);
519             P32 = -cos_theta(i)*sin_phi(i)*cos_phi(i);
520             P33 = cos_phi(i)^2;
521             P = [ P11 P12 P13; P21 P22 P23; P31 P32 P33];
522             I = eye(3,3);
523             Q = I-P;
524
525             % misc matrices to obtain positive modulas of matrix PV and QV
526             powsqrt = 0.5*ones(3,1);
527             powsqr = 2.0*ones(3,1);
528
529             PV = P * V;
530             QV = Q * V;
531
532             tempPV = realpow(PV,powsqr);
533             tempPV = realpow(tempPV,powsqrt);
534             tempQV = realpow(QV,powsqr);
535             tempQV = realpow(tempQV,powsqrt);
536             FDtmp = - 0.5*rho*C_N(i)*l(i)*d(i) * PV .* tempPV - (pi/2)*rho*
                    C_T(i)*l(i)*d(i)* QV .* tempQV ;
537
538             % populate segment drag vectors
539             FDSeg = [FDSeg;FDtmp];
540             %V = [V; V];
541         end; %end i stepping to create PV and QV matrices
542
543         % taking each of the segment values above, populate node drag based
                on
544         % average of drag on segment on each side of the lumped mass.
545         % this is where we would add extra values of we want to associate
              drag
546         % with inline items on the cable
547         % set up first and last to prevent out of bound errors
548         FDSeg1 = [0;0;0;FDSeg];
```

```
549         FDSeg2 = [FDSeg;0;0;0];
550         F = (FDSeg1 + FDSeg2)*0.5; % F now filled with force on each node
                based on drag
551
552         % add force at each node based on z direction buoyancy and gravity
                ...
553         F(3)=F(3) + 0.5*rho*g*l(1)*sigma(1) - m(1)*g;
554         % unstretched length as should not pick up more buoyancy if
                stretched
555         F(30)=F(30) + 0.5*rho*g*l(node_count-1)*sigma(node_count-1) - m(
                node_count)*g;
556         for i=2:(node_count-1),
557             F(3*i)=F(3*i) + 0.5*rho*g* (l(i-1)*sigma(i-1) + l(i)*sigma(i))
                    - m(i)*g + Buoys(i) + Clumps(i);
558         end; %end i stepping to add buoyancy and gravity to z terms..
559
560         % assemble rest of A, B, BC and sigmaE...
561         for i=3:(node_count-2),
562             A= zeros(3,3);
563             B= zeros(3,2);
564             C= zeros(2,9);
565             BCs_r=3*(i-1)-2; %BC start_row...
566             Bs_r=BCs_r; %vB start row is same as BC, both sub matricies
                    have 3 rows...
567             Bs_c=2*(i-1)-1; %B start col...
568             BCe_r=3*(i-1); % end_row...
569             BCs_c=3*(i-1)-5; %start_col...
570             BCe_c=3*(i-1)+3; %end_col...
571             As_r=BCs_r;
572             As_c=BCs_r; %3x3 placed on diagonal so same row and col
573             % row 1 at 3i-2...
574             A(1,1) = m(i) + (e(i)*(1-sin_theta(i)^2*cos_phi(i)^2) + (e(i-1)
                    *(1-sin_theta(i-1)^2*cos_phi(i-1)^2))); %A(1,1)
575             A(1,2) = -0.5*(e(i)*sin_theta(i)*cos_theta(i)*cos_phi(i)^2 + e(
                    i-1)*sin_theta(i-1)*cos_theta(i-1)*cos_phi(i-1)^2) ; % A
                    (1,2)
```

```
576             A(1,3) = -0.5*(e(i)*sin_theta(i)*sin_phi(i)*cos_phi(i) + e(i-1)
                    *sin_theta(i-1)*sin_phi(i-1)*cos_phi(i-1)); % A(1,3)
577
578             % row 2 at 3i-1...
579             A(2,1) = A(1,2); % A(2,1) = A(1,2)
580             A(2,2) = m(i) + 0.5*(e(i)*(1-cos_theta(i)^2*cos_phi(i)^2) + e(i
                    -1)*(1-cos_theta(i-1)^2*cos_phi(i-1)^2)); % A(2,2)
581             A(2,3) = -0.5*(e(i)*cos_theta(i)*sin_phi(i)*cos_phi(i) + e(i-1)
                    *cos_theta(i-1)*sin_phi(i-1)*cos_phi(i-1)); % A(2,3)
582
583             % row 3 at 3i...
584             A(3,1) = A(1,3); % A(3,1)=A(1,3)
585             A(3,2) = A(2,3); % A(3,2) = A(2,3)
586             A(3,3) = m(i) + 0.5*(e(i)*cos_phi(i)^2 + e(i-1)*cos_phi(i-1)^2)
                    ; % A(3,3)
587
588             % populate B...
589             B(1,1) = sin_theta(i-1)*cos_phi(i-1);
590             B(2,1) = cos_theta(i-1)*cos_phi(i-1);
591             B(3,1) = sin_phi(i-1);
592             B(1,2) = -sin_theta(i)*cos_phi(i);
593             B(2,2) = -cos_theta(i)*cos_phi(i);
594             B(3,2) = -sin_phi(i);
595
596             %create C
597             q1 = l(i-1)^2 * ((T(i-1)/(sigma(i-1)*E(i-1)))+1);
598             q2 = l(i)^2 * ((T(i)/(sigma(i)*E(i)))+1);
599             C(1,1) = -sigma(i-1)*E(i-1)*(x(i)-x(i-1))/q1;
600             C(1,2) = -sigma(i-1)*E(i-1)*(y(i)-y(i-1))/q1;
601             C(1,3) = -sigma(i-1)*E(i-1)*(z(i)-z(i-1))/q1;
602             C(1,4) = -C(1,1);
603             C(1,5) = -C(1,2);
604             C(1,6) = -C(1,3);
605             C(2,4) = -sigma(i)*E(i)*(x(i+1)-x(i))/q2;
606             C(2,5) = -sigma(i)*E(i)*(y(i+1)-y(i))/q2;
607             C(2,6) = -sigma(i)*E(i)*(z(i+1)-z(i))/q2;
```

```
608             C(2,7) = -C(2,4);
609             C(2,8) = -C(2,5);
610             C(2,9) = -C(2,6);
611
612             % add A to full matrix...
613             A_Full(As_r:As_r+2, As_c:As_c+2)=A ;
614
615             % create BC_tmp and then move into full matrix...
616             BC_tmp=B*C;
617             BC_Full(BCs_r:BCe_r, BCs_c:BCe_c)=BC_tmp(1:3, 1:9);
618             B_Full(Bs_r:Bs_r+2, Bs_c:Bs_c+1)=B(1:3, 1:2);
619
620             %create sigma_and move into full vector for
621             tmp_Sigma_E =[sigma(i-1)*E(i-1) sigma(i)*E(i)]';
622             sigma_E(Bs_c:Bs_c+1,1)=tmp_Sigma_E;
623
624         end; %end i stepping for A and BC matrix creation
625
626         % debug show A, BC etc...
627         A_Full=A_Full/(delta_t^2);
628         BC_Full;
629         sigma_E;
630         LHS_Full=A_Full+BC_Full;
631
632         % with LHS complete, now need to complete RHS...
633
634         % RHS made up as follows:
635
636         % debug show F...
637         F;  % 30 forces here but should be 24 to fit matrix dimensions...we
                know
638             % first and last conditions and so can remove these...
639         f_RHS = zeros(3*(node_count-2), 1);
640         f_RHS(1:3*(node_count-2),1) = F(4:3*(node_count-1),1);
641
642         % create vector of A/delta_t^2 x@j-1 == "AdtX_past"
```

```
643         % create interleaved x@j-1. We store as 3 arrays of x y and z.
644         % numerical process requires these as single array of
645         % [x2, y2, z2, x3, y3, ... etc]...
646         % lets call x@j-1 "X_past", x@j "X_curr" and x@j+1 "X_fut"...
647         % reset vectors...
648         X_past = []; % this is actually at j-2 as j is the future time step
                we are working out
649         X_curr = []; % this is j-1 i.e. last time step worked out...
650
651         for i=2:(node_count-1),
652             X_past = [X_past; x_data(j-2,i)'; y_data(j-2,i)'; z_data(j-2,i)
                    '];
653             X_curr = [X_curr; x_data(j-1,i)'; y_data(j-1,i)'; z_data(j-1,i)
                    '];
654         end;
655
656         AdtX_past = (A_Full)*X_past; % Note dont need to divide by delta_t
                ^2, already done it earlier...
657
658
659         % create vector of 2/delta_^2 x@j == "dtX_curr"
660         dtX_curr = (2 * A_Full) * X_curr;
661
662         % create vector of "BsigmaE"
663         BsigmaE = B_Full * sigma_E;
664
665         RHS_Full  = RHS_Full + f_RHS - AdtX_past + dtX_curr + BsigmaE;
666
667         RHS_Full;  %Debug show option...
668         LHS_Full;  %Debug show option...
669
670         % then simply solve...
671         X_pred = LHS_Full\RHS_Full;
672
673         % extract interleaved data from x positions and store...
674         % store current x y and z data in storage arrays...
```

```
675         for i=2:(node_count-1),
676             x(i) = X_pred(3*(i-2)+1);
677             y(i) = X_pred(3*(i-2)+2);
678             z(i) = X_pred(3*(i-2)+3);
679         end;
680
681         %save to storage arrays...
682         x_data = [x_data; x'];
683         y_data = [y_data; y'];
684         z_data = [z_data; z'];
685
686         %debug plot...
687         %plot(X_pred);
688
689         %subplot...
690         subplot(2,2,1);
691         plot (x_data(j,:),z_data(j,:), '-o')
692         title ('Side elevation');
693         axis equal;
694         xlabel('x (m)'); ylabel('z (m)');
695
696         %axis ([x_min x_max y_min y_max z_min z_max])
697         grid on
698         subplot(2,2,2);
699         plot (y_data(j,:),z_data(j,:), '-o')
700         title ('End elevation');
701         axis equal;
702         xlabel('y (m)'); ylabel('z (m)');
703         grid on
704
705         subplot(2,2,3);
706         plot (x_data(j,:),y_data(j,:), '-o')
707         title ('Plan');
708         axis equal;
709         xlabel('x (m)'); ylabel('y (m)');
710         grid on
```

```
711
712         subplot(2,2,4);
713         plot3 (x_data(j,:), y_data(j,:),z_data(j,:), '-o')
714         axis square;
715         axis equal;
716         xlabel('x (m)'); ylabel('y (m)'); zlabel('z (m)');
717         grid on
718         title(['Isometric Time - ' num2str(run_time*j/time steps, '%.3f') '
                seconds. Top tension - ' num2str(T(node_count-1)/1000, '%.1f')
               ' kN' ])
719         drawnow;
720
721         % only record data after run in period is over...
722         if j>(run_in_time steps+5000) % start recording after 70 secs
723             Max_Tension= [Max_Tension; max(T)/1000];
724             Tow_Tension= [Tow_Tension; T(1)/1000];
725             Tug_Tension= [Tug_Tension; T(node_count-1)/1000];
726             %M(j-2) = getframe;
727         end;
728
729         % before moving onto next time step calculate and store new node
730         % velocities and accelerations...
731
732         % velocities first...
733         for i=1:(node_count),
734             xv(i) = (x_data(j,i)-x_data(j-1,i))/delta_t;
735             yv(i) = (y_data(j,i)-y_data(j-1,i))/delta_t;
736             zv(i) = (z_data(j,i)-z_data(j-1,i))/delta_t;
737         end;
738         %save to storage arrays...
739         xv_data = [xv_data; xv'];
740         yv_data = [yv_data; yv'];
741         zv_data = [zv_data; zv'];
742
743                 % NOTE... Node accelerations not required for base code but
                        detail below
```

```
744                 % left to show how to store these as well if required for
                        post processing...
745
746         %for i=1:(node_count),
747         %    xa(i) = (xv_data(j,i)-xv_data(j-1,i))/delta_t;
748         %    ya(i) = (yv_data(j,i)-yv_data(j-1,i))/delta_t;
749         %    za(i) = (zv_data(j,i)-zv_data(j-1,i))/delta_t;
750         %end;
751
752         %save to storage arrays
753         %xa_data = [xa_data; xa'; xa'];
754         %ya_data = [ya_data; ya'; ya'];
755         %za_data = [za_data; za'; za'];
756
757
758     end; %end stepping j through time steps...
759
760
761 % here we store what we want to keep between runs...
762 Run_Max_Tension = [Run_Max_Tension; max(Max_Tension)]
763 Freqs = [Freqs; current_freq];
764
765 end; %end stepping through each simulation run...
```

Appendix B

Original completed tug master voyage log forms

HENRY ABRAM & SONS
ESTABLISHED 1899

Towing Vessel Details							
Towing Vessel Name	Displacement	Draught Aft	Draught Fwd	KMT	KML	VCG	LCG
AHT "ERACLEA"	2012, 76	5,70	5,30	7.242	42,494	4.698	21.692
Towed Vessel/Barge Details							
Tow/Barge Name	Displacement	Draught Aft	Draught Fwd	KMT	KML	VCG	LCG
BOA BARGE 35							

Tow Record			
Departure Port	Destination Port	Tow wire Diameter/Details	Notes
PORTSMOUTH	ROSYTH	60 mm	

Voyage Details						
Time	Date	Deployed length of tow line (m)	Estimated Sea State			Tug Utilisation
			Seastate (ref images over)	Significant Wave Height (m)	Wave Direction	Average Bollard Pull or Engine Power at time of record
24.00	26/08/2014	450 mt	FORCE 4	1,5	E	20/30 TON - 70% PITCH
04.00	27/08/2014	450 mt	FORCE 3	> 1,0	ENE	20/30 TON - 70% PITCH
08.00	27/08/2014	450 mt	FORCE 4	> 1,0	ENE	20/30 TON - 70% PITCH

1

Figure B.0.1: LB02 voyage tow record sheet 01

HENRY ABRAM & SONS
ESTABLISHED 1899

Voyage Details (Cont)						
Time	Date	Deployed length of tow line (m)	Estimated Sea State			Tug Utilisation
			Seastate (ref images over)	Significant Wave Height (m)	Wave Direction	Average Bollard Pull or Engine Power at time of record
12 00	27/08/2014	450 mt	FORCE 3	< 1.0	ENE	20/30 TON - 70% PITCH
16 00	27/08/2014	450 mt	FORCE 3/2	0,5	NE	20/30 TON - 70% PITCH
20 00	27/08/2014	450 mt	FORCE 2	0,5	NE	20/30 TON - 70% PITCH
24 00	27/08/2014	450 mt	FORCE 2	0,5	SE	20/30 TONS - 70% PITCH
04 00	28/08/2014	450 mt	FORCE 2	0,5	SE	20/30 TON - 70% PITCH
08 00	28/08/2014	450 mt	FORCE 4	1,0	SSE	20/30 TON - 70% PITCH
12 00	28/08/2014	250 mt	FORCE 3	1,0	SSE	10/15 TON - 40% PITCH
16 00	28/08/2014	250 mt	FORCE 3	1,0	SSE	10/15 TON - 40% PITCH
20 00	28/08/2014	250 mt	FORCE 2	< 1,0	SSW	10/15 TON - 40% PITCH

2

Figure B.0.2: LB02 voyage tow record sheet 02

HENRY ABRAM & SONS
ESTABLISHED 1899

Voyage Details (Cont)						
Time	Date	Deployed length of tow line (m)	Estimated Sea State			Tug Utilisation
			Seastate (ref images over)	Significant Wave Height (m)	Wave Direction	Average Bollard Pull or Engine Power at time of record
24 00	28/08/2014	250 mt	FORCE 2	> 0,5	SSW	10/15 TON - 40% PITCH
04 00	29/08/2014	250 mt	FORCE 2	> 0,5	SSW	10/15 TON - 40% PITCH
08 00	29/08/2014	250 mt	FORCE 3/4	1,5	SSW	10/15 TON - 40% PITCH
12 00	29/08/2014	250 mt	FORCE 3/4	1,5	SSW	10/15 TON - 40% PITCH
16 00	29/08/2014	250 mt	FORCE 3/2	< 1,0	SSW	10/15 TON - 40% PITCH
20 00	29/08/2014	250 mt	FORCE 3	1,0	SW	10/15 TON - 40% PITCH
24 00	29/08/2014	250 mt	FORCE 3	< 1,0	SW	10/15 TON - 40% PITCH
04 00	30/08/2014	250 mt	FORCE 2	> 0,5	SW	10/15 TON - 40% PITCH
08 00	30/08/2014	250 mt	FORCE 3	> 0,5	W	10/15 TON - 40% PITCH

3

Figure B.0.3: LB02 voyage tow record sheet 03

HENRY ABRAM & SONS
ESTABLISHED 1899

Voyage Details (Cont)						
Time	Date	Deployed length of tow line (m)	Estimated Sea State			Tug Utilisation
			Seastate (ref images over)	Significant Wave Height (m)	Wave Direction	Average Bollard Pull or Engine Power at time of record
12.00	30/08/2014	150 mt	FORCE 3	>0,5	W	10/15 TON - PITCH 35%
					→	ARRIVAL ROSYTH

6

Figure B.0.4: LB02 voyage tow record sheet 04

Appendix C

Inline submersible load cell logger

A high level design for an inline loadcell with a milled central section that can house the existing logger pcb on one side and a DCell battery array on the other. The device would benefit from having access to readings from the one board sensors (accelerometers, tilt and gyros thereby effectively giving acceleration information at a specific node of interest along the towlline) as well as using spare channels for access a strain guage that could be bonded to the central 10mm thick “strain” plate.

FEA analysis showed that under tensile loads of up to 120 Te, the deformation across the bolted plate opening as well as stresses in the central 10mm thick diaphram plate were all acceptable.

Time constraints were such that the device was never manufactured however costs for its creation and testing were obtained and were not prohibitive. By having it certified and tested by authorised test house, an inline sensor that could verify the data generated by the towline numerical analysis could be created. It would not meet the criteria for ease of use on any tow of opportunity however sporadic use could verify the towline tensions.

Its use would be worth consideration for future work on this subject.

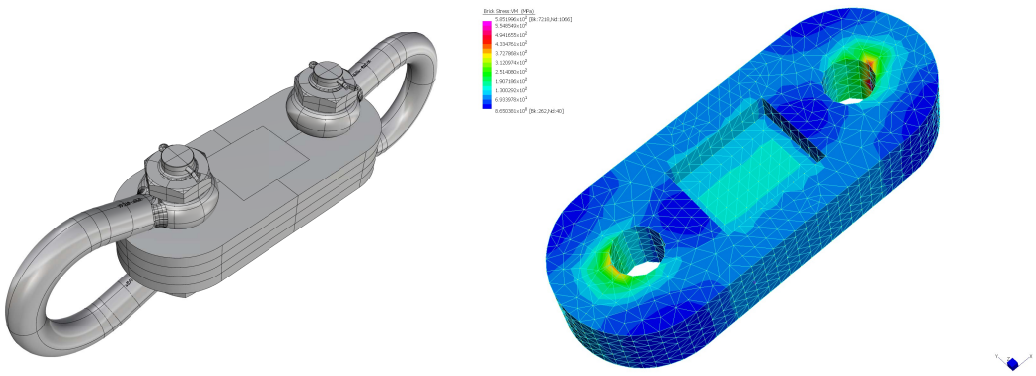

Figure C.0.1: Inline data logging submersible loadcell